Politecnico di Torino

UNIVERSITÀ DI TORINO

Doctoral Dissertation
Doctoral Program in Bioengineering and Medical-Surgical Sciences (35th Cycle)

Strategies for the molecular-level understanding of small molecule-target interactions and dynamics through tailored computational modelling

By

Eric Adriano Zizzi

Supervisor(s):
Prof. Marco A. Deriu, Supervisor
Prof. Jack A. Tuszynski, Co-Supervisor

Doctoral Examination Committee:

Prof. Dr. Donald Weaver, University of Toronto
Prof. Dr. Andrea Danani, Univ. of Applied Sciences of Southern Switzerland
Prof. Dr. Diego Gallo, Politecnico di Torino

Politecnico di Torino – Università degli Studi di Torino
2023

Declaration

I hereby declare that the contents and organization of this dissertation constitute my own original work and do not compromise in any way the rights of third parties, including those relating to the security of personal data.

This doctoral dissertation is based on material that was previously published and for which the author holds the right for inclusion. Original publications are acknowledged in the pertinent chapters.

Eric A. Zizzi

2023

* This dissertation is presented in partial fulfillment of the requirements for **Ph.D. degree** in the Graduate School of Politecnico di Torino (ScuDo) and the University of Turin (UniTo).

A Olivo, che lo sapeva sin dall'inizio…

Acknowledgments

I would like to express my deepest gratitude to my supervisors at Politecnico di Torino, prof. Marco A. Deriu and prof. Jack A. Tuszynski. The achievements that I earned throughout these years would most certainly not have been possible without their constant support, the insightful discussions, and their expert supervision. Also, I am very grateful for all their effort in managing a healthy and collaborative workplace as well as in making safe international mobility periods possible even within the limitations given by the challenging pandemic that struck most of the world during these PhD years.

A special thank you goes to all the lab members and colleagues at Politecnico. To Michela, Lorenzo, Marcello, Marco, Kostas and Taimoor, with whom I shared the successes and the failures, the achievements and the challenges, and who contributed greatly both to mitigate the little frustrations of the PhD journey, and to improve my technical and delivery skills. Here's to many more years of friendship and collaboration!

I am grateful to all the wonderful and talented young researchers that populate the Department of Mechanical and Aerospace Engineering at Polito, especially the 5th floor gang and all its current and past members (if you know who I am talking about, then you are surely included in this acknowledgement). Their expertise, kindness and support made me look forward to every day in the office, and they have set an example for me as researchers and as human beings since the beginning of my career. This includes the people I have looked up to since my undergraduate studies (yes, I am looking at you Bob, Alessandra, Giovanni and Gianpaolo, even if this makes you feel old!). Sharing the workplace with you has truly been a stroke of luck.

I am also in debt with all the people that have been by my side since I started my PhD studies, in the darker and in the brighter days: my family, who have never failed to support and encourage me. This PhD is the result of their long-term effort and investment, and I am committed to capitalizing on this talent they entrusted me with, instead of burying it into the ground.

Last, but most certainly not least, I am deeply grateful to Marta, who is always by my side, and who not only tolerates me at my worst (even when I'm unable to tolerate myself), but persistently encourages and supports me in working towards my goals and ambitions: your unconditioned love truly makes you the *last author* of this story.

Abstract

The investigation of how small molecules interact with their targets is arguably the cornerstone of biomedical research. This field is intrinsically multidisciplinary, involving many professional figures such as medicinal chemists, biologists, physicians, biophysicists, and bioengineers. In the context of bioengineering, computational molecular modelling can significantly assist our understanding of the molecular phenomena of target-ligand interactions, through the creation and simulation of *in-silico* models that mechanistically explain macroscopic behaviors and experimental observations. Computational modelling can be successfully applied both when the interaction between a small molecule and its receptor is *weak* – at most one order of magnitude above the thermal energy – and when such an interaction is *strong* – when the energy exceeds the thermal noise level by two or more orders of magnitude. At the same time, the modelling methodology must be tailored to the specific use case, since not every strategy yields meaningful results in any scenario. In this dissertation, the use of molecular modelling is discussed and applied for both weak binders with low molecular weight, such as volatile anesthetics, and for strong, anionic binders such as Rose Bengal and molecular glues.

In the case of volatile anesthetics, molecular dynamics studies of their interaction with cytoskeleton proteins allowed to map many energetically equivalent binding hotspots on the tubulin dimer, and to quantify the lifetimes and energies of the binding events. The analysis was subsequently extended to assess the effect of different anesthetics on the cell membrane in a concentration-dependent manner. The use of molecular dynamics allowed to predict the diffusion of the small molecules within the lipid core of the membrane with atomistic detail,

and to quantify the consequences thereof on membrane structure and behavior, such as on the membrane bending stiffness.

In a different set of investigations, MD simulations were employed to study strong binders, whose interactions are governed largely by electrostatic phenomena. One example is the anionic dye Rose Bengal, which is a candidate drug for photodynamic therapy and whose administration still presents significant challenges hindering its wide-scale clinical application. Through all-atom MD simulations, RB is herein shown to be unable to diffuse through the cell membrane without the presence of protein transporters, due to strong electrostatic interactions with the hydrophilic portion of the phospholipid membrane. Similar electrostatic interactions were investigated as the main driving force behind the formation of complexes between RB and dendrimer nanoparticles, which are promising delivery platforms able to overcome the current limitations related to RB-based therapies. Similarly, a strong electrostatic interaction is at the basis of the use of molecular glues to alter the assembly of biopolymers into custom shapes. Using molecular modelling, this strong interaction was elucidated with atomistic detail, highlighting how specific glues are able to alter the geometry of tubulin assemblies in order to promote the formation of GTP-responsive nanocapsules, which represent promising nanoformulations for the delivery of chemotherapeutic agents.

In summary, the research described in this dissertation shows how molecular modelling strategies can be developed and adapted to provide mechanistic explanations of molecular phenomena at different ends of the energetic scale. The reported results are relevant both at the *predictive* level, where molecular interactions are explored *a priori* to guide subsequent experimental studies, and at the *explanatory* level, where the macroscopic results obtained in experimental settings are explained using atomistic models. Both approaches allowed for the improvement of our understanding of how these molecular systems work, paving the way for novel rational drug design perspectives.

CONTENTS

List of Figures

List of Tables

Chapter I

Intermolecular interactions: biophysical signal transducers at the microscopic scale

1.1 Non-covalent interactions: flexible and reversible drivers of biological functions

Many of the biological functions of living systems can be defined as a collection of macroscopic and often observable properties which directly derive from the interplay of their underlying molecular building blocks, down to the single-atom length scale. Following a top-down approach, complex and emergent biological functions can be analyzed by building models of their constitutive blocks, which can range from in-vitro models such as organelles, static or dynamic cell cultures, to in-silico models based on the creation of (nano)mechanical atomistic models of proteins, lipids and small molecules in general. At the smallest length scales, i.e. when investigating molecular-level properties, biological function occurs not only as a direct consequence of the creation and destruction of chemical bonds, e.g. during the synthesis and breakdown of macromolecules, but also on the complex array of non-covalent interaction which constantly take place in most subcellular machineries. This includes phenomena such as the activation of receptors by their agonists, the inhibition of cellular pathways by specific small-molecule inhibitors, the assembly of the cytoskeleton, acting as a scaffold for the

overall cell structure, or the assembly of phospholipids into a bilayer, just to name a few. While such non-covalent interaction are fundamentally weaker than their covalent counterparts in terms of absolute energy associated with bond formation/disruption and force required to break the bond[1,2], the summation of many diverse non-covalent interactions, such as electrostatic or hydrophobic Van-der-Waals-type interactions, can lead not only to mechanically stable assemblies, as in the case of e.g. microtubules, but also to the triggering of complex conformational rearrangements, such as in GPCR receptors upon binding their agonist. In the biological and chemical context, non-covalent interactions drive fundamental processes such as the assembly and structural properties of materials, the secondary, tertiary and quaternary structure of proteins, the coupling of base pairs in nucleic acids.

The importance of non-covalent interactions in molecular assemblies is also indirectly testified by the exceptional growth and outreach of the scientific interest in how molecular building blocks assemble, a quest that nowadays involves many different disciplines, such as biomedicine, biophysics and biochemistry, as well as materials science[3–5]. Indeed, obtaining a mechanistic understanding of how the interplay of molecular-level interactions unfolds as a driving force for biologically relevant phenomena, can empower the design of new materials, the discovery of new pharmacological agents, or the optimization of current drug-like molecules. Obtaining such an insight is however far from trivial: perhaps the main issue to be overcome is the exceptionally small time- and length scale at which such interactions take place, which often hinders their direct experimental observation with the methodologies available today. While experimental techniques are rapidly increasing in space and time resolution, the level of expertise and cost associated with ultrahigh-resolution analyses often limits their large-scale deployment and restricts their applicability to very specific systems[6]. To this end, *in silico* models of molecular and atomistic systems can provide fundamental insights into the mechanistic underpinnings of molecular machineries, especially when coupled to experimental validation.

Broadly speaking, computational approaches can be distinguished based on their level of spatial and temporal accuracy as well as the computational effort required (Figure 1.1). As a consequence, the choice of the specific strategy largely depends on the system being investigated, and on the resolution required to successfully analyze and interpret the phenomena at hand. Starting from the highest possible resolution, i.e. the electronic structure of atoms, a first computational

strategy is Computational Quantum Mechanics (QM). In the QM approach, computational resources are used to directly solve Schrödinger equations related to the wave functions describing a given molecular system. Many theories exist to describe molecular systems at the quantum level, the most common being molecular orbital theory. One drawback of the QM approach derives from the complexity in solving the Schrödinger equation for systems containing many different atoms with more than one electron, as is the case for most biologically relevant (macro)molecules. Many different methodologies exist to tackle the complexity of QM calculations, and they might be distinguished into *ab initio* methods, relying solely on the fundamental physical constants as inputs (speed of light, masses of the particles, etc.), and *semi-empirical* methods, which simplify or ignore some of the terms and integrals of the QM equations. While such methods allow to directly study the motion of the electrons and hence the overall behavior of small molecules with great detail, they suffer from a very high computational cost, even in the case of semi-empirical approaches, which mostly limits their application to small systems, up to 10^2-10^3 atoms[7].

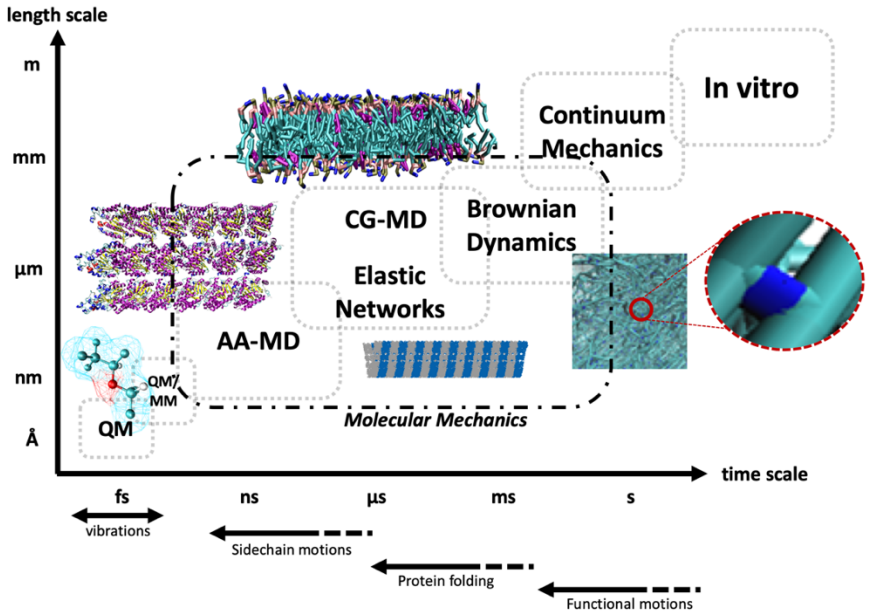

Figure 1.1. The different time and length scales accessible to in silico and in vitro approaches. All-atom molecular dynamics simulations lie in the lower end of molecular mechanics approaches, allowing for time resolutions down to the femtoseconds and spatial resolutions up to Ångstroms.

An alternative - and often complementary - computational strategy to describe the structure and dynamics of molecular systems goes under the term *Molecular Mechanics* (MM). In the MM approach, the electronic structure and quantum description of atoms is largely ignored in favor of a classical mechanical approximation of the molecular system at hand: in the most general MM approach, atoms are treated as point masses which interact with each other following a potential energy formulated as the sum of classical mechanical potentials (e.g. harmonic potentials, coulomb potentials, etc.) each modelling different aspects of the systems, such as covalent bond lengths and angles, dihedral angles, electrostatic interactions and Van-der-Waals interactions. The detailed description of the MM approach for molecular modelling is found in Chapter 2.

Given the importance of non-covalent interactions in biology and pharmacology, this chapter will briefly discuss the different types of non-covalent interactions and their biophysical underpinnings, and will introduce the notable examples of macromolecular assemblies which were computationally investigated in the present work.

1.1.1 Electrostatic interactions

Electrostatic interactions between molecules arise from the presence of (partial) electric charges distributed across the atoms, and in the context of molecular simulations they play a fundamental role to robustly model both the static (or structural) features of the molecular systems, e.g. the secondary structure, and possible dynamic interactions, e.g. between a protein and a ligand. Such charges can be the consequence of the ionization of chemical species, in which case a positive or negative charge is acquired by an atom following the loss or gain of electrons, or they can be caused by an uneven distribution of electrons in polar molecules. In both cases, the charge distribution generates weak electric fields and dipoles which in turn may interact with charge distributions and dipoles of nearby molecules, thereby determining a non-covalent attractive or repulsive force between them. This unequal charge distribution, determined by the difference of electronegativity of different atoms, can be modelled in many different ways depending on the required precision and on which approximations are acceptable within the investigation at hand. One common approach used in macromolecular force fields describes the charge distribution as an ensemble of *partial charges* distributed across the given molecule. Many methods exist to calculate such a partial charge distribution, with varying degrees of approximation, but it must be

underlined how the use of fixed partial charges for atomistic simulations is by its very nature an artificial representation of the underlying subatomic phenomena governing the interactions within matter. As such, the choice of the method for partial charge derivation must be carefully tailored to the specific system under investigation, and more importantly it is the responsibility of the modeler to ensure that the chosen partial charge calculation method is consistent and compatible with the molecular system at hand. Broadly speaking, the most common strategy for the determination of partial charges within the molecular mechanics scheme is the so-called ESP method, which relies on fitting molecular electrostatic potentials calculated at a QM level of theory, most frequently using the HF/6-31G* basis set, to a classical Coulomb-type model. When a restraint function is applied during the fitting procedure, which has the effect of decreasing the magnitude of the calculated charges, this approach takes the name of RESP[8], and is often chosen for use with additive force fields, such as the AMBER FF family. Due to the computational load of calculating quantum-level electrostatic potentials, an approximation of the RESP method has been developed, called AM1-BCC[9], combining AM1 population charges with additive bond charge corrections (BCC) that adjust the AM1 charges to emulate the 6-31G* potentials.

Another popular charge derivation method based on QM calculations goes under the name of Mulliken charges[10], also referred to as Mulliken Population Analysis, based instead on the Linear Combination of Atomic Orbitals (LCAO) technique followed by the analysis of electron populations of a molecule, where partial charges are finally derived for each atom by comparing the electrons on the atom in the free state vs. the atom population. On the other hand, since QM-based partial charge derivation methods usually involve time consuming calculations, other so-called *empirical* methods have been developed, which allow for a fast partial charge calculation at the cost of accuracy and generalizability. Such empirical charge derivation methods include the popular Gasteiger charges[11], which are derived from the electronegativity and connectivity of the atoms in a given molecule and which do not take the 3D conformation into consideration.

In summary, a variety of methods exist to approximate the electronic behavior at the atomistic scale as point charges, either by means of some form of post-processing of QM-level calculations, or through empirical methods which bypass the QM scale altogether. Ultimately, the choice of the method depends on the specific requirements in terms of computing time and accuracy: a large-scale *virtual screening* campaign designed to process a database of millions of drug-like

molecules might not afford the complexity of QM calculations, so an empirical approach able to assign charges in (fractions of) seconds can be the best choice. On the other hand, a more focused study with the aim of analyzing the behaviour of a few molecules on a specific target can greatly benefit from the accuracy provided by QM methods such as RESP, since absolute speed might not be the primary issue given the limited amount of ligands to be processed. Lastly, the choice of the partial charge derivation method should always be coherent with the parameters chosen to represent the molecular system (i.e. the *force field*), since the latter are often validated within a specific theoretical framework and might not yield valid results unless deployed with a specific charge derivation strategy.

1.1.2 Weak Van-der-Waals interactions

The electrostatic description of the interaction arising from uneven charge distributions in charged systems is insufficient to provide a complete mechanical picture of the non-covalent interactions in biomolecules, despite being fundamental to accurately account for e.g. salt-bridge interactions, hydrogen bonding and overall secondary structure stability in proteins. This concept is exemplified by the case of rare gas systems, which do not interact electrostatically (all multipole moments are zero) but most certainly exhibit mutual interactions, since they are able e.g. to condense into the liquid phase and to solidify. As a matter of fact, a second family of highly relevant interactions in biological systems exist and are referred to as Van-der-Waals interactions, after the Dutch physicists J. D. Van der Waals, who studied the deviations of rare gases from the ideal gas behavior. The term *Van-der-Waals interactions* specifically refers to the resultant of two distinct components of the force arising between apolar (portions of) molecules, namely a long-range attractive component and a short-range repulsive component.

The attractive component is related to interactions known as dispersion forces, first studied by F. London in the early 30's[12], which are a consequence of temporary dipoles induced by the fluctuations of electron clouds, which can in turn trigger the formation of instantaneous dipoles within the electron clouds of nearby atoms. Dispersion forces are among the weakest intermolecular interactions, but they have been shown to play a crucial role in many molecular assemblies[13].

Conversely, the repulsive component is particularly relevant at small inter-atomic separation, and rapidly decays exponentially as $\exp(-2r/a_0)$ with a_0 being the Bohr radius[7]. This repulsive force is a direct consequence of the Pauli exclusion

principle becoming relevant when two atoms are close enough that their electron clouds may occupy the same region of space. In this scenario, the Pauli principle postulates that two electrons in a system may not have the same set of quantum numbers. Hence, the contact between two atoms that are too close is discouraged.

Overall, despite the fact that Van-der-Waals interactions are energetically weaker than both covalent bonds and electrostatic interactions per se, they constitute the biophysical basis for many properties of (bio)chemical species, including but not limited to their solubility in water and in organic solvents, the reciprocal orientation of molecules, the tendency of aggregation and condensation. As such, *VdW* interactions represent a crucial aspect which is well worth investigating when studying interactions both of biomolecular assemblies among themselves, and between the latter and small molecules, e.g. drugs. Together with electrostatic interactions, they provide a model to analyze, quantify and tune specific properties of interest (e.g. binding affinity, binding/unbinding kinetics, binding specificity, etc.) and play a significant role in the estimation of interaction strengths.

1.2 Macromolecular assemblies of biological interest

As introduced in the previous section, electrostatic and *Van-der-Waals*-type interactions are the main driving force of many assemblies that play crucial roles in biological systems. Indeed, despite the diverse nature of such assemblies, both in terms of composition and in terms of biological function, they are all the result of highly orchestrated non-covalent interactions that occur on top of the covalent scaffold, with specific geometries and peculiar dynamics, which can be readily explored with computational techniques such as Molecular Dynamics, with time and space resolutions which are still largely inaccessible to experimental techniques.

The main biological assemblies investigated in the research presented herein are briefly described in the following, to provide a broad overview of their main characteristics and composition. While an exhaustive description of their biochemistry is beyond the scope of this work, the aim is to provide the biological context for the presented investigations and to highlight the importance as well as the power of computational modelling techniques in aiding our understanding of the atomistic phenomena beneath their behavior and macroscopic observables.

1.2.1 Cytoskeleton filaments

The cytoskeleton can be defined as the ensemble of biomolecules involved in establishing, maintaining, and adapting the mechanical structure of a eukaryotic cell. It is composed largely of protein filaments which extend across the cytoplasm and allow for structural integrity, cargo trafficking, cell adhesion, and for the active motion of cells or organelles such as cilia. Also, the cytoskeleton is a key player in cell division, a process in which the cell undergoes drastic morphological changes and which thus cannot be possible without highly specific dynamic rearrangements of cytoskeleton proteins.

Three main types of protein filaments constitute the backbone of the cytoskeleton, namely (a) microfilaments; (b) intermediate filaments and (c) microtubules.

Microfilaments are biopolymers of actin, which is the most abundant cytoskeleton protein (REF The Cell: a molecular approach). Single monomers of actin, which are referred to as globular actin (*G-actin*), present specific binding sites that allow for the longitudinal interaction with other G-actin monomers, to reversibly form filaments of up to several micrometers of length and with diameters of approximately 7 nm. The reciprocal rotation of adjacent actin monomers in a filament, which is of approximately 166°, causes the assembly to coil into a double-stranded helix, which has a specific polarity caused by the constant orientation of actin monomers within the filament. Actin filaments may further assemble into networks or bundles, based on their interaction with specific actin-binding proteins. The dynamic and reversible polymerization of G-actin into microfilaments is driven by non-covalent interactions between actin monomers and between filaments and actin-binding proteins.

Intermediate filaments (IF) encompass a rather heterogeneous group of protein polymers with a diameter in the order of 10^1 nm. They are composed of proteins which have been categorized into six different groups based on their amino acid compositions, the most important of which are keratins (groups I and II), desmin and vimentin (group III), neurofilament proteins (group IV), lamins (group V) and nestin (group VI). IFs share a common assembly scheme consisting of a central rod domain with an alpha-helix secondary structure, an N-terminal head and a C-terminal tail. Two central rod domains subsequently further assemble into dimers, and subsequently into tetramers, which associate longitudinally into protofilaments and laterally into filaments. While generally more stable than actin microfilaments,

also IFs are the result of many synergistic electrostatic and Van-der-Waals-type interactions between their protein constituents, again highlighting the fundamental role of non-covalent interactions in biomolecular assemblies.

Microtubules (MTs) are the largest class of cytoskeleton filaments, forming hollow cylinders with a diameter of around 25 nm composed of adjacent strands of consecutive αβ tubulin heterodimers (called *protofilaments*). They play a key role in the cell, where they act not only as a structural scaffold for the overall shape of the cell, but also as tracks along which intracellular cargo might be trafficked to different locations within the cytoplasm, a process which is driven by motor proteins which proceed along the MTs. Also, the dynamics of MTs are responsible for the segregation of chromosomes during mitosis, which makes them a target of interest for many antimitotic agents[14]. The stability of MTs is guaranteed by electrostatic interactions and hydrogen bonds which stabilize (a) tubulin dimers; (b) the protofilaments in the axial directions; (c) the MT wall in the lateral direction. Typically, microtubules are composed of 13 protofilaments[15], although different assemblies have been observed with fewer or more protofilaments across the animal kingdom[16]. Just as actin microfilaments, MTs undergo a dynamic polymerization/depolymerization process which goes under the term *dynamic instability*, leading to the continuous alternation between growing and shrinking phases: more in detail, protofilaments continuously assemble and disassemble into tubulin heterodimers with a specific spatial polarization (as in the case of actin), whereby the β subunit of the dimer is oriented towards the *plus* end and the α subunit is oriented towards the *minus* end. Even during the depolymerization phase, which occurs as a consequence of the hydrolysis of GTP into GDP, the MT maintains its ability to perform mechanical work[17].

The constitutive protein of MTs, tubulin, is a protein composed of three subdomains called the Rossman fold, the intermediate domain and the C-terminal domain, and is able to spontaneously self-assemble first into αβ heterodimers, and subsequently into protofilaments, through the hydrolysis of Guanosine Triphosphate (GTP) into Guanosine Diphosphate (GDP), a process which can occur only at the exposed tubulin surface[18,19]. Tubulin exists in different forms characterized by the mutation of single amino acids in the sequence. These take the name of *isotypes*, and living systems present a diversified expression pattern of such isotypes depending not only on the species, but also on the specific tissue type and cell environment. This abundance of tubulin isotypes together with experimental evidence of a wide range of post-translational modifications occurring in tubulin

has recently led to the formulation of the so-called *tubulin code* hypothesis, stating that organism are able to tailor the structure and function of microtubules by modulating their specific composition and modifications[20] . Just as for the previously mentioned cytoskeleton filaments, MTs rely on non-covalent interactions to maintain their stability and to carry out their specific functions. Their unique structural features, including the specific architectural and functional characteristics of MTs in the human brain[21], together with their responsiveness to GTP in the polymerization/depolymerization process, are the starting point for the investigations reported in the present work, where the high spatial and temporal resolution allowed by Molecular Dynamics has been exploited to shed light on key interactions of tubulin dimers with different sets of small molecules which are of interest for neuroscience as well as material science.

1.2.2 Phospholipid membranes

Phospholipid membranes constitute a prime example of heterogeneous molecular assembly with unique mechanical, structural, and functional properties. As discussed in the previous paragraph, the structural integrity and mechanical strength of the cell is mostly provided by intracellular biopolymers such as the cytoskeleton filaments. Thus, at least in mammalian cells, the key design requirement for cell membranes is not so much the mechanical robustness per se, but rather the ability to function as a highly selective, plastic and dynamic barrier, separating the intracellular environment for the exterior aqueous surrounding. In terms of their chemical and physical characteristics, membranes are required to interact favorably with water on both sides – at the cytoplasmic side and at the extracellular side – since both of these environments are composed largely of water. One class of biomolecules satisfying such requirements are *amphiphiles*, i.e., molecules possessing both hydrophobic and hydrophilic moieties, and more specifically phospholipids, which are molecules composed of two fatty acid chains linked to a glycerol group and a polar phosphate headgroup. Many different types of phospholipids make up biological cell membranes, and they can be classified based on the length of the hydrocarbon chains or the chemical composition of the hydrophilic headgroup. In addition, phospholipids can be divided into *saturated*, which only present single C-C bonds in their hydrocarbon tails, or *unsaturated*, containing one or more double C=C bonds. From a mechanical perspective, the former type of lipids tends to pack into tighter and more organized bilayers, yielding typically higher mechanical strength, decreased fluidity and a higher liquid/gel transition temperature, whereas the latter (unsaturated) usually present the opposite

behaviour, with a higher fluidity (decreased viscosity) when assembled into bilayers due to the distortion of the symmetry of the hydrocarbon tails induced by the double bond.

As anticipated, biological membranes are usually composed of a mixture of different phospholipids in different proportions depending both on the species and on the specific function (or *phenotype*) of the cell[22–24]. The most common types of headgroups in eukaryotic cells are *serine*, *ethanolamine*, *glycerol* and *choline*, while the typical lengths of the hydrocarbon chains are between 15 and 18 carbon atoms. Overall, the most common phospholipid type in mammalian membranes are *glycerophospholipids*, such as members of the phosphatidylcholine (PC), phosphatidylethanolamine (PE) and phosphatidylserine (PS) families. PC phospholipids are usually unsaturated, i.e. they present a double C=C bond in one of the acyl chains, which increases the fluidity of the membrane. In addition to glycerophospholipids, mammalian membranes present two other main components, i.e. sterols (mostly cholesterol) and sphingolipids[23]. Both of these components have the mechanical effect of decreasing membrane fluidity and compliance, effectively countering the fluidifying effect of unsaturated lipids, thereby conferring increased structural stability, bending rigidity and robustness to the membrane. In typical mammalian membranes, the percentage of cholesterol with respect to the overall lipid composition is around 25 to 30% mol/mol[23]. Lastly it is worth highlighting how the membrane lipid composition can be asymmetric in the two leaflets, meaning that the two monolayers composing the membrane can feature different proportions and types of lipids based on the specific cell type and function.

In this highly complex scenario, the experimental investigation of lipid membranes has benefitted from remarkable advances in the recent years[25]: techniques such as single-particle tracking[26], mass spectrometry, nuclear magnetic resonance (NMR)[27] and fluorescence correlation spectroscopy[28] have effectively empowered the study of model membrane systems in terms of both their composition and their dynamics. Indeed, the study of cell membranes appears crucial to understand fundamental biological mechanisms such as the spontaneous and facilitated diffusion of solutes across the membrane, *mechanosensing* and signal transduction from the extracellular environment to the cytoskeleton, the conformational dynamics of transmembrane proteins and channels, or processes such as endocytosis, phagocytosis and neurotransmitter release, just to name a few. Due to the very nature of the membrane, all these processes are intrinsically dynamic, meaning that they are the result of a continuous and highly orchestrated

motion of lipid molecules, solutes and proteins at the picosecond to millisecond timescale. For this reason, in addition to the aforementioned experimental advances, molecular modelling and more specifically molecular dynamics has emerged as a very powerful tool to obtain molecular-level insights into these highly complex systems. This is testified by the ever-increasing number of published studies relying on molecular dynamics to investigated specific membrane properties[29], ranging from simple single-lipid models to complex assemblies including different lipid types as well as embedded proteins. In this regard, all of the above-mentioned considerations regarding membrane composition, asymmetry and dynamics constitute a challenge in the context of the computational modelling and investigation of membrane behavior. As a matter of fact, a large part of the computational studies published in the last twenty years employed membrane models composed of a single lipid type, most commonly *palmitoyloleoylphosphatidylcholine* (POPC) or *dipalmitoylphosphatidylcholine* (DOPC), with simulations including up to 128 lipid molecules and reaching time scales of 10^{-11} s, due to the limitations given by the lipid force fields and by the computational resources available at the time[29]. Nowadays, the increase in computational power and the availability of accurate and validated lipid force fields allowing for a robust parametrization of a wide range of lipid types, has effectively allowed for the modelling and simulation of larger, heterogeneous lipid patches in a variety of modelling contexts[30,31]. This bears the benefit of being able to explicitly account for the presence of different lipid species, each with their distinctive molecular behavior, as well as to extend the simulation time scales well beyond the microsecond, which allows the simulation to capture motions and mechanisms of great relevance occurring at longer timescales.

1.2.3 Engineered constructs in drug design and delivery

Beyond biomolecules such as proteins and lipids, many other assemblies can be successfully investigated exploiting the synergy of combined computational and experimental approaches. Indeed, a great number of resources have been invested into the design and characterization of custom assemblies with tailored molecular properties, based on the goals and requirements of the specific application. Examples of this range from materials science applications, where the aim is to improve existing materials in terms of e.g. mechanical strength, resistance to high temperatures or environmental sustainability throughout the material's lifecycle, to biomedical applications such as the design of novel drug carriers, or even at the

interface between these research fields, e.g. for the design of biocompatible materials for tissue engineering.

In the context of drug design, finding innovative means for the targeted delivery of medicinal compounds remains in many cases an open challenge, which has the potential of not only increasing the therapeutic efficacy of drug-like molecules, but also to reduce off-target effects and to improve shelf stability. Especially in the field of anticancer therapies, the presence of severe side effects and/or a poor understanding of the biomolecular target still constitute major obstacles throughout the *bench-to-bedside* development cycle of drug candidates, leading to estimated failure rates of as many as 9 out of 10 compounds[32].

In the research presented in this dissertation, computational modelling strategies have been applied to study two main types of engineered platforms for drug delivery. The first investigated structure are dendrimers, which are branched organic particles of approximately spherical shape with symmetric, radially extending branches originating from a central core. These are monodisperse structures whose electrostatics, solubility, stability and drug-loading capacity can be tuned for specific cargos and deployments[33]. The combined experimental and computational study of custom dendrimers for the delivery of Rose Bengal for photodynamic therapy is discussed in detail in section 4.3. The second type of nanoformulated constructs for drug discovery investigated herein is represented by innovative tubulin-based nanocapsules which have the ability to selectively respond to GTP-rich environments. The molecular underpinnings of the assembly of tubulin into nanocapsules through the use of molecular glues is reported in section 4.4, which also represents an additional example of how molecular modelling can be employed to obtain additional atomistic insights which are complementary to experimental findings.

1.3 Computational molecular modelling of ligand-target interaction dynamics

In the context of the macromolecular structures described above, the overarching goal of the present work is to illustrate the application of Molecular Mechanics methodologies to the investigation of different types of small molecule-target interactions, in scenarios where there is an incomplete understanding of specific binding sites, or where the ligands are expected to exert a multi-modal and dynamic action on their target as opposed to a *lock-and-key* binding paradigm. Examples of

such systems include (a) volatile anesthetics, small gaseous molecules able to cause reversible loss of consciousness; (b) molecular glues, which are molecules able to alter polymer assemblies through aspecific interactions; (c) nanoparticle-drug complexes, where the binding between the nanoparticle and the drug cargo is driven by non-covalent and mostly electrostatic interactions. Each of these systems requires specific computational approaches and modelling choices: the computational strategies and specific methodologies shall be tailored so as to capture the relevant mechanisms driving the interactions and to allow the mechanistic understanding of the system. As such, there is no *one-size-fits-all* methodology that can be applied to any protein-ligand or target-ligand molecular system, but rather a plethora of strategies for the parametrization of the systems, for the generation of initial conditions, e.g. the positions of the atoms of both the ligand and the target, for improving the sampling throughout the simulation, or for the estimation of the strength of a protein-ligand interactions, just to name a few. These strategies will be discussed in detail in the following chapters, which will describe the how the modelling strategies were chosen and tailored based on the molecular system at hand and based on the overall goal of the specific investigation.

After an in-depth review of the theoretical background of molecular modelling, provided in chapter 2, and after the detailed description of the specific investigations that were carried out, each with its own modelling approach (chapters 3 to 4), a birds-eye view is provided in chapter 5, where the different approaches and methods for the modelling of small molecule-target interactions are discussed in light of the physical and chemical characteristics of the systems under investigation, underlining the power of molecular dynamics simulations in this field of study.

All supplementary figures and information mentioned throughout the text are included in the appendix, which is included at the end of the document.

Chapter II

Computational Modelling of biological systems at the molecular scale

2.1 Introduction and aim

As anticipated in the previous chapter, a wide range of computational methodologies exist to investigate the behavior and dynamics of biomolecular systems. The selection of a specific methodology, and thus of a specific theoretical foundation for the model being used, mostly depends on the desired resolution, the acceptable approximations, and the available computational power. Within the scope of the present work, the size of the systems being studied, in the order of 10^5 atoms, discourage the use of ab initio approaches, and determined the choice of Molecular Mechanics as the overarching methodological framework. An outline of the MM theory is provided in the following, together with a brief overview of the necessary background in statistical mechanics and the description of the molecular force fields and simulation engines used in the present work.

2.2 Molecular Mechanics

The broad field of molecular mechanics is erected onto the fundamental idea of applying classical Newtonian mechanics to particle systems representing the atomic structure of (bio)molecules. The underlying concept postulates that molecules can

be modelled as an ensemble of point masses which are interconnected as harmonic oscillators, and which additionally interact at longer ranges with coulomb-type and Lennard Jones (LJ) potentials progressively decaying at longer ranges. Thus, a molecular system can in principle be described mathematically by defining a potential energy function (PEF) which only depends on the (reciprocal) positions of the particles composing the system, as well as from a set of predefined parameters which go under the term *Force Field* (FF) and which describe e.g. the fundamental characteristics of the harmonic potentials describing covalent bonds, angles, dihedrals as well as collision radii for non-bonded interactions, etc. In spite of the apparent simplicity of this approach, especially when considering the complexity of the phenomena occurring at the atomic scale, the molecular mechanics paradigm is surprisingly powerful to both provide mechanistic explanation to macroscopic observables and make predictions about the interaction dynamics of existing and novel molecular systems. Indeed, even though describing atomistic systems using classical physics might seem a task deemed to fail, the ever increasing number of success stories in which computational molecular modelling - based on classical mechanics - has significantly enhanced the mechanistic understanding of specific molecular machineries unmistakably confirms the relevance of this methdology[31]. The following paragraphs provide a description of the fundamental theoretical background behind molecular mechanics, together with an overview of the methodologies employed in this work.

2.2.1 Fundamentals of Statistical Mechanics

Statistical mechanics represents the theoretical foundation linking the macroscopic observables, i.e. the quantities commonly measured in a laboratory setting during experiments, and the properties of the single particles composing the system, e.g. the velocities of individual molecules or atoms. In other words, quantities that were historically studied as intrinsic properties of the system under investigation, e.g. heat, were subsequently shown to be *emergent* properties, originating from the movement of the individual components of the system. As such, statistical mechanics can be sees as the theoretical instrument to connect the behaviour of atoms to the macroscopic laws of thermodynamics by means of statistical methods. Intuitively, this means averaging the detailed microscopic properties of the particles to obtain higher-level descriptions which can be directly compared to what is measurable macroscopically.

This statistical link, explaining how these fundamentally different levels of abstraction can be connected, becomes especially crucial in the context of assisting experiments using computational techniques which rely on the simulation of ensemble of individual particles, since it allows to bridge the gap between the microscopic and the macroscopic and to interpret empirical findings in the light of the microscopic behavior of biomolecules.

The fundamental requirement to allow for such a *bottom-up* approach, i.e. to obtain information about the macroscopic condition of a system starting from the collection of its microscopic properties, is to carry out a *sampling* process. Sampling involves the space of all possible physical microstates, e.g. the positions and velocities (or momena) of the individual particles, that are accessible to a system, which is called the *phase space*: the grand challenge when performing simulations at the microscopic scale is to obtain a representative ensemble of conditions of the system, or in other words to *sufficiently sample the phase space*. If we consider the velocities and positions of the particles as the variables defining the state of the system, which is to say that we are considering a classical mechanical representation, then a system composed of N particles will have a total of 6N variables defining its location in the phase space, if these quantities are defined in a three-dimensional space. More in general, the degrees of freedom will be *2dN*, where *d* is the dimensionality of the input variables. In the case of a quantum description of the system, the positions and momenta might instead be replaced by the value of the wavefunction. Most importantly, the statistic link between the thermodynamic equilibrium properties of the system and the location of its individual components in the phase space postulates that multiple discrete *microstates* (e.g., combinations of positions and momenta in the classical framework) can give rise to the same thermodynamic *macrostate* (e.g, the temperature, pressure or entropy of the system). The collection of microstates corresponding to the same macrostate is also called the *statistical ensemble* or the *density of states*. The underlying assumption is that given a certain macrostate, any corresponding microstate is equiprobable *a priori*. Mathematically, the connection between microscopic properties and macroscopic observables can also be expressed by the following equation:

$$\langle A \rangle = \iint A(p^N, r^N)\rho(p^N, r^N)dp^N dr^N \qquad (2.1)$$

where $\langle A \rangle$ denotes the ensemble average of the property $A(p^N, r^N)$ which is a function of the positions, r^N, and the momenta, p^N, and $\rho(p^N, r^N)$ is a probability density function characterizing the ensemble. This probability density depends on the energy of the system, E, in a given configuration:

$$\rho(p^N, r^N) \propto e^{\frac{-E(p^N, r^N)}{k_B T}} \tag{2.2}$$

where k_B is the Boltzmann constant and T is the absolute temperature. The proportionality factor follows the requirement that $\rho(p^N, r^N)$ is a probability density, which is to say that the probabilities of all the microstates must sum to one. Mathematically, this implies that a normalization factor, Z, must be defined as:

$$Z = \sum e^{\frac{-E(p^N, r^N)}{k_B T}} \tag{2.3}$$

This quantity is called the *partition function* (or *Zustandssumme*), whose inverse constitutes the proportionality constant in the Maxwell-Botzmann distribution:

$$\rho(p^N, r^N) = \frac{1}{Z} e^{\frac{-E(p^N, r^N)}{k_B T}} \tag{2.4}$$

Since the overarching goal is to determine averages of the properties of the system, this introduces the problem of exhaustively sampling the individual states to determine $\rho(p^N, r^N)$ to ultimately solve equation (2.1). Indeed, the analytical solution of equation (2.3) is only feasible in a very limited amount of scenarios. However, remembering that the goal is to obtain average quantities, it is useful to remember that said averages can be calculated for any given system either by observing the evolution of its degrees of freedom over time, and the considering the amount of time the system spends in a given state, or by observing many different systems, all corresponding to the same macrostate, at the same time. The former approach yields the *time averages*, whereas the latter intuitively corresponds to the *ensemble averages*. A system for which these two quantities coincide for arbitrarily long observation times is said to be *ergodic*. Mathematically:

$$\langle A \rangle_{ensemble} = \langle A \rangle_{time}$$

(2.5)

where, starting from equation (2.1), $\langle A \rangle_{time}$ can be calculated as:

$$\langle A \rangle_{time} = \lim_{T \to \infty} \int_{0}^{T} A(p^N(t), r^N(t))\, dt$$

(2.6)

The quantity in equation (2.6) is the one calculated during computational simulations, where the continuous integral over time *dt* is replaced by its discrete-time counterpart, i.e. a sum over the total number of performed timesteps. This represents the fundamental theoretical background justifying the use of discrete-time computer simulations to obtain useful pieces of information regarding the thermodynamic state of an atomistic system, which may then be compared to macroscopic observables and experiments. Also, it explains the quest towards increasingly longer simulation times and/or enhanced sampling techniques, so that equation (2.5) holds and ensemble averages can be inferred.

2.2.2 Molecular Mechanics: Force Fields

As anticipated in the introductory section, the term molecular *force field* refers to the ensemble of parameters defining the potential energy function, which is generally an additive composition of a set of *bonded* and *non-bonded* terms, which allows for the prediction of the motion of the particles. This idea can be formalized with the following equation:

$$V(\vec{r}) = V(\vec{r})_{bonded} + V(\vec{r})_{non-bonded}$$

(2.7)

This most general formulation of the potential energy function reported in euqation (2.7) is usually a function of only the positions of the particles, $\vec{r}$. In greater detail, the $V(\vec{r})_{bonded}$ is defined as the composition of classical mechanical potentials, most commonly of harmonic type, which describe the oscillations of the atoms about their equilibrium bond lengths and angles, as well as terms describing the behavior of proper and improper dihedrals:

$$V(\vec{r})_{bonded} = V(\vec{r})_{bonds} + V(\vec{r})_{angles} + V(\vec{r})_{dihedrals}$$

(2.8)

Conversely, the non-bonded terms of the PEF, which are designed to account for the electrostatic and Van-der-Waals interactions between particles that are not linked by covalent bonds, can be summarized as:

$$V(\vec{r})_{non-bonded} = V(\vec{r})_{Elec} + V(\vec{r})_{VdW}$$

(2.9)

The key characteristic distinguishing the different molecular mechanics-based approaches is what type of equation is employed to model each of these terms. This choice largely depends on the system under investigation and the desired tradeoff between speed and accuracy[7]. In its general form, the potential energy function can be written as:

$$\begin{aligned} V = & \sum_{i,j \in S_B} \frac{1}{2} K_{ij}(d_{ij} - \bar{d}_{ij})^2 + \sum_{i,j,k \in S_{BA}} \frac{1}{2} \xi_{ij,k}(\theta_{ijk} - \bar{\theta}_{ij,k})^2 \\ & + \sum_{i,j,k,l \in S_{DA}} \sum_{n} \psi_{i,j,k,l}\left[1 + \cos\left(n\phi_{i,j,k,l} - \bar{\phi}_{i,j,k,l}\right)\right] \\ & + \sum_{i,j \in S_{NB}} \left\{ 4\varepsilon_{i,j} \left[\left(\frac{\sigma_{i,j}}{d_{i,j}}\right)^{12} - \left(\frac{\sigma_{i,j}}{d_{i,j}}\right)^{6} \right] + \frac{q_i q_j}{4\pi\varepsilon_0 \varepsilon_r d_{i,j}} \right\} \end{aligned}$$

(2.10)

In equation (2.10) each term of the *bonded* and *non-bonded* potential between any two given particles, *i* and *j*, has been explicitly described. Briefly, the first term models the harmonic potential between bonded atoms, oscillating about an equilibrium bond length value of $\bar{d}$. The second terms describes the analogous behavior for the angle defined between any three bonded particles, i, j and k. The third term describes the dihedral rotations about the bonds of quartets of atoms i,j, k and l. The last term represents the non-bonded interactions, i.e., the coulomb potential between two atoms with charge q_i and q_j, and the Lennard-Jones potential between two atoms i and j, respectively. Taken together, the form of the potentials

used to describe the PEF in equation (2.7) and the set of parameters used in said equations (e.g. K_{ij} , $\bar{d}_{ij}$, etc. in equation (2.10)) constitute the *force field*.

Different force fields are build, optimized and validated for the simulation of specific classes of biomolecules in specific thermodynamic conditions, since the parameters are usually obtained empirically, with or without the aid of quantum mechanics calculations. Thus, the choice of the force field when approaching a given molecular modelling problem heavily depends on the system under investigation. It is the responsibility of the modeler to opt for parameters and simulation methodologies that are coherent with the research being carried out and that are validated within its scope, so that sound estimates and predictions can be obtained.

2.2.3 Molecular Dynamics simulations

As explained in greater detail in section 2.2.1, obtaining robust estimates of thermodynamic properties of interest, i.e. *emergent* properties that depend on the population of microscopic states, requires an extended sampling of the latter to obtain a representative statistical *ensemble*. In the context of molecular modelling, this directly implies the need of generating a sufficient number of molecular conformations to obtain a sufficient degree of sampling of the phase space. In practical terms, this means that it is often not enough to extract a specific conformation of the system being investigated, e.g. a local minimum of a potential energy function as defined in section 2.2.2, to obtain relevant insights into molecular interactions. This caveat is moreover implied whenever the overarching goal is to characterize the *dynamics* of the system, which is to say how the different molecular players evolve over time under specific conditions.

To overcome this limitation, different methods have been developed to generate ensembles of conformations, i.e. to sample the phase space of a molecular system: two widely employed strategies are (a) Monte Carlo (MC) simulations and (b) Molecular Dynamics (MD) simulations. As the name suggests, MC simulations generate new conformations through random perturbation of the degrees of freedom followed by the evaluation of the induced energetic change (which can be calculated using the Boltzmann factor described in equation 2.2.). While the MC approach historically represents the first method applied for molecular simulations, it is not suitable to explore dynamic non-equilibrium properties, since it does not include the contribution of the momenta and does not generate an ensemble representing the time-evolution (or *trajectory*) of the system. Also, it has been

shown that MC simulations do not allow for a better sampling of the phase space in a given amount of time if compared to other techniques such as MD[34], and imply significant technical hurdles in their implementations – due to e.g. the problem of random number generation or due to the internal degrees of freedom in complex molecular systems leading to high energetic penalties and high rejections[7].

On the other hand, the Molecular Dynamics (MD) method relies on Newton's equation of motion to iteratively calculate how the molecular system evolves over time, starting from the definition of its potential energy (see equation (2.10)). As such, MD is said to be a *deterministic* method, as opposed to MC which is *stochastic* in nature. Mathematically, the foundation of the MD method is that the force acting on a given particle, *i*, is linked to its mass and acceleration as:

$$m_i \frac{d^2 r_i}{dt} = F_i$$

(2.11)

with r_i indicating the position of the particle, m_i its mass and t is the time. The law expressed in equation (2.11) is a fundamental principle in classical mechanics, and as anticipated in section 1.1, the use of this paradigm in place of QM-level calculations greatly decreases the computational burden of the simulations, since there is no need to explicitly solve Schrödinger's equations. From a practical standpoint, the trajectories can thus be calculated by obtaining the force, F_i, as the negative derivative of the PEF (see equation (2.10)), which can subsequently be used to recalculate the accelerations, velocities and positions of the particles by integrating equation (2.11). Since computer simulations intrinsically rely on numerical solutions, this process is practically solved in discrete time steps, in the order of 10^{-15} seconds. At each step, the forces, positions and velocities on each atom are updated and used to progressively obtain the trajectory of the system. Finally, provided that the simulation proceeds for a sufficient number of time steps, ensemble averages can be calculated by averaging their evolution in time obtained through the simulation, as discussed in section 2.2.1, equation (2.5):

$$\langle A \rangle_{time} = \frac{1}{T} \sum_{i=1}^{T} A(p^N, r^N)$$

(2.12)

which represents the numerical solution of equation (2.6), with T being the number of simulated timesteps. While the amount of timesteps that can be simulated largely depends on the size and parametrization of the system at hand, typical all-atom MD simulations can nowadays reach timescales of tens of microseconds, thanks to modern HPC resources and GPU acceleration.

2.3 Methods for binding mode and binding energy prediction

The computational prediction or estimation of the binding energy between a macromolecule and a small ligand is a main area of interest within the molecular modelling community. Indeed, the quantification of the strength of interaction between a drug and a target allows both for the explanation of the effects of small molecules on their targets, and the strength thereof, and for the design of improved molecular scaffolds which might be characterized by an enhanced binding energy to their target of interest and/or a decreased binding energy towards unwanted molecular players. Many methods have been developed to provide an estimate or prediction of this binding energy, with varying degrees of accuracy and computational complexity. The methods employed throughout the present dissertation are briefly described in the following paragraph, to provide an additional theoretical background to the methodology and to make the reader aware of the advantages and disadvantages characterizing their use. Indeed, it can be argued that an in-depth comprehension of the approximations and theoretical foundations of a given binding energy calculation strategy is what can ultimately constitute an important guiding light for the choice of the method in a specific application scenario, based on the assumptions that can or cannot be satisfied and on the tradeoff between speed and accuracy that can be accepted in each use-case.

2.3.1 Docking and scoring functions

The term *docking* (or *molecular docking*) refers to a computational methodology that is designed to predict how a small molecule might place itself within a specific cavity or region on a macromolecular target, e.g. a protein. This placement is called the *binding mode* of the ligand, and constitutes the main output of docking computations, together with a rough estimate of the bending affinity.

Usually, a typical docking algorithm consists of two main phases: (a) the placement of the ligand and (b) the scoring of the pose. Different docking tools

apply different algorithmic (for the *placement*) and methodological (for the *scoring*) approaches to each of these stages. In the most common scenario, the inputs required for a docking run are (i) the 3D coordinates of the atoms of the target biomolecule, such as e.g. a crystallography obtained from the PDB[35] or a homology model[36]; (ii) the atomic coordinates of the ligand(s), which should ideally be represented in the dominant protonation state under the investigated conditions and which should also have the atomic partial charges calculated using one of the methods mentioned in section 1.1.1; (iii) the approximate location of the binding site, although so-called *blind docking* approaches exist which search the whole target for putative binding[37], and which have recently benefitted from the application of Machine Learning techniques to enhance their reliability and effectiveness[38].

The goal of the first phase, i.e. the *ligand placement*, is to sample the conformational space of the ligand when the latter is placed within the defined binding site, i.e. to generate an ensemble of conformations which explore the possible reciprocal interactions between the ligand and the target. Broadly speaking, the algorithms designed to perform this conformational search can be *stochastic*, based on *matching*, or *systematic*. Stochastic search algorithms, as the name suggests, use approaches such as evolutionary strategies or Monte Carlo (MC) methods to randomly generate new ligand conformations by stochastically altering its different degrees of freedom, e.g. bond rotations, in the hopes of exhaustively sampling the conformation space and thus to find a satisfactory solution to the placement problem. On the other hand, placement methods which are based on matching rely on the concept of shape complementarity between the small molecule and the target binding site, to extract likely ligand conformations and discard incompatible placements. Also, matching algorithms can include considerations regarding the chemical compatibility of interacting atoms, e.g. hydrogen bonding or π-stacking, to further refine the conformational search. Lastly, systematic approaches aim at exhaustively sampling the conformational space of the ligand along all its degrees of freedom to obtain the most representative statistical ensemble of binding poses and ultimately extract the most favorable ones. Based on the specific strategy that is being adopted, systematic methods can be further categorized into (a) exhaustive algorithms, which progressively explore all possible rotations of all the dihedrals in the query ligand; (b) methods that are based on ensembles, i.e. that first generate representative populations of ligand conformations which are subsequently placed rigidly within the target cleft; (c) fragment-based methods, which individually place sub-groups of ligand atoms

within the binding site and only subsequently reconnect them to form the original query ligand.

Whatever the strategy to generate new conformations of the ligand in the binding site, these must subsequently be scored. The general goals of scoring are: (a) providing a rough estimate of the putative binding energy associated to a specific conformation; (b) discarding conformations that are unreasonable from a biophysical standpoint (e.g., due to atomic clashes); (c) providing a quantitative ranking of the ensemble of conformations. The scoring function shall thus take the positions of the atoms as the only input, which is the result of the previous ligand placement phase, and provide a quantitative estimate (a number) of the "goodness" of the pose as an output.

One possible approach to the scoring problem is to rely on the already-described force fields, i.e. to use equations such as (2.10) to obtain an estimate of the potential energy as a function of atomic positions. This approach satisfies the above-mentioned input/output requirement, but is not the most computationally efficient in a context where speed is often a key issue, such as massive virtual screening campaigns[39] which should be able to dock up to 10^6 molecules in reasonable amounts of computation time. In addition, while MD forcefields generally deal with the minima of the energy profiles in the phase space, the goal of docking is rather to approximate the binding free energy, which also depends on factors such as the temperature[40]. For these reasons, a second, more popular approach to scoring is to define so-called empirical scoring functions. These are conceptually similar to force fields, in the sense that they provide an energetic estimate starting from the atomic positions, but are explicitly optimized to weigh the different contributions of intermolecular interactions to the binding free energy, to account for the above-mentioned differences. Intuitively, empirical scoring functions divide the final binding energy into contributions yielded by e.g. hydrogen bonding, electrostatics, Van der Waals interactions, etc., weighted by specific coefficients that are obtained in order to match experimental results and to implicitly account for the temperature.

As an example, in the *AutoDock-Vina* docking program, which was used in the research described herein, the scoring function is the result of the combination of knowledge-based potential energy formulations and empirical scoring approaches[40]. For a given conformation, i, it takes the following form:

$$s_i = g(c_i - c_{intra_1})$$

(2.13)

where:

$$c_i = c_{intra} + c_{inter} = \sum_{i<j} f_{t_i,t_j}(r_{ij})$$

(2.14)

In equation (2.13) c_{intra_1} represents the intramolecular contribution to scoring of the best binding pose. The *conformation-dependent* term *c*, formalized in equation (2.14), is the sum of the intra- and inter-molecular contributions, and is given by the sum over all possible atom pairs with possible reciprocal displacements. f_{t_i,t_j} represents the interaction between an atom of type t_i and an atom of type t_j, and is given by:

$$f_{t_i,t_j}(r_{ij}) = e^{-\left(\frac{d_{ij}}{0.5}\right)^2} + e^{-\left(\frac{d_{ij}-3}{2}\right)^2} + \delta_{ij} + h_{ij} + \eta_{ij}$$

(2.15)

Where d_{ij} is the surface distance ($d_{ij} = r_{ij} - R_{ti} - R_{tj}$) with R indicating the *VdW* radius for the specific atom type. The terms δ_{ij}, h_{ij} and η_{ij} represent the steric repulsion term, hydrophobic term and hydrogen bonding term, respectively. These are defined based on the inter-atomic distances:

$$\delta_{ij} = \begin{cases} d_{ij}^2 \,, if\ d_{ij} < 0 \\ 0 \,, if\ d_{ij} \geq 0 \end{cases}$$

(2.16)

$$h_{ij} = \begin{cases} 1, if\ d_{ij} < 0.5\text{Å} \\ 0, if\ d_{ij} > 1.5\ \text{Å} \\ 1.5 - d_{ij}, if\ 0.5 \leq d_{ij} \leq 1.5 \end{cases}$$

(2.17)

$$\eta_{ij} = \begin{cases} 1, if\ d_{ij} < -0.7\ \text{Å} \\ 0, if\ d_{ij} > 0 \\ -\left(\frac{x}{0.7}\right), if\ 0.7 \leq d_{ij} \leq 0 \end{cases}$$

(2.18)

Finally, the function g of equation (2.13) is conformation-independent, and is given by:

$$g(c_{inter}) = \frac{c_{inter}}{1 + wN_{rot}}$$

(2.19)

Where N_{rot} is the number of rotatable bonds (excluding hydrogen atoms), and *w* is the weight.

This scoring function represents an example which combines the advantages of knowledge-based scoring and empirical fitting. A further refinement of scoring can be obtained when different scoring approaches are combined, an approach called *consensus scoring*. In consensus scoring, the generated poses are scored according to N different scoring methods, and the final results are compared. The final combination of the different scores can be obtained e.g. by means of a weighted sum or by consensus given a certain threshold. Consensus scoring can improve the accuracy of docking and aid in the rejection of decoys in a virtual screening process, at the expense of an increased computational cost due to the repeated scoring. Depending on the specific implementation and research question, this cost might however be negligible or acceptable.

Whatever the method for ligand placement and scoring, one important aspect must be held in mind when choosing the computational strategy for a modelling problem, which is the goal under which each method was developed and the conditions in which it was validated. In other words, its *applicability domain* must be understood, to avoid overinterpreting the results (in the best case) or improperly using a specific method thereby obtaining meaningless results (in the worst case). In the case of docking, the modeler should keep in mind that it is a computational strategy designed to screen rather large libraries of small molecules with high computational efficiency, and it is tuned to be able to retrieve promising drug-like compounds for a given druggable binding site and to mimic experimental binding poses for a given protein-ligand complex. Also, its search and scoring methods are

developed in order to be able to retrieve a reasonable binding pose that is consistent with the biophysical characteristics of the binding site, and to consistently discard conformations that are grossly overlapping with the target atoms or that are unlikely to properly fit. Also, most docking scoring functions are unable to effectively discriminate between binding modes whose energy differs by less than one order of magnitude[41]. Although many evolutions and variations of docking exist, nowadays often aided by machine learning[38,42,43], the aforementioned tasks can be regarded as the core application scenario of docking. Indeed, when the goal of a modelling task is beyond the scope of docking, e.g., when a more precise estimate of the binding affinity is desired, when complex induced-fit phenomena are expected to take place, or when the ligand-target interaction dynamics is under investigation, one should recur to most advanced strategies, e.g. through the use of Molecular Dynamics. A more detailed discussion regarding possible suggested strategies and workflows for different modeling tasks is provided in chapter 5.

2.3.2 MM/PBSA and MM/GBSA

As anticipated in section 2.3.1, docking can be a fundamental strategy to perform rapid screening experiments on large compound libraries, or to provide a first estimate of likely inter-molecular interactions of ligands in a specific binding site. However, the result given by the scoring function is often a gross approximation of the true binding energy between a ligand and e.g. a protein, as observed experimentally, due to the approximations and assumptions beneath the method and the speed requirements which often hinder more accurate computations.

More refined binding energy estimation methods exist that rely on the extensive sampling of the ligand conformations provided by classical or enhanced sampling molecular dynamics simulations. Of course, the gain in accuracy comes at a cost, which is the need to perform MD simulations of the ligand-target complex covering a sufficient amount of timesteps. This not only bears the additional complexity of properly parametrizing the target and the ligand, which is a step that often requires extensive validation, but also requires computational resources and time which are orders of magnitude greater compared to docking, when considering the performance on a single ligand-target complex (*days* vs. *seconds*). However, when the focus is on a limited amount of targets and/or ligands, this added cost is often affordable, and it is also often superseded by the fact that many additional insights can be obtained from MD simulations other than binding affinity estimates (e.g.,

kinetic information, conformational characteristics of the target, principal motions and fluctuations, etc.).

One popular strategy to estimate the binding free energy between a ligand and a target is called the *Molecular Mechanics/Poisson-Boltzmann Surface Area solvation*, or *MM/PBSA* for short. This method, whose accuracy lies in the middle between docking simulations and more advanced, statistical-mechanics-based strategies such as alchemical perturbation (AP)[44], was employed in the research described in this dissertation, and is briefly explained in the following.

The MM/PBSA[41] method belongs to the family of so-called *end-point* strategies. The term refers to the fact that they only require sampling of the end states, which is to say the bound conformation of the ligand-target complex as well as the free ligand and the free target, without any explicit sampling of the binding pathway. It is arguably one of the most popular methods to estimate binding free energies[45,46], due to its fairly easy implementation and reasonable computational efficiency if compared to e.g. AP. In the MM/PBSA method, the predicted binding affinity, $\Delta G_{binding}$, is given by:

$$\Delta G_{binding} = \langle \Delta G_{T-L} \rangle - \langle \Delta G_{T} \rangle - \langle \Delta G_{L} \rangle = \Delta E_{MM} - T\Delta S + \Delta G_{S} \quad (2.20)$$

In equation (2.20), the binding energy $\Delta G_{binding}$ is calculated as the difference between the contribution of the target-ligand complex, the contribution of the target alone and the contribution of the ligand alone. This quantity can be calculated as the sum between a first term given by the molecular mechanics energy, ΔE_{MM}, as well as the contribution given by conformational entropy, $T\Delta S$, and a second term representing the differences in free energy of solvation following ligand binding. From a technical standpoint, each of the three terms on the right-hand side of equation (2.20) is calculated with a specific approach.

The energetic contribution given by molecular mechanics, ΔE_{MM}, can be calculated using the MM force field as the difference in average energies in the bound and in the free state:

$$\Delta E_{MM} = \Delta E_{MM_{bound}} - \Delta E_{MM_{free}} \quad (2.21)$$

The entropic term, $T\Delta S$, can be calculated using normal mode analysis (NMA), or disregarded altogether if the focus is on the enthalpic contribution. Finally, the difference in free energy due to solvation, ΔG_S, can be again obtained as the difference between the bound and the free states:

$$\Delta G_S = \Delta G_{S_{T-L}} - \Delta G_{S_L} - \Delta G_{S_T} \quad (2.22)$$

where the subscript *T-L* indicates the target-ligand complex, *L* the free ligand and *T* the free target. ΔG_S is the result of polar and non-polar contributions, the former of which are calculated using the Poisson-Boltzmann equation (or, as an alternative, the Generalized Born model, in which case the method is called *MM/GBSA*), whereas the latter, non-polar, contributions are calculated from the solvent-accessible surface area (SASA).

Despite being arguably more accurate than a docking scoring function, the MM/PBSA method contains several approximations designed to improve the computational efficiency, such as the use of an implicit model of the solvent. This can introduce crude inaccuracies, partly due to the fact that in most scenarios the input snapshots used for MM/PBSA calculations stem from MD simulations performed with an explicit solvent, which is then removed prior to MM/PBSA. Thus, since the energy function used to obtain the MD trajectory is not consistent with the one used in MM/PBSA, which uses the PBSA implicit solvent model, the introduced inconsistency can have significant repercussions on the estimate of the binding affinity. Nevertheless, the efficiency of the MM/PBSA method, together with the possibility of applying it after performing MD simulations (with the above-mentioned caveat in mind) and the option to decompose the binding energy into individual contributions of single residues, have made it a widely employed technique to obtain energetic insights between the interaction of small molecules and biomolecular targets, as well as to perform comparative studies between different ligands and/or different targets and thereby spot key molecular interactions able to enhance or weaken the binding process.

Chapter III

Molecular modelling and simulation of anesthetics

3.1 Introduction[1]

The very definition of human consciousness has baffled philosophers, spiritualists, and modern scientific scholars alike for a long time, but is yet to be found with consensus. The underlying issue is the lack of understanding of where and how consciousness arises in the brain. A first, pragmatic step toward understanding consciousness is to inspect the role of general anesthesia (GA), whose mechanism is still an enigma in spite of the fact that its discovery dates back to 1860. Indeed, GA is routinely used for reversibly extinguishing consciousness prior to and during surgery, but without a clear knowledge of its mechanisms of action, especially at the cellular and molecular levels. Scientific inquiries aimed at defining the neural correlates of consciousness, and hence the susceptibility thereof to general anesthetics, have been conducted at all investigative levels, from molecular/genetic

[1] Part of the work described in this chapter has been published in the following authored scientific publications:

Zizzi, Eric A., et al. "Insights into the interaction dynamics between volatile anesthetics and tubulin through computational molecular modelling." Journal of Biomolecular Structure and Dynamics 40.16 (2022): 7324-7338.

Zizzi, Eric A., et al. "Alteration of lipid bilayer mechanics by volatile anesthetics: Insights from μs-long molecular dynamics simulations." Iscience 25.3 (2022): 103946.

Cavaglià, Marco, et al. "Alteration of Consciousness by Anaesthetics: A Multiscale Modulation from the Molecular to the Systems Level." Journal of Consciousness Studies 29.5-6 (2022): 21-49.

to systems biology, but with inconclusive results. From a molecular point of view, this type of investigation is complicated by the fact that in spite of their diverse molecular structures and different putative molecular targets, all general anesthetics consistently induce reversible loss of consciousness and memory[47]. Indeed, GA represents an extraordinary clinical procedure that allows for a temporary and reversible manipulation of the person's consciousness level in a dose-dependent manner and with only minor variations among subjects and a similar mode of action in humans as well as animals. Thus, exploring the relationship between general anesthesia and the associated field of neuroscience becomes intriguing. Understanding the mechanisms underlying anesthesia may help to resolve the mysteries surrounding consciousness. At the same time, understanding the cellular and molecular mechanisms involved in consciousness could help the design and development of new anesthetic agents and psychoactive mood-altering drugs. It may also explain what mechanism of neuronal processing mediates the qualitative feeling associated with subjective experience. What exactly is measured or monitored during general anesthesia? Could there be a more reliable measure of consciousness when patients are under the influence of General Anesthesia? The so-called Hard Problem in answering any question related to consciousness is the nature of reality that one experiences [48]. The complexity of brain structure, function, and behavior further explains the broad spectrum of neuroscience research, ranging from philosophy to quantum physics [49]. While consciousness at present is not known to be directly measurable or even observed, modern science continues to seek quantitative measurements of its possible neural correlates. Current neuroscience research related to the investigations of general anesthetics, is being conducted at different biological levels, from the whole organism (to determine clinical effects such as changes in the cardiac and respiratory rhythms, blood pressure, sweat production, tears or pupil dilation), to the cellular level (to identify cortical/neural mechanisms and pathways), and deeper to the molecular level (in order to identify and characterize both the sites and microscopic mechanisms of action of anesthetic molecules).

As extensively described in the upcoming sections, the unique chemical and physical characteristics of anesthetic molecules, together with the inconclusive theories of anesthetic action formulated to this date, justify the application of molecular modelling strategies in the search for mechanistic explanations for their molecular-level effects at the smallest scale of investigation. Section 3.2 provides a brief background on the class of volatile anesthetics (VA), their physical and chemical characteristics, as well as their unique idiosyncrasies in the context of

modern pharmacology. Section 3.3 describes a comparative investigation of microtubules (MT) as putative molecular targets for different types of anesthetics using computational modelling strategies, ranging from docking to molecular dynamics. Section 3.4 reports the computational investigation of the effects of VAs on the phospholipid membrane at different concentrations, providing atomistic insights into the consequences of VA partitioning on overall membrane structure and geometry as well as mechanical stiffness.

3.2 Volatile Anesthetics: outliers in modern pharmacology

General anesthetics are a unique class of drugs in modern medicine. They are able to reversibly suspend conscious brain activity while sparing most of the other brain functions with extraordinary selectivity. This, along with their analgesic and amnesic properties, has effectively made them a cornerstone of modern surgery, yet little is known about their molecular mechanism of action. This is partly due to the high chemical and physical diversity of available VAs, which range from single-atom gases such as Xenon, to more complex molecules such as halogen-substituted ethers and even steroids. Also, this issue encompasses a rather large subset of open questions at many different scales: research failed to determine a single biological site of action capable of explaining not only the clinical manifestation of general anesthetics, but also the lack of any anesthetic effects in certain molecules with similar physicochemical properties[50]. In the past decades, several different theories of anesthetic action have been proposed with the aim of explaining anesthetic behavior despite this lack of structural similarity, starting from the Meyer-Overton correlation between the lipid solubility of VAs and their clinical potency (in terms of Minimum Alveolar Concentration, MAC). This theory paved the way towards what is known as the lipid theory, which postulates that the main mechanism of action of anesthetics lies in the alteration of the structure of lipid bilayers – in particular cell membranes – in a non-specific fashion [51]. Some shortcomings of this hypothesis, including the lack of any anesthetic effect of other lipid-altering factors, e.g. temperature, steered the interest of research around anesthesia towards finding specific molecular targets – i.e. proteins – which could explain the clinical effects of VAs. Indeed, an increasing amount of evidence points toward ion channels located in the Central Nervous System as relevant targets for anesthetics, starting from the works of Franks and Lieb [52,53]. A detailed review of molecular targets of anesthetics can be found in Campagna et al. [54]. Interestingly, despite the increasing evidence of interactions with ion channels, the exact mechanism of action remains unclear, and researchers failed to agree on the most-relevant effectors of anesthesia

at clinically relevant VA concentrations. Most recently, after further studies highlighted significant involvement of cytoskeletal proteins based on post-anesthetic-exposure proteomic alterations [55–57], investigations focused on possible involvements of the cytoskeleton, specifically microtubules (MTs), in the processes of memory formation, consciousness and side effects of anesthesia.

3.3 Elucidating the interaction between volatile anesthetics and human tubulin assemblies[2]

3.3.1 Abstract

General anesthetics, able to reversibly suppress all conscious brain activity, have baffled medical science for decades, and little is known about their exact molecular mechanism of action. Given the recent scientific interest in the exploration of microtubules as putative functional targets of anesthetics, and the involvement thereof in neurodegenerative disorders, the present work focuses on the investigation of the interaction between human tubulin and four volatile anesthetics: ethylene, desflurane, halothane and methoxyflurane. Interaction sites on different tubulin isotypes are predicted through docking, along with an estimate of the binding affinity ranking. The analysis is expanded by Molecular Dynamics simulations, where the dimers are allowed to freely interact with anesthetics in the surrounding medium. This allowed for the determination of interaction hotspots on tubulin dimers, which could be linked to different functional consequences on the microtubule architecture, and confirmed the weak, Van der Waals-type interaction, occurring within hydrophobic pockets on the dimer. Both docking and MD simulations highlighted significantly weaker interactions of ethylene, consistent with its far lower potency as a general anesthetic. Overall, simulations suggest a transient interaction between anesthetics and microtubules in general anesthesia, and contact probability analysis shows interaction strengths consistent with the potencies of the four compounds.

[2] Part of the work described in this paragraph has been published in:

Zizzi, Eric A., et al. "Insights into the interaction dynamics between volatile anesthetics and tubulin through computational molecular modelling." Journal of Biomolecular Structure and Dynamics 40.16 (2022): 7324-7338.

Contribution of the author: study design, creation of computational models and simulations, data analysis and interpretation.

3.3.2 Introduction

The theory elaborated in the 1980s by Penrose and Hameroff proposed to explain consciousness as the result of quantum resonance in the microtubule bundles extending to a neuron and eventually an entire brain, and is referred to as the 'Orch OR' theory [58], later expanded to what is known as the Quantum Mobility theory [50], based on computational evidence of alterations in the oscillation frequencies of π-electrons in aromatic amino acids of microtubules in the presence of anesthetics, with possible long-term effects also on MT polymerization. While the Orch OR theory has not been confirmed experimentally yet, the binding of anesthetics to tubulin is known to occur experimentally [59], and interactions between the latter and anesthetic agents are of particular interest due to potential implications in (a) Post-operative cognitive dysfunction (POCD), which is associated with microtubule instability and the separation of microtubule-associated protein (MAP) tau from MTs [60,61]; (b) memory formation, a process relying on synaptic plasticity [62–64] which is impaired during general anesthesia and has been linked in previous computational studies to the microtubule lattice [21]; (c) the unique spatial organization of microtubules in neurons [65,66] and their putative ability to create specific conduction pathways, hypothesized to be involved in information processing [21,67–69]; (d) clinical decisions regarding anesthesia in patients undergoing chemotherapy or with neurodegenerative comorbidities, both of which can imply pathological or drug-induced alterations of the microtubule cytoskeleton respectively, which might be influenced by the simultaneous presence of anesthetics [70,71].

These considerations support the investigation of microtubules, and their constitutive protein tubulin, as a putative target for anesthetic molecule interactions.

Indeed, volatile anesthetics (VAs) exhibit many different chemical structures and cover a wide range of molecular weights, from single atoms such as Xenon to heavier halogen-substituted ethers such as Sevoflurane. Among these, Halothane (2-bromo-2-chloro- 1,1,1-trifluoroethane) is a volatile haloalkane with a MAC of 0.74% [72]. Experimentally, it has been found to alter the genetic expression of tubulin [56] and to directly bind to it [59]. Also, it is known to alter the polymerization rate of tubulin in microtubules in vivo [73,74], and thus is of particular interest in the context of VA-tubulin interaction. Conversely, Desflurane (2-(difluoromethoxy)-1,1,1,2-tetrafluoroethane) is a poorly soluble, fluorinated ether with a slightly higher MAC value of 6% in oxygen [75], also causing alterations in tubulin expression after exposure *in vivo* [55]. Methoxyflurane (2,2-dichloro-1,1-difluoro-1-

methoxyethane) is a potent anesthetic gas, also belonging to the class of halogenated methyl ethyl ethers, with a MAC value of just 0.16% [76], and now mostly abandoned as a general anesthetic due to the nephrotoxicity of its metabolites [77]. It has been shown, just as Halothane, to influence the polymerization of tubulin *in vitro* and significantly alter the axonal microtubule structure [78]. Lastly, ethylene (or ethene) is the simplest alkene and has a comparably low molecular weight of just 28.054 g/mol. It is highly volatile and with a MAC value of as much as 67% [79], but it is not used as a general anesthetic due to its very low potency.

The four above-mentioned VAs were chosen for our investigation not only due to experimental evidence of interaction with tubulin, but also to cover a wide range of clinical potencies (MAC values of 0.16% for Methoxyflurane up to 67% for ethylene), and to include molecules belonging to different classes (namely, ethers, alkanes and gases as classified in [75]).

To investigate the effect of said anesthetics on the cytoskeleton network, in the present work tools provided by Computational Molecular Modeling, namely Homology Modelling, Molecular Dynamics and Molecular Docking were deployed to provide new insights into their interaction at an atomic scale as those tools have widely demonstrated their value in investigating the molecular basis of biological effects [80–87].

3.3.3 Materials and Methods

Homology Modelling of human tubulin isotypes

Due to the lack of experimentally determined 3D structures for most human tubulin isotypes, αβ-tubulin dimers were modeled according to previous tubulin modelling protocols based on crystallographic data for bovine and porcine tubulin [88,89]. Following the nomenclature also found in Leandro-García et al. (2010)[90], human isotypes βVI (Beta-1, Class VI, Gene TUBB1), βIIa (Beta 2A, Gene TUBB2A) and βIVa (Beta 4A, Gene TUBB4) were chosen for this analysis; βIVa and βIIa were chosen due to their highest reported expression in the brain tissue with respect to other tubulin isotypes (46% and 30%, respectively); βVI was chosen as a non-brain-specific control[90]. Manually annotated and reviewed amino acid sequences for human tubulin isotypes αIa, βVI, βIIa and βIVa were downloaded from the UniProt database (accession codes Q71U36, Q9H4B7, Q13885 and P04350, respectively). Since the goal was to model human tubulin in its dimeric form, the 3J6F[91] entry

from the Protein Data Bank (www.rcsb.org) was selected as a template, consisting of a minimized structure of GDP-bound microtubules with a resolution of 4.9 Å. First, the alpha and beta tubulin isotypes were modeled as single monomers. To do so, sequence alignment to the 3J6F target was carried out using UCSF Chimera software[92] and missing residues were modelled using modeller 9.21[93]. Then, the homology model was built using modeller 9.21 with the options of building models with hydrogens, using thorough optimization and performing loop refinement. All models were built including their C-terminal domains. The generated models were evaluated based on the GA341 and zDOPE score, inspected manually by visual comparison to the target structure, and further checked using the packages PROCHECK[94], WHATCHECK[95], ERRAT[96] and Verify-3D[97]. A further quality assessment was carried out using the QMEAN score[98,99] implemented in the SWISS-MODEL server[36]. The same general protocol was subsequently used to generate αIa-β-tubulin dimers for every β isotype mentioned, since data regarding β tubulin isotype expression is readily available in the literature and the present interaction study was also aimed at assessing differences between β tubulin isotypes.

Molecular Docking

To evaluate putative binding sites for anesthetic molecules of interest, conformations for each tubulin dimer were extracted every 10 ns from the second halves of each of three 100ns MD simulations of the tubulin dimer with each VA and exported in pdb format, yielding 18 protein snaphots for each of the three dimers, each simulated with one of the four anesthetics, for a total of 18 snapshots * 3 isotypes * 4 anesthetics = 216 protein snapshots. AutodockTools [100] was subsequently used to add Gasteiger charges information and export the snapshots in pdbqt format. The 4 anesthetics were obtained in 3D-SDF format from the DrugBank database (www.drugbank.ca), energy minimized with explicit hydrogens and exported in pdbqt in AutodockTools, again assigning Gasteiger charges. Docking was performed in AutoDock-Vina [101], which accounts for ligand flexibility by continuously rotating rigid parts of the ligands around rotatable bonds and keeping the protein rigid. The search box, centered at the center of mass (COM) of the dimer was built in order to encompass the whole dimer and perform blind docking, and the center of the search box was conserved at the COM of the dimer in all blind docking runs, for all anesthetics. For all docking runs, the exhaustiveness was set to of 64 and the maximum number of binding modes to be generated was left at the program's default setting of 9 poses per run, providing a good compromise between speed and pose sampling. With 9 conformations

generated in each docking run, repeated for a total of 216 protein snapshots as discussed above, a total of 9*216=1944 docked conformations were generated, 162 for each anesthetic-isotype pair. Considering the low affinity difference between predicted poses, around tenths of kcal/mol, all of these 162 docking poses were analyzed for each ligand-isotype blind docking run. To facilitate the analysis and comparison of individual docking results, said 162 binding poses obtained from blind docking for each isotype-VA pair were exported in pdb format with the dimer, and residues within 6 Å of the ligand were extracted using GROMACS, and saved along with the corresponding predicted affinity of the pose into a simple text file. A custom MATLAB code was subsequently deployed to count the occurrence of each residue across all the 162 poses of each docking run, and the 50 most recurring residues were deemed as involved in binding sites with the highest consensus, given the negligible difference in affinity among different docking poses, below the noise level of k_BT, and further analyzed. The predicted binding affinity of each anesthetic for each tubulin dimer is also reported, as mean ± standard deviation of all output poses.

To check and refine the above-described blind docking approach, a local docking validation has been carried out as exhaustively explained in the Supplementary Information.

Molecular Dynamics

For molecular dynamics simulations tubulin isotypes βVI, βIIa, βIVa were chosen for investigation, each in its dimeric form with αIa tubulin. Each dimer was completed with GTP, GDP and the Mg^{2+} ion from the 3J6F template, and each was simulated both without anesthetics, and separately with halothane, desflurane, methoxyflurane and ethylene present in the surrounding solvent at a concentration of 10 mM, which experimentally showed polymerization inhibition of microtubules [102] and is at the upper end of the range of clinical concentrations for more potent volatile anesthetics. It is to be noted that data regarding intracellular concentration of volatile anesthetics during general anesthesia is fairly dispersed, reporting concentrations ranging from a few mM[103] up to hundreds of mM [104], possibly due to the large differences in potency between different compounds. Overall, a total of 15 systems for Molecular Dynamics simulations were obtained – 3 isotypes times 4 anesthetics + control without anesthetics– and each was simulated in three replicates by re-initializing velocities from the Maxwell distribution at 300K at the beginning of the NVT equilibration. The Visual Molecular Dynamics [105] (VMD)

environment was used for visual inspection of the systems and trajectories and for further roto-translational corrections. GROMACS 2019.1 [106] was used for MD simulations, specifically with the AMBER ff99SB-ILDN force field [107]. Molecular 3D structures for the 4 volatile anesthetics were obtained in 3D-SDF format from DrugBank [108], energy minimized with explicit hydrogens, and their topologies, just as for GTP and GDP, were generated through the ANTECHAMBER [109] package employing the AM1-BCC charge method [110] and the general AMBER force field. The MD system was configured in GROMACS in a dodecahedral box with xyz periodic boundary conditions and a minimum distance between the protein and the box edge of 1.0 nm, to avoid interaction with periodic images. All the systems were solvated with TIP3P explicit water and neutralized with counterions. Moreover, a physiological ionic strength of 0.1 M was imposed by adding appropriate amounts of Na+ and Cl- ions. In the case of systems with anesthetics, a custom script was deployed to add an appropriate number of molecules given the target concentration of 10 mM. The minimization was carried out using the steepest descent method, with 1000 kJ/(mol*nm) maximum force and no restriction on maximum steps. All subsequent steps, namely equilibration in NVT and NPT ensembles along with the production NPT simulations were carried out remotely on HPC resources. The NVT and NPT equilibrations were carried out at T=300K and P=1.0 bar, respectively, with the protein restrained and a total of 100 ps each. In the case of NVT, the modified Berendsen thermostat[111] was used with τ constant of 0.1, while NPT equilibration was carried out using the Parrinello-Rahman barostat [112] with isotropic coupling and a τ constant of 2.0. For both NVT and NPT equilibrations, PME [113] Electrostatics were used, with an interpolation order of 4 and an FFT grid spacing of 0.16 nm. Production simulation followed in the NPT ensemble, without any restraint, for 100 ns per replica with a 2 fs timestep and coordinate saving set every 1000 steps, i.e. every 2 ps. The stability of the tubulin dimer during the simulation was determined by the RMSD of the protein backbone followed by cluster analysis, both carried out in GROMACS.

Analysis

Structural Effects

The structural effects on the dimer in the presence of the VAs were evaluated by analyzing the RMSF with and without anesthetic molecules, as calculated with GROMACS excluding the highly fluctuating C-terminal regions, and separately for the alpha and beta subunit of the dimer. Structural effects were further assessed using cluster analysis on each simulation, as implemented in the gmx cluser tool of

GROMACS, using the single linkage method with 0.15 nm RMSD cutoff. Effects on secondary structure were assessed using DSSP 3.0.0 [114] after extracting snapshots every 100 ps from the last 50 ns of each simulation.

Contact Probability

To quantitively assess the interaction between each of the four anesthetics and the tubulin dimer, the raw trajectory was analyzed: for each frame, the minimum distance between each residue and any ligand molecule in the solvent was calculated with GROMACS. A custom script subsequently calculated the per-residue contact probability by averaging interactions in each frame between residues and ligands. Following previous computational work [87], the ligand was considered to be in close contact with a residue whenever its distance to that residue fell below 2.8 Å, corresponding roughly to the diameter of a water molecule, and at the end the overall probability of contact with the anesthetic was obtained for each residue over the whole trajectory consisting of the concatenation of the last 50 ns of each of the 3 replicates. The individual contribution of the second half (50ns) of each replica of a given system to the per-residue contact probability was also calculated and is reported in the Supplementary Information. Residence times of each contact event were calculated by counting the number of consecutive frames in which the ligand stayed within 5 Å of a given residue. This cutoff was chosen to include consecutive frames in which the ligand briefly repositions itself, temporarily increasing its distance to the residue above the 2.8 Å cutoff used for contact probability calculation, but effectively staying in the same binding pocket. To efficiently compare contact areas between different isotypes and different anesthetics, the system was analyzed in a spherical coordinate system, built as follows: the position of each dimer was aligned with a custom VMD script so that the origin of the cartesian coordinate system relocated to the center of mass of the dimer, between the alpha and beta subunit: this way, residues belonging to the alpha subunit had coordinate $z > 0$, residues on the beta subunit had $z < 0$ and residues at the alpha-beta interface had $z \cong 0$. Subsequently, another custom VMD script rotated the dimer so that the x axis was parallel to the vector connecting the Cα of residues α128Q and α285Q, which are known to be involved in lateral contacts between adjacent protofilaments [18]. This allowed to broadly discriminate between residues located towards the abluminal side of the microtubule, residues located towards the luminal side and residues involved in lateral contacts, based on their y coordinate ($y > 0$ corresponds to residues facing the outer surface of the MT, $y < 0$

residues facing the lumen and y ≅ 0 residues involved in lateral contacts between adjacent protofilaments), as highlighted in Figure 3.1.

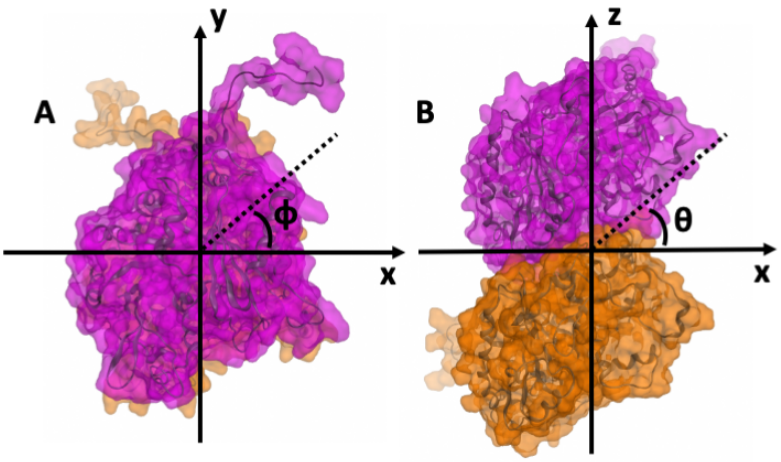

Figure 3.1. (a) Schematic representation of the phi angle from a top view of the tubulin dimer, which represents the azimuthal position in the xy plane, around the z axis: positive values correspond to the outer side of the protofilament while negative values correspond to the inner side; (b) Schematic representation of the theta angle from a side view of the tubulin dimer. Elevation theta represents the angular position between the z axis and the xy plane: negative values correspond to the beta subunit (shown in orange), while positive angles represent residues on the alpha subunit (shown in pink).

To better represent and interpret the data, the geometrical center of each residue was determined using the MDAnalysis[115,116] toolbox for python, and its (x,y,z) Cartesian coordinates subsequently transformed into spherical coordinates with an *ad-hoc* python script. In this new system, the elevation angle theta was calculated starting from the xy-plane, so that $\theta > 0$ corresponds to points with $z > 0$ and vice versa. The φ angle on the other hand represents the azimuth, i.e. the rotation around the original z axis. A 3D rendering of the tubulin dimer in this new spherical coordinate system is shown in Supplementary Video S1. Residues were represented in this new coordinate system, with the radial coordinate ignored. As a matter of fact, since contact in the 100ns trajectories only occurs on the surface, there is no chance of radial ambiguity and a single couple of (θ, φ) always identifies a single surface residue in this spherical approximation, except for the highly fluctuating C-terminus, which was checked for contact by visual inspection of the trajectories. To further enhance this representation, the surface on the tubulin dimer has been divided into sectors on the theta-phi plane. Instead of plotting the contact probability of individual residues, the contact probability was evaluated on a per-

sector basis: contact was recorded on a given sector of the dimer surface in a frame of the MD trajectory if any of the residues within that sector were within 2.8 Å of any anesthetic molecule. Contact counts were subsequently normalized to the total number of frames to yield the contact probability. The resulting coordinate system, as previously discussed, implies that the four quadrants qualitatively represent distinct areas on the dimer, as reported in Table 3.1.

Table 3.1. Quadrants on the (theta,phi) plane and corresponding gross locations on the dimer.

Quadrant	θ	φ	Subunit	MT surface
I	> 0	> 0	Alpha	Abluminal
II	< 0	> 0	Beta	Abluminal
III	< 0	< 0	Beta	Luminal
IV	> 0	< 0	Alpha	Luminal

After qualitatively assessing the location of highly interacting residue groups in this representation and checking for recurring interaction patterns across different anesthetics and different tubulin isotypes, each trajectory was further analyzed manually, and the regions of interaction inspected and reported. The main binding clefts where interaction consistently occurred across different replicas (corresponding to dark areas on the contact probability maps) were precisely defined – in terms of residues forming the clefts – and reported. Their location is also reported in the previously mentioned coordinate system to aid their visual localization on the dimer and allow for a direct comparison with overall contact probabilities.

To statistically assess whether the differences in per-residue contact probability between the four tested ligands for a given isotype were significant, a one-way ANOVA was used, testing the null hypothesis that the means of the contact probabilities for each group (i.e. with each of the four ligands) are equal, rejected at $p<0.05$. This allowed to determine if at least one of the ligands had a significantly different probability of interacting with the tubulin dimer. To further compare the contact probabilities of Ethylene, the weakest molecule used as a control reference, versus the contact probabilities of the other three ligands (Desflurane, Halothane and Methoxyflurane), Dunnett's Test was used with a significance threshold of $p<0.05$.

MM/PBSA Binding Energy estimation

To provide a further quantitative assessment of the interaction between the four simulated anesthetics and the tubulin dimer, MM/PBSA [117] estimations of binding energies were performed for all four tested anesthetics. More in detail, for each of the four anesthetics, the following workflow was adopted: starting from the contact maps obtained from the MD simulations with anesthetics, the main binding clefts were identified as described above. Subsequently, the concatenated trajectories containing the last 50 ns at equilibrium of each of the three replicas, from which the contact probability maps were built as described previously, were iteratively filtered for frames where the given anesthetic was present in the cleft. This was repeated for all anesthetics and for all clefts, so that sub-trajectories were generated for each ligand and each cleft, representing different snapshots of the bound state. These trajectories were used for MM/PBSA calculations using the *pbsa* tools included in AmberTools 20 [118], after converting GROMACS trajectories and topologies into their respective amber counterparts using ParmEd. Calculations were performed using one every two frames. The final binding affinity and the contributions of the VDWAALS, EEL, ENPOLAR and EDISPER components are also reported on the same, sectorized (θ,φ) plots as the contact probability maps, to provide a direct comparison and a visual localization of the different clefts.

Plots and Figures

Data plots for RMSD and RMSF distributions were generated using the Grace package. Three-dimensional representations of the tubulin dimers were rendered in VMD and in MOE, while auxiliary figures for the spherical coordinate system were assembled in Microsoft PowerPoint. The animated 3D-view of the tubulin dimer within its spherical coordinate system, with the theta and phi angles highlighted, was generated using a 3D rendering of the dimer in Blender 2.80 and is available in the Supplementary Information. Sectorized contact probability plots, residue count histograms from docking runs and MM/PBSA binding energy maps and their corresponding decomposition maps were generated in MATLAB. Detailed, 3D views of docking pose ensembles and of interesting MD contact sites on the dimer and Ramachandran plots reported in Appendix, Figure S.3.2, were generated in MOE 2019.01 [119].

3.3.4 Results

Homology Modelling

Modeller 9.21 [120] was used to build homology models for human isotpyes βVI, βIIa and βIVa in dimeric for with α1a tubulin, starting from the 3J6F PDB template. The four modeled sequences αIa, βVI, βIIa and βIVa shared an identity with the respective 3J6F templates of 99.32% (sequence Q71U36), 80.80% (sequence Q9H4B7), 99.06% (sequence Q13885) and 97.19% (sequence P04350) respectively. The obtained models all showed comparable zDOPE scores fluctuating around -1.55 ± 0.1 for β tubulin and -1.49 for the α1a isotype. PROCHECK [94] validation reported more than 94% of residues in most favoured regions and no residue in disallowed regions for every isotype modeled. QMEAN4 values for the three modelled α-β dimers were -1.56 for αβVI, -1.49 for αβIIa and -1.67 for αβIVa, respectively, while the 3J6F template dimer had a QMEAN4 value of -0.37. The quality of the models was confirmed through the tools Verify-3D [97], WHAT_CHECK [95] and ERRAT [96] as shown in detail in the Supplementary Material.

Docking

Firstly, blind docking was performed for all isotypes with all anesthetics by setting the grid box geometry so as to encompass the whole dimer, centered at the COM of the latter. Across all the 162 blind docking poses determined for each anesthetic-isotype pair, the average predicted binding affinities are shown in Table 3.2. Data points are reported in kcal/mol, as mean ± standard deviation.

Table 3.2. Predicted binding affinities in kcal/mol with each anesthetic, reported as mean and standard deviation calculated among the 162 docking poses for each isotype-anesthetic pair.

	Isotype		
	αβVI (kcal/mol)	αβIIa (kcal/mol)	αβIVa (kcal/mol)
Ethylene	-2.00 ± 0.14	-2.00 ± 0.16	-2.01 ± 0.15
Desflurane	-5.15 ± 0.24	-5.02 ± 0.22	-5.02 ± 0.23
Halothane	-4.45 ± 0.26	-4.14 ± 0.17	-4.45 ± 0.34
Methoxyflurane	-4.22 ± 0.18	-4.26 ± 0.30	-4.25 ± 0.26

Overall, blind docking yielded binding affinity ranges consistent with combinations of hydrophobic Van der Waals-type interactions. Ethylene consistently showed very low affinity values hovering around -2.00 kcal/mol with little differences among different poses on the same snapshot and among different snapshots of the same isotype (as seen by the comparatively low std. dev.), along with little differences between isotypes. The differences in affinity between the other three ligands were more subdued, and with a slightly higher std. dev., highlighting how some docking poses and sites were predicted to be more energetically favorable for hosting these molecules with respect to others. Overall, Desflurane reported the best predicted affinity across all three isotypes, while the predicted affinities for Halothane and Methoxyflurane were comparable.

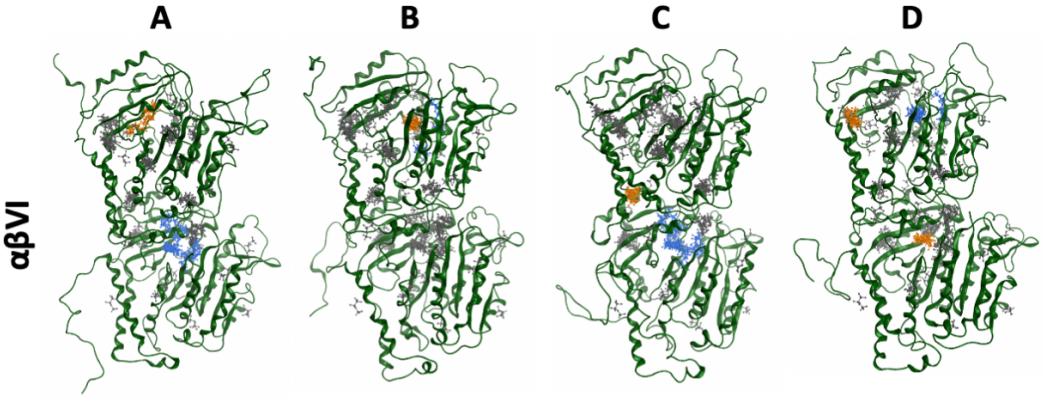

Figure 3.2. Ensemble of docking poses on the αβVI dimer, with individual poses shown in grey: (**a**) Desflurane; (**b**) Halothane; (**c**) Methoxyflurane and (**d**) Ethylene. The largest clusters of recurring poses are highlighted in blue, clusters of poses with highest average predicted binding affinity (most negative) are highlighted in orange.

In terms of binding sites, isotype αβVI (shown in Figure 3.2) featured with Desflurane a large number of docking poses around βILE368, βLEU250, βALA314, βILE236, βLEU253 and βASP249, while the binding site with highest predicted affinity was located around αPHE202, αALA201 and αMET203. In the case of Halothane, the most frequently involved residues were αTRP21, αALA65, αPRO63, αGLY17, αPHE67, with the best overall affinity at the sites around αGLU168, αVAL137, αLEU167 and αPHE202. Methoxyflurane consistently docked as Desflurane near βLYS252, βLEU253, βALA254, βALA314, βASP249, βMET257, βILE316, βASN247, an area delimited at the top by αASN101 at the inter-monomer interface, with peaks of highest affinity around βARG251, αALA99 and αSER178. Ethylene did not show specific preferred binding sites, but docked with slightly more frequency around αPHE138, αVAL235 and αPHE169, with best

affinities at the sites around βILE368 and αTRP388. In the case of isotype αβIIa with Desflurane, the most recurring sites were two, located between αTYR172, αSER187, αHIS139, αSER140, αSER170, and αPHE141, with one of them, involving also αTHR190 and αTHR191, αGLU168, and αTHR194 also showing the lowest average affinity across the poses. With Halothane, the frequent locations were at βARG251, αPHE141, αSER187 and αPRO173, with low-energy sites around αLEU92, αILE122, αALA65, αARG121, αGLU90, αGLN91, αPRO63, αVAL62 and αVAL66. Methoxyflurane frequently docked at αPHE141, αSER147, αTHR194, αGLY142, αTHR190 and αTHR191, with the highest affinities predicted around βPHE294, βTYR310 and βVAL313, βMET293. Ethylene again was not predicted to have preferred sites, with a slightly higher count of poses around αTRP388, αMET203, αPHE267, αALA201 and αPHE202, αPRO173. A lower-energy binding site was predicted around βPHE294, also found in the previous case. Lastly, docking of Desflurane to isotype αβIVa predicted three recurring binding sites around αILE384, between βVAL236, βTHR237 and βGLU198, and near αTHR239 and αLEU136 respectively, with the latter also with comparatively high affinity across the different sampled poses, especially in poses in close contact with αPHE138 or αPHE135. Halothane frequently docked into a cleft lined by αLEU92, αPHE67, αGLN91, αVAL14, αVAL78, αPHE87 and αASN18. The binding site with lowest average binding energy was instead located between βVAL333, βGLN334, βMET330 and βVAL349. Docking of Methoxyflurane frequently accommodated the ligand in a cleft lined by βALA248, βASP249, βLEU240, βLEU253, βLYS252, βASN247, βLEU250 and βILE368, which was also predicted in [102], with high-affinity sites located instead surrounded by αGLY81, αPHE67, αPHE87, αTHR82, αTYR83, αVAL78 and αARG84. Lastly, ethylene frequently docked into a broader area delimited by αTRP21, αHIS8, αPHE67, αTYR24, αGLY17 and αVAL235. Poses near αHIS8 were also the ones with lowest mean energy, along with poses docked to a second site near αTHR150. For a graphical summary of frequently found residues across all docking poses, along with the mean predicted affinity associated with the respective poses, see supplementary information.

To check and further refine the ligand-protein binding estimation, a second set of local docking runs was performed, which confirmed data and trends reported from blind docking (see the Appendix and Supplementary Table ST3.1).

Overall, the binding sites found by docking were generally lined by a majority of hydrophobic residues, which again suggests a predominantly hydrophobic

interaction, consistent with the predicted affinity estimates. In blind docking, isotype αβVI showed putative interactions on both subunits, isotype αβIIa had more overall binding poses on the alpha subunit, and isotype βIVa showed a similar number of binding poses on both subunits. The results from blind docking, and their subsequent validation through local docking refinement, confirmed the main drawbacks of docking techniques in the context of ligands interacting with low affinity, possibly within multiple, energetically equivalent binding sites on the dimer simultaneously. This level of investigation is not accessible to plain docking. Overall, the lack of an experimentally known set of binding sites against which to perform docking, along with the mentioned methodological drawbacks such as the inaccuracy of predicted affinity[121], especially in the context of the systems under investigation in the present work, justified a more detailed analysis of the sites of interaction through the use of Molecular Dynamics, in the light of the low interaction strength and absence of evidence for a specific, 'lock-and-key'-type binding site for anesthetics. Indeed, the adopted molecular dynamics approach allows for a more efficient sampling of multiple, simultaneous, low-affinity binding sites on the dimer surface, by simulating the dimer with a fixed anesthetic concentration in the solvent. This enables the statistical investigation of the most explored areas, which is not feasible through docking alone.

Protein Ligand binding dynamics

Molecular Dynamics stability analysis

First, the stability of all the simulations was checked by examining the RMSD over each 100ns trajectory. All three isotypes had reached a plateau after about 50 ns, with the αβIVa dimer in the presence of Desflurane being the only case with slightly more accentuated fluctuations up to about 70 ns. See Supplementary Figure S3 for the complete RMSD details. Potential energy plots for all simulated systems are reported in Supplementary Figure S4.

Protein-Ligand interaction dynamics

Molecular Dynamics simulations allow to overcome the limitations of the docking approach in the context of low-affinity ligands, such as the volatile anesthetics investigated in the present work, which interact simultaneously in multiple sites on the tubulin dimer. Simulating the dimers in the presence of VAs in the surrounding solvent at a fixed concentration enables a more significant sampling of frequent interaction clefts, including simultaneous interaction in multiple, low-affinity

binding sites, and provides a quantitative assessment thereof, which is precluded to single-ligand docking in the case of weak binding events.

Per-residue contact probabilities extracted from MD simulations show preferential interaction with specific residues for each anesthetic and for each isotype. The contact probability plots, reported in the Supplementary Information, visually highlight how the different anesthetics interact with partially different strengths and in specific locations, both on the same tubulin isotype and across different isotypes, albeit some commonly involved residues emerge. Ethylene clearly displays lower overall contact probabilities, in a manner consistent both with its considerably lower potency in clinic and with the significantly lower predicted affinities in blind and local docking runs. To better highlight the actual location where binding occurs, both longitudinally along the major axis of the dimer (i.e. *on which subunit and how far from the inter-monomer interface*), and circumferentially around said axis (i.e. *where around the dimer*), the contact probabilities are reported on a sectorized spherical coordinate system in terms of theta and phi angles, where elevation theta discriminates between subunits and azimuth phi locates residues around the dimer (see details described in the Methods section). Such contact maps highlight the patterns of interaction between each anesthetic and specific tubulin isotypes and provide qualitative information about preferential binding location both around the dimer (luminal vs. abluminal side in the MT) and longitudinally along the major axis (top α-subunit vs. α-β interface vs. bottom β-subunit). The resulting high-probability contact areas are shown in Figure 3.3 for the most highly interacting isotype, namely αβIVa, which is also the most highly expressed in the brain.

To visualize the proximity of tryptophan residues, which is a key requirement of the Quantum Mobility theory of anesthetic action[67], also in comparison to previous computational work[50] predicting aromatic amino acids as functional targets of anesthetics on tubulin, the location of Trp residues on the tubulin dimer in this spherical coordinate representation is shown as orange crosses on the heatmaps in Supplementary Figure S3.8 in the Appendix.

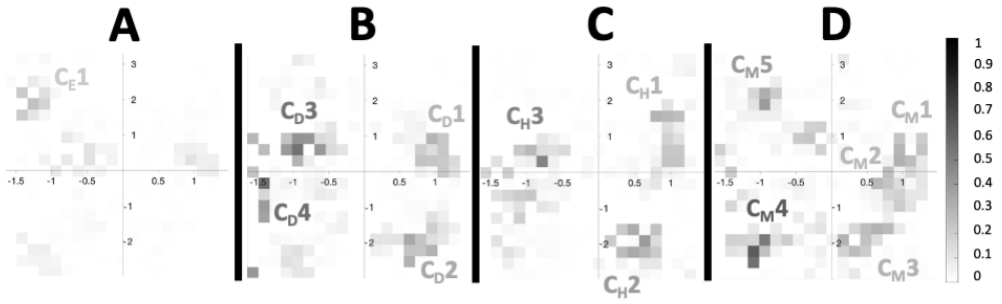

Figure 3.3. Per-area contact probability for isotype αβIVa, the one with the most overall interactions, with all the tested ligands. (**a**) Ethylene; (**b**) Desflurane; (**c**) Halothane and (**d**) Methoxyflurane. Color scale is 0 to 1, i.e. 0% to 100% probability of interaction with any residue within a given area. The main recurring interaction clefts are also highlighted, with the subscript differentiating the four ligands.

Briefly, Desflurane interacts substantially on the β subunit of isotype αβVI, both on the luminal and abluminal side of the dimer, along with different inter-monomer transient contact clefts. A distinct interaction zone also emerges on subunit alpha laterally (where φ is close to 0), enclosed by residues α293ASN on helix αH9 and α334THR on helix αH10. On isotype αβIIa, interaction was recurring more markedly on the α subunit mainly at the same lateral contact area already seen in the previous case between H9 and H10. Minor contact probabilities were also recorded on the luminal side of the alpha subunit, and on the abluminal and lateral area of subunit beta. The interaction is similar on isotype αβIVa (Figure 3.3B), with a high probability of residence laterally between H9 and H10 subunit alpha, with the addition of recurring interaction on the β subunit, laterally in close proximity to the exchangeable GTP binding site, between helix H6 and the start of H7, near residues β208TYR, β221THR and β225LEU, and transiently on the rest of the surface. Halothane showed slightly lower overall contact probabilities, especially on isotype αβIIa. A high probability of residence is again visible on the α subunit's H9-H10 lateral contact zone on all three simulated isotypes. Interaction sites were more abundant on isotype βIVa (Figure 3.3C), a substantial fraction of which on the luminal side of the dimer, with two distinct clusters on the α and β subunit and the addition of an interaction site on the lateral contact area of the β subunit, a semi-closed cleft defined by residues β231ALA and β227HIS belonging to helix H7 and capped by the sidechain of β276ARG of loop S7-H9 which folds over the ligand molecules (up to two halothane molecules at the same time seen during the simulation). Methoxyflurane, the most potent anesthetic – i.e. the one with the lowest MAC – showed the highest number of high-probability contact sites for all

three simulated isotypes, with the addition of the highest overall residence times (and thus contact probabilities). Interaction was ubiquitous on isotype αβVI, with contacting residues localized on both subunits and on either side, luminal and abluminal. Isotype αβIIa showed mostly overlapping areas of preferential residence. The interaction with isotype αβIVa (Figure 3.3D) was recorded both on the luminal and abluminal sides of both the α and β subunit. Notably, this isotype showed a unique interaction area located on the luminal side of the beta subunit, in a binding site near βGLY79 at the end of helix H2. The lateral contact area towards the top of the α subunit was again involved in numerous contacts with methoxyflurane on all three isotypes.

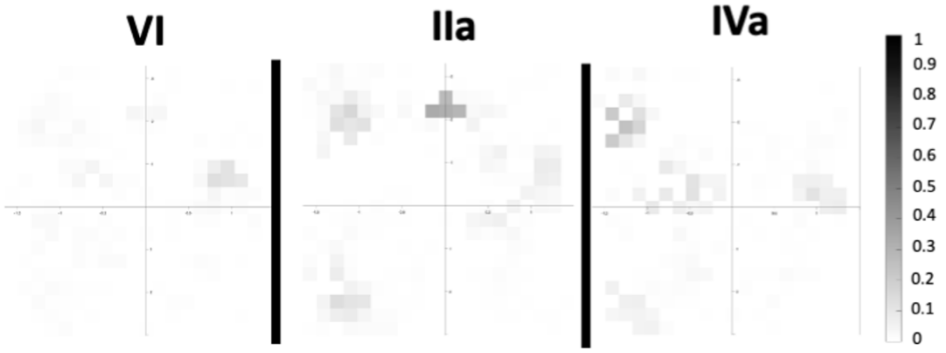

Figure 3.4. Contact probabilities of Ethylene with all three simulated isotypes (left to right: αβVI, αβIIa, αβIVa), which is visibly lower than the amount of contact of the other three anesthetics.

Ethylene (Figure 3.4) showed a much weaker overall interaction with the tubulin dimer, visible both during the simulations themselves and on the contact probability analysis. With the exception of a more frequent interaction on isotype αβIIa, on the abluminal site of the α-β inter-monomer interface (a cleft between H11 and H12, on H11', lined by residues β413MET, β415GLU, β409VAL, β418PHE and β408TYR), residence on the surface of the dimer was transient and with very low overall probability, demonstrating how the ligand spends most of the simulation time floating freely in the solvent. This is consistent not only with the significantly lower predicted affinities through docking and low molecular weight of the molecule, but also with the much lower efficacy as a volatile anesthetic if compared to the other compounds.

In summary, the analysis of the described interaction hotspots, i.e. the areas with highest contact probabilities visible as dark zones in Figure 3.3 and Figure 3.4, pinpoints the location of specific transient binding clefts. These were characterized in detail, and are marked in Figure 3.3, numbered progressively and with the subscript indicating the involved anesthetic. The detailed description of the main binding clefts, with their adopted nomenclature and the list of involved residues, is provided in Table 3.3 for isotype αβIVa. The corresponding table for isotypes αβVI and αβIIa is provided in the Supplementary Information.

Table 3.3. Binding clefts for isotype αβIVa for all the simulated anesthetics

Ligand	Cleft	Residues
Desflurane	C_D1	αILE335, αLYS336, αILE332, αASN329, αVAL328, αPRO325, αGLY350, αPHE351, αVAL353, αILE355
	C_D2	αGLU90, αGLN91, αPRO89, αLEU125, αLYS124
	C_D3	βARG306, βPRO305, βPHE294, βASN295, βALA296, βASN337, βSER339
	C_D4	βASN204, βGLU205, βTYR208, βVAL175, βTHR221, βTYR222, βPRO220
Halothane	C_H1	αILE335, αLYS336, αILE332, αASN329, αVAL328, αPRO325, αGLY350, αPHE351, αVAL353, αILE355
	C_H2	αGLU90, αGLN91, αPRO89, αLEU125, αLYS124, αILE75, αVAL78, αARG79, αARG84
	C_H3	βARG306, βPRO305, βPHE294, βASN295, βALA296, βASN337, βSER339
Methoxy-flurane	C_M1	αILE335, αLYS336, αILE332, αASN329, αVAL328, αPRO325, αGLY350, αPHE351, αVAL353, αILE355
	C_M2	αSER287, αGLU290, αALA294, αILE276, αLYS280, αALA281, αGLU284
	C_M3	αTHR82, αTYR83, αARG84, αARG79, αPHE87
	C_M4	βASP74, βGLY71, βPRO70, βPRO87, βASN89, βPHE90, βVAL91, βMET73, βVAL76
	C_M5	βARG390, βPHE389, βMET415, βASN414, βASP417
Ethylene	C_E1	βPRO182, βALA185, βVAL170, βSER168, βSER188, βVAL189

The interaction sites are distinct with each anesthetic but with notable overlaps, the most important of which is a vast binding area located on the upper part of the α subunit in the lateral PF-PF contact zone, and comprising clefts C_D1, C_H1 and C_M1

in all isotypes and C_M2 (isotype αβIVa and αβVI) and C_D2 (isotype αβVI). Every anesthetic, except ethylene, stuck to a cleft in this area for a significant portion of the simulation, on all three isotypes. As discussed, this cleft is in fact formed by two distinct hydrophobic patches located at the proximity of helices H9 and H10, respectively, the latter located towards the top of the alpha subunit, thus actually on the longitudinal dimer-dimer interface. The first area, corresponding to clefts C1 and shown in Figure 3.5A, largely consists of a hydrophobic patch delimited on the lower part by the start of the S7-H9 loop and the final residues of S7, and on the upper part by helix H9 and the last residues of the S7-H9 loop, able to accommodate lipophilic ligands.

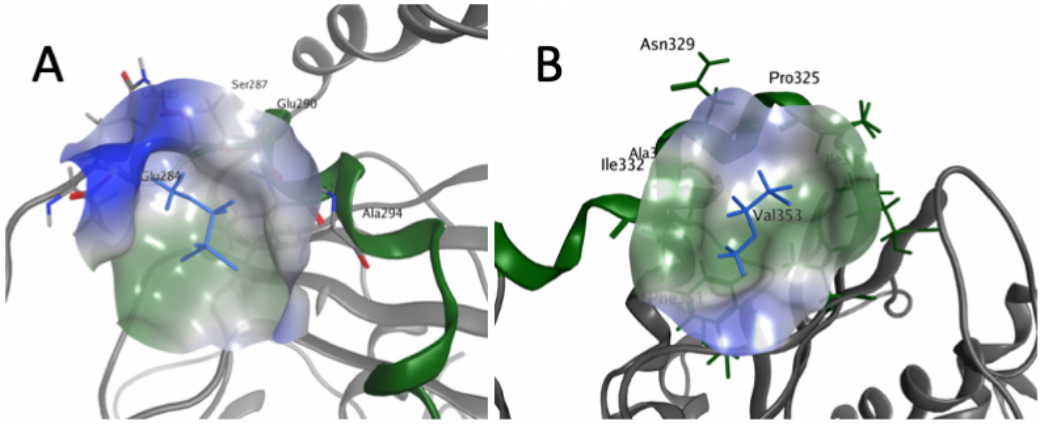

Figure 3.5. Rendering of the two sites on the alpha subunit. (**a**) cleft C_M2 near helix H9 (shown in green ribbons); (**b**) cleft C_M1 near helix H10 (shown in green ribbons), at the top of the dimer. The ligand shown in purple is Methoxyflurane, as extracted from a snapshot of the simulation with isotype αβVI. Rendering includes molecular surface in transparency, with lipophilic areas shown in green and hydrophilic areas shown in blue. Labels indicate nearby residues forming the cleft.

The second cleft, which corresponds to cleft C_M1 shown in Figure 3.5B, is a nearby, mostly lipophilic patch located at the top of the alpha subunit and formed by helix H10 at the top and delimited by sheet S9 at the bottom.

The broader picture of the binding patterns highlights how contact probabilities for each residue change with different ligands (ANOVA $p<0.0001$ for all three isotypes), more specifically pointing towards a clearly weaker interaction of Ethylene with all three isotypes, with mean contact probabilities significantly lower than the other three anesthetics (Dunnett's multiple comparisons test: $p<0.0001$ for all isotypes and ligands, except αβIIa with Halothane vs. Ethylene $p=0.0015$), and

a global contact probability peak of 0.27 only with isotype αβIIa. Ethylene also showed a substantially lower predicted binding energy, coherently with the previous finding. Also, Methoxyflurane shows the most ubiquitous interactions with high overall contact probabilities during the simulation, peaking at 0.48 with αASN329 on isotype αβIVa, located in cleft C_M1 (also visible as a darker area in Figure 3.3). Desflurane and Halothane show similar interaction patterns, both in terms of locations and probabilities, consistent with interactions in sterically compatible lipophilic patches located around the dimer. Notably, some interaction occurs on the side of the dimer facing the MT lumen (corresponding to the lower part of the graphs in Figure 3.3, Figure 3.4 and Figure 3.6 where $\varphi<<0$), especially on isotype αβIVa with methoxyflurane. Whether the MT lumen remains actually accessible to these ligands when the MT is assembled requires further investigations, but given the dimensions of these anesthetics, this appears to be feasible.

Protein-Ligand interaction energies

Binding energies for each anesthetic were predicted using the MM/PBSA method implemented in AmberTools, separately for each of the clefts reported in Table 3. Overall, predicted binding energies for Desflurane ranged from -7.10 ± 3.58 kcal/mol (isotype αβVI, cleft C_D1) to -14.89 ± 6.83 kcal/mol (isotype αβVI, cleft C_D4). In the case of Halothane, energies ranged from -6.31 ± 3.16 kcal/mol (isotype αβIIa, cleft C_H1) to -12.91 ± 3.17 kcal/mol (isotype αβIVa, cleft C_H3). Methoxyflurane featured binding energies from -7.13 ± 3.80 kcal/mol (isotype αβVI, cleft C_M1) to -14.55 ± 4.39 kcal/mol (isotype αβIIa, cleft C_M2). Lastly, in comparison, the predicted energies of Ethylene ranged from a minimum of -4.43 ± 0.97 kcal/mol (isotype αβIVa, cleft C_E1) to a maximum of -6.72± 1.74 kcal/mol (isotype αβIIa, cleft C_E1). The detailed map containing only the interaction clefts for all four ligands on isotype αβIVa is reported in Figure 3.6, where color intensity represents the predicted binding energy. The latter are also reported for all clefts and all ligands in Figure 3.7 as means with standard deviations. The decomposition of binding energies into VDWAALS, EEL, ENPOLAR and EDISPER components is reported for isotype αβIVa in Supplementary Figure S3.9 and shows the relative contribution of each term to the overall calculated binding energy, separately for each anesthetic and each binding site.

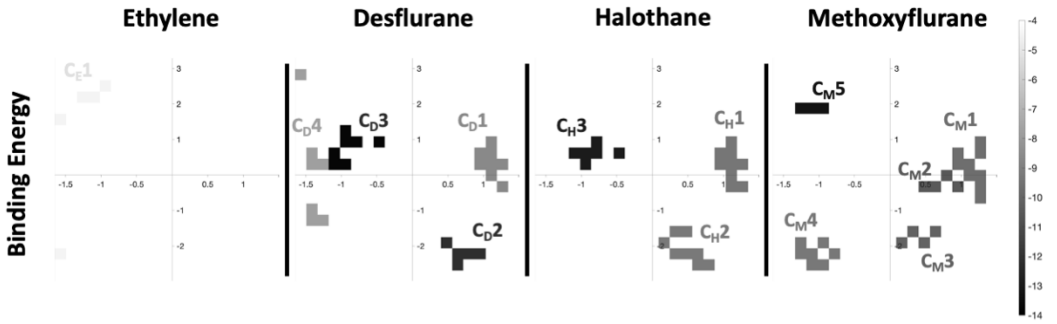

Figure 3.6. Per-area MM/PBSA binding energy estimate for isotype αβIVa, the one with the most overall interactions, with all the tested ligands. Left to right: Ethylene; Desflurane; Halothane; Methoxyflurane. Color scale is -4 kcal/mol to -14 kcal/mol. The different clefts are highlighted in the figure.

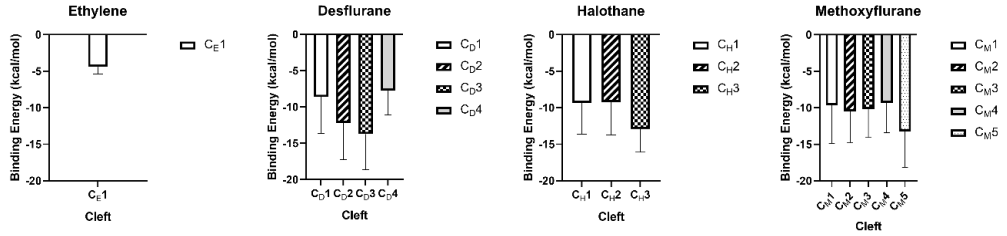

Figure 3.7. MM/PBSA binding energy estimates for isotype αβIVa with all the simulated ligands. Left to right: Ethylene; Desflurane; Halothane; Methoxyflurane. Data reported as mean with standard deviation bars for all clefts determined for each ligand.

Rather than representing definitive estimations for binding affinities, the collected data do however allow for a quantitative comparison between clefts and between different ligands, and show how the predicted binding energy is dependent of the specific surface cleft the ligand interacts with; the energy ranges and standard deviations yielded by MM/PBSA calculations are explainable with the transient nature of surface contacts inside the reported clefts, which do not allow, in the time scales investigated in the present work, for the formation of a protein-ligand complex which remains stable throughout the simulation. Rather, local alterations of sidechain arrangements permit the temporary accommodation of dissolved ligand in specific clefts, with average residence times as reported below. Interestingly, while all anesthetics tend to preferentially sample specific locations of the dimer surface, as discussed in the contact probability analysis and shown in Figure 3.4, Figure 3.5, Supplementary Figure S3.6 and Supplementary Figure S3.7, the actual clefts where they eventually accommodate into are not always exactly

the same, as detailed in Table 3.3. Binding clefts for isotype αβIVa for all the simulated anesthetics and visible in Figure 3.6. In the case of isotype αβIVa, all ligands interact in the same cleft C1, whereas cleft C2 is largely the same for Desflurane and Halothane, but slightly shifted for Methoxyflurane, where it corresponds to cleft C3. The latter also featured three additional clefts C2 (near C1), C4 and C5 where no consistent binding emerged for the other anesthetics. Desflurane also showed a specific binding cleft, C4, located at the bottom of subunit beta towards the polymerization interface. This data confirms at the same time both the consistency of some binding sites, able to accommodate different ligands, and the existence of interaction areas which are selective towards some of the anesthetics. Also, as visible in Figure 3.6 and Figure 3.7, Ethylene consistently showed the weakest predicted binding energy – and with lowest standard deviation – and the existence of only one weak binding site, in line with the previous contact probability analysis highlighting only negligible interaction.

Residence Times

Residence times were generally consistent with the reported contact probabilities: on isotype αβVI, Desflurane (Supplementary Figure S3.22A) showed residence times in high-probability contact areas between 8 and 25 ns. Interestingly, the area with highest reported contact probability featured at the same time short average residence times, which is indicative of frequent short contacts, as opposed to stable binding. Halothane (Supplementary Figure S3.22D) featured residence times between 3 and 25 ns near highly interacting residues, again with the area of peak probability showing frequent contacts of 7.5 ns on average. Methoxyflurane (Supplementary Figure S3.22G) consistently showed average residence times between 6 and 24 ns near residues with high reported contact probabilities, most of them being above 15 ns where contact probability was the highest. As for the previous ligands, it showed an area on the alpha chain with frequent and short contacts (between 2 and 7 ns on average), as seen by the high reported per-residue contact probabilities, up to 0.37. Ethylene on the other hand (Supplementary Figure S3.22L) featured residence times consistently below 5 ns, in good agreement with the low reported contact probabilities. On isotype αβIIa the average residence times of Desflurane (Supplementary Figure S3.22B) spanned from 5 to 12 ns in areas with high contact probability. Again, high-probability contact residues on the alpha chain featured short mean residence times, below 10 ns, despite contact probabilities up to 0.35. Residence times for Halothane (Supplementary Figure S3.22E) were between 7 and 22 ns on average around highly interacting residues, with the same area of short contacts below 10 ns on the alpha chain, with contact

probabilities up to 0.22. Methoxyflurane (Supplementary Figure S3.22H) featured the highest mean residence times, up to 23 ns and consistently above 12 ns in areas with high contact probability of up to 0.41. Ethylene (Supplementary Figure S3.22M) confirmed the short residence times seen in the previous isotype, below 7 ns in most of the interacting residues, and with a maximum below 8 ns in the area with the highest contact probability (0.27). Lastly on isotype αβIVa, Desflurane (Supplementary Figure S3.22C) interaction lasted on average up to 25 ns on chain alpha, and spanning from 4 to 19 ns in most other areas with high contact probability. Interestingly, the residue group with highest contact probability (0.56) also showed low average residence times, below 5 ns, indicative again of frequent short contacts, i.e. lower stability inside the cleft. Halothane (Supplementary Figure S3.22F) residence times were higher on average, between 10 and 25 ns in most interaction areas. Also, contact probability peaks correspond to higher average residence times in all cases except one, near β295ASP, where a contact probability of 0.48 corresponded to mean residence times of 12 ns. In the case of Methoxyflurane (Supplementary Figure S3.22I), areas with high contact probability corresponded to average residence times of the ligand between 4 and 25 ns, while the highest-probability cleft interacted on average for 14 ns. Finally, average residence times of ethylene (Supplementary Figure S3.22N) never topped 5 ns, in agreement with the comparably low contact probability (0.21 at most). Interestingly, most areas with high contact probability showed particularly low residence times, below 1 ns, indicative of the lack of stable binding clefts.

Conformational Analysis

The RMSF analysis in the presence and absence of anesthetic molecules, respectively, focused on differences in C-alpha backbone fluctuations, for each of the three dimers. It is reported in detail in the Supplementary Information. Overall, different isotypes show slightly different behaviors in the presence of different anesthetics: The β M loop was destabilized on isotype αβVI with Desflurane and Methoxyflurane, while it showed decreased mobility in isotype αβIIa with Halothane, Methoxyflurane and Ethylene and in isotype αβIVa with halothane. A visible increase in fluctuations is reported in the area of residues 235-245 on the beta chain of isotype αβIIa in the presence of Methoxyflurane and Desflurane. The same isotype showed a similar spike in RMSF around residue 320 in the presence of Desflurane and Ethylene. Isotype αβIVa showed increased fluctuations on the β subunit at residues 325 to 340 with anesthetics compared to the control condition, which was not evident for the αβVI and αβIIa dimers. Overall, no major

conformational changes were observed over the course of the simulations: cluster analysis of the trajectories, performed with a 0.15 nm cutoff, both with and without anesthetics, yielded a single dominant conformation for each run. In terms of secondary structure, possible alterations were assessed quantitively using DSSP, comparing the secondary structure in the control simulations with the secondary structure in the ligand-bound state, separately for each binding site. As shown in Figure 3.8 for isotype αβIVa, no significant secondary structure alteration emerges throughout the dimer upon ligand binding in the different clefts. Differential interaction with different anesthetics might thus not be directly related to major conformational changes of the tubulin dimer.

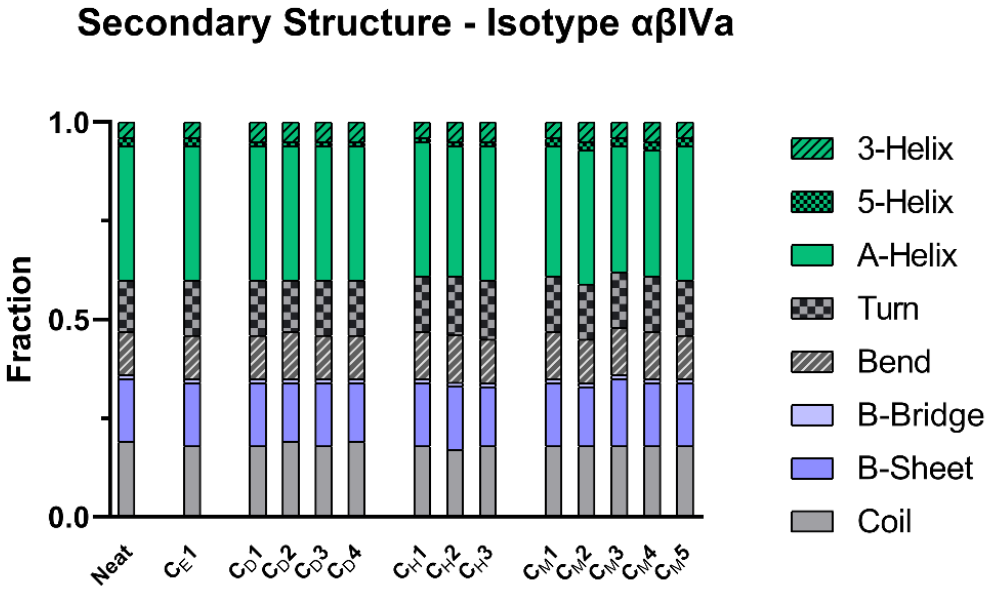

Figure 3.8. DSSP average Secondary Structure of the dimer in the control simulation without any ligands ("Neat") vs. in the ligand-bound states, differentiated between different binding clefts. No significant alterations emerge.

3.3.5 Discussion

Blind docking of anesthetics to tubulin dimers αβVI, αβIIa and αβIVa highlighted low binding affinities compatible with a combination of hydrophobic interactions with surrounding residues. What emerges is a substantially indistinguishable predicted affinity between Halothane and Methoxyflurane, at a thermal noise level of k_BT, while affinity of Desflurane was predicted to be minimally better with respect to all three isotypes. What is consistently predicted is a much weaker affinity of Ethylene to all three isotypes, barely completing docking runs successfully and

averaging at around -2.00 kcal/mol in every run. The important hint provided by blind docking experiments points toward the lack of a precise binding site, rather a preference for specific hydrophobic pockets of the tubulin dimers, able to transiently accommodate the anesthetic molecules. This underlined the weakness of the docking approach alone in the case of weak binders which interact at multiple sites simultaneously, and warranted a more thorough investigation of the interaction, in its dynamic nature, by simulating the dimer in the presence of anesthetic agents in the surrounding medium at fixed concentration.

Analysis of residue groups on the dimer surface with high probability of contact with each anesthetic confirmed that the tested compounds do not seem to have a single, specific binding site on the target, but they do, however, stay in contact with the dimer for prolonged times in specific clefts. These areas are partially overlapping for all isotypes and all tested VAs, with the notable exception of Ethylene, the weakest among the four, which showed a tendency to remain floating in the solvent rather than sticking to the dimer surface. The transient residence of volatile anesthetics may alter local mobility of residue sidechains with functional consequences on the MT, especially in the light of the high amount of predicted contact both in the luminal and lateral side of the tubulin dimers, where adjacent protofilaments assemble, as well as on the dimer-dimer polymerization interface. Contact probability, directly correlated to residence time at specific locations, confirmed similar interactions of Desflurane and Halothane, and a slightly increased interaction of Methoxyflurane with all isotypes. Moreover, the significantly weaker interactions of Ethylene emerged, consistent both with blind docking affinity estimates and with clinical potencies. Above all, the existence of different binding clefts, some of which shared between different anesthetics, some specific to a particular ligand, was confirmed. MM/PBSA predicted binding energies that were comparable, within error, between Desflurane, Halothane and Methoxyflurane, but again visibly lower for Ethylene, in agreement with the much lower contact probability.

Most notably, the three VAs Desflurane, Halothane and Methoxyflurane interacted in all the simulations of all three isotypes on the upper portion of the alpha subunit, predominantly in two lipophilic patches located near helices H9 and H10, an area corresponding in spherical coordinates to values of φ close to 0 and θ between 0.75 and 1.25. The patch around H9 is located on the lateral PF-PF contact area of the dimer, and might alter PF assembly in the presence of ligands, while the lipophilic pocket at helix H10, at the top of subunit alpha, might have functional consequences

on tubulin polymerization in the process of dimer-dimer assembly. Ethylene did not show any interaction within these pockets.

Contact probability heatmaps also hint at how some high probability interaction zones were located near tryptophan residues, especially in the case of Halothane and Methoxyflurane on the alpha subunit in the area where αTRP21 is localized, i.e. $0.7<\theta<1.1$ and $0<\varphi<1$ in the spherical coordinate system (Supplementary Figure S3.8). The quantitative assessment of the involvement of Tryptophans in the interaction with anesthetic molecules requires further, more detailed work, possibly with higher-resolution methodologies. A direct role of tryptophan residues in the analyzed binding clefts was not confirmed with the methodologies used in the present work.

The interaction between volatile anesthetics and tubulin has been evaluated synergistically both through blind docking and Molecular Dynamics. The former approach confirmed the weak and transitory nature of putative binding sites suggested by previous research[102], by failing to highlight a single specific region of interaction and consistently reporting low predicted affinities across the different binding pockets. This consideration, along with the known limitations of blind docking[121], and the lack of single, high-affinity binding site following the more traditional lock-and-key paradigm for the investigated ligands, justified a more in depth analysis of the interaction through the use of molecular dynamics. In this last approach, the three different αβ-tubulin dimers have been simulated in the presence of a fixed concentration of anesthetics in the surrounding medium. To account for the dynamic nature of the interaction, *hotspots* of interaction have been determined on the dimer by sampling the contact probability between tubulin and anesthetic molecules on different portions of the dimer surface. Subsequently, precise binding clefts were determined from the contact map for further binding energy estimation. First, this clearly showed that interaction does feature preferential areas on the dimer surface and does not occur randomly. Rather, it appears to be driven mostly by the lipophilicity of the tested VAs. Secondly, it highlighted differences in interaction mostly between different anesthetics rather than between different tubulin isotypes: a given anesthetic tends to interact with specific areas of the dimer for tens of nanoseconds, and interaction may occur in close proximity of key functional residues of the microtubule. The areas of interaction were reproduced consistently, although with different residence times, in the different replicas, despite the low affinity of VAs for tubulin and the lack of a single, high-affinity binding site. There is no predicted preference of the simulated anesthetic agents for a specific tubulin isotype. More interestingly, a consistent amount of interaction is

predicted to occur on the luminal surface of the assembled microtubule. Whether this area is accessible to volatile anesthetics and under which conditions, along with the functional and structural consequences of this on the microtubule structure, warrants further computational and experimental research. Since larger molecules, such as paclitaxel or epothilone, are known to bind on the luminal surface of microtubules due to the diffusion through the nanopores formed between neighboring tubulin dimers, a similar ability to reach the microtubule lumen appears entirely possible.

3.3.6 Conclusions

The present work computationally investigated the interaction between four distinct Volatile Anesthetics with different clinical potencies with human tubulin dimers, through Molecular Docking and Molecular Dynamics. The simulated isotypes are highly homologous, but each features a unique distribution across different organs and tissues, and the interaction of VAs with each of them appeared to be similar, but not identical. Results confirmed the absence of a lock-and-key type of interaction, and highlighted transient interactions on specific hotspots of the tubulin dimer, i.e. hydrophobic patches able to transiently accommodate the ligands. Methoxyflurane, the most potent among the tested VAs, showed the highest contact probability on all three simulated isotypes, while Ethylene, the weakest VA, had the lowest predicted binding affinity in Docking, the lowest overall contact probability in molecular dynamics simulations, and the lowest predicted binding energy in MM/PBSA calculations. These findings are consistent with previous works exploring the weak interaction between tubulin and anesthetics[59,73,78,122,123]. No distinct preference for a specific isotype emerges, while different anesthetics did show different interaction hotspots on the dimer surface, with only partial overlaps between them, the most notable of which is composed of two hydrophobic patches at the top of the alpha subunit, which interacted with all VAs except ethylene for a significant fraction of the simulations. Whether VAs can actually disrupt or alter microtubule assembly and dynamics, and how this process may occur, demands further investigations. While this process may not be directly involved in the primary mode of action of General Anesthetics, several considerations underline the importance of possible VA-tubulin interactions in the clinical context, including the abundance and peculiar anisotropic spatial organization of tubulin and microtubules in the brain; the role of microtubules in disorders such as POCD; putative cross-interactions with MT-targeting chemotherapies in oncological patients; side-effects in the presence of

neurodegenerative diseases involving an altered MT cytoskeleton. In this context, effects of anesthetics could be of significance in the clinical setting and are worth exploring further.

3.4 Characterization of the modulation of cell membrane mechanics by volatile anesthetics[3]

3.4.1 Abstract

Very few drugs in clinical practice feature the chemical diversity, narrow therapeutic window, unique route of administration and reversible cognitive effects of volatile anesthetics. The correlation between their hydrophobicity and their potency and the increasing amount of evidence suggesting that anesthetics exert their action on transmembrane proteins, justifies the investigation of their effects on phospholipid bilayers at the molecular level, given the strong functional and structural link between transmembrane proteins and the surrounding lipid matrix. Molecular dynamics simulations of a model lipid bilayer in the presence of ethylene, desflurane, methoxyflurane and the non-immobilizer 1,2-dichlorohexafluorocyclobutane (also called F6 or 2N) at different concentrations highlight the structural consequences of VA partitioning in the lipid phase, with a decrease of lipid order and bilayer thickness, an increase in overall lipid lateral mobility and area-per-lipid, and a marked reduction in the mechanical stiffness of the membrane, that strongly correlates with the compounds' hydrophobicity.

3.4.2 Introduction

In most research works, the two approaches to explaining anesthesia mentioned in paragraph 3.2 – namely the lipid theory and the receptor theory – are largely regarded as irreconcilable. What seems often overlooked however, is the intimate connection between transmembrane receptors such as ion channels and their surrounding lipid environment, which highlights the duality, rather than the contrast, of the two theories. Indeed, the membrane-spanning portions of integral membrane proteins are known to be affected by the surrounding lipids, so that the conformational characteristics of specific sections of the transmembrane regions may change in response to alterations of the lipid bilayer. It has been shown for example that bilayer thickness can directly influence protein activity [124,125].

[3] Part of the work described in this paragraph has been published in:

Zizzi, Eric A., et al. "Alteration of lipid bilayer mechanics by volatile anesthetics: Insights from μs-long molecular dynamics simulations." Iscience 25.3 (2022): 103946.

Contribution of the author: study design, creation of computational models and simulations, data analysis and interpretation.

Conversely, there is increasing experimental evidence that the presence of proteins embedded in the membrane has profound effects on the latter's stabilization, mediated mainly by hydrophobic interactions [126]. At higher scales, the reciprocal interaction of the membrane's lipid environment and embedded proteins has also been shown to be mediated by so-called lipid rafts [127], which are sub-μm domains of spatially organized lipids, typically sphingomyelin and cholesterol [128–130].

It appears thus entirely reasonable that an interaction of increasingly hydrophobic compounds, such as VAs, within biological membranes might have significant effects on membrane organization and structure, but at the same time this cannot happen without altering the energetic landscape of the interactions between membranes and transmembrane receptors. The idea that small solutes such as VAs bear the potential of altering the mechanics and thermodynamics of the lipid bilayer, with possible consequences on the dynamics of embedded proteins, was already introduced in the work of Cantor [131], who elegantly discussed the possible relevance of lateral pressure profiles within the lipid bilayer and suggested the mechanistic link between anesthetics, the lipid bilayer and embedded ion channels [132]. Indeed, earlier molecular dynamics simulations by Huang et al. had predicted a possible structural effect of anesthetics within the phospholipid bilayer, in the form of an increased lateral diffusion of lipids and an increase in the overall fluidity of the bilayer [133]. More recently, following earlier speculations suggesting a role of lipid rafts in anesthesia [134–136], Pavel et al. demonstrated a membrane-mediated effect of anesthetics, whereby the anesthetic-induced alteration of lipid raft organization is able to modulate the sensitivity of channel proteins to anesthetics [137]. In addition to these considerations, the direct effect of anesthetics on transmembrane receptors might be exerted within the transmembrane portion of the receptors rather than on the intracellular or extracellular domains alone and might thus be connected to the ability of compounds to partition inside the membrane and laterally diffuse within the lipid phase prior to interacting directly with cryptic, hydrophobic sites on the target. As a matter of fact, compounds that are more soluble in oil-like media, as is the case for VAs as shown by the Meyer-Overton correlation, tend to partition inside the membrane rather than in aqueous solutions, and vice versa.

In the context of investigating the properties of lipid bilayers, a vast literature exists exploring the behavior of model phospholipid membranes in different physical contexts and the structural and functional link between membranes and embedded proteins and peptides. Indeed, it is well-known that the structure of phospholipid bilayers has strong functional consequences [138]. The structural parameters usually reported in both experimental and computational studies include (a) the Area-per-

Lipid (APL), which can be calculated from molecular densities or geometrically from the membrane patch surface; (b) the bilayer thickness δ, which is directly related to the APL; (c) deuterium order parameters (S_{CD}), which provide quantitative evidence of lipid chain order and the membrane rigidity resulting from this; (d) direct measures of the mechanical characteristics of the membrane, such as the bilayer bending modulus (K_c). Due to the limitations, both methodological and economical, of experimental settings aimed at investigating such properties for a vast array of model membranes in different physical and biochemical contexts, computational approaches such as molecular dynamics (MD) have proven a valuable tool for exploring and rationalizing the structural characteristics and interaction phenomena within model bilayers at the molecular level. While a great number of computational investigations employed single-component lipid patches [133,139,140], mostly of phosphatidylcholines (PCs) or phosphatidylethanolamines (PEs), recent advances in lipid force fields [141–145] and the increasing power of computational resources have paved the way for the simulation of complex, composite bilayers formed by multiple lipid species and varying cholesterol concentrations, both at all-atom (AA) and coarse-grained (CG) resolutions[146].

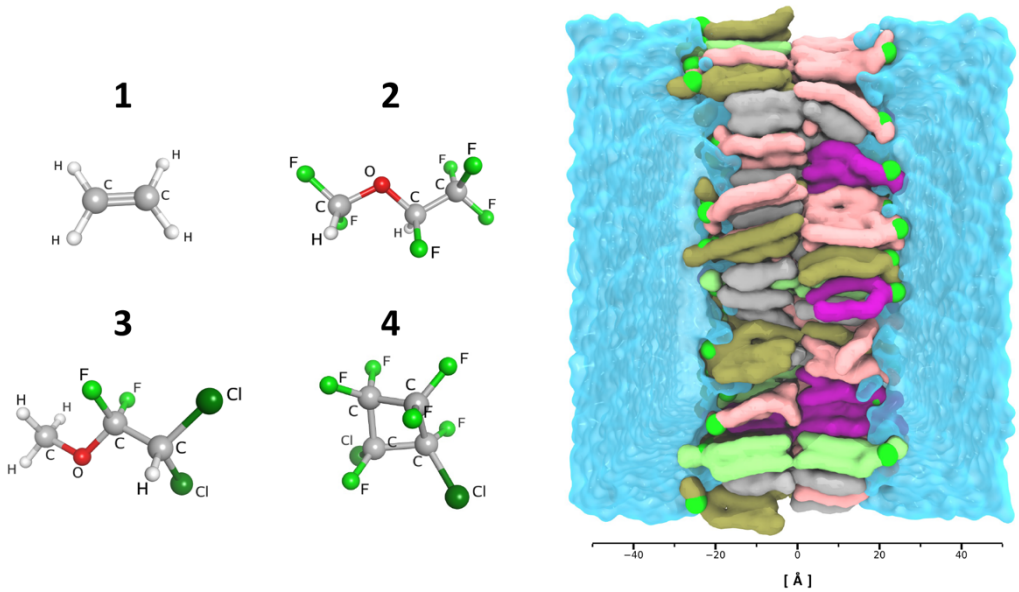

Figure 3.9. Visual overview of the simulated systems. Left: visualization of the three simulated VAs (1) ethylene, (2) desflurane, (3) methoxyflurane, and the nonimmobilizer (4) F6. Right: visualization of the membrane system in its explicit TIP3P water box with ions and ligands omitted for clarity. P atoms highlighted in green, POPC lipids in pink,

Cholesterol in light grey, POPE in purple, POPS in dark green, PSM in bright green. Length scale in Ångstrom reported below for reference, centered at the membrane core region.

With this in mind, the present work focuses on investigating the interaction between volatile anesthetics and a composite model mammalian cell membrane through the use of computational molecular modelling, to explore the effects of VAs on lipid bilayers. With the goal of exploring the effect of a chemically and physically diverse set of hydrophobic compounds spanning a wide range of clinical potencies, we carried out simulations with desflurane (2-(difluoromethoxy)-1,1,1,2-tetrafluoroethane), a fluorinated ether with a MAC of 6% [75], methoxyflurane (2,2-dichloro-1,1-difluoro-1-methoxyethane), a potent halogenated methyl ethyl ether with a MAC value of 0.16%, now largely abandoned in the light of its nephrotoxicity [76], and ethylene, which is only mildly anesthetic with a MAC value of 67% [79]. Simulations were also carried out with F6 (1,2-dichlorohexafluorocyclobutane), a widely investigated nonimmobilizer which does not follow the Meyer-Overton correlation in that it does not induce complete anesthesia as would be expected from its lipophilicity, but it has been demonstrated to induce amnesia [147–149].

A graphical summary of the model membrane and of the simulated VAs is reported in Figure 3.9.

3.4.3 Materials and Methods

System Setup

To overcome the intrinsic simplifications of single-component bilayers, and to account for the presence of cholesterol, which has a well-documented ordering effect on membranes [150] with profound consequences on their mechanical properties [151,152], we chose to simulate a composite asymmetrical lipid patch representative of the mammalian cell membrane, as first described by Zachowski (1993) [153] and employed in computational studies by Klähn and Zacharias [154] and, more recently, Shahane et at. [155], composed of POPC (1,2-palmitoyl-oleoyl-sn-glycero-3-phosphocholine), POPE (1-Palmitoyl-2-oleoyl-sn-glycero-3-phosphoethanolamine), POPS (1,2-palmitoyl-oleoyl-sn-glycero-3-phosphoserine), PSM (palmitoylsphingomyelin) and Cholesterol (CHOL). The detailed amounts of the lipids in the two leaflets are reported in Table 3.4.

Table 3.4. Number of different lipid molecules in the two leaflets of the model mammalian membrane.

Lipid	Inner Leaflet	Outer Leaflet	Total
POPC	40	106	146
POPE	132	34	166
POPS	82	8	90
PSM	10	116	126
CHOL	136	136	272
Total	**400**	**400**	**800**

Bilayer systems were assembled using the Membrane Builder[156–158] tool of CHARMM-GUI[159], with a fixed number of 50 TIP3P waters per lipid to ensure adequate lipid hydration even at higher ligand concentrations, and a physiological NaCl concentration of 0.15M. In addition to the control simulation without any anesthetic, different systems were set up by randomly inserting desflurane, methoxyflurane, ethylene and F6 (1,2-Dichlorohexafluorocyclobutane) respectively in the surrounding aqueous solvent at 12.5%, 25% and 50% anesthetic/lipid molar ratios, for a total of 10 simulated systems, using the *insert-molecules* tool of GROMACS 2020.4[160]. The higher concentrations (25%, 50%), while not intended to be representative of clinical concentrations, were included to enhance the sampling of the lipid-anesthetic interaction and to accelerate ligand partitioning, as seen in previously published studies[161–163]. The 12.5% concentration on the other hand is more representative of clinical scenarios, with the molar ratio of e.g. Halothane at MAC being in the range of 5%[164] to 14%[165]. The detailed composition of each simulated system is reported in Table 3.5 below.

Table 3.5. Components of each simulation system

System	Lipids	Water molecules	Cl^- ions	Na^+ ions	VA molecules	Total Molecules
C	800	40000	96	186	0	41082
E12.5	800	39754	96	186	100	40936
E25	800	39527	96	186	200	40809
E50	800	39062	96	186	400	40544
D12.5	800	39414	96	186	100	40596
D25	800	38892	96	186	200	40174
D50	800	37749	96	186	400	39231

M12.5	800	39210	96	186	100	40392
M25	800	38484	96	186	200	39766
M50	800	36755	96	186	400	38237
F6 12.5	800	39149	96	186	100	40331
F6 25	800	38381	96	186	200	39663
F6 50	800	36486	96	186	400	37968

Simulation Protocol

Simulations were carried out in GROMACS 2020.4[160] using the CHARMM36 force field[145], which is well-validated for membrane simulations over a wide range of lipid compositions[138], according to the following protocol: after an initial 5000-step energy minimization, systems were equilibrated stepwise with gradually decreasing harmonic restraints (from 1000 to 0 $kJ \times mol^{-1} \times nm^{-1}$), first in the NVT ensemble for 250 ps with a conservative timestep of 1 fs, using the Berendsen thermostat with a coupling time constant of 1 ps and a reference temperature of 303.15K, which is above the phase-transition temperature for the studied lipid mixture, and subsequently in the NPT ensemble for 125 ps with the same 1 fs timestep, followed by a further simulation of 375 ps with a 2 fs timestep, using the Berendsen thermostat with the same parameters as before and the Berendsen barostat [166] with semi-isotropic pressure coupling at 1 atm with a coupling time constant of 5 ps. Overall, systems underwent 750 ps of equilibration, and were subsequently simulated for production runs for a total of 1 μs each in the NPT ensemble, using the Nosé-Hoover thermostat [167] with a time constant of 1 ps and a reference temperature of 303.15K, and the Parrinello-Rahman barostat [112], with semi-isotropic pressure coupling at 1 atm with a time constant of 5 ps. Bonds involving hydrogens were constrained using the LINCS algorithm [168], while the Particle Mesh Ewald (PME) algorithm [113] was used for electrostatics, with a cutoff radius of 1.2 nm, and a cutoff of 1.2 nm was used for Van der Waals interactions, with a force-switch modifier from 1.0 to 1.2 nm. The first 250 ns of the production MD runs were regarded as additional structural equilibration, while the remaining 750 ns were used for the subsequent analyses described below, in line with previous literature regarding the computational simulation of biological lipid bilayers [155,169]. Properties were sampled every 200 ps, unless otherwise specified. Molecular visualizations were generated using the VMD software package [105].

Structural Analyses

Geometric Area-per-Lipid (gAPL), Bilayer Thickness (δ) and water permeation were calculated using the MDAnalysis [170] library for Python [171]. Briefly, the gAPL was calculated as the *xy* area of the simulation box divided by the number of lipids in each membrane leaflet (N=400) and is reported in $Å^2$. To calculate the bilayer thickness, the position of all P atoms of each leaflet was extracted and their average z coordinate calculated for each leaflet. Bilayer thickness was calculated as the distance between the avg. z coordinates the P atom cloud. Water permeation events were calculated by tracking individual water molecules throughout the simulation. Density distribution profiles along the z coordinate were calculated using the *gmx density* tool. Acyl chain deuterium order parameters, S_{CD}, for the sn1 and sn2 chains of each lipid were calculated to directly quantify structural effects on the packing of the membranes' hydrophobic core. Order parameters were calculated following equation (1), using the *gmx order* tool:

$$S_{CD} = \frac{1}{2}\langle 3cos^2\theta - 1\rangle \quad (1)$$

where θ is defined as the angle between the bilayer normal and the vector C-D between the given carbon atom and the bound hydrogen atom, as sampled from the equilibrium MD simulations[172]. Unsaturated lipid chains were accounted for following the methodology described in Pluhackova et al.[142].

To quantify the tendency of ligands to partition inside the bilayer, which can bear profound consequences on protein-ligand interaction affinity and kinetics on transmembrane protein targets, the ligand molal concentration inside the lipid bilayer was calculated as follows. MDAnalysis was used to extract the number of ligand molecules whose center-of-mass z coordinate lied between the two P-atom point clouds, i.e. between the two layers delimiting each leaflet's boundary. These ligands were regarded as being embedded inside the membrane. The remainder of the ligands was considered outside of the membrane. The molality of the anesthetics inside the membrane was calculated as number of moles of embedded ligands divided by the total weight of the membrane in kg.

To calculate the bilayer bending modulus, K_c, for each simulated system, the methodology proposed by Khelashvili and colleagues[173] was employed, leveraging on the relationship between the splay modulus, χ_{12}, and the macroscopic bending modulus: in this approach, an improved ability of adjacent lipids to change the

reciprocal orientation of their hydrophobic tails with respect to the local membrane normal, which is quantified by their splay angle (α), is associated to a decreased membrane bending rigidity. Briefly, this approach first calculates the Potential of Mean Force (PMF) of the distribution of splay angles sampled during equilibrium MD simulations, normalized with respect to the probability distribution of a non-interacting particle system[174], denoted here $P_0(\alpha)$, as shown in equation (2):

$$PMF(\alpha) = -k_B T \, ln \frac{P(\alpha)}{P_0(\alpha)} \tag{2}$$

where T represents the system temperature and k_B the Boltzmann constant. The overall splay modulus, which is linked to the bilayer bending modulus as:

$$K_c = 2k_m = 2\chi_{12} \tag{3}$$

can be calculated by means of a quadratic fit of the PMF obtained from Eq. (2) [175,176].

In the present work, we employed the python implementation previously demonstrated by Johner et al.[177] to first extend the trajectories to neighboring periodic images, followed by wrapping the trajectory around the central unit cell and re-aligning. Finally, the provided python modules were used to calculate the tilt and splay angle distributions for all lipids and subsequently extract the membrane elastic properties of interest following the above-mentioned methodology. We refer to [177] and references therein for a more complete theoretical background of the methodology and details on the python implementation relying on the OpenStructure[178] toolkit.

Quantification and statistical analysis

For a more accurate estimation of the error of the sampled properties[179–182], the equilibrium part of the MD simulations (i.e. the last 750 ns) was further divided into 250-ns long trajectory blocks, in line with previous literature reporting findings in μs-long MD simulations of complex lipid membranes[155,169]. First, the block average of each structural property was calculated for each block as the arithmetic mean of the data points of the given property *p* within the block:

$$\bar{\mu}_j = \frac{1}{N_b} \sum_{i=1}^{N_b} p_i \tag{4}$$

where $\bar{\mu}_j$ denotes the mean within the *j*-th block of property *p* and N_b is the number of samples composing the *j*-th block. The final estimate of the ensemble average $\langle\mu\rangle$ of the given property *p* is given by the arithmetic mean of the block averages:

$$\langle\mu\rangle = \frac{1}{n}\sum_{j=1}^{n}\bar{\mu}_j \tag{5}$$

where *n* is the total number of blocks. Then, the experimental standard deviation of the mean, $\overline{\sigma_\mu}$, of each property was calculated as:

$$\overline{\sigma_\mu} = \sqrt{\frac{\sum_{j=1}^{n}(\bar{\mu}_j - \langle\mu\rangle)^2}{n-1}} \tag{6}$$

where $\bar{\mu}_j$ is the arithmetic mean of a given property over the *j*-th block and *n* is the number of blocks. Finally, the estimate of the standard deviation is given by:

$$\sigma_\mu = \frac{\overline{\sigma_\mu}}{\sqrt{n}} \tag{7}$$

This quantity is the reported standard deviation, represented as error bars on the plots, and was also used to calculate 95% confidence intervals which are reported throughout the text and in shaded colors on the plots, unless where explicitly specified.

3.4.4 Results

Potent VAs alter the membrane structure upon partitioning

To quantitatively assess both the quality of the membrane model itself and the effect of volatile anesthetics on overall membrane structure, the geometric Area per Lipid (gAPL) and Bilayer Thickness (δ) were evaluated and are reported for all systems in detail in Table 3.6. The former is a crucial parameter influencing lipid diffusion profiles, lipid chain order and overall membrane elastic properties. It also represents a metric to assess the reached equilibrium of membrane simulations, along with the closely related bilayer thickness. The control simulation without any ligands yielded an average gAPL of 42.89 Å^2 (95% CI: 42.83 – 42.95 Å^2) and an average bilayer thickness of 46.85 Å (95% CI: 46.81 – 46.89 Å), and proved consistent both

with previous computational studies of membranes with similar lipid composition and comparable cholesterol content[154,155,183] and with experimental data on cholesterol-enriched membranes [184], although it is to be noted that bilayer thickness heavily depends on the specific bilayer composition [185] and experimental data of membranes with the exact lipid composition of the present model is, to the best of our knowledge, not available. Nevertheless, the reduced gAPL and δ values are consistent with the high cholesterol content (~ 34%) inducing membrane condensation, as demonstrated in earlier literature[151,186–188].

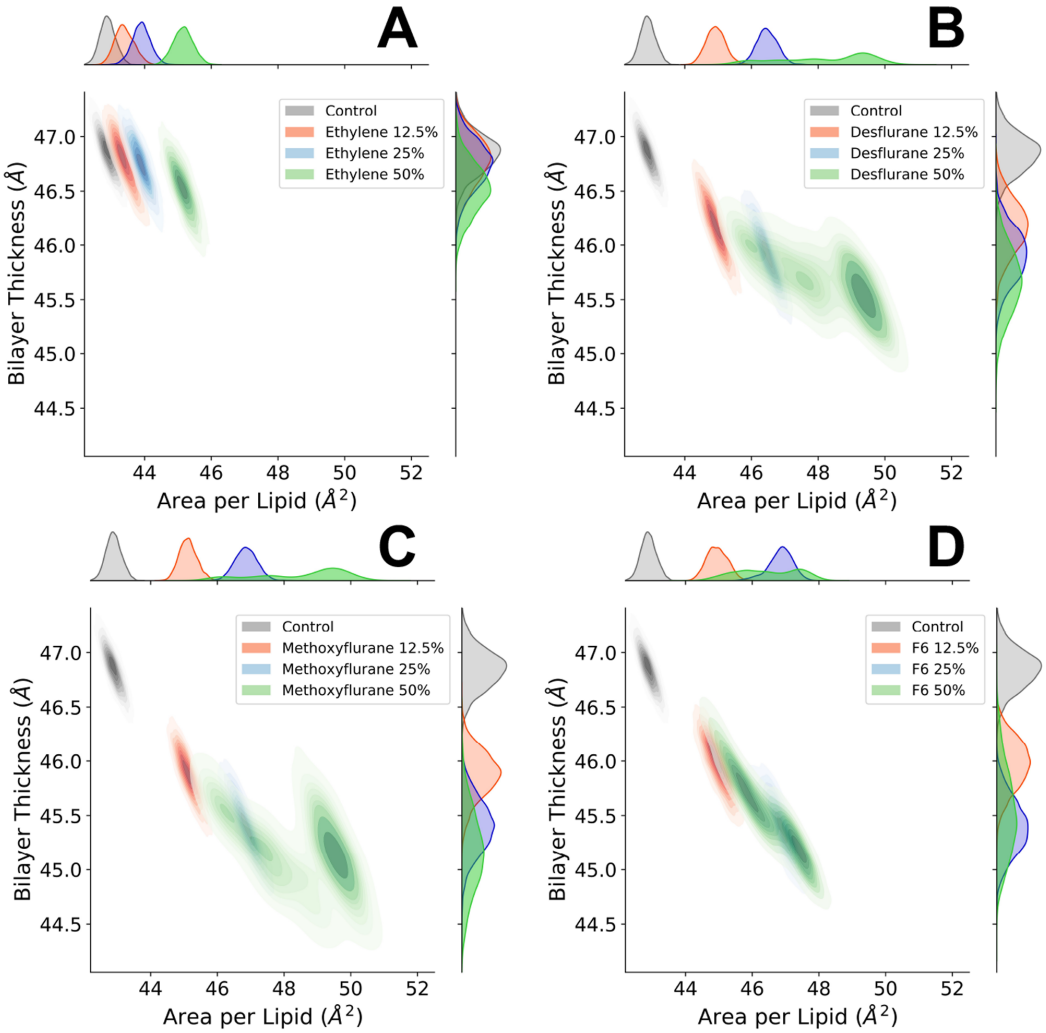

Figure 3.10. Distribution of the bilayer thickness (δ) and geometric area per lipid (gAPL). Control simulation vs. ethylene (A), desflurane (B), methoxyflurane (C) and F6 (D) at increasing concentrations. Marginal axes show the individual data distributions collected

in the last 750 ns of the simulations. Control simulation without anesthetics shown in grey, 12.5% concentration in red, 25% in blue and 50% in green.

Figure 3.10 shows the effect of increasing ligand concentrations on both gAPL and thickness. In the case of ethylene (Figure 3.10A) no significant effect of ligand concentration on bilayer thickness is observed (from 46.85 Å to 46.52 Å), with only a mild increase in area per lipid, which reaches 45.16 $Å^2$ with 50% ethylene. Desflurane (Figure 3.10B) and methoxyflurane (Figure 3.10C) on the other hand induce a marked reduction in bilayer thickness down to 45.67 Å with 50% desflurane and 45.16 Å with 50% methoxyflurane, despite the steric hindrance of the high number of ligand molecules partitioned within the membrane. At the same time, these two anesthetics induce a marked increase in gAPL, up to 48.18 $Å^2$ and 48.53 $Å^2$ for systems with 50% desflurane and methoxyflurane, respectively. Overall, the latter two ligands induce a progressive reduction of membrane thickness, along with a lateral spreading of the lipids on the xy plane, both in a fashion proportional to ligand concentration. This effect is totally absent for ethylene concentrations up to 25%, with only a mild increase in gAPL induced at 50% and no measurable thickness reduction effect. These results are in agreement with earlier computational studies reporting a significant lateral expansion and simultaneous thickness contraction induced in lipid membranes by halothane, another VA, over a wide range of molar fractions [163,189,190]. Lastly, simulations with the nonimmobilizer F6 (Figure 3.10D) highlight a reduction in bilayer thickness (from 46.85 Å to 45.52 Å with 50% F6) comparable to the simulations with desflurane and methoxyflurane, whereas the increase in gAPL is more subdued at higher concentrations, reaching at most 46.44 $Å^2$ with 50% F6.

Table 3.6. Average geometrical Area per lipid, bilayer thickness and frequency of water permeation for all simulated systems. 95% confidence intervals are reported in square brackets for block-averaged quantities.

System	gAPL [$Å^2$]	Bilayer Thickness (δ) [Å]	Water permeation frequency [H2O/μs]
C	42.89 [42.83 – 42.95]	46.85 [46.81 – 46.89]	16
E12.5	43.40 [43.36 – 43.44]	46.77 [46.71 – 46.83]	40
E25	43.90 [43.80 – 44.00]	46.74 [46.68 – 46.80]	37
E50	45.16 [45.12 – 45.20]	46.52 [46.46 – 46.58]	112

D12.5	44.93 [44.81 – 45.05]	46.17 [46.03 – 46.31]	75
D25	46.47 [46.41 – 46.53]	45.91 [45.89 – 45.93]	163
D50	48.18 [46.49 – 49.87]	45.67 [45.45 – 45.89]	285
M12.5	45.12 [45.08 – 45.16]	45.88 [45.87 – 45.89]	64
M25	46.86 [46.83 – 46.89]	45.40 [45.38 – 45.42]	160
M50	48.53 [46.92 – 50.14]	45.16 [44.89 – 45.43]	391
F6 12.5	44.95 [44.81 – 45.09]	45.97 [45.89 – 46.05]	93
F6 25	46.85 [46.65 – 47.05]	45.39 [45.28 – 45.50]	206
F6 50	46.44 [45.30 – 47.58]	45.52 [45.09 – 45.95]	155

The increase in gAPL induced by ligand partitioning came alongside an increase in spontaneous water permeation through the membrane, reported as the number of water molecules crossing the bilayer per microsecond in Table 3.6: throughout the control simulation a water permeation frequency of 16 water molecules/μs was observed, whereas this frequency increased to up to 285 molecules/μs and 391 molecules/μs in the case of 50% desflurane and 50% methoxyflurane, respectively. Conversely, just as for gAPL and bilayer thickness, more subdued differences were observed with ethylene, with at most 112 molecules/μs at the highest concentration of 50%. Throughout the simulations with F6, a permeation frequency of up to 206 molecules/μs was observed at 25% simulated fraction, with a slightly lower frequency of 155 molecules/μs at 50% concentration, consistent with the trends of gAPL and bilayer thickness. Despite the increase in spontaneous permeation frequency with increasing ligand concentrations, no pore formation was observed throughout the whole set of simulations, with no disruption of the overall structural integrity of the bilayer.

Anesthetics and nonimmobilizers are predicted to have specific localization areas within the bilayer

The partitioning of ligands inside the lipid bilayer not only plays a crucial role in ligand-receptor interaction with transmembrane proteins[191], but can also significantly alter the bilayer's structural and mechanical properties[163,190,192,193]. The analysis of the density distributions of the different membrane components and of the ligands along the z coordinate highlights a marked tendency of the four ligands to partition inside the bilayer in specific hydrophobic regions.

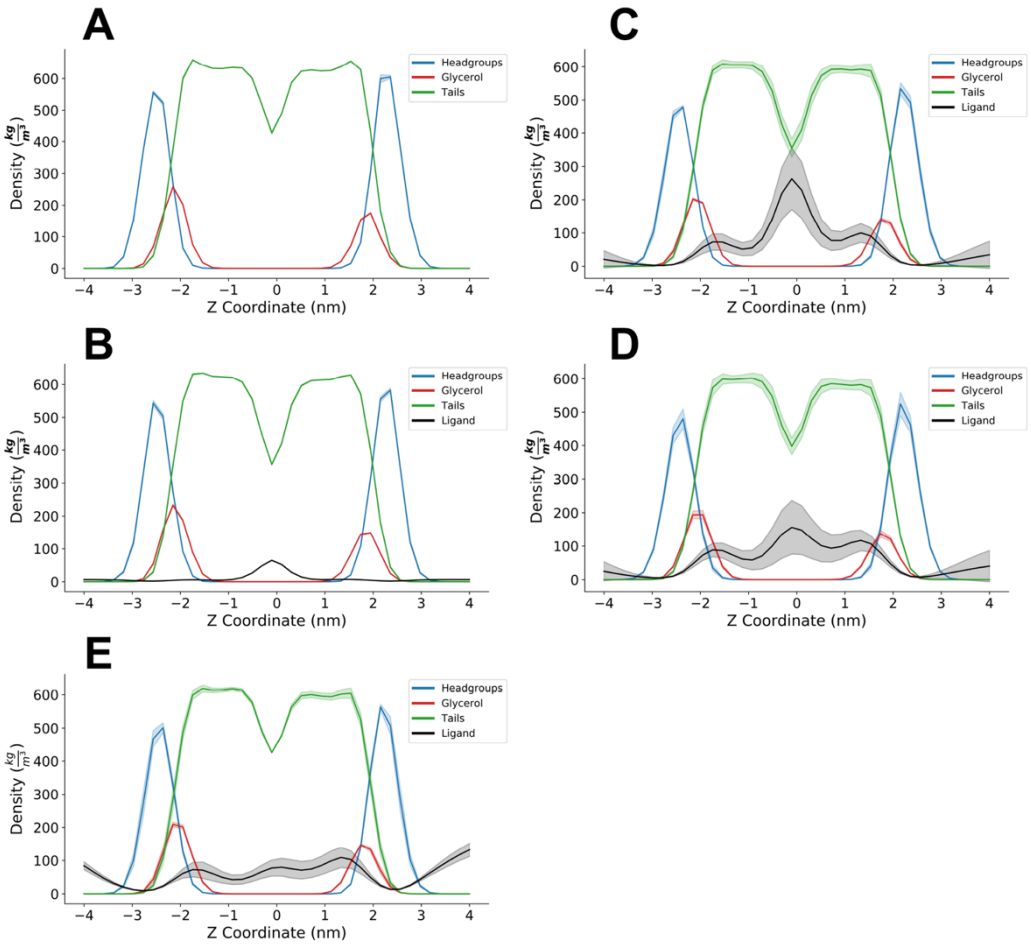

Figure 3.11. Density distributions of lipid headgroups (blue), glycerol backbone (red), lipid tails (green) and anesthetics (black). (A) control simulation, (B) with 50% ethylene, (C) with 50% desflurane, (D) with 50% methoxyflurane and (E) with 50% F6. Shaded colors represent 95% confidence intervals.

Figure 3.11 reports the density distributions for the control simulation (Figure 3.11A) and the simulations at the highest concentration of ethylene (Figure 3.11B), desflurane (Figure 3.11C), methoxyflurane (Figure 3.11D) and F6 (Figure 3.11E). The corresponding plots for 12.5% and 25% ligand concentrations, which highlight the same qualitative distribution pattern, are reported in Supplementary Figures S3.23 and S3.24 in the Appendix, respectively. For desflurane and methoxyflurane, three main areas of localization clearly emerge: the main peak is located at the bilayer center, corresponding to the minimum of lipid tail density. This is consistent with the hydrophobic nature of these compounds, and explains why the massive

ligand partitioning inside the membrane does not result in a simultaneous increase in bilayer thickness, as would be expected by the effect of steric hindrance and molecular volume alone. Indeed, due to the low lipid tail density in the membrane core, resulting in less occupied molecular volume, many freely diffusing hydrophobic species are known to temporarily localize in this region, including cholesterol during flip-flop transitions[194]. The secondary peaks on the other hand are located near the membrane-water interface, immediately below the glycerol groups. This is in agreement with earlier computational findings by Pohorille et al., who predicted this very area of localization to be involved in the molecular mechanism of anesthesia[195–197]. Interactions of volatile anesthetics near the water-lipid interface region have also been reported in the past by Tang and Xu, who employed MD simulations to evaluate the effect of halothane on a gramicidin A channel protein embedded in a DMPC bilayer[140]. While these earlier simulations employed more simplistic membrane models composed of a single lipid type, and investigated remarkably lower timescales, the localization near the water/lipid interface is herein predicted to partially occur also in our composite, cholesterol-enriched membrane model, albeit not as predominantly as the localization at the membrane core. On the contrary, in the case of F6, the localization at the interface appeared comparable to that at the membrane core, resulting in a different density pattern with respect to the other compounds, with no predominant peak at the membrane core. These findings are consistent with the different effects observed for F6 on gAPL with respect to the VAs.

Quantitative measures of the tendency of ligands to reside inside the lipid bilayer with respect to the aqueous solvent are reported in literature in the form of either ligand equilibrium partition coefficients[191] – usually calculated as the ratio between the ligand concentration in the solvent and the concentration within the membrane – or directly as molar[198] or molal[199] ligand concentration inside the membrane. Whatever the metric, these quantities depend, among others, on the chemical and physical nature of the ligand itself, in particular its hydrophobicity and the presence of hydrophilic moieties, on the temperature of the membrane, i.e. its phase state, and on the membrane cholesterol concentration[191].

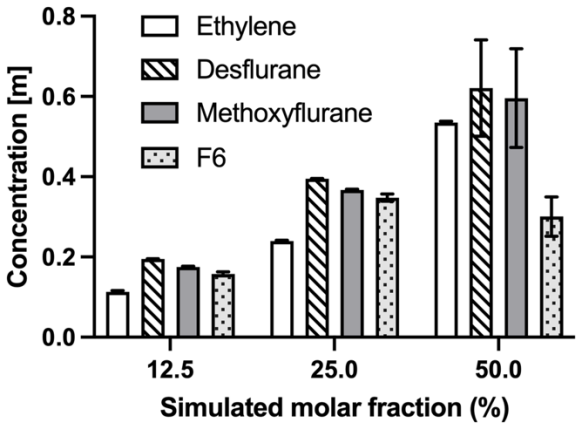

Figure 3.12. Molal concentration of the four simulated ligands inside the bilayer. Concentrations calculated as number of moles of anesthetic per kilogram of membrane. Error bars on the histograms represent the error estimate after block averaging.

To provide a direct quantitative measurement of the amount of ligand able to dissolve into the membrane, Figure 3.12 reports the molal concentration reached by the four simulated ligands within the lipid bilayer. Results confirm that the concentration of ligands inside the membrane increases with increasing amounts of simulated ligand molecules, as expected by the physical characteristics of these compounds. One notable exception is represented by F6 (dotted bars in Figure 3.12), whose concentration inside the bilayer is comparable to that of the other compounds at 12.5% and 25% simulations, reaching up to 0.35 mol/kg (at 25% simulated molar fraction, 95% CI 0.33 – 0.37), but showing no further increase in the case of 50% simulations, plateauing at 0.30 mol/kg (95% CI 0.20 – 0.40) and with a considerable amount of ligand aggregating in the water phase without entering the membrane. Also, the analysis of ligand concentration inside the membrane highlights that ethylene (white bars in Figure 3.12) also partitioned inside the bilayer, albeit at lower rates in the 12.5% and 25% simulations. Conversely, when simulated at 50% molar fraction, the reached concentration (0.535 mol/kg, 95% CI: 0.529-0.541) is comparable to the one of desflurane (patterned bars in Figure 3.12, 0.621 mol/kg, 95% CI: 0.385-0.856) and methoxyflurane (shaded bars in Figure 4, 0.596 mol/kg, 95% CI: 0.355-0.837). Also, it is worth noting how the considerable number of ligands present at 50% molar fraction leads to greater fluctuations in ligand partitioning in the case of the latter two ligands, but not in the case of ethylene. This is a consequence of the key differences in behavior between ethylene and the other simulated ligands: firstly, ethylene does not form aggregates in the water phase even at 50% concentration as

opposed to the other three ligands. Indeed, desflurane and methoxyflurane are observed to enter the membrane in the form of aggregates of up to tens of molecules, while F6 forms aggregates at 50% concentration that are partially unable to enter the bilayer and remain in the water phase throughout the simulations, resulting in lower overall membrane partitioning (see dotted bars in Figure 3.12). Secondly, ethylene did not show the secondary localization areas below the glycerol groups inside the membrane (see Figure 3.11), which are instead present for the other three ligands, but rather preferably positions itself at the membrane core, making ligand exchange between the membrane and the water phase less frequent.

VAs and F6 decrease lipid chain order already at 12.5% molar fraction

Deuterium order parameters S_{CD} represent a quantitative measurement of lipid packing and provide insights into the mobility of the hydrophobic chains. Data for POPC from the control simulation without ligands (Figure 3.13, blue lines) is in good agreement with recently published results of compositionally similar, cholesterol- and sphingomyelin-enriched POPC/POPE membranes [183], and confirms the membrane-ordering effect induced by cholesterol. Conversely, in the presence of desflurane (Figure 3.13B and F) and methoxyflurane (Figure 3.13C and G), the mechanical consequence of ligand partitioning within the hydrophobic core as well as below the glycerol groups is a reduction in acyl chain order parameters, with a trend proportional to the ligand concentration (Figure 3.13). This behavior is also present in the simulations with F6, (Figure 3.13D and h), with the exception of simulations at 50% molar fraction, where the effect of the ligand on lipid chain order is comparable within error to that at 25% concentration. This is coherent with the finding that there are no remarkable differences in the concentration reached by F6 within the bilayer at 25% and 50% simulated molar fraction (see results above), hence a comparable effect on lipid packing is not unexpected.

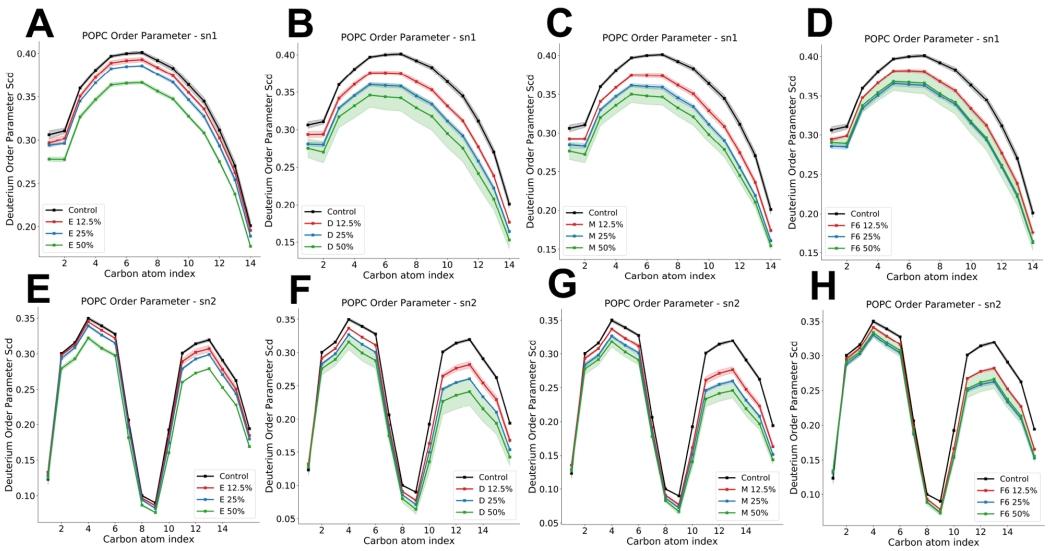

Figure 3.13. Lipid tail order parameters for POPC sn1 (top row) and sn2 (bottom row) chains, with different ligands. (A) and (E) ethylene; (B) and (F) desflurane; (C) and (G) methoxyflurane;(D) and (H) F6. For the corresponding data for POPE, POPS and PSM see Supplementary Information. Shaded intervals correspond to 95% confidence intervals.

The effect on lipid order is more subdued in the case of ethylene (Figure 3.13A and D), where the decrease in S_{CD} is particularly evident only at 50% concentration, with only marginal reductions (< 0.01) at lower ligand concentrations. These trends, reported in Figure 3.13 for POPC, are analogous for the other lipid species included in the employed membrane model (see the Appendix), and hint at a membrane-destabilizing effect of ligand partitioning, with consequences on overall bilayer mechanics.

Desflurane, methoxyflurane and F6 decrease membrane bending rigidity in a concentration-dependent manner

In the light of the ligands' tendency to partition inside the lipid bilayer, and of the structural consequences thereof observed by the analysis of area per lipid, bilayer thickness and acyl chain order parameters, a more specific quantification of the bilayer's mechanical characteristics was carried out by directly determining the bilayer bending modulus using a previously proposed methodology relying on the analysis of lipid splay.

The bilayer bending modulus for the control simulation is 88.80 kT (95% CI: 87.16 – 90.44), and while a direct comparison with other computational and experimental

studies is often not trivial due to the differences in membrane composition, temperature and methodology, this result is remarkably consistent with earlier studies of membranes with similar cholesterol content (around 0.3 molar fraction) which induces structural condensation of the lipid phase yielding a considerable increase in membrane stiffness and a shift towards the liquid-ordered phase [173,200]. Furthermore, the obtained value for the control simulation agrees with earlier literature reporting experimentally determined stiffness values for plasma membrane vesicles (PMVs, K_c = 99.75 kT), which are representative systems of the pure plasma membrane *in vitro* (see [201] and references therein).

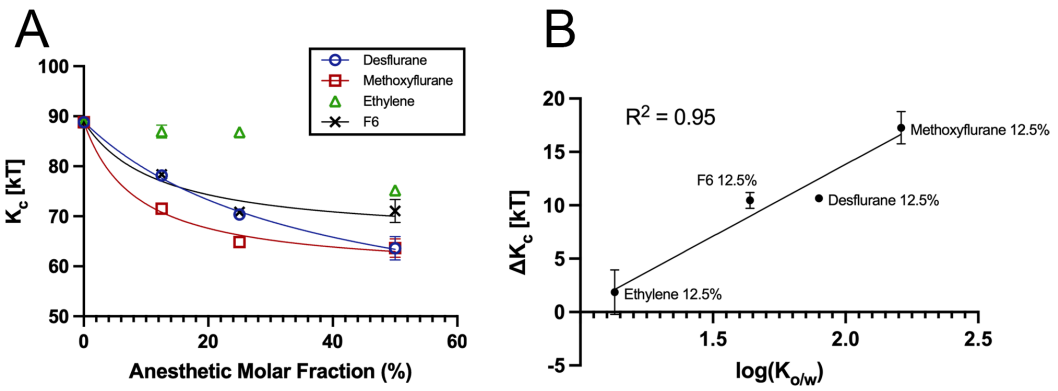

Figure 3.14. Effect of ligands on membrane stiffness. (A) Bilayer bending modulus in kT units for the different systems. Control system represented as 0% ligand concentration. Error bars represent the error estimate after block averaging, omitted when smaller than the datapoint for clarity. (B) Correlation between anesthetic lipophilicity (in terms of the logarithm of the octanol/water partition coefficient, log(Ko/w)) and the decrease in membrane bending modulus in kT units, ΔKc. Error bars represent the error estimate after block averaging, omitted when smaller than the datapoint for clarity.

The trend of reduction of bilayer bending stiffness at increasing anesthetic concentrations is visible in Figure 3.14A. At 12.5% anesthetic concentration, the presence of desflurane, methoxyflurane and F6 leads to a reduction in monolayer bending stiffness by 12.01%, 19.44% and 11.78%, respectively, compared to a mere 2.10% reduction with ethylene. At 25% anesthetic concentration, the bending stiffness is reduced by 20.80% and 26.95% by desflurane and methoxyflurane, respectively, and by 20.20 % with F6, compared to a limited 2.48% reduction caused by ethylene. Lastly, in the simulations with 50% anesthetic molar fraction, the bending stiffness is reduced by 28.38% with desflurane and 28.30% by methoxyflurane, while the effect of F6 remains again comparable to the 25% simulation, yielding a reduction of the bilayer bending modulus of 19.98%. Only at this higher concentration does ethylene lead to a noticeable reduction in bending

stiffness by 15.32%. This is consistent with order parameter results, which showed a decrease in lipid tail packing in the presence of ethylene only at 50% concentration (see Figure 3.13).

Overall, the trends in reduction in membrane bending stiffness are consistent with the hydrophobicity of these compounds. From the analysis of the data from the 12.5% concentration simulations, which is the closest to clinical concentrations, a linear relationship emerges between the lipophilicity of the ligands – quantified by the octanol/water partition coefficient $\log(K_{o/w})$ – and the reduction in bilayer stiffness (ΔK_c) observed in simulations ($R^2 = 0.95$, Figure 3.14B). Interestingly this relationship seems to hold true also for F6, which is not an anesthetic but a convulsant with amnesic properties, supporting the hypothesis that the alteration of bilayer mechanics might not be *per se* the mechanistic cause of anesthesia, but might be implicated in some of the effects caused by these compounds, especially at *supra*-clinical concentrations.

3.4.5 Discussion

In the present work, we employed long all-atom molecular dynamics simulations to assess the structural effects of the volatile anesthetics desflurane, methoxyflurane, ethylene, a low-potency control, and the nonimmobilizer F6 on a model composite lipid bilayer composed of POPC, POPE, POPS, PSM and cholesterol. Anesthetics rapidly partition inside the bilayer, reaching intra-membrane concentrations of approximately 0.6 molal, while F6 is unable to reach concentrations higher than 0.3 molal even when simulated at 50% ligand/lipid molar fraction. Desflurane and methoxyflurane preferentially localize at the membrane core region and immediately below the glycerol groups of the bilayer, with structural consequences on both area per lipid and bilayer thickness. Indeed, the partitioning of ligands causes a contraction in bilayer thickness while at the same time reducing lateral condensation and causing an increase in area per lipid and in spontaneous water permeation, albeit with no pore formation or disruption of overall membrane integrity. The convulsant F6 shows a different localization pattern within the membrane, with preferential interaction below the lipid/water interface and a less prominent residency at the membrane core region, but with similar structural effects with respect to the aforementioned VAs. The structural rearrangement of the membrane has direct consequences on its mechanical properties, as testified by a progressive reduction in lipid hydrocarbon chain packing. The reduced energetic cost of splaying adjacent lipid tails caused by ligand

partitioning leads to a reduction in bilayer bending rigidity in a fashion proportional to ligand concentration. These structural effects are not observed for ethylene at a molar ratio of up to 0.25 with respect to the lipids, with only marginal effects at 0.5 molar ratio. Consistently with these considerations, ethylene also constitutes the least hydrophobic among the three studied VAs. It is to be underlined how the non-immobilizer F6 caused a comparable reduction in bilayer bending rigidity despite its lack of potency as a general anesthetic. Hence, also bearing in mind that the simulated concentrations are above the typical concentrations reached in clinical settings, these findings shed light on important aspects of anesthetic-membrane interactions. Firstly, the two potent VAs and the nonimmobilizer F6 studied herein have, even at the smallest studied concentration, the capacity to alter the energetic landscape of a model mammalian lipid bilayer, which results in profound changes of its mechanical characteristics in terms of a marked reduction in bending stiffness and an overall shift towards a liquid-disordered phase, as shown by the reduction in thickness, the increase in APL, the increase in spontaneous water permeation and the reduction of lipid chain order. This effect appears as antagonistic to the role of cholesterol, which induces instead a shift towards the liquid-ordered phase and an overall increase in membrane rigidity[200]. Interestingly, VAs and cholesterol seem to have instead a similar effect in the context of lipid raft microdomains, whose number and size has been recently shown to increase with both anesthetics and cholesterol[137] . Given the fundamental role of the cell membrane not only in overall cell mechanics and structural stability, but also in the function of several transmembrane proteins, including important ion channels thought to be directly involved in anesthesia or its side effects[53,202–205], it appears entirely reasonable that bilayer alterations might be, directly or indirectly, involved in some of the effects exerted by VAs and F6, in the same way in which cholesterol is a crucial modulator of membrane mechanics and essential for many membrane functions. As a matter of fact, a hybrid protein/lipid mechanism based on the alteration of the physics of the lipid membrane has been recently proposed by Pavel et al., who described and demonstrated *in vivo* the indirect effect of volatile anesthetics on membrane-embedded channel proteins by means of an alteration of sphingomyelin lipid rafts[137]. Despite failing to highlight any effect of VAs on pure DOPC liposomes, employed as a model system of the pure membrane, the research provided further evidence for the key role of membrane biophysics in the molecular mechanisms of anesthetics, and supports the speculation that anesthetics directly interact with the phospholipid membrane, with diversified effects not only at different time and length scales, e.g. on local lipid arrangement vs. on larger-scale lipid microdomains, but also at different concentrations, e.g. clinical vs. *supra*-clinical. Indeed, not only

does the alteration of the surrounding lipid environment bear the potential of altering the function of channel proteins, e.g. by modifying the energetic cost of key functional motions, but the rapid partitioning of VAs into the hydrophobic core might also be an essential prerequisite for anesthetics to reach cryptic hydrophobic binding sites of such proteins within regions embedded in the membrane, which are inaccessible from the external water phase. In this sense, the findings reported herein do not clash with earlier evidence of a direct action of anesthetics on ion channels[206,207], which is still debated to be the final mechanism of action causative of anesthesia. Instead, the computational predictions provide a quantification of the interaction between VAs and the lipid phase and the mechanical alterations of the latter at increasing VA concentrations. This mechanism might thus be necessary, but arguably not sufficient, for a compound to exhibit anesthetic potency, thereby explaining both the Meyer-Overton correlation and outliers thereof such as nonimmobilizers, featuring considerable hydrophobicity but low to no anesthetic potency. This is confirmed by analyzing the effect on bilayer mechanics of the nonimmobilizer F6, which is herein predicted to alter membrane behavior in a similar manner to potent anesthetics. This further suggests that the alteration of the lipid membrane *per se* is unlikely to be the sole mechanistic cause of anesthesia as a whole. Rather, it might be a biophysical mechanism involved in some of the effects that are exerted both by anesthetic agents and nonimmobilizers such as F6, which has been shown e.g. to induce convulsions and amnesia *in vivo*. Also, the direct action on membrane mechanics might rather provide a mechanistic basis to explain the side effects of anesthetics, which arise at higher concentrations and are in common with convulsants[208,209]. Indeed, given the exacerbation of the alteration of bilayer structure and mechanics predicted herein at such higher concentrations – 0.25 and 0.5 molar fractions –, it is reasonable that such a mechanism might be involved in the molecular basis of the side effects of VAs at *supra*-clinical concentrations.

3.4.6 Conclusions

The molecular mechanisms of general anesthesia are to this day an unsolved medical puzzle. While recent literature generally considers transmembrane proteins as the main functional target of volatile anesthetics, the Meyer-Overton correlation clearly hints at the ability of these compounds to interact with the lipid bilayer of cell membranes, even if the final functional action is not exerted directly on the membrane itself. Long molecular dynamics simulations of the three VAs ethylene, desflurane and methoxyflurane and of the nonimmobilizer F6 confirm the strong

tendency of these ligands to partition within the hydrophobic environment of a model membrane, and allowed to quantify the structural effects this determines: a reduction in bilayer thickness, a decrease in lipid chain order and a reduction of membrane stiffness, with a trend proportional to the amount of partitioned ligands. Given the strong correlation observed between the compounds' lipophilicity and the reduction in the membrane bending modulus caused by their inclusion within the membrane, it appears that the phospholipid membrane might be a key component in determining some of the effects of anesthetics on channel proteins, by altering their structural and mechanical characteristics in the presence of VAs with possible consequences on embedded protein function and on the intracellular link between the membrane and the cytoskeleton. Moreover, the remarkable tendency to dissolve in the lipid phase followed by lateral diffusion within the membrane, might be an essential step to reach key functional hydrophobic binding pockets in transmembrane proteins, which would be inaccessible from the aqueous solvent, such as some transmembrane domains which have been shown to bind anesthetics[206]. These considerations are well in line not only with the strong relationship between potency and hydrophobicity, but also with the most recent theories indicating ion channels as ultimate targets for general anesthetics, and pointing at the lipid environment of the membrane as a first transducer of anesthetic action[137]. At the same time, the functional distinction between general anesthetics and compounds without any anesthetic effect but high lipophilicity, such as F6, might involve processes and molecular players downstream of the interaction with the membrane. This concept highlights how the lipid-centered and the protein-centered theories of anesthetic action are not, in fact, irreconcilable, but might rather be two aspects of a composite mechanism, which sees the interaction with the lipid membrane as a necessary but perhaps not sufficient condition. A more thorough analysis of how this occurs and to which extent, especially as to where the discrimination between general anesthetics and non-anesthetic Meyer-Overton outliers takes place, as well as of the effect of the membrane alteration on the cytoskeleton linked at the intracellular interface, certainly warrants further computational and experimental investigations, and seems well worth pursuing further.

3.4.7 Limitations of the Study

- While the membrane model employed in this work is a multi-component membrane which accounts for the major lipid constituents of mammalian cell membranes, it still represents a simplified representation, especially in

the context of neural membranes which include several types of different phosphatidylcholines, phosphatidylethanolamines, sphingomyelins, phosphatidylserines, glycolipids, cerebrosides and phosphatidylinositols, just to name a few. Building increasingly realistic models of cellular membranes is an active topic of research and requires major computational efforts, often demanding the use of coarse-grained modelling and extended parameter validations to accurately capture the physical and chemical characteristics of the simulated species.

- The present work focuses on the effects of three different VAs of different chemical structure and spanning a wide range of clinical potencies. However, several other VAs exist that were not included in the present work, and are very well worth investigating in further studies. Also, we herein included a compound that would be expected to have high potency as an anesthetic based on its hydrophobicity and structural similarity to actual VAs, but actually lacks any anesthetic effect, namely F6. Given the comparable effect of this compound on pure membrane mechanics, further investigations are needed to explore downstream events (e.g. the interaction with transmembrane proteins) that would ultimately set apart potent anesthetics from hydrophobic nonimmobilizers and other similar negative controls.

Chapter IV

Investigation of non-covalent molecular assemblies for drug delivery using molecular simulations

4.1 Introduction[4]

As discussed in section 1.2.3, many drugs and drug-like molecules that are currently both approved for clinical use or still under investigation in the context of anticancer therapy present significant shortcomings limiting their scope and efficacy. Such shortcomings can be broadly categorized into (a) *delivery* shortcomings, whereby the accumulation of the compound in the target tissue is insufficient, or (b) off-target and systemic *toxicity*, when the action of the compound is also exerted in

[4] Part of the work described in this chapter has been published in the following authored scientific publications:

Sztandera, Krzysztof, et al. "Noncovalent interactions with PAMAM and PPI dendrimers promote the cellular uptake and photodynamic activity of rose bengal: the role of the dendrimer structure." Journal of Medicinal Chemistry 64.21 (2021): 15758-15771.

Uchida, Noriyuki, et al. "Reconstitution of microtubule into GTP-responsive nanocapsules." Nature Communications 13.1 (2022): 5424.

Sztandera, Krzysztof, et al. “Cellular uptake of rose bengal is mediated by OATP1B1/1B3 transporters”, Bioelectrochemistry (2023): 108449.

healthy tissue, which often determines a significant physical and psychological burden on both patients and caregivers. Ideally, innovative pharmaceutical solutions, including those for anticancer therapy, would tackle both these interconnected issues, by means of customized drug delivery platforms which not only effectively deliver the small molecules to their targets, but also limit their accumulation and potentially nefarious effects elsewhere.

The goal of the present chapter is to illustrate how such goals can be effectively tackled with the help of computational molecular modelling and molecular dynamics, which can be employed in synergy with experimental techniques to gain important insights into the molecular interactions of small molecules with key components such as cell membranes and nanocarriers, e.g. dendrimers or nanocapsules, to ultimately assist the definition and optimization of therapeutic strategies which can overcome the current limitations described above. Employing *in-silico* modelling with atomistic resolutions can improve our understanding of how drugs interact with their surroundings, as well as the dynamics of such processes, enabling the so-called *computer-aided* design and optimization of both improved therapeutic agents and specialized delivery platforms, even when the interactions of such molecules with their surroundings are aspecific and occur on multiple potential binding sites.

Section 4.2 reports a combined experimental and computational study of the mechanisms of cellular permeation of Rose Bengal, highlighting the need for protein transporters and the lack of spontaneous membrane diffusion, which was explored using molecular dynamics. Section 4.3 expands the scope of the investigation of RB by reporting the findings regarding how the photosensitizer interacts with dendrimers, which are organic nanoparticles that can form stable but reversible molecular complexes with RB, thereby acting as promising nanocarriers. The comparative study of the molecular-level interactions between stoichiometric RB and different types of dendrimers was carried out with the help of molecular dynamics simulations. In section 4.4 the application of computational molecular modelling techniques to study nanoformulations for drug delivery is extended to the case of custom GTP-responsive nanocapsules for anticancer therapy, assembled through the use of molecular glues. Molecular modelling and dynamics allowed to shed light on how the molecular glues alter tubulin conformations to allow for the stabilization of the latter into capsules, which were experimentally shown to selectively collapse and release the payload in response to GTP, with potential applications in precision oncology.

4.2 Mechanisms for cellular uptake of Rose Bengal[5]

Rose bengal (4,5,6,7-tetrachloro-2',4',5',7'-tetraiodofluorescein, RB) is a water-soluble, dianionic fluorescein derivative that functions as an organic fluorescent dye and belongs to the xanthene family of synthetic dyes[210]. Originally used as a wool colorant, RB has been subsequently approved as a food dye, and is also used in ophthalmology to stain damaged conjunctiva and cornea[211]. Indeed, RB is currently approved as an ocular diagnostic tool, and has been designated by the Food and Drug Administration (FDA) for the treatment of several types of cancers and skin conditions [212]. Due to its fluorescent properties and high yield of singlet oxygen, RB has been proposed as a photosensitizer in photodynamic therapy[213–216]. However, its shortcomings include its hydrophilic nature, negative charge, tendency to aggregate, and short half-life time, which hinder the transmembrane cellular uptake of RB, and consequently, the efficiency of RB treatments[217]. Such shortcomings justify the investigation of the molecular mechanisms through which RB interacts with the cellular environment, with the overarching goal of both understanding how the dye is able to cross cell membranes, and to design novel nanocarriers which can improve its uptake and efficacy for photodynamic therapy.

4.2.1 Abstract

Due to its fluorescent properties and high yield of singlet oxygen, rose bengal (RB) is one of the most promising photosensitizers for cancer treatment. However, the negative charge of RB molecule may significantly hamper its intracellular delivery by passive diffusion through the cell membrane. Thus, specific membrane protein transporters may be needed. The organic anion transporting polypeptides (OATPs) family are a well-characterized group of membrane protein transporters, responsible for cellular uptake of a number of drugs. To our knowledge, this is the first study that evaluates cellular transport of RB mediated by the OATP transporter family. First, electrified liquid-liquid interface, together with biophysical analysis and molecular dynamics simulations were used to characterize the interaction of RB with several models of a cellular membranes. These experiments proved that

[5] Part of the work described in this paragraph has been published in:

Sztandera, Krzysztof, et al. "Cellular uptake of rose bengal is mediated by OATP1B1/1B3 transporters", Bioelectrochemistry (2023): 108449.

Contribution of the author: creation of computational models and simulations of lipid bilayer patches, data analysis and interpretation.

RB interacts only with the membrane's surface, without spontaneously crossing the lipid bilayer. Evaluation of intracellular uptake of RB by flow cytometry and confocal microscopy showed significant differences in uptake between liver and intestinal cell line models differing in expression of OATP transporters. The use of specific pharmacological inhibitors of OATPs, together with Western blotting and in silico analysis, indicated that OATPs are crucial for cellular uptake of RB.

4.2.2 Introduction

One of the first obstacles hindering the wide-scale clinical application of RB for photodynamic therapy lies in the fact that the mechanisms of its cellular uptake remain poorly understood; for this reason, the investigation of nanocarriers to overcome such obstacles has recently seen a great rise in scientific interest[210].

The three main pathways of transmembrane transport of low molecular weight compounds are as follows: diffusion, assisted transport, and active transport. The type of transport depends on the properties of the compound such as its shape, charge, and size. The cell membrane components contain negatively charged phosphate groups; therefore, hydrophilic and negatively charged molecules require membrane protein transporters for cellular entry [218]. The organic anion transporting polypeptide (OATP) family is a well-characterized group of membrane protein transporters, coded by solute carrier family (SLC) genes. OATPs are multi-specific transporters that mediate the transport of various compounds including xenobiotics (OATP1A2) and prostaglandins (OATP2A1). This transport is ATP- and sodium-independent; however, the exact mechanism remains under evaluation[219]. Inhibition of OATP activity may lead to drug-drug interactions[220]. To date, more than 300 OATPs have been reported, 11 of which are expressed in human tissues. OATPs are divided into six families according to their amino acid sequence; they consist of 643 to 724 amino acids and possess 12 transmembrane domains [219]. Depending on the type, OATPs occur primarily in the brain, heart, testis, kidney, and liver, where they are located mainly in epithelial cells.

To the best of our knowledge, this is the first study that combines the experimental evaluation of cellular transport of RB mediated by the OATP transporter family to a computational study of the interaction between RB and cell membranes using Molecular Dynamics (MD). Biophysical analysis showed that RB at low concentrations could not interact with negatively charged micelles, at the same time interacting to a limited extent with the cell membrane surface; this latter aspect was confirmed by MD simulations. Therefore, it was concluded that RB

cannot cross the cellular membrane, suggesting the requirement for membrane transporters. Evaluation of intracellular uptake of RB by flow cytometry and confocal microscopy showed significant differences in uptake between cancer cell lines expressing different levels of OATP transporters. The application of specific pharmacological inhibitors of OATPs, together with Western blotting and in silico analysis, indicated that OATPs are crucial for cellular uptake of RB.

4.2.3 Materials and Methods

The detailed experimental methodology, including the construction of the electrified liquid-liquid interface, the hydrodynamic diameter measurements, the details of the cell cultures, the fluorescence anisotropy measurements, the intracellular uptake inhibition assay and the cytotoxicity studies are reported in the original publication and in section 4.2.1 of the Appendix. The detailed computational methodology is discussed in the following.

MD simulations of lipid bilayers in the presence of RB molecules were carried out using GROMACS 2021.3 [221] and the CHARMM36 force field [222]. Graphical visualizations of molecular systems were assembled using the Visual Molecular Dynamics (VMD) software package [223].

System Construction

To obtain atomistic insights into the interaction between RB and the lipid membrane, we built a computational model of the lipid bilayer and carried out a set of Molecular Dynamics (MD) simulations in the presence and absence of RB. To account for the intrinsic heterogeneity of cell membranes, we chose to construct and simulate a multi-component lipid bilayer composed of POPC (1,2-palmitoyl-oleoyl-sn-glycero-3-phosphocholine), POPE (1-Palmitoyl-2-oleoyl-sn-glycero-3-phosphoethanolamine), POPS (1,2-palmitoyl-oleoyl-sn-glycero-3-phosphoserine), PSM (palmitoylsphingomyelin) and Cholesterol (CHOL). This specific composition, which is representative of a mammalian cell membrane, was described in detail in earlier literature [224,225] and employed in the previous computational study investigating the interaction between volatile anesthetics and the cell membrane[226]. The precise composition of the simulated membrane is reported in Table 4.1 below:

Table 4.1. Number of different lipid molecules in the two leaflets of the membrane model.

Lipid	Inner Leaflet	Outer Leaflet	Total
POPC	20	53	73
POPE	66	17	83
POPS	41	4	45
PSM	5	58	63
CHOL	68	68	136
Total	200	200	400

The bilayer model was constructed and simulated following a previously published protocol. Briefly, the bilayer was assembled using the Membrane Builder [227,228] of CHARMM-GUI [229], using 50 TIP3P water molecules per lipid to ensure full hydration and sufficient solvent for the addition of rose bengal. A concentration of 0.15 NaCl was imposed. The simulations with rose bengal were setup by randomly inserting 1 or 10 RB molecules for the two systems respectively (1RB and 10RB) in the aqueous solvent, corresponding to a mole fraction with respect to the lipids of 0.025% and 2.5%. This latter higher concentration, corresponding to roughly 7 mM concentration, was included to enhance the sampling of membrane:RB interaction and possible permeation events. The final compositions of the simulated systems are reported in Table 4.2:

Table 4.2. Components of each simulation system.

System	Lipids	Water molecules	Cl^- ions	Na^+ ions	RB molecules	Molecules	Atoms
C	400	20000	47	92	0	20539	104076
1RB	400	19953	46	93	1	20493	103978
10RB	400	19670	37	102	10	20219	103516

Simulation Protocol

The systems were simulated using GROMACS 2021.3 and parametrized with the CHARMM36 force field[230]. Rose bengal was parametrized using CGenFF version 4.6 [231,232]. Energy minimization and NVT/NPT equilibrations were carried out following the recommended CHARMM-GUI protocol, as described in detail in a previous study [226]. After equilibration for 250 ps in the NVT ensemble at 303.15K and in the NPT ensemble for 500 ps at T=303.15 K and p=1 atm, systems were simulated for production MD runs for a total of 1 μs each in the NPT ensemble, using semi-isotropic Parrinello-Rahman pressure coupling [233] at 1 atm and the

Nosé-Hoover thermostat [234] at a reference temperature of 303.15 K. Electrostatic interactions were described using the Particle Mesh Ewald (PME) algorithm [235] with a cutoff of 1.2 nm. Van-der-Waals interactions were also cutoff at 1.2 nm, with the addition of a force-switch modifier from 1.0 nm to 1.2 nm. All bonds involving hydrogen atoms were constrained using the LINCS algorithm [236].

Out of the total of 1 μs of production MD simulations, the first 250 ns were regarded as additional structural equilibration and excluded from the subsequent analyses. The remaining 750 ns of the simulations were analyzed, and the properties of interest were sampled every 200 ps (unless otherwise stated). The visualizations of the molecular systems reported herein were generated using the VMD software [223].

Structural and Statistical Analyses

The methodology for the determination of the structural membrane properties reported in this chapter, and the statistical analysis thereof, follows the same procedure described in Chapter 3. In addition to this, to obtain further insights into the energetic landscape of the RB-lipid interaction, we obtained an estimate of the binding free energy between the single RB molecule and the outer bilayer interface using the MM/PBSA methodology[237]. Briefly, frames of the membrane/RB complex were extracted every 10 ns from the equilibrium phase (last 750 ns) of the 1RB simulation, for a total of 75 uncorrelated snapshots. These frames, divided into three blocks spanning 250 ns each (25 snapshots per block), were used for the MM/PBSA analysis using the gmx_MMBPSA[237,238] tool to calculate the total free energy of interaction between the RB molecule and the lipids. Since no ligand permeation occurs throughout the MD simulations, and thus the RB molecule stays solvated in water even while in contact with the lipid headgroups, the continuum solvent model used in the MM/PBSA approach remains applicable to approximate the contribution of solvation to the interaction strength[239]. The obtained total free energy, ΔGTotal, is reported together with the 95% confidence interval determined after block averaging as described in Chapter 3.

The complete set of computational modelling data, including all the necessary input files to reproduce the simulations, are available on Zenodo at https://zenodo.org/record/7861624.

4.2.4 Results and Discussion

As observed in previous studies of RB using spectroelectrochemical methodology (AC-modulated voltammetry involving fluorometric measurements) by Kakuchi *et al.*, RB can undergo an interfacial ion transfer reaction with transient interfacial adsorption when doubly charged [240,241]. Figure 4.1B shows a series of cyclic voltammograms (CVs) of increasing RB concentrations (always initially added to the aqueous phase), starting from 10 µM. Observed signals at approx. -0.120 V (negative peak current corresponding to the transfer of the doubly charged RB anion from the aqueous to the organic phase) and approx. -0.05 V (positive peak current corresponding to the transfer of the doubly charged RB anion from the organic to the aqueous phase) indicate that the electrochemically triggered ion transfer is reversible (the forward and reversed peak current ratio approaches unity). This was further confirmed by calibration curves where the negative and positive peak currents were plotted as a function of the RB aqueous phase concentration, which were linear over the studied concertation range (10–80 µM). This provides a voltammetric detection sensitivity (0.230 for positive and -0.252 $A \cdot M^{-1}$) with the expected order of magnitude, with similar absolute values expected for the revisable reaction [242,243]. Using the linear fit parameters, we additionally calculated the limit of detection and limit of quantification of RB for voltammetric detection at the electrified liquid-liquid interface. Obtained electroanalytical parameters are summarized in Table 4.3.

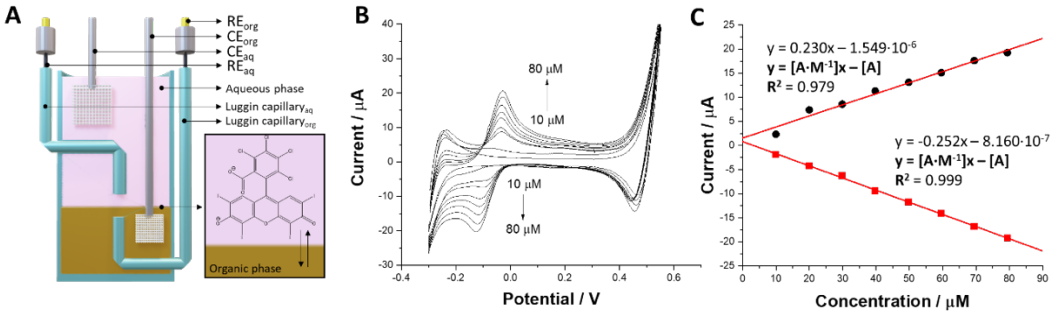

Figure 4.1. **(A)** The electrochemical cell used to study interfacial behavior of RB (RE: reference electrode, CE: counter electrode, aq: aqueous phase, org: organic phase). **(B)** CVs recorded for increasing concentrations of RB initially added to the aqueous phase. Concentrations ranged from 10 to 80 µM and the scan rate was 20 mV/s. **(C)** Calibration curves plotted based on the positive (-0.05 V) and negative (-0.12 V) peak current signals from CVs depicted in (B). Linear fit equations are placed next to the corresponding calibration curve.

The carboxylic group and phenolic site present within the xanthene-based moiety of the RB chemical structure are the acid-base centers responsible for molecule ionization. At acidic pK_a values, pK_{a1} = 1.89 and pK_{a2} = 3.93 [244], RB is expected to be negatively charged within the full conventional pH scale, which is further depicted on a concentration fraction diagram in Figure 4.2A. At pH < 1, the non-dissociated RB fraction predominates; as the pH increases, the concentration of monoanionic RB species reaches its maximum value with a concentration fraction slightly exceeding 80% at pH 2.9. Further aqueous phase alkalization changes the RB speciation. At pK_{a2}, the concertation of monoanionic RB is equal to the concentration of doubly anionic species. From approximately pH 6.3 onwards, only doubly charged RB species are expected to be present in the bulk of the aqueous phase. Thus, the aqueous phase was fixed at pH 7 to perform the scan rate dependency allowing the calculation of the diffusion of interfacially active species (Figure 4.2 B and C). Using the Randles-Sevcik equation, which is valid for reversible ion transfer reactions, the aqueous phase diffusion coefficient was calculated as 1.55 ± 0.60 cm^2/s (experiment performed in triplicate).

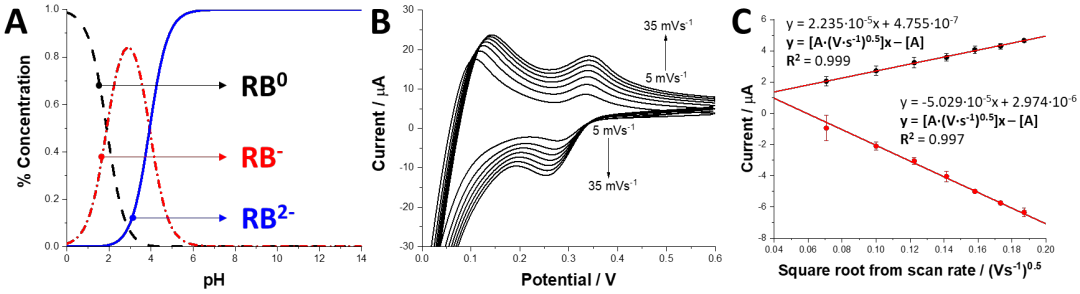

Figure 4.2. **(A)** Concentration fraction diagram plotted for RB using pKa1 = 1.89 and pKa2 = 3.93. **(B)** CVs recorded in the presence of 50 µM RB in the aqueous phase at different scan rate values (5, 10, 15, 20, 25, 30, and 35 mV/s). **(C)** Ionic current values for the interfacial transfer of RB plotted as the square root of the scan rate. The linear fit equation is given next to the corresponding dependencies.

Table 4.3. Summary of electroanalytical, physicochemical, and pharmacochemical parameters extracted from the voltammetric study.

Analytical, physicochemical, and pharmacochemical parameters of RB

Sensitivity[6] **(+) / A·M^{-1}**	0.230	$\Delta^{aq}_{org}\phi'$ / V	-0.095
Sensitivity (-) / A·M^{-1}	0.252	$\Delta^{aq}_{org}G'$[7] / kJ·mol^{-1}	21.8
LOD[8] **(+) / µM**	8.91	$\log P_{DCE}$[9]	3.26
LOD (-) / µM	2.18	D[10] (+) / cm^2·s^{-1}	0.35 ± 0.07
LOQ[11] **(+) / µM**	29.70	D (-) / cm^2·s^{-1}	1.55 ± 0.60
LOQ (-) / µM	7.26	z[12] (pH = 7)	-2

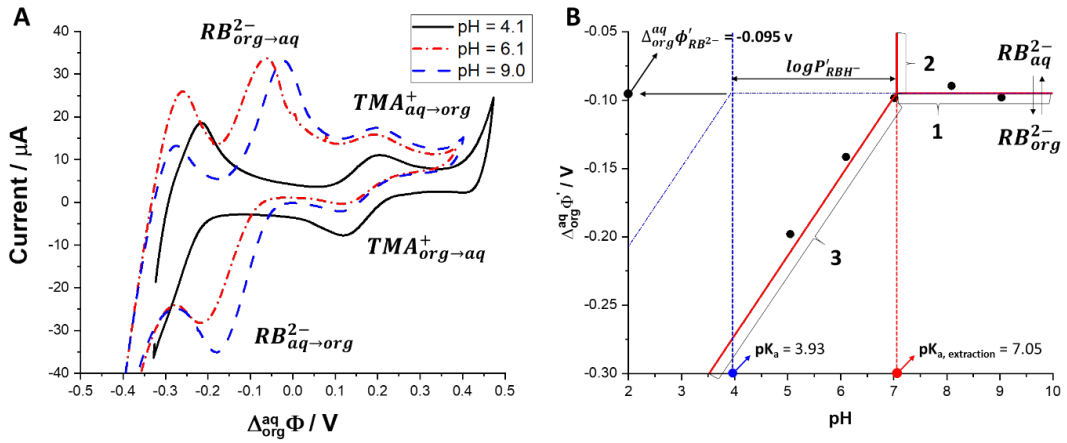

Figure 4.3. (A) CVs recorded in the presence of 100 µM RB and 50 µM TMA+Cl- in the aqueous phase at three different aqueous phase pH values, which were as follows: 4.09 (solid black line), 6.1 (dash-dot red line), and 9.0 (dashed blue line). (B) Ionic partition diagram for double anionic RB. The boundary lines affected by the RB extraction pKa are marked with the solid red line. The theoretical ionic portion diagram for RB is marked with the dotted blue lines. For more details, see the discussion section [245–248]

Finally, the CVs recorded at different pH values (Figure 4.3A; pH = 4.1, 6.1, and 9.0) were used to plot the ion partition diagram (Figure 4.3B). Here, solid red

[6] Taken as the slope of the calibration curve plotted as the ion transfer current vs the corresponding concentration.

[7] Free Gibbs energy of ion transfer reaction is given as $\Delta^{aq}_{org}G' = -\Delta^{aq}_{org}\phi' \cdot z \cdot F$.

[8] Calculated using the limits of detection (LOD) = 3SD·S^{-1} where SD is the standard deviation of the calibration curve intercept and S is the slope (sensitivity value).

[9] Calcualted using $\log P_{DCE} = -(\Delta^{aq}_{org}\phi' \cdot z \cdot F)\cdot(2.303 \cdot R \cdot T)^{-1}$ where F is the Faraday constant, R is the gas constant, and T is the temperature in K.

[10] Calculated using the Randles-Sevcik equation; the error was derived from three independent experiments.

[11] Calculated using the LOD = 10SD·S^{-1}.

[12] Charge was derived from the concertation fraction diagram.

lines correspond to the equivalent concentration boundary lines that were plotted using equations developed in [245].

Boundary line 1 corresponds to a situation where the concentration of RB^{2-} in the aqueous phase is equal to the concentration of RB^{2-} in the organic phase:

(2) $$\Delta_{org}^{aq}\phi = \Delta_{org}^{aq}\phi'_{RB^{2-}} - \frac{2.3RT}{F}\left(logP'_{RB^-} + pK_a^{aq}\right) + \frac{2.3RT}{F}pH$$

Boundary line 2 describes a scenario where the aqueous concentration of RB^{2-} is equal to the organic phase concentration of RB^- and is given by:

(3) $$\Delta_{org}^{aq}\phi = \Delta_{org}^{aq}\phi'_{RB^{2-}} - \frac{2.3RT}{F}\left(logP'_{RB^-} + pK_a^{aq}\right) + \frac{2.3RT}{F}pH$$

Finally, boundary line 3 is predicted with the following equation:

(4) $$\Delta_{org}^{aq}\phi = \Delta_{org}^{aq}\phi'_{RB^{2-}} - \frac{2.3RT}{F}\left(logP'_{RB^-} + pK_a^{aq}\right) + \frac{2.3RT}{F}pH$$

The presence of RB in the aqueous phase lies above boundary line 1, corresponding to a potential difference of -0.095 V. As the pH decreases from 7 toward pK_a = 3.93, the fraction of doubly charged RB species decreases and the $\Delta_{org}^{aq}\phi'$ shifts toward more negative potential values, finally giving a signal (Figure 4.3A, black solid line recorded at pH 4.1) that is partly overlaid with the potential window limiting ion transfer. Since complex splitting voltammetric signals expected for chemical species with more than one ionizable functional group were not observed, we concluded that the points marked within boundary line 3 (Figure 4.3B) were due to the facilitated transfer of protons by the monoanionic RB species, which may partition to the organic phase (the $logP_{DCE}$ for RB^- is expected to be lower than 3.26 calculated for RB^{2-}), and are overlaid with the simple RB^{2-} ion transfer reaction. From the ion partition diagram, the extraction p*K*a value, defined as the apparent p*K*a of RB^- dissolved in the organic phase, was found to be approximately 7.05. Therefore, we can conclude that the interfacial transfer of RB follows a simple ion transfer reaction. The $logP_{DCE}$ value indicates that RB displays

moderate hydrophobicity; thus, its affinity for the hydrophobic domains of the lipidic membrane cannot be neglected.

To further investigate the interactions of RB with membrane models, we first analyzed the interactions of RB with negatively charged micelles comprised of LPS using DLS measurements. Changes in the size or disruption of LPS micelles were used as a measure of RB-membrane interactions. LPS-based soft objects were visible as two distribution peaks (a smaller peak at 20 nm and a bigger peak at 140 nm (see Appendix, Supplementary Figure S4.1)), with the latter attributed to LPS micelles [249]. The addition of RB up to 50 μM did not change the sizes of the distribution curves; however, further increases in the RB concentration (100 μM and 200 μM) changed the sizes of the distribution curves, revealing a smaller sized peak. This change suggests that RB addition dissociated the LPS micelles and that a threshold concentration of RB must be exceeded to change the size of negatively charged micelles. However, it should be emphasized that the concentrations of RB used for this analysis are significantly higher than the concentrations used in our previous cytotoxicity studies [213,216].

Next, using fluorescence anisotropy measurements of two fluorescent probes (DPH and TMA-DPH), we measured changes in membrane fluidity in various layers of the cell membrane. DPH binds to the hydrophobic part and TMA-DPH binds to hydrophilic part of the bilayer [250]. The subsequent addition of RB resulted in an increase in only TMA-DPH fluorescence anisotropy, indicating stiffening of the cellular membrane due to the interaction of RB with the hydrophilic part of the membrane (Figure 4.4B). Here it should be noted here that the limitation of the method did not allow the study of the impact of higher concentrations of RB. These results suggest that RB does not possesses the ability to diffuse into deeper layers of the cellular membrane.

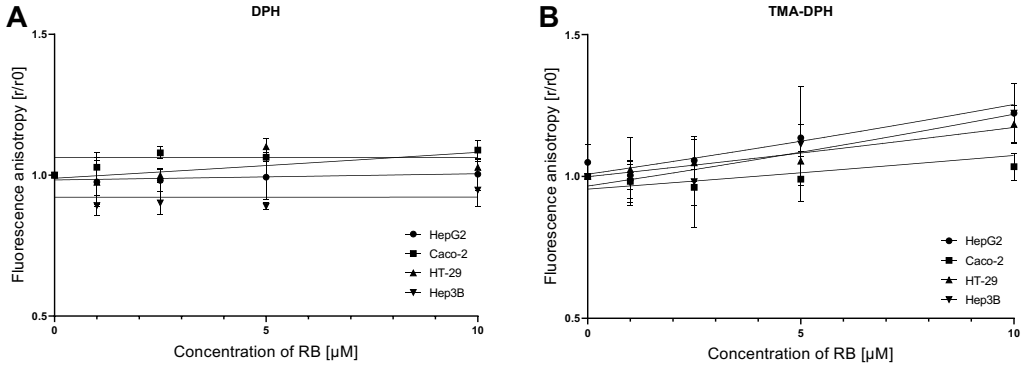

Figure 4.4. Changes in fluorescence anisotropy of **(A)** DPH and **(B)** TMA-DPH incorporated in the membranes of HepG2, Hep3B, HT-29, and Caco-2 cells with increasing concentrations of RB (0.5 to 10 μM in PBS, pH 7.4, 37 °C).

RB molecules carry two ionizable groups (-OH and -COOH) that are predominantly found in the deprotonated form (indicated as O^- and CO_2^-, respectively) at physiological pH values. This consideration, together with the DPH and TMA-DPH results, led us to hypothesize that RB might interact with the positive surface charge of lipid membranes through electrostatic interactions, without being able to penetrate spontaneously inside the lipid phase.

Thus, we next used all-atom MD simulations to obtain additional insights into how RB interacts with lipid bilayers at the molecular level. MD simulations with a mammalian phospholipid bilayer model, representative of the cell membrane, in the presence of RB molecules in the surrounding aqueous solvent, revealed a strong interaction between RB and hydrophilic lipid heads. After an initial equilibration phase, RB rapidly formed stable interactions with the membrane outer surface (Figure 4.5A and B); no subsequent spontaneous permeation events were observed at either low (1 RB molecule) or high (10 RB molecules) RB concentrations throughout the 1 μs MD sampling time period (see ESA2 and ESA3).

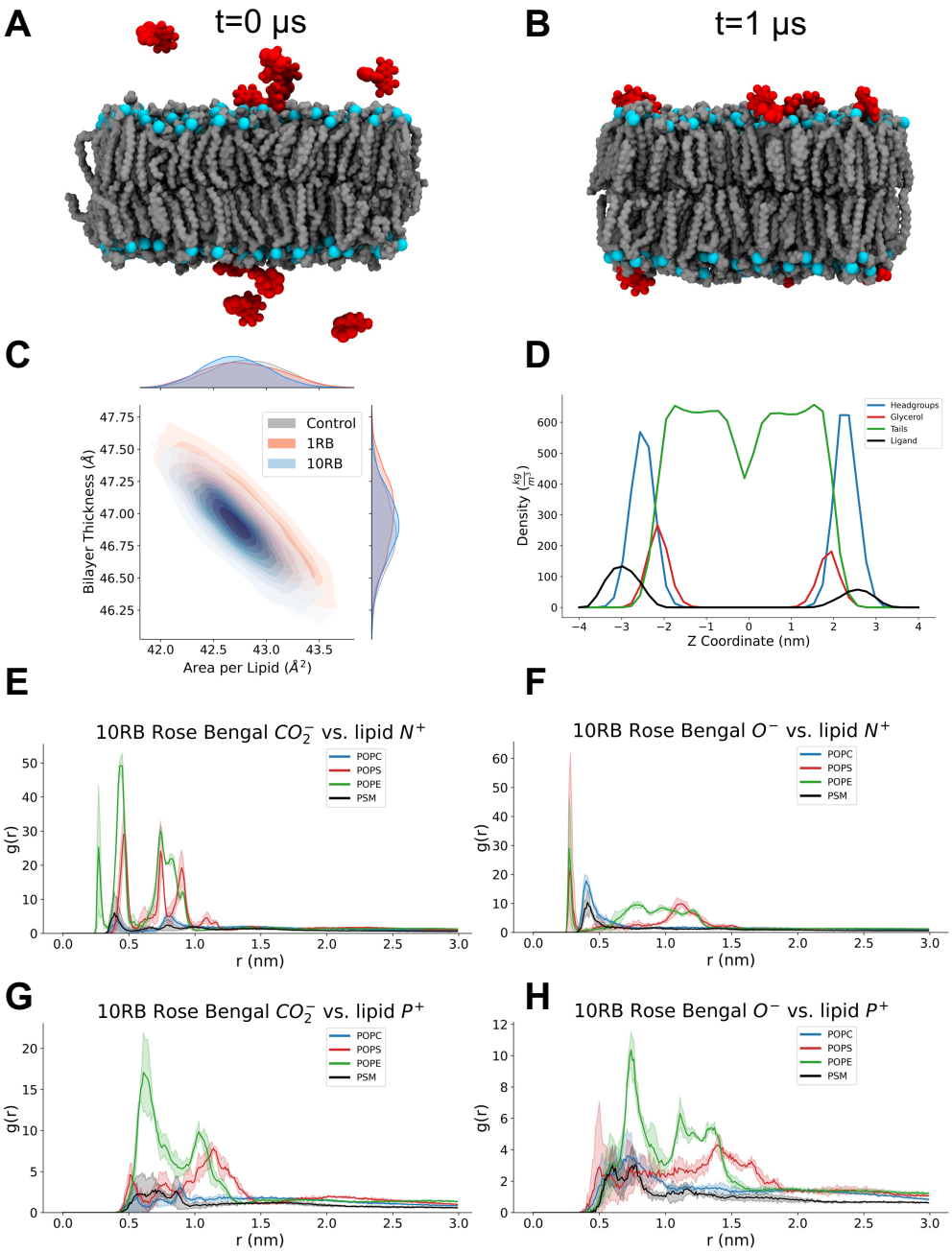

Figure 4.5. Results of MD simulations of the lipid bilayer with RB. (**A**) Snapshot of the initial conditions of the MD simulation with 10 RB molecules (in red), with ligands dispersed in the solvent. **(B)** Snapshot of the same MD trajectory with 10 RB molecules at the end (t = 1 μs) of the simulation, showing the system had reached equilibrium. Lipids are shown in gray, with phosphorus headgroups highlighted in cyan. **(C)** The distributions of the gAPL (x axis) and bilayer thickness (y axis) in the control simulation (gray), at low RB concentration (red), and at high RB concentration (blue) are shown. Marginal axes show the individual distributions. **(D)** Density profiles of lipid headgroups (blue), glycerol

groups (red), acyl chains (green), and RB (black) in the high-concentration simulation (10 RB). The plot is centered at the bilayer core, where z = 0. **(E-H)** Radial distribution functions highlighting the distances between RB CO2- groups and lipid head nitrogen atoms **(E)** and phosphorus **(G)** atoms, in addition to the distances between RB O- groups and lipid head nitrogen **(F)** and phosphorus **(H)** atoms. Shaded intervals in panels (E-H) represent 95% confidence intervals calculated from block averaging.

The analysis of the geometrical parameters of the membrane, i.e., the membrane thickness (δ) and the geometric area per lipid (gAPL), provided an initial assessment of both the quality of the simulated bilayer and of the effects of RB on membrane structure (Figure 4.5**C**). Indeed, the gAPL is a parameter that is directly linked to the molecular order and diffusion pattern of the lipids, and together with the membrane thickness constitutes a quantitative measurement of the equilibrium of the simulations. As shown in Table 3.1, the control simulation without RB yielded an average gAPL value of 42.82 $Å^2$ (95% CI: 42.67 – 42.97) and an average thickness value of 46.87 Å (95% CI: 46.76 – 46.98). These values are consistent both with earlier simulations using the same membrane model [224–226] and with experimental data describing lipid bilayers with a comparable cholesterol content (approximately 34%) [251], thus confirming the convergence of the bilayer simulation.

Table 4.4. gAPL and bilayer thickness calculated from the MD simulations (95% CIs are reported in square brackets).

System	gAPL ($Å^2$)	Bilayer Thickness (δ) (Å)
Control	42.82 [42.67 – 42.97]	46.87 [46.76 – 46.98]
1 RB	42.78 [42.66 – 42.90]	46.98 [46.88 – 47.08]
10 RB	42.72 [42.56 – 42.88]	46.90 [46.78 – 47.02]

The addition of up to 10 RB molecules in the simulation box, in random initial positions in the aqueous solvent, resulted in no remarkable effect on membrane geometry in terms of gAPL and thickness, which is consistent with the lack of membrane permeation events (Figure 4.5C).

The density profile analysis of different membrane components in the presence of RB with respect to the z axis provides additional information regarding membrane geometry and the exact localization of RB. As shown in Figure 4.5D and Supplementary Figure S4.7, the addition of RB in the simulations did not alter the

overall density profiles of the different lipid groups, and the position of the density peaks of RB molecules confirmed that they were localized in close proximity to lipid headgroups in the aqueous phase throughout the simulation.

Furthermore, the effects of RB on the overall mobility of the lipid chains and lipid packing were analyzed using deuterium order parameters, S_{CD}. The control simulation results were in good agreement with previously published MD simulation results of membranes with similar lipid compositions[252], confirming the quality of the membrane model and highlighting the ordering effect induced by cholesterol in lipid bilayers. As shown in Supplementary Figure S4.7, the addition of RB and its interaction with the membrane surface did not significantly alter lipid order parameters, which remained comparable, within error, to those of the control simulation at both low and high RB concentrations.

Overall, MD simulations of RB with the lipid bilayer suggest no remarkable effect of RB on bilayer geometry and packing, both at low (1 RB) and high (10 RB) concentrations. The exact nature of the interaction of RB with the polar headgroups of lipids was investigated by calculating radial distribution functions (RDFs) between the ionized groups of RB, i.e., the deprotonated CO_2^- and O^- groups, and the positively charged P^+ and N^+ atoms on the lipid heads. The RDF is related to the probability of finding two given atom groups at a given distance with respect to each other. The results suggest a strong interaction of the deprotonated groups of RB with positively charged amine groups in the lipid heads (Figure 4.5E and F), as highlighted by the presence of substantial RDF peaks below 5 Å for both CO_2^- and O^- of RB with respect to the lipid N^+ species. Conversely, peaks were localized at slightly higher distances (between 5 and 15 Å) when calculated with respect to lipid P^+ atoms. The corresponding results for the simulation at low RB concentration (Supplementary Figure S4.8) revealed the same overall trend, with RB ionized groups in close proximity to lipid head N^+ atoms. These results suggest that the largely deprotonated CO_2^- and O^- groups of RB at physiological pH values rapidly form an electrostatic interaction with the membrane surface, maintaining the anchoring of RB to the bilayer and hindering its penetration into the hydrophobic membrane core. To further explore this hypothesis, we quantified the strength of the interactions between the RB molecule and the lipid headgroups using the MM/PBSA approach. RB interacts with the solvent-exposed portion of the lipid bilayer with a predicted total free energy of -75.54 kcal/mol [95% CI: -80.04 to -71.05 kcal/mol], which is of the same order of magnitude of previously reported predictions of RB-protein binding[253]. While the aim of this method is not to

accurately quantify the energy barrier preventing the RB from penetrating the bilayer (e.g. due to the lack of the entropic contribution), the negative binding free energy values that were obtained, resulting from the overall interactions between RB and the lipid headgroups, are about 10-fold above the thermal noise level (0.6 kcal/mol at room temperature) and thus indicative of its resistance to spontaneous membrane crossing, caused by strong electrostatic effects between the charged groups of the ligand and the hydrophilic portion of the membrane.

Indeed, the results obtained from the MD simulations are consistent with the those obtained with the DPH and TMA-DPH probes, which suggested close proximity of RB to the hydrophilic part of the lipid bilayer, with a negligible interaction with the aliphatic core and no membrane permeation.

4.2.5 Conclusions

RB is a promising photosensitizer for anticancer photodynamic therapy. Previous and current scientific efforts have focused on using nanocarriers to transport this photosensitizer inside cells, since the success of RB treatment depends on its cellular uptake and intracellular accumulation. Interestingly, the mechanism of cellular entry of RB has remained unclear. In the present study, electrochemical studies performed at the junction between two immiscible electrolyte solutions, as well as model DLS and fluorescence polarization assays, showed that RB displays moderate-to-no interactions with hydrophobic domains of the lipid bilayers. These observations were strengthened by molecular modeling, showing that RB can interact with the membrane surface, but cannot cross cellular membranes by itself, indicating the necessity for membrane protein transporters. In vitro experiments showed a significant difference in intracellular uptake and phototoxicity between hepatocellular carcinoma and colorectal cancer cell lines, which differ in their expression of OATP transporter family proteins. Further studies using specific inhibitors of OATP transporters revealed their crucial role in transporting RB into cells. The results reveal the previously unknown importance of OATP transporters in facilitating RB uptake, which could have implications for photodynamic therapy with RB and lead to the development of effective RB delivery systems.

4.3 Dendrimeric nanoparticles as candidate nanocarriers for Rose Bengal[13]

As discussed in the previous section, photodynamic therapy (PDT) is one of the most promising methods for the treatment of basal cell carcinoma and different types of skin cancer [254]. This highly specific approach is primarily based on the application of a light-sensitive compound (so-called photosensitizer, PS), which upon excitation with light of a certain wavelength generates reactive oxygen species (ROS). This, in turn, leads to the oxidation of cellular nucleic acids, lipids, and proteins, disrupting cell signaling cascades or gene regulation, ultimately activating several cell death pathways [255]. Such specific mechanism enables treatment to be targeted precisely to the area of a neoplastic lesion upon direct application of PS and light [256]. Thus, the benefits of PDT are its non-invasiveness and lack of adverse side effects. However, the level of damage and the mechanisms of cell death depend not only on the clinical setup (e.g., time of irradiation and light intensity), but also on the properties, concentration, and subcellular localization of PS[257]. Consequently, to take full advantage of the potential of PDT, it is essential to select the appropriate phototoxic drug.

The ideal PS should have the following properties: maximum absorbance between 650 and 850 nm, high efficiency of free radical production, low photodegradation, and non-toxicity in the dark. Additionally, PSs should have long half-lives and efficient cellular uptake, enabling sufficient intracellular accumulation to trigger a toxic effect [212,257]. Despite many years of research, clinically used PSs, such as Rose Bengal, remain far from perfect, due to the aforementioned shortcomings.

4.3.1 Abstract

Rose bengal is an anionic dye considered as a potential photosensitizer for anticancer photodynamic therapy. The clinical utility of rose bengal is hampered by its short half-life, limited transmembrane transport, aggregation, and self-

[13] Part of the work described in this paragraph has been published in:

Sztandera, Krzysztof, et al. "Noncovalent interactions with PAMAM and PPI dendrimers promote the cellular uptake and photodynamic activity of rose bengal: the role of the dendrimer structure." Journal of Medicinal Chemistry 64.21 (2021): 15758-15771.

Contribution of the author: creation of computational models and simulations of dendrimer nanoparticles, data analysis and interpretation.

quenching; consequently, efficient drug carriers that overcome these obstacles are urgently required. In this study, we performed multilevel in vitro and in silico characterization of interactions between rose bengal and cationic poly(amidoamine) (PAMAM) and poly(propyleneimine) (PPI) dendrimers of the third and fourth generation and assessed the ability of the resultant complexes to modulate the photosensitizing properties of the drug. We focused on explaining the molecular basis of this phenomenon and proved that the generation- and structure-dependent binding of the dye by the dendrimers increases the cellular uptake and production of singlet oxygen and intracellular reactive oxygen species, leading to an increase in phototoxicity. We conclude that the application of dendrimer carriers could enable the design of efficient photodynamic therapies based on rose bengal.

4.3.2 Introduction

Due to its high efficiency of singlet oxygen generation [258], RB is considered a good candidate to serve as a PS in anticancer PDT. However, the potential use of RB in the photodynamic therapy of neoplasms is limited mainly by its short half-life, hydrophilic nature, and tendency to aggregate. RB is negatively charged at physiological pH, hindering transmembrane transport and preventing the accumulation of clinically relevant intracellular concentrations. Its half-life (~30 min) further limits distribution and tissue accumulation; consequently, multiple dosing may be needed to reach the optimal therapeutic effect. In addition, RB forms aggregates in solution, which affects the spectral properties of the dye and causes a decrease in its photodynamic activity, including the ability to generate singlet oxygen and other ROS [212].

To overcome the limitations associated with photo-instability, poor biodistribution, and cellular uptake, the use of the appropriate RB formulation or delivery system may be a promising approach. Clinically used lipidic and organic formulations of PSs may yield unpredictable distribution patterns, allergic reactions, hypersensitivity, and systemic toxicity [259]. To overcome these problems, researchers have turned to the field of nanotechnology, which has the potential to generate nanoscale particles with precisely defined features [210,260]. Here, dendrimers are a class of nanoparticles that has been studied comprehensively both *in vitro* and *in vivo* in the context of anticancer drug delivery [261–263]. These sphere-shaped, water-soluble polymers of symmetrical, well-defined structure protect drugs from degradation, extend their half-life, promote intracellular transport [264], and provide

semi-specific accumulation in tumor regions; the latter phenomenon is referred to as the enhanced permeability and retention (EPR) effect [265].

The three-dimensional architecture and chemical composition of dendrimers offers several options for the attachment of drugs. In particular, therapeutics can be physically entrapped inside the dendritic scaffold or linked by non-covalent interactions or covalent bonds, both on the surface and within the dendrimer structure [266]. In the context of PDT, an additional advantage is that optimized release of PS from the carrier at the target site is not required for the cytotoxic effect, so long as the nanocarrier does not limit the diffusion of molecular oxygen [210]. However, although dendrimer:drug conjugates are generally more stable in solutions and *in vivo*, the use of covalent linkers can drastically alter the photosensitive properties of PS, thus decreasing its phototoxicity [254]. Therefore, numerous studies on the use of nanoparticles, including dendrimers, as RB carriers have focused on non-covalent interactions [212], demonstrating the efficient intracellular uptake and superior photodynamic properties of such formulations [215,267,268]. Because complex formation is usually based on ionic interactions, the process itself, as well as the physicochemical and biological properties of dendrimer:drug complexes, are greatly influenced by pH, ionic strength, buffer composition, and most importantly by the structure of the dendritic carriers [269,270].

In this study, we focused on well-characterized and commercially available cationic poly(amidoamine) (PAMAM) and poly(propyleneimine) (PPI) dendrimers of the 3rd (G3) and 4th (G4) generation. We took a holistic approach, performing an in-depth characterization of dendrimer:RB interactions both *in vitro* and *in silico*, and performed further assessment of the multilevel biophysical and biological activity of the resultant complexes: singlet oxygen generation, cellular uptake, intracellular ROS production, and phototoxicity. To the best of our knowledge, this is the first attempt to compare the ability of cationic dendrimers of different types and generations to serve as carriers for anionic RB, and to link the dendrimer structure to the activity of complexes.

4.3.3 Materials and Methods

The detailed experimental methodology, including the employed materials and reagents, the spectrofluorometric and zeta potential methods, the preparation of the dendrimer:RB complexes, the singlet oxygen and ROS generation assays, the cell culture and cellular uptake methodology, and all the related statistical analyses, are reported in the original publication and in the appendix. The detailed computational

methodology describing the modelling of the complexes using Molecular Mechanics is reported in the following.

Molecular Dynamics Studies

System setup

Initial configurations for PAMAM and PPI dendrimers were built using the Dendrimer Builder Toolkit (DBT) [271] and the General Amber Force Field (GAFF) [272]. The protonation state was chosen based on neutral pH, as reported previously [271,273–275]. Under these conditions, the amine groups in the external layers of PAMAM dendrimers were fully protonated, whereas all the primary amines present at the periphery and the tertiary amines in alternating layers of the PPI dendrimers were protonated, resulting in 2/3 protonation according to the Ising Model [276,277]. The assigned protonation states resulted in a total charge of +32, +64, +42, and +84 for PAMAM G3, PAMAM G4, PPI G3, and PPI G4, respectively. RB was described by the GAFF forcefield, and partial charges were assigned using the AM1-BCC charge method (see also Supplementary Figure S4.22 in the Appendix) [278]. Topology and parametrization were constructed using antechamber and GROMACS tools [279,280].

Single-dendrimer conformational dynamics

Each dendrimer was positioned in a dodecahedral box filled with TIP3P (transferable intermolecular potential 3P) water molecules [281] and ions to neutralize the system charge at a physiological NaCl concentration (0.15 M). Each system was energy-minimized using the steepest descent energy minimization algorithm (2000 steps). After randomly initializing atom velocities following a Maxwell–Boltzmann distribution, a 100 ps position-restrained molecular dynamics (MD) was performed in the canonical ensemble (NVT) at 300 K using the v-rescale algorithm [282] for temperature coupling. Then, an NPT position-restrained MD was executed for 500 ps using the v-rescale thermostat [282] and the Berendsen barostat [283] to equilibrate temperature (300 K) and pressure (1 atm), respectively. Finally, an unrestrained 200 ns MD simulation was performed in the isothermal–isobaric ensemble (NPT) at 300 K and 1 atm using the v-rescale and Parrinello–Rahman coupling algorithms [233,282]. The GROMACS 2020 package was used for all MD simulations [221]. Long-range electrostatic interactions were calculated at every step with the Particle mesh Ewald method [284] with a cutoff radius of 1.2 nm; the same cutoff was also applied to Lennard–Jones interactions. The simulation time step

was 2 fs, using the LINCS (LINear Constraint Solver) algorithm [236]. To ensure the reproducibility of the data, a second replicate was performed after re-initializing velocities after the minimization step and following the same simulation protocol as described above. The final 50 ns of MD simulations were considered as a single ensemble trajectory representing the structural stability of each treated system.

Dendrimer:RB complexation and interaction dynamics

The final configuration from the aforementioned equilibrium ensembles was extracted for each dendrimer type. The structure was again inserted into a dodecahedral box, and 10 RB molecules were added in random positions around the dendrimer to obtain a 1:10 molar concentration ratio. The box was filled with TIP3P water molecules and NaCl at a physiological concentration (0.15 M) to neutralize the system charge. The systems were then simulated using the same simulation protocol described in the previous section. Two replicates were performed to ensure data reproducibility, and the last 50 ns of these MD simulations were considered as a single ensemble trajectory representing the structural stability of each investigated system.

Simulation analysis

As reported previously [271,273,275,285], the geometrical characterization of the investigated dendrimers was evaluated using the radius of gyration (RoG), which measures the size of the dendrimers, and three main geometrical descriptors (Ix/Iy, Ix/Iz and δ) that evaluate the shape of the dendrimers. In more detail, we calculated the three principal momenta of inertia (Ix, Iy, Iz) and derived two aspect ratios (Ix/Iy and Ix/Iz) and asphericity (δ) as defined by Rudnick and Gaspari [286]:

$$\delta = 1 - 3\frac{< I_2 >}{< I_1^2 >} \quad (1)$$

where $I_1 = I_x + I_y + I_z$, $I_2 = I_x I_y + I_y I_z + I_x I_z$, and angle brackets denote time averaging. In this formulation, the closer to zero the value of δ, the more spherical the molecule.

The volumes of dendrimer internal cavities were calculated as described previously [287,288]. First, volumes associated with accessible surface areas (V_{sasa}) were calculated at different probe radii. Then, a linear fitting on the cubic root values of V_{sasa} was performed at different probe radii, starting from 0.4 nm. The

deviation of the calculated volume from the aforementioned fitting line, at a probe radius of 0.3 nm, provides an estimate of the volumes of internal voids. Internal cavities have been evaluated both for the neat dendrimer systems and for the dendrimer:RB complexes. In the latter case, to ensure a consistent comparison, the volumes of dendrimer cavities were evaluated after removing RB molecules from the complex snapshots, thus excluding the volume occupied by RB molecules from the calculations. This ensures that we evaluated the actual structural effects on the dendrimer itself, rather than the volume occupancy of RB.

We also analyzed the dendrimer:RB complexes by comparing electrostatic potentials in the absence and presence of bound RB using the APBS package [289]. Specifically, the nonlinear Poisson–Boltzmann equation was applied using single Debye–Huckel sphere boundary conditions on a 200 × 200 × 200 grid with a spacing of 1 Å centered at the Center of Mass (CoM) of the molecular system. The relative dielectric constants of the solute and the solvent were set to 4 and 78.4 [289,290], respectively. The ionic strength was set to 150 mM, and the temperature was fixed at 300 K.

Visual inspection of simulations and all molecular renderings was carried out with the Visual Molecular Dynamics (VMD) package [223].

4.3.4 Results

In vitro evaluation of dendrimer:RB complexation

To characterize complex formation between the tested dendrimers and RB, we exploited their characteristic properties, i.e., dye fluorescence and the zeta potential of nanoparticles in solution. Spectrofluorometric studies revealed that the addition of dendrimer to RB solution caused a sharp reduction in dye fluorescence. Subsequent titration caused progressive quenching of RB fluorescence until a red shift of the emission wavelength from 564 to 575 nm was observed, with a subsequent increase in the fluorescence signal (Figure 4.6), indicating polarity changes in the vicinity of the chromophore molecule [291]. Based on this phenomenon, the F_{564}/F_{575} ratio was calculated and plotted vs. the RB:dendrimer molar ratio. Using Job's method [292], we approximated the stoichiometry of binding in fully saturated complexes as 1:27 for PPI G3:RB, 1:33 for PPI G4:RB, 1:20 for PAMAM G3:RB, and 1:34 for PAMAM G4:RB (Figure 4.6, insets). This outcome was confirmed by the measurement of changes in the zeta potential of dendrimers

during titration with RB. Upon addition of subsequent portions of RB to the solution, the initial positive zeta potential of the dendrimers began to decrease until it reached a plateau at approximately –30 mV, indicating full saturation of the polymers with PS. Based on the titration curves, we determined the stoichiometry of the formed complexes; the resultant values were similar to those obtained by spectrofluorometric analyses: 1:21 for PPI G3:RB, 1:33 for PPI G4:RB, 1:22 for PAMAM G3:RB, and 1:26 for PAMAM G4:RB (Figure 4.7).

For the following experiments, the 1:10 dendrimer:RB molar ratio was used to ensure the stability of the complex and to maintain its positive surface potential, as positively charged nanoparticles have a greater ability to cross the barrier of biological membranes [293,294].

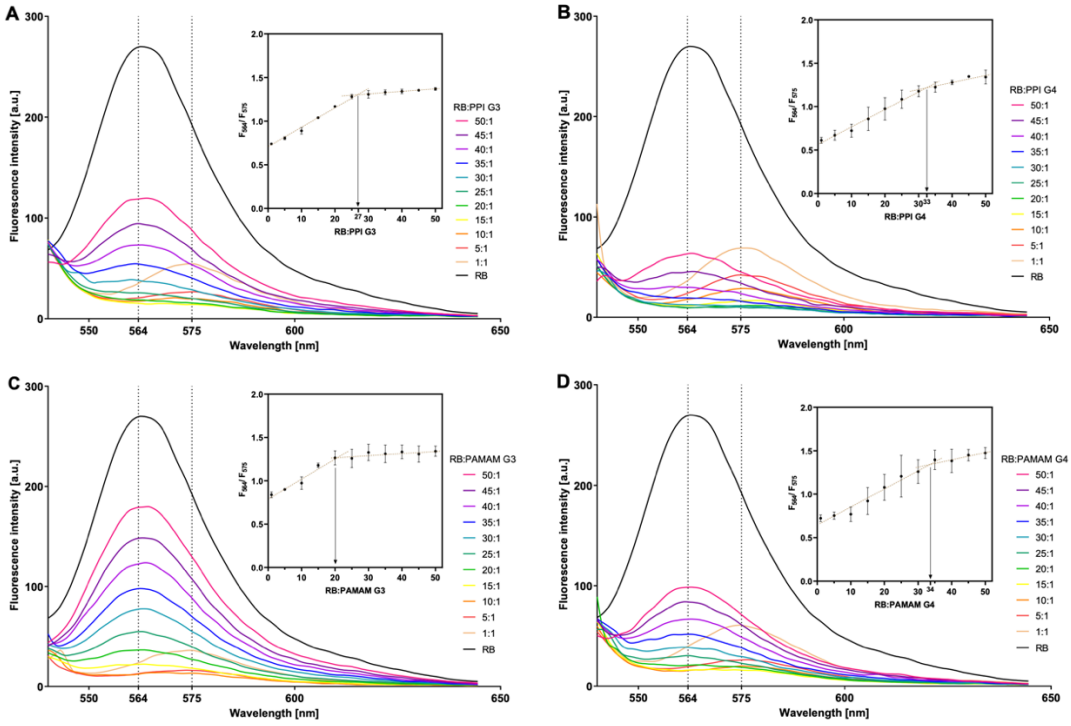

Figure 4.6. Changes in the fluorescence spectrum of RB (1 µM) upon titration with (A) PPI G3, (B) PPI G4, (C) PAMAM G3, (D) PAMAM G4, maintaining a dendrimer:RB molar ratio of 1:50 to 1:1. The insets show the determination of the stoichiometry of complexes fully saturated with RB, using Job's method based on the plots of F564/F575 vs. RB:dendrimer molar ratio. Data are presented as means ± SD; n = 3.

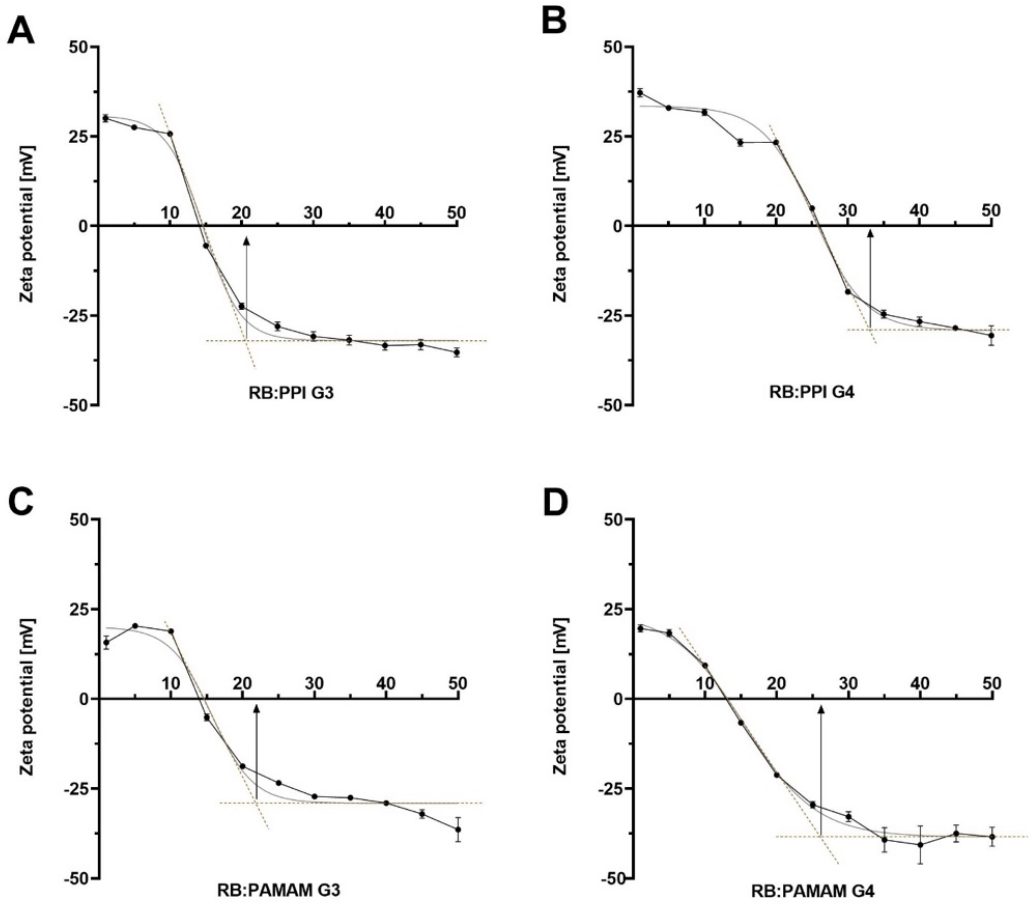

Figure 4.7. Titration curves for the measurements of zeta potential: effects of titration of 10 μM solutions of (A) PPI G3, (B) PPI G4, (C) PAMAM G3, (D) PAMAM G4 dendrimers with RB, maintaining the dendrimer:RB molar ratio of 1:1 to 1:50. Analysis of the course of titration curves allowed us to use Job's method to determine the stoichiometry of complexes fully saturated with RB. Data are presented as means ± SD; n = 3.

In vitro photodynamic and phototoxic properties of RB and dendrimer:RB complexes

Singlet oxygen generation assays using the ABDA probe showed that the tested compounds were able to increase the singlet oxygen levels. At the highest concentration tested, free RB caused a ~3-fold increase in singlet oxygen generation relative to the control, slightly less than for the case of complexes with dendrimers of the 4th generation (~4-fold for PAMAM G4 and ~6-fold for PPI G4). On the other hand, complexes of RB with dendrimers of the 3rd generation caused a greater

increase in the generation of singlet oxygen (~16-fold for PAMAM G3 and ~19-fold for PPI G3), significantly exceeding the effect observed with free PS (Figure 4.8). Free dendrimers did not generate singlet oxygen (data not shown).

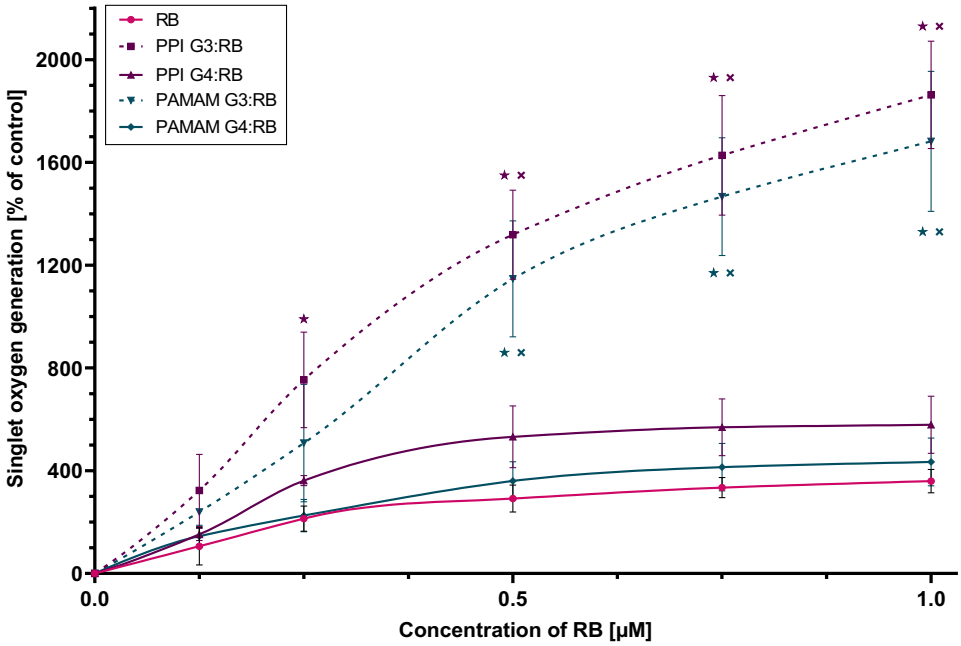

Figure 4.8. Singlet oxygen generation by RB and dendrimer:RB complexes in a 1:10 molar ratio. Singlet oxygen generation assay was performed using the ABDA probe as an indicator. Data are presented as a percentage of the singlet oxygen generation in the control sample containing only ABDA probe, means ± SD, n = 4. *Statistically significant difference vs. free RB ($p < 0.05$). ×Statistically significant difference between generations of dendrimers of the same type ($p < 0.05$).

The cytotoxicity of tested compounds was evaluated in three basal cell carcinoma cell line models, as basal cell carcinoma is the most common form of skin cancer and the most frequently occurring form of cancer overall [295,296]. The complexes revealed higher phototoxicity relative to free RB (Figure 4.9A and Figure S4.10 in the Appendix), and this trend was maintained in all tested cell lines: RB in complex with PPI dendrimers was more toxic than RB in complex with PAMAM dendrimers, regardless of the generation. Cells treated with the free RB solution exhibited the highest viability. We did not observe cytotoxicity of free dendrimers or dark toxicity of RB and dendrimer:RB complexes (data not shown). The cell lines exhibited a range of susceptibilities to all treatments, with AsZ cells being the most susceptible (e.g., PPI:RB complexes in highest RB concentration reduced the viability of AsZ cells to ~ 20%; in the case of BsZ cells, viability was

~30%, and for CsZ cells, ~50% [Figure 4.9A and Appendix Figure S4.10]). Accordingly, we used AsZ for intracellular ROS production and cellular uptake assays.

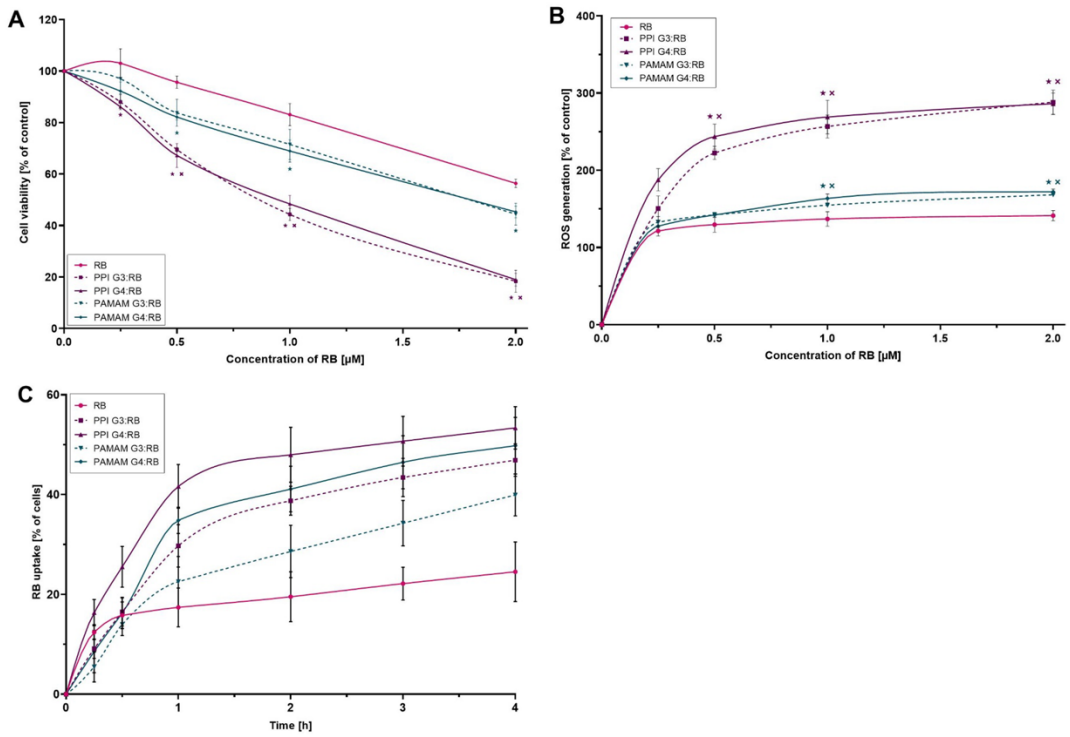

Figure 4.9. (A) Phototoxic effect of RB and dendrimer:RB complexes in 1:10 molar ratio in AsZ cells. Cell viability was determined using MTT assay. Data are presented as percentages of the viability of control (untreated) cells; means ± SD; n = 6. *Statistically significant difference vs. free RB; $p < 0.05$. ×Statistically significant difference vs. dendrimers of different type, regardless of generation; $p < 0.05$. (B) ROS production in AsZ cells triggered by RB and dendrimer:RB complexes in 1:10 molar ratio upon irradiation, determined with the use of 2′,7′ dichlorodihydrofluorescein diacetate (H2DCFDA) probe. Data presented as percentage of intracellular ROS generation in control (untreated) cells; means ± SD; n = 4. *Statistically significant difference vs. free RB; $p < 0.05$. ×Statistically significant difference vs. dendrimers of different type, regardless of generation; $p < 0.05$. (C) Uptake of RB and dendrimer:RB complexes in 1:10 molar ratio by AsZ cells, as determined by flow cytometry assay. Data are presented as percentage of cells in the population exhibiting RB-associated fluorescence; means ± SD; n = 5. For statistical analysis, see Table S1.

The outcome of the intracellular ROS production assay coincided with the results of the cytotoxicity evaluation (Figure 4.9B). The tested compounds induced production of ROS, with PPI:RB complexes exerting the greatest effect. The

activity of the PAMAM:RB complexes was significantly lower but still exceeded the effect observed for free PS. The phenomenon was independent of the generation of dendrimers. Free dendrimers did not generate ROS (data not shown).

Complexation of RB with the tested dendrimers significantly increased the intracellular concentration of PS (Figure 4.9C). The PPI G4 dendrimer turned out to be the most effective carrier, with PAMAM G3 being the least efficient, but even in the latter case, the uptake of RB was almost 2-fold higher than when AsZ cells were treated with free PS. The effects of the PPI G3 and PAMAM G4 dendrimers were similar and intermediate between the PPI G4 and PAMAM G3. Overall, when comparing dendrimers of the same type, 4th generation dendrimers had a greater ability to transport RB intracellularly than 3rd generation dendrimers. When comparing dendrimers of the same generation, PPI dendrimers were more efficient carriers than PAMAM dendrimers.

Molecular modelling

Single-dendrimer conformational dynamics

We assessed the geometrical properties of dendrimers over the last 50 ns of two independent 200 ns MD simulations. The RoG, which represents a reliable metric for assessing the overall size of a dendrimer, and shape descriptors aspect ratio and asphericity (δ), were calculated as described in the Experimental Section. Geometrical properties of the two MD replicas were averaged over the last 50 ns of simulation, with snapshots taken every 2 ps (Table 4.5). The data obtained were in close agreement with *in silico* and experimental data from the previous literature for all the simulated systems (as reported in detail in the Appendix in Table ST4.4), confirming that the dendrimer structures were well equilibrated.

Table 4.5. Radius of gyration (RoG), aspect ratios, and asphericity values for the simulated dendrimers, presented as means ± SD.

	RoG [nm]	**I_x/I_y**	**I_x/I_z**	**δ**
PAMAM G3	1.460 ± 0.058	0.708 ± 0.128	0.581 ± 0.087	0.026 ± 0.012
PAMAM G4	1.859 ± 0.064	0.839 ± 0.086	0.705 ± 0.069	0.012 ± 0.006
PPI G3	1.284 ± 0.024	0.792 ± 0.080	0.685 ± 0.068	0.013 ± 0.006
PPI G4	1.590 ± 0.020	0.826 ± 0.050	0.746 ± 0.042	0.008 ± 0.003

Figure 4.10 shows the probability density function (PDF) of the RoG during the last 50 ns of MD replicas, highlighting the greater flexibility of PAMAM dendrimers relative to PPI dendrimers. Time series of the RoG during the entire simulations are reported in Appendix Figure S4.11.

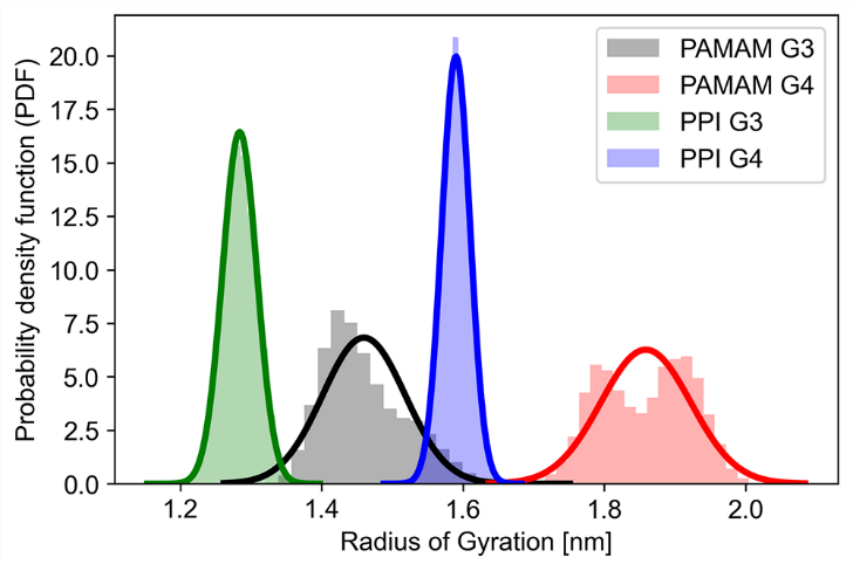

Figure 4.10. Probability density function (PDF) of the radius of gyration during the last 50 ns of two independent MD simulations.

Dendrimer:RB complexation and interaction dynamics

To assess the structural effects of RB on each dendrimer type and analyze the mode of dendrimer:drug interaction, dendrimer structures from the previous equilibration were simulated in the presence of 10 RB molecules (maintaining a 1:10 dendrimer:RB stoichiometry). MD trajectories showed early and stable complexation of all 10 RB molecules after ≤ 16 ns, with no unbinding events observed throughout the 200 ns simulations (see also Appendix Figures S4.12, S4.13, S4.14).

We again assessed the structural effects of RB on the dendrimers again using RoG, aspect ratios, and asphericity measures, but we observed no remarkable effects upon ligand complexation (see Figures S4.15 and S4.16 in the Appendix). Similarly, the particle density of dendrimers with respect to the dendrimer central core was not remarkably altered in the presence of RB molecules (see Appendix Figure S4.17).

The radial distribution function (RDF) of the RB with respect to the dendrimer core (Figure 4.11) revealed that PPI dendrimers had a greater ability to internalize RB molecules. On the other hand, drug molecules were more exposed to the external solvent when bound to PAMAM dendrimers. It is worth mentioning that, despite this difference in ligand internalization, we observed no marked differences in the dendrimer:RB interaction surface among the dendrimers examined (see Appendix Figure S4.18).

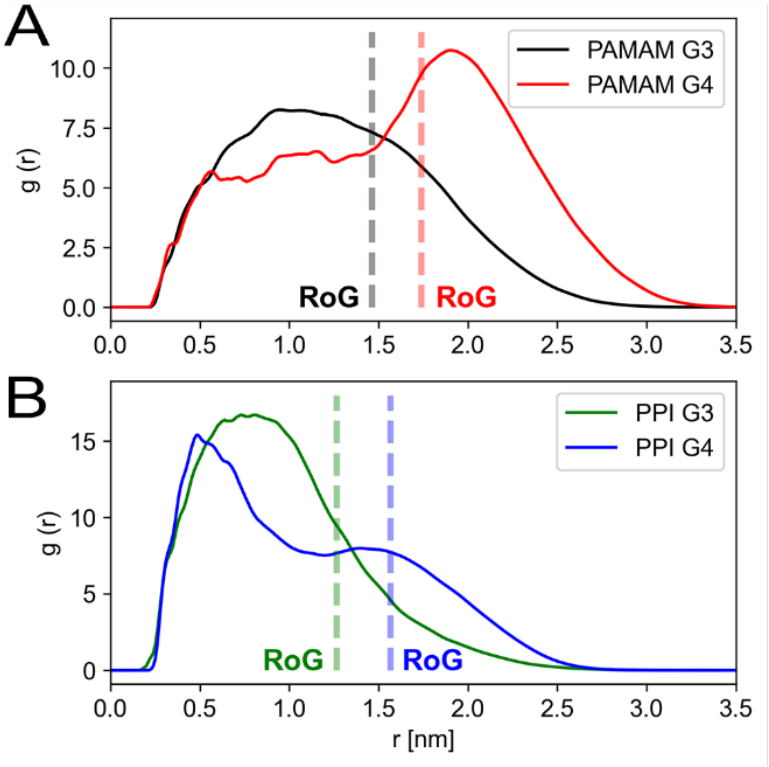

Figure 4.11. Radial distribution function (RDF) of RB with respect to the dendrimer central core for (A) PAMAM and (B) PPI dendrimers; dotted lines represent the radius of gyration for each dendrimer.

The RDFs for the external amino groups, water molecules, chlorine and sodium ions are shown in Figure 4.12, in the presence and absence of RB, to compare the effects of the drug inclusion. The RDF trends of the external amines were unaltered in the presence of the RB for PPI dendrimers, confirming the more rigid behavior of these dendrimers (green and blue lines in Figure 4.12A and Figure 4.12E). On the other hand, the RDF peaks of external amines of PAMAM dendrimers changed markedly upon drug complexation (black and red lines in Figure 4.12A and Figure 4.12E), suggesting a major conformational change in the dendrimer structure. The

reduced values of water molecules RDF in the internal layers are also indicative of the fact that these molecules are forced out by the entrance of RB, especially in the case of PPI dendrimers (Figure 4.12B and Figure 4.12F). Similarly, the presence of RB leads to the ejection of chlorine ions from the internal layers of the dendrimers of the 3rd generation (Figure 4.12C and Figure 4.12G). The positively charged sodium ions on the other hand were not noticeably displaced with respect to the dendrimer core in the presence of RB if compared to the neat systems (Figure 4.12D and Figure 4.12H).

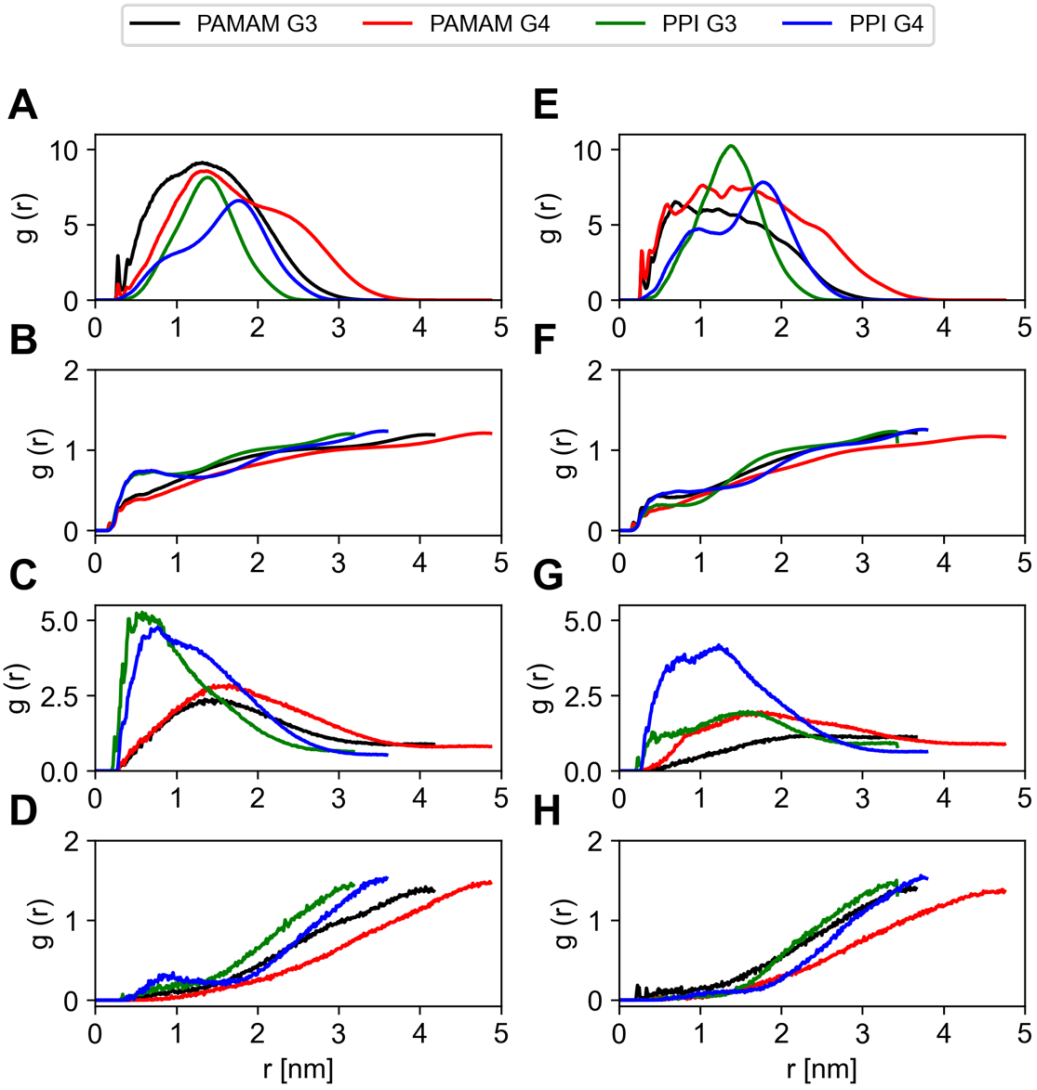

Figure 4.12. Radial Distribution Functions of external amines (A, E), TIP3P water (B, F), chlorine ions (C, G) and sodium ions (D, H) with respect to the dendrimer core from the

concatenated trajectory of the last 50 ns of simulation of two independent MD replicas in the absence (A, B, C, D) and presence (E, F, G, H) of RB.

We further assessed the structural characteristics of both the free dendrimers and their complexes with RB molecules by analyzing hydrogen bonds (H-bonds). As highlighted in Figure 4.13A, PAMAM dendrimers of both G3 and G4 are able to form an intramolecular network of H-bonds, mainly due to the presence of acceptor oxygen atoms within their underlying chemical structure [297]. No intramolecular network of hydrogen bonds was observed for PPI dendrimers. Interestingly, the number of intramolecular H-bonds in PAMAM dendrimers did not seem to be influenced by the presence of RB. H-bonding between dendrimers and the surrounding water was more prominent in PAMAM dendrimers than in PPI dendrimers, with only a marginal decrease caused by RB complexation (Figure 4.13B).

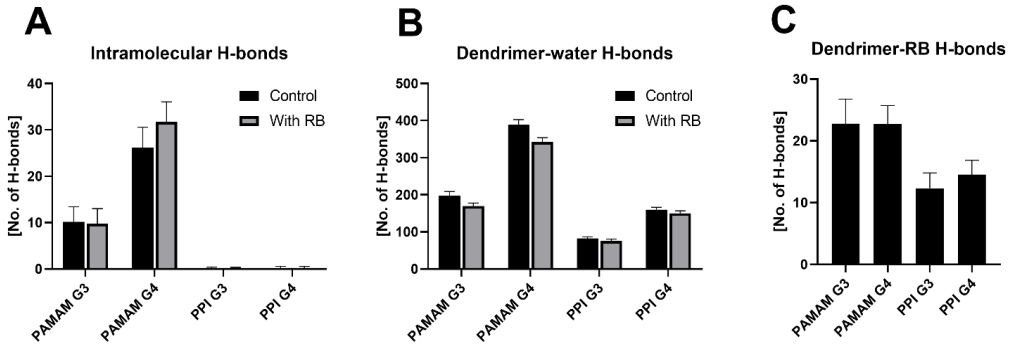

Figure 4.13. (A) Number of internal H-bonds in each dendrimer investigated. (B) Number of H-bonds between dendrimers and surrounding water molecules. (C) Number of H-bonds between dendrimers and RB. Data are presented as means ± SD across the last 50 ns of two 200 ns replicas.

Overall, PPI dendrimers formed fewer H-bonds with the solvent than PAMAM dendrimers, whereas 4th generation dendrimers formed more H-bonds with the solvent, as expected from the increase in the number of surface amino groups. Finally, PAMAM dendrimers formed significantly more H-bonds with RB than PPI dendrimers, with no difference between dendrimer generations (Figure 4.13C). Overall, PAMAM dendrimers formed the largest number of H-bonds internally, with both solvent and with RB molecules.

Void volume analysis revealed that the presence of RB reduces the internal volumes of PAMAM dendrimers, whereas internal cavities of PPI dendrimers were

not altered by the drug (Figure 4.14, see also Figure S4.19 in the Appendix). Specifically, the ratios between the void volumes in the presence and absence of RB were 0.82 for PAMAM G3, 0.77 for PAMAM G4, 0.98 for PPI G3, and 0.97 for PPI G4.

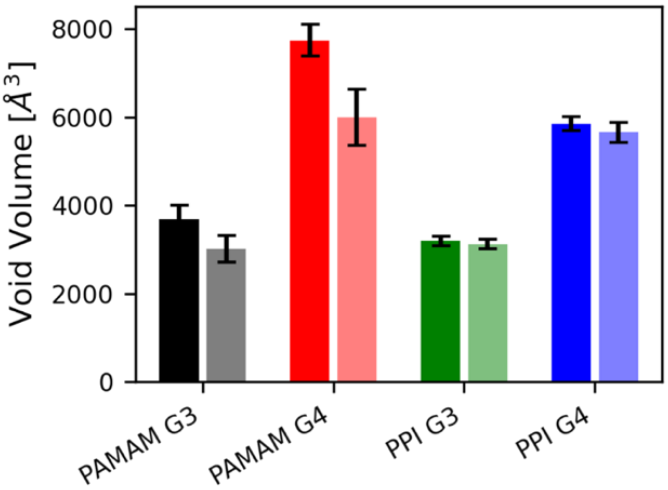

Figure 4.14. Volumes of dendrimers' internal cavities. Solid colors refer to simulations of the free dendrimer systems, whereas shaded colors refer to simulations of the dendrimer:RB complexes.

Finally, we investigated the surface electrostatic potential of the complexes by extracting frames from the dendrimer:RB simulations and evaluating the dendrimer electrostatic potential in the presence of RB (Figure 4.15). We observed predominantly positive potential up to 5 kT/e on the dendrimer surface for all simulated systems; only PAMAM G3 had a prominent number of neutral surface patches (Figure 4.15A), indicating the ability of RB to locally neutralize the surface electrostatic potential of this specific dendrimer more effectively than for other systems. Overall, dendrimers of the 4th generation (Figure 4.15B and Figure 4.15D) were characterized by a more positive surface potential even in the presence of bound RB, whereas 3rd generation dendrimers (Figure 4.15A and Figure 4.15C) had a more neutral surface potential resulting from the shielding effect of bound RB.

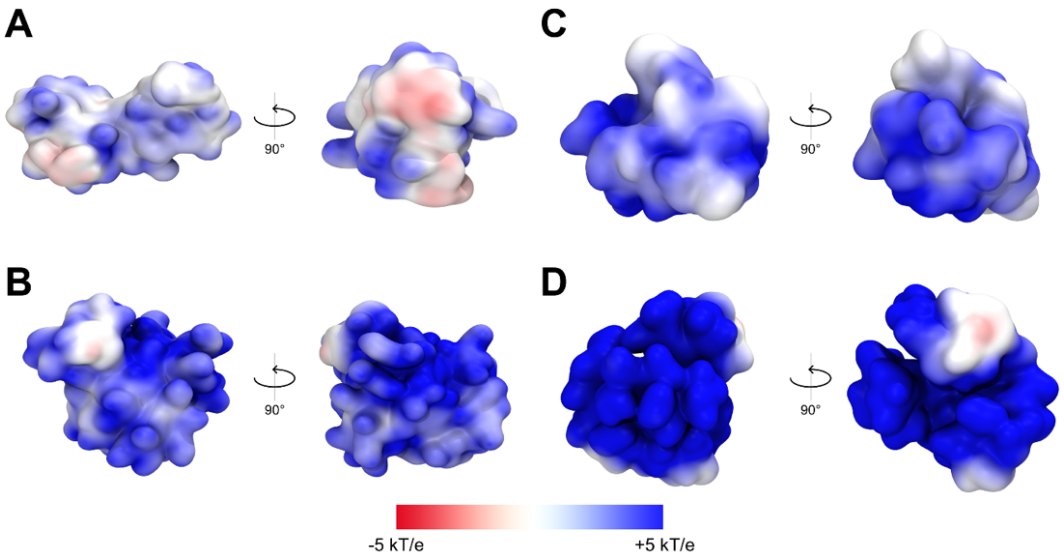

Figure 4.15. Front and side electrostatic maps for dendrimer:RB complexes (1:10): (A) PAMAM G3; (B) PAMAM G4; (C) PPI G3; (D) PPI G4. Potential isocontours (obtained by solution of the NLPBE at 150 mM ionic strength with a solute dielectric of 4 and solvent dielectric of 78.4) in the range from +5 kT/e (blue) to -5 kT/e (red).

4.3.5 Discussion

Photodynamic therapy (PDT), which relies on the use of a PS and a light source to induce singlet oxygen and ROS formation in the presence of molecular oxygen, is a promising therapeutic strategy against basal cell carcinoma. The use of dendrimers as drug carriers has the potential to overcome the known drawbacks of currently investigated PSs, such as self-quenching, short half-life, and suboptimal cellular uptake. In this work, we performed an in-depth characterization of the complexes of cationic poly(amidoamine) (PAMAM) and poly(propyleneimine) (PPI) dendrimer of the 3rd and 4th generation with anionic rose bengal. A combined *in vitro* and *in silico* approach allowed for a complementary characterization of the effects of the dendrimers' physical and chemical properties on their interactions with RB, and ultimately on the phototoxic activity of the latter. Interestingly, most previous research concentrated on RB as a model molecule, which, due to its spectral properties, was used to study interactions with dendrimers (usually PAMAM, less often PPI and other types of macromolecules) [268,298–303]. Significantly fewer studies have analyzed the phototoxic activity of the dendrimer:RB complexes [215,267,268].

The PAMAM and PPI dendrimers used in this study were inspected at atomic resolution at the single-dendrimer level. The analysis of neat dendrimer trajectories yielded geometrical shape descriptors consistent with the existing literature [271,273,275,285,304–316] in terms of RoG, asphericity, and aspect ratios, implying well-converged simulations. Both types of dendrimers are spherical in shape. In general, G3 dendrimers have a smaller radius and smaller internal cavities than G4 macromolecules. When comparing dendrimers of the same generation, PPIs are smaller, more rigid, and more compact than PAMAMs. PAMAM dendrimers form intramolecular H-bonds (more in the case of generation 4), whereas PPI dendrimers do not; moreover, PAMAM dendrimers form more hydrogen bonds with water than PPI dendrimers.

In our initial studies of the formation of dendrimer:RB complexes and the determination of their stoichiometry, we analyzed the changes in the spectral properties of the dye upon complexation. As a result of titration of the RB solution with dendrimers, the fluorescence intensity of RB decreased, followed by a red shift of the maximum spectrum and subsequent increase in fluorescence. A similar red shift of both RB absorbance [301] and fluorescence [302] most often indicates the binding of the dye to the dendrimer surface [291]. We exploited this phenomenon to determine binding stoichiometry. As we expected, G4 dendrimers could bind more RB molecules (approx. 35 per dendrimer molecule) than G3 dendrimers (20–25 RB molecules per dendrimer molecule), likely due to differences in the dendrimers' volume and the level of protonation [276,312,317]. The interactions of RB with the cationic phosphorus dendrimer were analyzed in an analogous manner, but the binding stoichiometry was significantly lower. This is probably due to the use of a different buffer (HEPES vs. PBS), since it has been shown that the buffer composition has a significant influence on the formation of the complex [302,317] Furthermore, stoichiometry was affected by NaCl concentration; consistent with our hypothesis, this indicates the essential role of electrostatic interactions in the formation of complexes between anionic RB and cationic dendrimers [302]. These results were confirmed by Fourier transform infrared spectroscopy (FTIR). Additionally, RB does not form complexes with anionic phosphorus dendrimers [303]. Other research groups also identified electrostatic interactions as the main driving force for the formation of complexes between RB and surface-modified PAMAM and PPI dendrimers [268,301], and also reported a strong influence of the type of solvent on the binding stoichiometry [268].

The determined stoichiometry of the PAMAM:RB and PPI:RB complexes was confirmed by titration of the dendrimer solutions with RB with the accompanying measurement of the zeta potential. The findings roughly coincided with those of the spectrofluorimetric method, with minor variations attributable to differences in the specificities of the two techniques. The results indicated that complexes fully saturated with RB exhibit negative zeta potential values. Assuming a surface binding mechanism, we can conclude that in the final stages of titration, anionic RB molecules completely covered the outer layer of positively charged dendrimers [270]. In light of these observations, in subsequent investigations we set a sub-saturation concentration of RB (namely, 1:10 dendrimer:RB molar ratio), which retained a residual positive surface charge for increased cellular uptake and decreased aggregation of complexes [294].

Our molecular investigation of 1:10 dendrimer:RB complexes was carried out in silico, allowing the characterization of the binding mechanism and its effect on dendrimer geometry. Previous computational investigations of PPI:RB complexes clearly demonstrated the potential of atomistic simulations to complement experimental analyses by elucidating dendrimer:RB interaction dynamics [318]. Herein, we extended the computational approach to substantially longer timescales, as well as to different dendrimer types and generations, and expanded the analysis by including a higher number of ligands as well as by randomizing their initial placement in the solvent. Although these differences hinder a direct comparison of the present and earlier results, the strong complexation of RB with positively charged dendrimers is confirmed. Indeed, MD simulations revealed short complexation times, below 16 ns, and the ability of the investigated dendrimers to carry all 10 RB molecules, with no subsequent unbinding event detected over 200 ns in each MD replica, suggesting binding energies significantly exceeding thermal fluctuation (kT) and a strong tendency of RB to bind to each type of dendrimer. This behavior was primarily driven by electrostatics, consistent with previous observations. Interestingly, despite the predominant role of electrostatic interactions, we also observed formation of H-bonds between dendrimers and RB, more strongly in the case of PAMAM than PPI.

The binding of RB did not significantly affect the geometrical characteristics of the dendrimers, and the estimated dendrimer:RB interaction areas were similar in all investigated systems. The volumes of the internal cavities decreased in the case of PAMAM dendrimers while remaining unchanged for PPI dendrimers. This was also reflected in the arrangement of the surface amino groups, which was

influenced by RB binding only for PAMAM dendrimers. The attachment of RB also caused the displacement of water molecules (more evident in case of PPI dendrimers) and negatively charged chlorine ions (in the case of G3 dendrimers) from the inside of the dendritic scaffolds.

Notably, we found that RB has the ability to penetrate the structure of dendrimers, positioning itself preferentially inside the scaffold rather than on the surface. Comparison of these findings with the previously discussed fluorescence red shift indicates that the dendrimer:RB binding mechanism is more complex than indicated solely by spectrofluorimetric studies. Overall, the *in silico* investigation highlighted the greater ability of PPI dendrimers to internalize RB molecules within the inner dendrimer branches (see RDF data, Figure 4.11B). The size of the dendrimers and the specific arrangement of the RB molecules also influenced the surface potential of the complexes, which was significantly reduced (to values close to neutral) in the case of G3 dendrimers. Given the characteristics of the surface potential, it is plausible that interactions among multiple dendrimers occur in the presence of RB. This idea is consistent with preliminary data concerning interacting systems consisting of two dendrimers and 20 RB molecules, in which G3 complexes exhibited a marked tendency to engage in dendrimer–dendrimer interactions (see Appendix, Figure S4.21). Interestingly, the complexes with PPI G4 also showed a tendency to aggregate during longer measurement times, which was consistent with the results of the analysis of the hydrodynamic diameter of the complexes by dynamic light scattering (DLS) (Table ST4.5, Appendix).

Our approach allowed us to highlight significant differences in complex formation and interaction patterns as a function of dendrimer type and generation. Because the photodynamic properties of RB are determined by several factors, including the chemical environment, it seems reasonable that these observed differences could significantly influence the ultimate cytotoxic effect.

Because the level of singlet oxygen generation is thought to be directly related to the efficacy of photodynamic therapy [319], we assessed the activity of tested compounds in this regard. RB complexes with G3 dendrimers exhibited significantly higher production of singlet oxygen, whereas the effect of G4 dendrimers was only slightly higher than that of free RB. At the same time, free dendrimers did not generate singlet oxygen. A similar effect was previously observed for supramolecular complexes of PSs and various polymers [320], including RB and cationic dendrimers [215]. On the other hand, no increase in singlet oxygen

production was observed in the case of RB complexed with anionic half-generation PAMAM dendrimers [267]; for PEG2000-modified PPI and PAMAM G4 dendrimers, the singlet oxygen level was reduced upon encapsulation of RB. In the latter case, however, the effect was attributed to RB aggregation and quenching due to the high local concentration of PS inside dendrimers (approx. 180 RB molecules per dendrimer) [268]. Such complexes exhibited no increase in phototoxic activity (relative to free RB) in HeLa cells. These observations underlie the influence of both the dendrimer:RB interaction and their molar ratio on the ultimate photodynamic effect.

The increase in singlet oxygen production can be explained by the immobilization of RB by the nanoparticle in more than one dimension, translating into a change in optical properties. Analysis of the Jablonski diagram reveals that excited RB can return to the ground state through photon emission or the transition to the triplet excited state responsible for singlet oxygen generation [254]. Considering the decrease in fluorescence during RB binding by the tested dendrimers, it is likely that in this case the second process is favored [321]. Nanoparticles can affect the fluorescence of the dye in solution in several ways, including the internal fluorescence filter effect, dynamic quenching, static quenching, surface enhancement, and modulation of the quantum yield of the fluorophore. These phenomena are related to the binding-induced conformational changes in the structure of PS [322,323]. Furthermore, the patterns of interaction between the dye, nanoparticle, and solvent can significantly affect aggregation, causing changes in the behavior and properties of PS in the vicinity of different nanoparticles suspended in the same solvent.

Indeed, the effect of dendrimer binding on RB-triggered singlet oxygen generation might be directly linked to the fact that RB tends to aggregate under physiological conditions [324] due to π-stacking, and that PS aggregation has a detrimental effect on singlet oxygen generation due to self-quenching of excited states [325]. Hence, better encapsulation of individual RB molecules by dendrimers would lead to a reduction in RB–RB aggregation and thus of self-quenching, yielding more efficient generation of singlet oxygen.

From this standpoint, the difference in the generation of singlet oxygen by G3 and G4 complexes is worth noting and remains difficult to explain at this stage of our research. The difference may be associated with better prevention of RB aggregation and improved stabilization of the excited state by G3 dendrimers. Further stabilization of the transition state might also be achieved through complex–

complex interactions. In addition, given the observed displacement of anions from inside the G3 dendrimers caused by RB, we can assume that anions play an active thermodynamic role in RB binding; thus the latter might be more favored for G3 than G4 dendrimers. Such a binding strength- and mode-dependent production of singlet oxygen by PSs has already been observed during interactions with DNA [326]. These observations highlight the need for further biophysical analyses, including confirmation using more direct, probe-independent methods of singlet oxygen detection; such techniques are currently under development in our lab.

Surprisingly, the results of the singlet oxygen generation assay were not reflected in our studies of cellular models. In these analyses, we observed the highest phototoxic activity in basal cell carcinoma models using PPI:RB complexes, regardless of generation. A similar lack of dependence on generation was observed in the case of PAMAM:RB complexes, whose cytotoxicity was intermediate between the action of PPI:RB complexes and free RB. It should be emphasized that in the tested concentration range, free dendrimers did not exhibit phototoxicity, and no dark toxicity was observed for any of the compounds examined. Similar results were obtained when analyzing the production of intracellular ROS. Because the cellular factor is the most important difference between the singlet oxygen generation assay and subsequent studies, we hypothesized that the differences observed in cellular models are related to another crucial aspect of RB application: cellular uptake and subcellular localization. Indeed, dendrimer:RB complexes were able to deliver PS intracellularly much more effectively than intracellular transport of free RB [215].

The efficiency of the intracellular transport of complexes perfectly matched the differences in their surface potential, evaluated based on the APBS electrostatic map analysis (Figure 4.15) of dendrimer:RB MD simulations: the PAMAM G3:RB complex with the surface electrostatic potential closest to neutral was the least efficient carrier, whereas the most cationic PPI G4:RB complex had the greatest intracellular transport capacity. These observations are consistent with reports of the efficient crossing of cell membranes by positively charged nanoparticles, and allow us to predict the behavior of complexes depending on their surface potential [293,294,327,328].

The different delivery capacities of the investigated dendrimers may also be related to their chemical composition, as well as mechanical and structural properties. In this regard, PAMAM and PPI dendrimers exhibited differences in

flexibility throughout the MD simulations, with PPIs exhibiting higher rigidity than PAMAMs. This behavior was emphasized by (i) the RDF, which showed that that external amines of PPI dendrimers were not affected by the presence of RB; (ii) the RoG, which indicated that PAMAM dendrimers were more flexible; and (iii) the void volume, which revealed that the volumes of PPI internal cavities were not affected by the inclusion of the drug. Thus, the rigid and compact structure of PPI dendrimers may favor the intracellular delivery of RB.

On its own, more efficient singlet oxygen generation is insufficient to explain the ultimate effects on cell viability, as the efficacy of PDT also depends on cellular uptake and subcellular location of PS [329]. Indeed, because the generation of singlet oxygen outside the cell is unlikely to significantly affect cell viability due to the limited lifespan of singlet oxygen molecules [329], the ability of dendrimers to efficiently cross the cell membrane might be a decisive factor. Therefore, the observed cytotoxic effect, likely related to the production of intracellular ROS, may be the result of an increase in cellular RB uptake and production of singlet oxygen. The latter effect, in turn, may differ significantly between cellular and extracellular systems, due to the difference in light penetration and the changes in properties of the complexes upon transfer from a buffer with a limited composition into culture medium and subsequently into the cell interior.

4.3.6 Conclusions

The joint effects of dendrimer structural and mechanical properties, the tendency of RB to penetrate the dendrimer, and the dendrimer surface electrostatics are crucial factors determining the ability of complexes to induce cell death. Based on our results, we conclude that cationic PAMAM and PPI dendrimers can serve as efficient carriers of RB in photodynamic therapy. Due to their structural properties, the patterns of interaction with RB, and the characteristic features of the dendrimer:RB complexes, PPI dendrimers outperform PAMAM dendrimers, providing the most efficient uptake in the case of PPI G4, and significantly increasing generation of singlet oxygen in the case of PPI G3. Particular attention should be paid to the selection of appropriate drug and dendrimer concentrations, ensuring a uniform distribution of RB within the structure of the dendrimer, thus preventing aggregation of the PS, and allowing the maintenance of a positive surface charge of the delivery system.

4.4 Tailoring tubulin assemblies as GTP-responsive drug delivery nanocapsules[14]

As described in the previous section, the design of *nanoformulations* for drug delivery purposes can greatly benefit from the support given by molecular modelling, provided that atomistic information about the system under investigation is available, which is often the case. Indeed, the simulation of nanoparticle-drug complexes at the atomistic scale, which can realistically reach the microsecond time scale with today's computational resources, can not only allow for the mechanistic understanding of experimental results, but also assist the design of novel and/or improved formulations based on the predicted and desired biophysical characteristics. This approach can be applied not only to organic synthetic nanoparticles, as shown in the previous examples, but also to biomolecules such as proteins, which can be reengineered for the specific purpose of drug delivery. This latter approach, e.g. tailoring the characteristics of selected protein assemblies to optimize payload delivery, bears many benefits. Firstly, the choice of biomolecules instead of synthetic constructs greatly enhances the intrinsic biocompatibility of the delivery platform as opposed to solutions which require ad-hoc shielding solutions to avoid severe adverse effects[330–332]. Also, it allows for the exploitation of the extensive pre-existing experimental and computational knowledge regarding proteins and protein-ligand interactions. This aspect is particularly relevant from a molecular modelling perspective, since many validated strategies are available to construct reliable computational models of proteins and small molecules which are able to accurately capture their underlying interactions and dynamics. Lastly, specific protein systems can be highly selective towards specific targets and/or environments without the need of complex additional functionalizations. One example is tubulin, a highly abundant cytoskeleton protein whose polymerization and depolymerization dynamics selectively respond to the presence of Guanosine Triphosphate (GTP) and its hydrolyzation into Guanosine Diphosphate (GDP), making it a potential candidate building block for custom, GTP-responsive delivery constructs.

[14] Part of the work described in this paragraph has been published in:

Uchida, Noriyuki, et al. "Reconstitution of microtubule into GTP-responsive nanocapsules." Nature Communications 13.1 (2022): 5424.

Contribution of the author: creation of computational models and simulations of tubulin sheets and molecular glues, data analysis and interpretation.

In the research described in this section, we explored the assembly of custom tubulin constructs into selective drug carriers against cancer and RNA-virus-induced disease.

4.4.1 Abstract

Nanocapsules that collapse in response to guanosine triphosphate (GTP) have the potential as drug carriers for efficiently curing diseases caused by cancer and RNA viruses because GTP is present at high levels in such diseased cells and tissues. However, known GTP-responsive carriers also respond to adenosine triphosphate (ATP), which is abundant in normal cells as well. Here, we report the elaborate reconstitution of microtubule into a nanocapsule that selectively responds to GTP. When the tubulin monomer from microtubules is incubated at 37°C with a mixture of GTP (17mol%) and non-hydrolysable GTP* (83 mol%), a tubulin nanosheet forms. Upon addition of photoreactive molecular glue to the resulting dispersion, the nanosheet is transformed into a nanocapsule. Cell death results when a doxorubicin-containing nanocapsule, after being photochemically crosslinked for properly stabilizing its shell, is taken up into cancer cells that overexpress GTP.

4.4.2 Introduction

An ideal nanocarrier for drug delivery would be the one that can selectively collapse to release preloaded drugs in response to endogenous reporters overexpressed in disease tissues[333–341]. Since adenosine triphosphate (ATP) is known to be present at high levels in cancer tissues[342], ATP-responsive nanocarriers might be a promising candidate[335–339]. In 2013, using partially modified biomolecular machine chaperonin GroEL as a monomer, we succeeded in developing a one-dimensional supramolecular polymer that can be depolymerized by the action of ATP to release its cargo[335]. However, ATP is also present in normal cells at rather high concentrations (>1 mM)[343], and thus disease- selective drug delivery using ATP as the endogenous reporter cannot always be ensured.

In the present work, we developed a nanocarrier ($^{CL}NC_{GTP/GTP*}$; Figure 4.16e) that selectively responds to guanosine triphosphate (GTP). GTP is an intracellular molecule involved in many essential biological processes[344–357], such as cell division, nucleotide synthesis, and cell signaling. In the cell division process, the tubulin heterodimer (THD), which constitutes microtubules (MTs), uses GTP as an energy source to induce its polymerization and depolymerization[347–352]. GTP is also

used as a component for the self-replication of RNA viruses[358–361] such as coronaviruses. Notably, GTP is abundant in certain diseased cells (1.5–4.5 mM)[362] such as rapidly proliferating cancer cells[363] and RNA virus-infected cells[364], whereas the concentration of GTP, unlike that of ATP, is negligibly low in normal cells (<0.3 mM)[365]. Therefore, GTP-responsive nanocarriers have the great potential to efficiently cure cancer and RNA virus-induced diseases including coronavirus disease 2019 (COVID-19)[361]. Although GTP-responsive carriers have already been reported, those carriers also respond to ATP[337]. So far, nanocarriers capable of responding solely to GTP have never been reported.

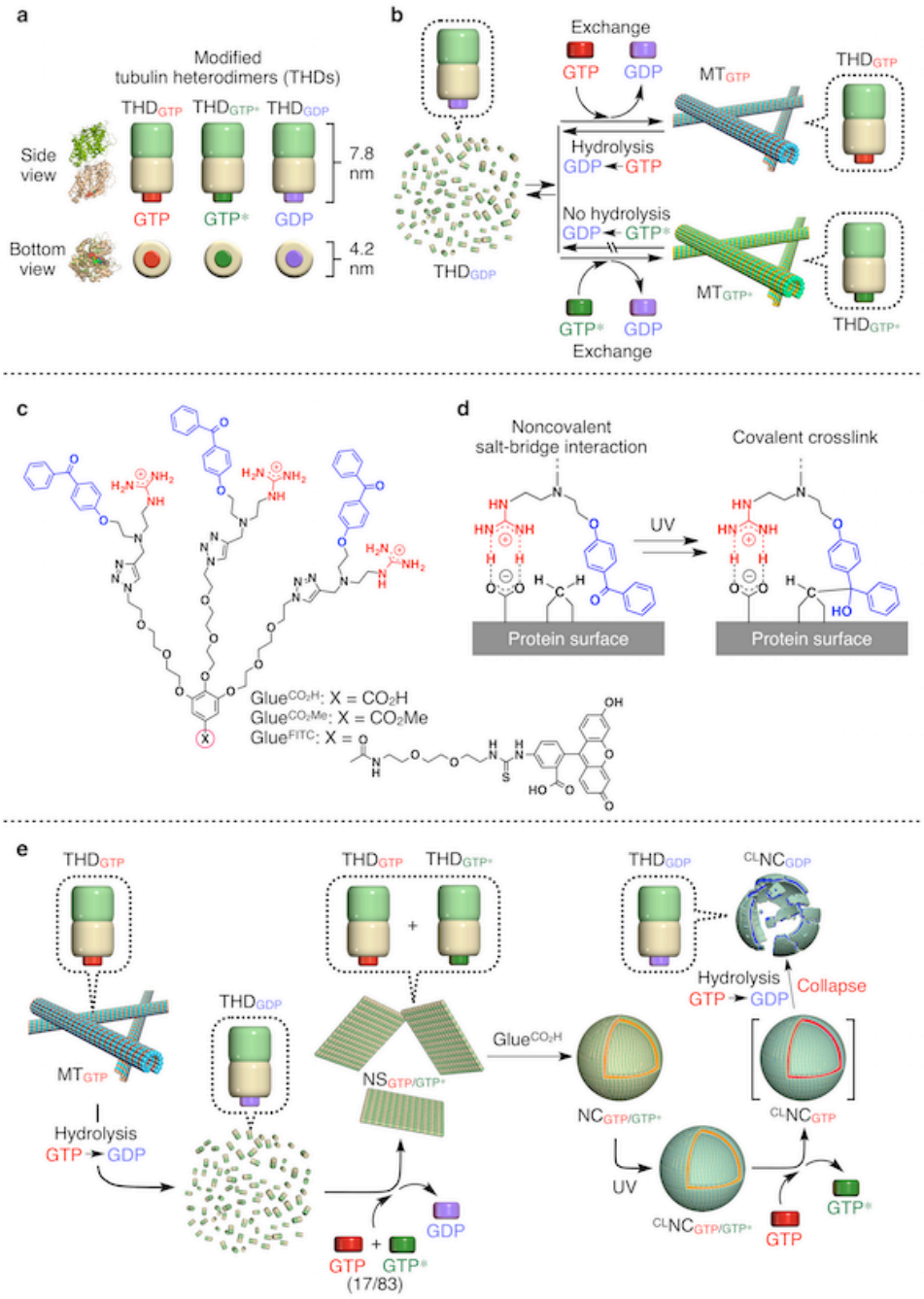

Figure 4.16. Strategy used to prepare THD-based GTP-responsive $^{CL}NC_{GTP/GTP*}$. a Schematic illustrations of tubulin heterodimers (THDs) hybridized with GTP (THD_{GTP}), its nonhydrolysable analogue GTP* (THD_{GTP*}), and GDP (THD_{GDP}) at its β-tubulin unit. b Schematic illustration of two self-assembling modes of THD into microtubules (MTs). MT_{GTP} depolymerizes into THD_{GDP} upon GTP hydrolysis. THD_{GDP} rehybridizes with GTP after a GTP treatment, facilitating the formation of MT_{GTP}. In contrast, MT_{GTP*} does not

undergo depolymerization. c Molecular structures of photoreactive molecular glues ($Glue^{CO2-}$, $Glue^{CO2-Me}$, and $Glue^{FITC}$) bearing three guanidinium ions (Gu^+) and benzophenone (BP) groups at their periphery and CO_2-, CO_2Me, and FITC groups at the focal core. d The molecular glue covalently binds to the protein surface at its photoexcited BP groups after the noncovalent adhesion via a Gu^+/oxyanion multivalent salt-bridge interaction. e Schematic illustration of the multistep procedure for the synthesis of crosslinked nanocapsules ($^{CL}NC_{GTP/GTP*}$) from MT_{GTP}. MT_{GTP} is depolymerized into THD_{GDP}, which is incubated with a mixture of GTP* (83 mol%) and GTP (17 mol%) to form nanosheet $NS_{GTP/GTP*}$. Upon treatment with $Glue^{CO2-}$, $NS_{GTP/GTP*}$ is transformed into spherical nanocapsules ($NC_{GTP/GTP*}$), which are further exposed to UV light, affording $^{CL}NC_{GTP/GTP*}$. Upon addition of GTP, $^{CL}NC_{GTP/GTP*}$ collapses through the conformational change of the THD units induced by GTP hydrolysis.

The nanocapsule (NC) that selectively responds to GTP to release a preloaded drug consists of THD. As shown in Figure 4.16a, THD is composed of α-tubulin (green) and β-tubulin (cream), both of which bind to GTP. Notably, GTP attached to the α-tubulin unit is neither hydrolysable into GDP nor replaceable with other nucleoside phosphates. In contrast, GTP attached to the β-tubulin unit is known to be hydrolysable to GDP, which can be replaced with, e.g., GTP*, a nonhydrolysable GTP analogue (guanylyl 5'-α,β-methylenediphosphonate), affording THD_{GTP*} (for convenience, only variable nucleoside phosphates attached to the β-tubulin unit are shown as a subscript). Both THD_{GTP} and THD_{GTP*}, when heated at 37 °C, have been reported to self-assemble into microtubules MT_{GTP} and MT_{GTP*}, respectively (Figure 4.16b)[366,367]. Although MT_{GTP} depolymerizes into THD_{GDP} synchronously with the hydrolysis of hybridized GTP to GDP, MT_{GTP*} does not depolymerize into THD_{GDP*} because of the non-hydrolysable nature of GTP*. Therefore, our original motivation was to tackle a challenge of modulating the stability of MTs against depolymerization by changing the THD_{GTP}/THD_{GTP*} molar ratio. However, we unexpectedly found that the coassembly of THD_{GTP} and THD_{GTP*} at a certain mixing molar ratio resulted in the formation of a leaf-like 2D nanosheet (NS) rather than MT (Figure 4.16e). Because of the increasing importance of 2D objects[368,369], this finding prompted us to functionalize NS using the molecular glue technology[370–372], which we developed for noncovalently functionalizing biomolecules such as proteins, nucleic acids, and phospholipid membranes, and also inorganic materials. Molecular glues are designed to carry multiple guanidinium ion (Gu^+) groups and strongly adhere to such biomolecules under physiological conditions by taking advantage of a multivalent salt-bridge interaction with their oxyanionic functionalities (Figure 4.16d). For this purpose, we chose $Glue^{CO2-}$ (Figure 4.16c) and incubated it with NS. To our surprise, NS was transformed into a spherical nanocapsule NC (Figure 4.16e). Using its

photochemically modified version ($^{CL}NC_{GTP/GTP*}$; Figure 4.16e), we successfully encapsulated and delivered doxorubicin (DOX)[373], an anticancer drug, into GTP-overexpressing cancer cells to cause cell death.

4.4.3 Materials and Methods

All-atom molecular dynamics (MD) simulations were performed using AmberTools20[118] to create the molecular systems and the GROMACS 2020.5 package[106] to carry out the simulations, as described in greater detail below. The Visual Molecular Dynamics (VMD) package[105] was used to create all MD-related visualizations and images.

Folding of GlueCO2– in aqueous solution

An atomistic molecular model of $Glue^{CO2-}$ was created and parameterized according to the general AMBER force field (GAFF)[272]. As a first step, one $Glue^{CO2-}$ molecule was placed in the center of a periodic simulation box filled with explicit TIP3P water molecules[281]. Neutralizing chloride (3) and sodium (1) counter ions were added to neutralize the system and to reach 0.15 M of ionic strength. After preliminary minimization, the system was initially heated to 37 °C via 1 ns of MD simulation conducted in NVT (constant N: number of atoms, V: volume, T: temperature) conditions. Then, $Glue^{CO2-}$ was equilibrated for 200 ns of MD simulations under constant NPT (N: number of atoms, P: pressure, T: temperature) periodic boundary conditions at 37 °C and 1 atm using a 2 fs time step and a 1.2 nm cut-off.

Arrangements of $Glue^{CO2-}$ and THD_{GTP*}:

The $[THD_{GTP*}]_3$ system was obtained from a full MT model built using the Protein Data Bank (PDB) structure for THD_{GTP*} (PDB code: 3J6E)[91]. Missing residues in the THD_{GTP*} structure were compensated from another THD structure (PDB code: 1TUB)[18]. In the $[THD_{GTP*}]_3$ system, 30 equivalents of pre-equilibrated (folded) $Glue^{CO2-}$ molecules were placed randomly in a periodic simulation boxes. As a control, the $[THD_{GTP*}]_3$ system without $Glue^{CO2-}$ was also simulated. All MD simulations have been conducted in explicit TIP3P water molecules and in the presence of the necessary number of counterions to neutralize the systems.

Adhesions of Glue^{CO2-} on THD$_{GTP*}$:

After preliminary minimization, all systems were first heated during two short MD runs under NVT (1 ns) and NPT (1 ns) periodic boundary conditions, during which the atoms of the THD$_{GTP*}$ were restrained (position restraint of 1000 kJ/mol/nm^2). During these phases, the system reached the simulation temperature of 37 °C, and the solvent density inside the simulation box was preadjusted. After this preliminary equilibration, each system underwent a short MD simulation (20 ns) under NVT conditions at 37 °C while the THD$_{GTP*}$ was maintained at a fixed position to allow Glue^{CO2-} to approach the THD$_{GTP*}$ surface. Then, all restraints were removed, and all systems underwent 200 ns of MD simulation under NPT periodic boundary conditions at 37 °C and 1 atm. The AMBER99-ILDN force field was used to treat the protein topology[107]. A cut-off of 1.2 for both electrostatic and van der Waals interactions was used in the MD simulations. The Particle-Mesh Ewald method was applied to treat with a 1.2 nm cut-off for the Lennard-Jones interactions[284]. A v-rescale thermostat[282] with a coupling time step of 0.1 ps and Parrinello-Rahman barostat[112] with a reference pressure of 1 atm and coupling time step of 5.0 ps were used during the MD runs. The effects of Glue^{CO2-} on the hydrophobicity and total solvent-accessible surface area of the THD$_{GTP*}$ surface were calculated with the GROMACS *gmx sasa* tool. Electrostatic potentials of the THD$_{GTP*}$ surface depending on the binding Glue$_{CO2-}$ were studied using the Adaptive Poisson-Boltzmann Solver (APBS) software package[374]. All data have been extracted from the equilibrated phase MD trajectories.

Interactions of Glue^{CO2-}:

To quantify the strength of the interactions of Glue^{CO2-}, the radial distribution functions g(r) between key groups in the glues and in the tubulins were extracted from the MD trajectories. High and sharp peaks at short distances in g(r) identify a high relative probability to find groups close to each other during the MD. This identifies the presence of strong and persistent interactions between groups, while no evident peaks and g(r) values <1 typically indicate no, or negligible, interactions. To assess the glue-tubulin interactions, g(r) curves were calculated between (i) the Gu$^+$ groups of Glue^{CO2-} and the anionic amino acids (aspartic acid and glutamic acid) of THD$_{GTP*}$, (ii) the Gu$^+$ groups of Glue^{CO2-} and the OH groups of neutral amino acids (serine, threonine, and tyrosine) of THD$_{GTP*}$, and (iii) the CO_2^- groups of Glue^{CO2-} and the cationic amino acids (lysine and arginine) of THD$_{GTP*}$. In addition, the g(r) were calculated to investigate the nature of Glue^{CO2-}-to-Glue^{CO2-}

interactions. To this end, we estimated the g(r) for CO_2^- vs. Gu^+ groups belonging to different $Glue^{CO2-}$ molecules in the simulated systems. Complete modeling data, structures and parameters used for, and extracted from simulations are available at https://zenodo.org/record/7070651#.Yx80t9JBxkg.

Reconstitution of MT_{GTP} into $^{CL}NC_{GTP/GTP*}$

THD_{GTP} was obtained by purification from porcine brain[375] by two cycles of polymerization and depolymerization in PIPES buffer (100 mM PIPES, 2 mM MgSO4, 0.5 mM GTP, 4 μg ml^{-1} leupeptin, and 0.4 mM PefaBlock, pH 6.8). A solution of THD_{GTP} (5.8 mg ml^{-1}) in PIPES buffer (100 mM PIPES, 5 mM $MgCl_2$, 2 mM $MgSO_4$, 1.5 mM GTP, and 10% DMSO, pH 6.8) was incubated at 37 °C for 30 min to afford MT_{GTP}. The reaction mixture was centrifuged at 17,900 × g for 20 min at 24 °C. The resulting precipitate was dissolved in PIPES buffer (100 mM PIPES, 100 μM $MgCl_2$, and 20 μM GDP, pH 6.8) and incubated at 4 °C for 3 h to afford THD[376]. Subsequently, THD (0.3 mg ml^{-1}) thus obtained was incubated in PIPES buffer (100 mM PIPES, 1 mM $MgCl_2$, 250 μM GTP*, and 50 μM GTP, pH 6.8) at 4 °C for 60 min and then at 37 °C for 30 min to afford $NS_{GTP/GTP*}$. $NS_{GTP/GTP*}$ (13 μg ml^{-1}) was incubated in a solution of $Glue^{CO2-}$ (100 μM) in PIPES buffer (14 mM PIPES, 1 mM $MgCl_2$, and 200 μM GTP*, pH 6.8) at 37 °C for 30 min. The reaction mixture was exposed to UV light at 300 nm for 2 min, affording $^{CL}NC_{GTP/GTP*}$. FITC-labeled $NS_{GTP/GTP*}$ and $^{CL}NC_{GTP/GTP*}$ were prepared using FITC-labeled THD_{GDP} (14% labeling rate)[375] under conditions that were otherwise identical to those listed above. Prior to the NMR measurement of the $NS_{GTP/GTP*}$ sample, unbound GTP and GTP* were removed by centrifugation (286,000 × g) of the reaction mixture at 37 °C for 60 min. Zeta potentials of $NS_{GTP/GTP*}$ (1.3 μg ml–1) and $NC_{GTP/GTP*}$ (1.3 μg ml^{-1}) were measured at 37 °C in PIPES buffer.

GTP-responsiveness of $^{CL}NC_{GTP/GTP*}$

A solution of $^{CL}NC_{GTP/GTP*}$ (12 μg ml^{-1}) in PIPES buffer (9 mM PIPES, 0.9 mM $MgCl_2$, and 180 μM GTP*, pH 6.8) was incubated in the presence of GTP (0.1 mM, 0.2 mM, 0.5 mM, and 1 mM), ATP (0.5 mM), CTP (0.5 mM), and UTP (0.5 mM) at 37 °C for 100 min. For the evaluation of the GTP hydrolysis activities of $^{CL}NC_{GTP/GTP*}$ (12 μg ml^{-1}) and THD_{GDP} (12 μg ml^{-1}), Biomol Green™ reagent (100 μl) was added to the reaction mixtures, incubated for 30 min at room temperature and subjected to electronic absorption spectroscopy at 620 nm.

Preparation of $^{CL}NC_{GTP/GTP*}\supset NP_{Au}$

$^{CL}NC_{GTP/GTP*}\supset NP_{Au}$ was prepared after the incubation of a mixture of $NS_{GTP/GTP*}$ (13 μg ml^{-1}), $Glue^{CO2-}$ (100 μM), and gold nanoparticles (NP_{Au}; 14 pM) in PIPES buffer (14 mM PIPES, 1 mM $MgCl_2$, and 200 μM GTP*, pH 6.8) at 37 °C for 30 min, followed by UV irradiation at 300 nm for 2 min. For the asymmetric field flow fractionation analysis, a sample solution of $^{CL}NC_{GTP/GTP*}\supset NP_{Au}$ in PIPES buffer was subjected to ultra-filtration (1500 × g) for 5 min using a regenerated cellulose membrane (cutoff MW = 5000) prior to analysis. PEG-coated NP_{Au} was used to avoid nonspecific adhesion of THD[377].

GTP-triggered release of DOX from $^{CL}NC_{GTP/GTP*}$

$^{CL}NC_{GTP/GTP*}\supset DOX$ was prepared after the incubation of a mixture of $NS_{GTP/GTP*}$ (13 μg ml^{-1}), $Glue^{CO2-}$ (100 μM), and DOX (10 μM) in PIPES buffer (14 mM PIPES, 1 mM $MgCl_2$, and 400 μM GTP*, pH 6.8) at 37 °C for 30 min, followed by UV irradiation at 300 nm for 2 min. The reaction mixture was incubated with GTP (1 mM) at 37 °C for 100 min and then subjected to ultrafiltration (2400 × g) using a regenerated cellulose membrane (cutoff MW = 5000) for 10 min. The resulting residue was subjected to fluorescence spectroscopy (λ_{ext} = 470 nm). A reference sample without GTP was likewise prepared.

Intracellular delivery

Hep3B cells (3.0 × 103 cells/well) plated onto an 8-well chambered cover glass were incubated in EMEM containing 10% FBS at 37 °C with 5% CO_2 for 24 h. The cell samples were rinsed twice with D-PBS prior to use. Typically, the cells were treated with FITC-labeled $^{CL}NC_{GTP/GTP*}$ (0.5 μg ml–1) and incubated at 37 °C with 5% CO_2 for 2.5 h. Then, the cells were rinsed twice with D-PBS and further incubated at 37 °C for 1.5 h (4-h incubation in total) or 21.5 h (24-h incubation in total) with 5% CO_2 in EMEM containing 10% FBS. Analogous cell samples treated with FITC-labeled THD_{GDP} (0.5 μg ml^{-1}), FITC-labeled $NS_{GTP/GTP*}$ (0.5 μg ml^{-1}), $^{CL}NC_{GTP/GTP*}$ (0.5 μg ml^{-1}) with NaN_3 (5 mM)[378], $^{CL}NC_{GTP/GTP*}\supset DOX$ ($[^{CL}NC^{GTP/GTP*}]$= 2.6 μg ml^{-1}, [DOX] = 2 μM), $^{CL}NC_{GTP/GTP*}$ (2.6 μg ml^{-1}), and DOX (2 μM) were likewise prepared. For a cell viability assay using $^{CL}NC^{GTP/GTP*}\supset DOX$, $^{CL}NC_{GTP/GTP*}$, and DOX, the cell samples were incubated with Cell Counting Kit-8 reagents (10 μl) for 30 min, and subjected to electronic

absorption spectroscopy at 450 nm. Hep3B cell samples treated with Tween 20 (0.2%) were used as a positive control.

Statistics and reproducibility

All experiments including the preparation of $^{CL}NC_{GTP/GTP*}$, the investigation of its GTP-responsive collapse, and the intracellular delivery using $^{CL}NC_{GTP/GTP*}$ were performed at least three times to check the reproducibility.

Further details of the experimental methodologies are reported in the Appendix section 4.4.1.

4.4.4 Results

Reconstitution of MT_{GTP} into $NC_{GTP/GTP*}$

Figure 4.16e illustrates the overall procedure for the synthesis of $NC_{GTP/GTP*}$ from microtubule MT_{GTP}. As a typical example of the procedure depicted in the flow chart in Figure 4.17a, a 1,4-piperazinediethanesulfonic acid (PIPES) buffer (pH 6.8) solution of MT_{GTP} (5.8 mg ml^{-1}, Figure 4.17c) was cooled at 4 °C, whereupon MT_{GTP} underwent complete depolymerization within 3 h to yield THD_{GDP} quantitatively (Figure 4.17d)[379]. As observed by dynamic light scattering (DLS), the characteristic polydisperse feature of one-dimensional (1D) MT_{GTP} (Figure 4.17b, gray) changed to a monodisperse feature with a reduced hydrodynamic diameter of 8 nm (Figure 4.17b, blue). Then, THD_{GDP} (0.3 mg ml^{-1}) was immersed in a PIPES buffer solution of a mixture of GTP and GTP* (300 μM in total) with a GTP* content of 83 mol% at 37 °C for 30 min. Under the present conditions, THD_{GDP} was converted via the exchange events of GDP → GTP and GDP → GTP* into a mixture of THD_{GTP} and THD_{GTP*}, which then spontaneously coassembled into $NS_{GTP/GTP*}$ (Figure 4.17e). The small-angle X-ray scattering (SAXS) profile of $NS_{GTP/GTP*}$ showed that its scattering intensity was proportional to q^{-2} in a small q region, which is characteristic of two-dimensional (2D) structures (Appendix, Supplementary Fig. S4.36). As determined by atomic force microscopy (AFM), the average thickness of leaf-like $NS_{GTP/GTP*}$ was 5 nm (Figure 4.17f). Here, the content of GTP* in the mixture of GTP and GTP* employed for the assembly of THD_{GDP} was critical for its successful transformation into $NS_{GTP/GTP*}$. When the content of GTP* ranged from 85–100 mol%, THD preferentially assembled into MT rather than NS (Appendix, Supplementary Fig. S4.37), whereas THD barely assembled when its GTP* content was in the range of 0–70 mol% (Appendix, Supplementary

Fig. S4.38). Namely, the optimum THD_{GTP}/ THD_{GTP*} molar ratio for the coassembly into NS is narrow, roughly with a GTP* content of 70–85 mol%. By means of nuclear magnetic resonance (NMR) spectroscopy in DMSO, $NS_{GTP/GTP*}$ prepared at a GTP* content of 83 mol% was found to contain 65 mol% of THD_{GTP*} (Appendix, Supplementary Fig. S4.39). It is known that MT_{GTP} and MT_{GTP*}, prepared from THD_{GTP} and THD_{GTP*}, respectively, are formed by edge-closing of NS_{GTP} and NS_{GTP*} as transient precursors[376]. Note that the longer axis of THD_{GTP} is shorter than that of THD[380]. We suppose that this mismatch possibly affords unfolded $NS_{GTP/GTP*}$ rather than folded $MT_{GTP/GTP*}$. Indeed, when THD_{GTP*} (GTP* content of 83 mol%) was coassembled with $THD_{GTP\gamma S}$ (THD hybridized with guanosine 5'-O-(3-thiotriphosphate), GTPγS), whose length is likewise shorter than THD_{GTP}[380], $NS_{GTP\gamma S}$ was formed (Appendix, Supplementary Fig. S4.40), whereas the coassembly of THD_{GTP} and $THD_{GTP\gamma S}$ (GTPγS content of 83 mol%), whose longer axes are close in length to each other[380], resulted in $MT_{GTP/GTP\gamma S}$ (Appendix, Supplementary Fig. S4.41). $NS_{GTP/GTP*}$ was transformed into $NC_{GTP/GTP*}$ when it was incubated with $Glue^{CO-}$ (100 μM) in PIPES buffer at 37 °C for 30 min (Figure 4.16e). This anomalous transformation was accompanied by a large change in the hydrodynamic diameter from 65 nm (Figure 4.17b, green) to 660 nm (Figure 4.17b, orange) with a slight increase in the zeta potential from –42.2 to –39.0 mV. Transmission electron microscopy (TEM) showed that the newly formed object $NC_{GTP/GTP*}$ was a hollow sphere (Figure 4.17g). When MT_{GTP*} and THD_{GDP} instead of $NS_{GTP/GTP*}$ were likewise treated with $Glue^{CO2-}$, ill-defined agglomerates resulted (see Appendix, Supplementary Figs. S4.42 and S4.43).

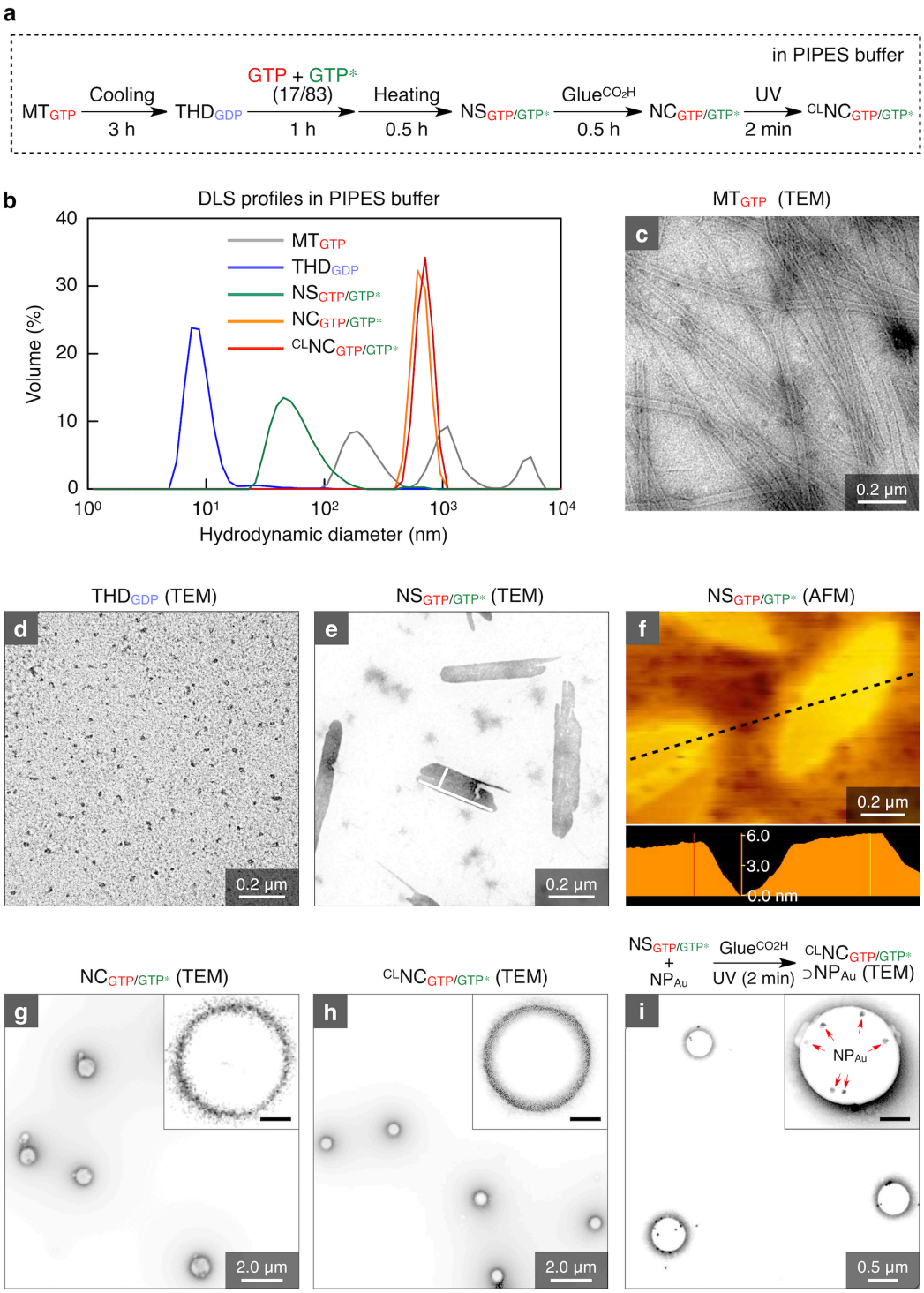

Figure 4.17. Reconstitution of MT into $^{CL}NC_{GTP/GTP*}$.a A typical synthetic procedure for the preparation of $^{CL}NC_{GTP/GTP*}$. b DLS profiles of MT_{GTP} (gray), THD_{GDP} (blue), $NS_{GTP/GTP*}$

(green), $NC_{GTP/GTP*}$ (orange), and $^{CL}NC_{GTP/GTP*}$ (red) in PIPES buffer. c–e TEM images of MT_{GTP} (5.8 mg ml^{-1}; c), THD_{GDP} (0.3 mg ml^{-1}; d), and $NS_{GTP/GTP*}$ (0.3 mg ml^{-1}; e). f AFM image of $NS_{GTP/GTP*}$ (0.3 mg ml^{-1}) and its height profile. g, h TEM images of $NC_{GTP/GTP*}$ (13 µg ml^{-1}; g) and $^{CL}NC_{GTP/GTP*}$ (13 µg ml^{-1}; h). All TEM samples were negatively stained with uranyl acetate. Inset scale bars, 250 nm.

Photochemical crosslinking of $NC_{GTP/GTP*}$

The physical stability of $NC_{GTP/GTP*}$ is important for its utilization as a carrier for drug delivery. Through several different experiments, we noticed that $NC_{GTP/GTP*}$ immediately collapsed upon incubation with albumin or serum in buffer, indicating its insufficient stability as a drug carrier. Here, we would like to point out a great advantage of $Glue^{CO2-}$ and its homologues that their multiple benzophenone (BP) groups upon photoexcitation enable covalent crosslinking with adhering proteins (Figure 4.16d). Successful examples so far reported include microtubule and kinesin[371], whose dynamic behaviors could be attenuated by the reaction with photoexcited molecular glues.

In the present work, by using fluorescent FITC-appended $Glue^{FITC}$ (Figure 4.16c, FITC; fluorescein isothiocyanate) derived from $Glue^{CO2-}$, we first confirmed that $Glue^{CO2-}$ has a sufficient photoreactivity with the constituent (THD) of $NC_{GTP/GTP*}$. As shown in Supplementary Fig. S4.44 (available in the Appendix), the reaction mixture, after being exposed to UV light (300 nm) in PIPES buffer, showed the presence of a fluorescence-emissive covalent adduct between THD_{GDP} and $Glue^{FITC}$ in sodium dodecyl sulfate polyacrylamide gel electrophoresis (SDS-PAGE). Then, we investigated whether this photochemical approach can provide $NC_{GTP/GTP*}$ with a sufficient physical stability by crosslinking the shell. Thus, a PIPES buffer solution of $NC_{GTP/GTP*}$ was exposed to UV light for 2 min, where TEM (Figure 4.17h) and AFM imaging results (Appendix, Supplementary Fig. S4.45) and DLS profiles (Figure 4.17b, red) showed that crosslinked (CL) $^{CL}NC_{GTP/GTP*}$ was spherical and remained intact even upon incubation with albumin (0.1 mg ml^{-1}) or serum (0.01%) (see Appendix, Supplementary Figs. 4.46 and 4.47). $^{CL}NC_{GTP/GTP*}$, when prepared using $Glue^{FITC}$ instead of $Glue^{CO2-}$, was fluorescent (Appendix, Supplementary Fig. S4.48), indicating the presence of the molecular glue in $^{CL}NC_{GTP/GTP*}$.

Computational simulation of the assembly of $NS_{GTP/GTP*}$

Considering that tubulin nanosheets $NS_{GTP/GTP*}$ are, on average, 0.04 µm^2 wide and 4.2 nm thick, the formation of $NC_{GTP/GTP*}$ (surface area; ~6.2 µm^2, membrane

thickness; 50 nm) requires at least 1000 pieces of $NS_{GTP/GTP*}$ to assemble. Note that $Glue^{CO2-}$ carrying both Gu^{+} and CO_{2-} groups in its structure can self-assemble via their salt-bridge interaction. In the initial stage of the transformation of $NS_{GTP/GTP*}$ into $NC_{GTP/GTP*}$, we postulate that a certain number of $Glue^{CO2-}$ molecules utilize their Gu^{+} groups to form a salt-bridged network with the surface CO_2 groups on $NS_{GTP/GTP*}$ (Figure 4.16d) as well as the focal-core CO^{-} group in $Glue^{CO2-}$. This adhesion event can lower the surface charge density of $NS_{GTP/GTP*}$ and enhance its hydrophobic stacking, which is secured by possible reorganization of the salt-bridged polymeric networks on $NS_{GTP/GTP*}$ (Figure 4.16e). We performed all atom molecular dynamics (MD) simulations[381] to explore the adhesion of $Glue^{CO2-}$ and the effect of this event on the tubulin assembly. From a full MT model (PDB code: 3J6E), we obtained its partial structure composed of three laterally assembled THD_{GTP*} units ($[THD_{GTP*}]_3$) as a model of NS (Figure 4.18a).

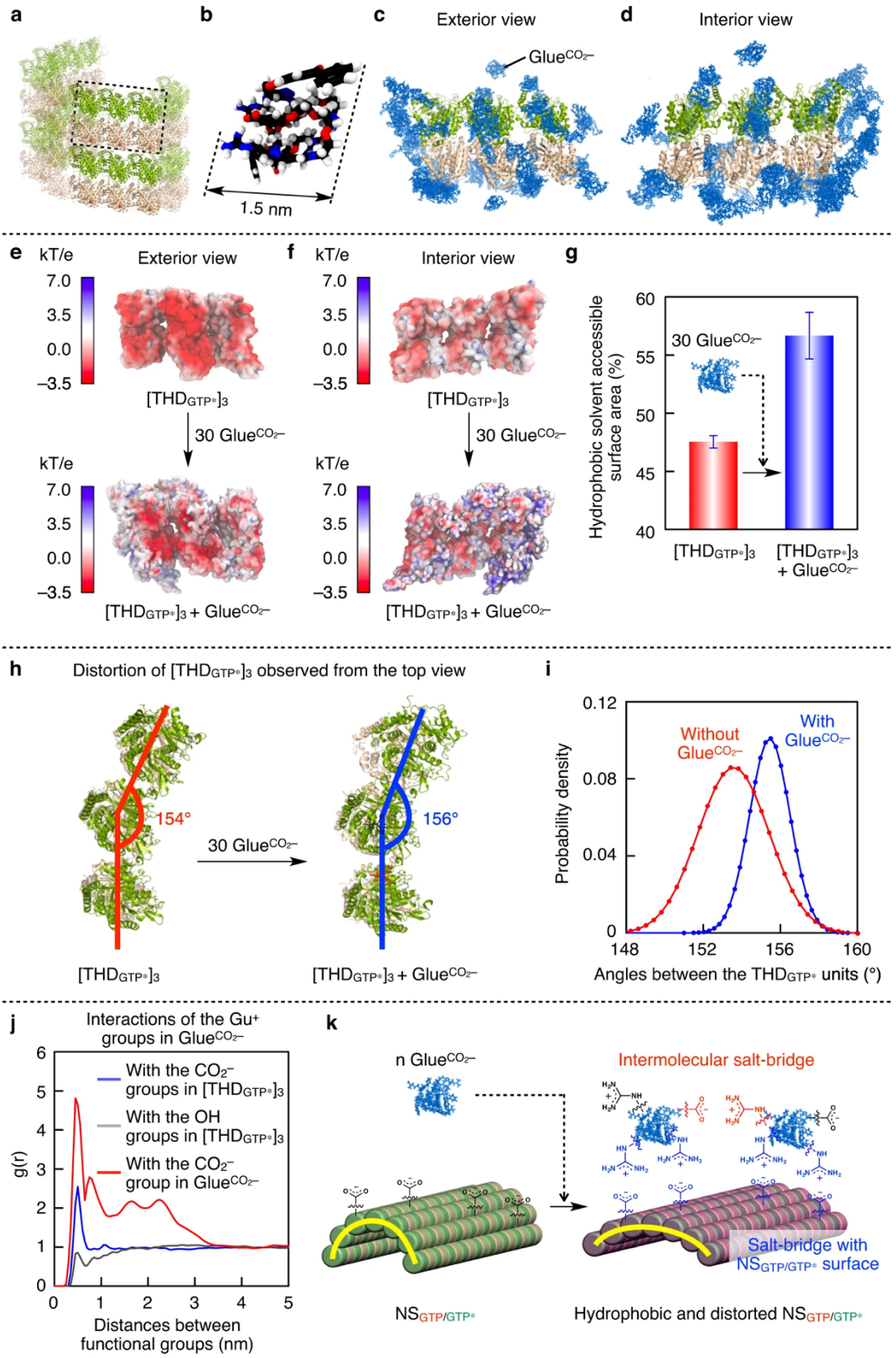
a
b
c
Exterior view
d
Interior view
Glue$^{CO_2-}$
1.5 nm
e
kT/e
7.0
3.5
0.0
−3.5
Exterior view
[THD$_{GTP*}$]$_3$
30 Glue$^{CO_2-}$
[THD$_{GTP*}$]$_3$ + Glue$^{CO_2-}$
f
Interior view
g
Hydrophobic solvent accessible surface area (%)
60
55
50
45
40
30 Glue$^{CO_2-}$
[THD$_{GTP*}$]$_3$
[THD$_{GTP*}$]$_3$ + Glue$^{CO_2-}$
h
Distortion of [THD$_{GTP*}$]$_3$ observed from the top view
154°
156°
i
Probability density
0.12
0.08
0.04
0
Without Glue$^{CO_2-}$
With Glue$^{CO_2-}$
148
152
156
160
Angles between the THD$_{GTP*}$ units (°)
j
Interactions of the Gu$^+$ groups in Glue$^{CO_2-}$
With the CO_2^- groups in [THD$_{GTP*}$]$_3$
With the OH groups in [THD$_{GTP*}$]$_3$
With the CO_2^- group in Glue$^{CO_2-}$
g(r)
Distances between functional groups (nm)
k
n Glue$^{CO_2-}$
Intermolecular salt-bridge
Salt-bridge with NS$_{GTP/GTP*}$ surface
NS$_{GTP/GTP*}$
Hydrophobic and distorted NS$_{GTP/GTP*}$

Figure 4.18. MD simulation of the adhesion events of $Glue^{CO2-}$ onto the surface of THD_{GTP*}.a Three laterally assembled THD_{GTP*} units ($[THD_{GTP*}]_3$) in MT_{GTP*} as a partial model of NS. b An equilibrated MD snapshot of $Glue^{CO2-}$. c, d The outer (c) and inner (d) views of $[THD_{GTP*}]_3$ hybridized with 30 equivalents of $Glue^{CO2-}$. e, f The outer (e) and inner (f) views of $[THD_{GTP*}]_3$ with its electrostatic surface potential in the absence (upper) and presence (lower) of 30 equivalents of hybridized $Glue^{CO2-}$. Negative and positive potential areas are colored in red and blue, respectively. g The percentage of hydrophobic solvent-accessible surface area in the absence (47.5 ± 0.5; red) and presence (56.7 ± 2.0; blue) of 30 equivalents of hybridized $Glue^{CO2-}$. Bars represent mean values ± SD from 2000 data points. h, i $[THD_{GTP*}]_3$ observed from the top view (h) and its angle distributions (i) in the absence (red) and presence (blue) of 30 equivalents of hybridized $Glue^{CO2-}$. j Radial distribution functions g(r) of the Gu^+ groups in $Glue^{CO2-}$ with carboxylates (blue) and non-ionic hydroxyl groups (gray) on the $[THD_{GTP*}]_3$ surface, and the carboxylate at the focal core of $Glue^{CO2-}$ (red). k Schematic illustration of a possible adhesion event of $Glue^{CO2-}$ onto $NS_{GTP/GTP*}$ and its effects on the features of $NS_{GTP/\ GTP*}$. The Gu^+ groups in $Glue^{CO2-}$ form a salt bridge with carboxylates on the $NS_{GTP/GTP*}$ surface and at the focal core of $Glue^{CO2-}$, and the $Glue^{CO2-}$-based polymeric network thus formed through this process increases the hydrophobicity of the $NS_{GTP/GTP*}$ surface, making $NS_{GTP/GTP*}$ more flatten.

The MD simulation suggested that $Glue^{CO2-}$ adopts a globular conformation in aqueous media with a hydrodynamic diameter of 1.5 nm (Figure 4.18b, see also Appendix Supplementary Fig. S4.49). When exposed to 30 equivalents of $Glue^{CO2-}$ (Figure 4.18c, d), $[THD_{GTP*}]_3$ enhances its hydrophobic nature (Figure 4.18e, f) as a result of the surface charge neutralization by adhering $Glue^{CO2-}$. In the solvent-accessible surface area of $[THD_{GTP*}]_3$, the hydrophobic dominancy increases from 48% to 57% (Figure 4.18g). Notably, when $Glue^{CO2-}$ was allowed to adhere onto $[THD_{GTP*}]_3$, the molecular simulations suggested that $[THD_{GTP*}]_3$ adopts a slightly more flattened conformation, characterized by a distribution angle with an average value of ~156° (Figure 4.18h, i, blue), compared with that of native $[THD_{GTP*}]_3$ (red). The simulations also showed that, even after the $Glue^{CO2-}$ adhesion, $[THD_{GTP*}]_3$ preserved a certain level of flexibility (Figure 4.18i). We also calculated radial distribution functions g(r) between the charged groups of $Glue^{CO2-}$ and the amino acid residues of $[THD_{GTP*}]_3$. Supposedly, the CO^- groups in aspartic acid and glutamic acid are interactive with the Gu^+ groups in $Glue^{CO2-}$, while the cationic groups in lysine and arginine are interactive with the focal CO_2^- group in $Glue^{CO2-}$. As expected, the g(r) data revealed that the Gu^+ groups in $Glue^{CO2-}$ are largely populated near the CO_2^- groups on the $[THD_{GTP*}]_3$ surface (Figure 4.18j, blue), whereas they are scarcely populated around the polar but nonionic hydroxyl groups in serine, threonine, and tyrosine (Figure 4.18j, gray). Meanwhile, the focal CO^- group in $Glue^{CO2-}$ is not populated around the cationic groups on the $[THD_{GTP*}]_3$ surface (see Supplementary Fig. S4.50 in the Appendix). The computational

calculation also showed that multiple adhering $Glue^{CO2-}$ molecules can interact and self-assemble via a salt-bridge interaction between their Gu^+ and CO^- groups (Figure 4.18j, red), which results in forming a dense Gu^+/CO^- salt-bridged polymeric network on the $[THD_{GTP*}]_3$ surface (Figure 4.18k). This may promote the self-assembly of flexible $NS_{GTP/GTP}$ and stabilize them in the gently curved multilayered configuration of $NC_{GTP/GTP*}$, as observed experimentally[382,383]. As a control experiment, the use of $Glue^{CO2-Me}$ (Figure 4.16c) having a focal ester group instead of its ionized form for the transformation of $NS_{GTP/GTP*}$ into $NC_{GTP/GTP*}$ resulted in an ill-defined agglomerate (Appendix, Supplementary Fig. S4.51).

GTP-responsiveness of $^{CL}NC_{GTP/GTP*}$

We investigated whether photochemically stabilized $^{CL}NC_{GTP/GTP*}$ is responsive to GTP or not. Notably, the concentrations of both extracellular and intracellular GTP are lower than 0.3 mM in normal cells[365]. However, as already described in the introductory part, rapidly proliferating cancer cells and RNA virus-infected cells contain GTP in a concentration range of 1.5–4.5 mM[362]. Therefore, drug-loaded $^{CL}NC_{GTP/GTP*}$, when taken up into such GTP-rich environments, might selectively collapse to release its preloaded guest. Upon incubation for 100 min at 37 °C in PIPES buffer with 0.2 mM GTP, $^{CL}NC_{GTP/GTP*}$ still maintained its spherical shape, as observed by TEM (Figure 4.19a). However, when the GTP concentration was increased to 0.5 mM, $^{CL}NC_{GTP/GTP*}$ gradually collapsed (Figure 4.19b), displaying a polydisperse DLS profile in 100 min (Figure 4.19c, green). This minimum concentration threshold is important for achieving the error-free delivery to GTP-enriched sites. We added Biomol Green™ as a phosphoric acid (PO^-) detector to a mixture of $^{CL}NC_{GTP/GTP*}$ and GTP (1 mM), and successfully detected PO^- by means of electronic absorption spectroscopy, indicating that $^{CL}NC_{GTP/GTP*}$ has a GTPase activity (Figure 4.19d). Although THD_{GTP*}, the constituent of $^{CL}NC_{GTP/GTP*}$, has no GTPase activity, the product upon incubation of THD_{GTP*} with GTP for 1 h in PIPES buffer at 37 °C showed a GTPase activity comparable to that of THD_{GTP} (Supplementary Fig. S4.52, Appendix), indicating the conversion of THD_{GTP*} into THD_{GTP}. Thus, under the GTP-rich conditions described above, GTP* in $^{CL}NC_{GTP/GTP*}$ is likely replaced with GTP to afford $^{CL}NC_{GTP}$, which possibly collapses along with the hydrolysis of GTP in a manner analogous to the depolymerization of MT_{GTP}. Of particular importance, $^{CL}NC_{GTP/GTP*}$ remained intact to the treatment with other triphosphates (0.5 mM), such as ATP, cytosine triphosphate CTP, uracil triphosphate UTP (Figure 4.19e, and Appendix Supplementary Figs. S4.53 and S4.54).

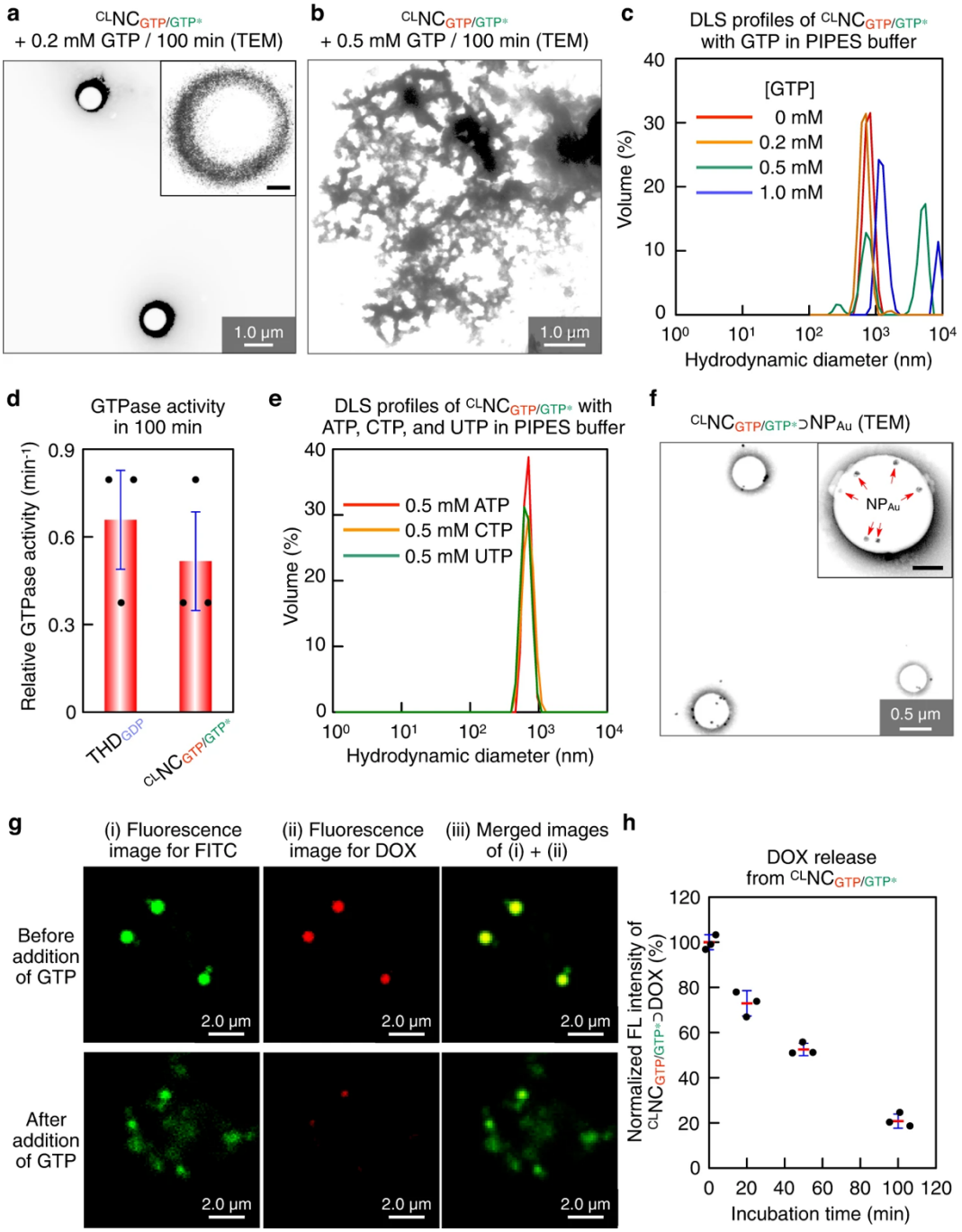

Figure 4.19. GTP-triggered collapse of $^{CL}NC_{GTP/GTP*}$. a, b TEM images of $^{CL}NC_{GTP/GTP*}$ after a 100-min incubation with GTP at its concentrations of 0.2 mM (a) and 0.5 mM (b). c DLS profiles of $^{CL}NC_{GTP/GTP*}$ (8.7 μg ml^{-1}) in PIPES buffer after a 100-min incubation with GTP at its concentrations of 0 mM (red), 0.2 mM (orange), 0.5 mM (green), and 1 mM (blue). d GTPase activities of THD_{GDP} (left) and $^{CL}NC_{GTP/GTP*}$ (right) in PIPES buffer. The data was

obtained from three biologically independent samples (n = 3). e DLS profiles of $^{CL}NC_{GTP/GTP*}$ (8.7 μg ml^{-1}) in PIPES buffer after a 100-min incubation with 1 mM of ATP (red), CTP (orange), and UTP (green). f TEM image of $^{CL}NC_{GTP/GTP*}\supset NP_{Au}$ ([$^{CL}NC_{GTP/GTP*}$] = 13 μg ml^{-1}, [NP_{Au}] = 13 pM). g CLSM images of FITC-labeled $^{CL}NC_{GTP/GTP*}\supset$DOX ([$^{CL}NC_{GTP/GTP*}$]= 13 μg ml^{-1}, [DOX] = 10 μM) incubated without (upper panel) and with (lower panel) 1 mM GTP at 37 °C for 100 min. Micrographs display locations of FITC (i, green) and DOX (ii, red), and their merged images (iii). Scale bars, 2.0 μm. h Fluorescence intensities at 590 nm (λ_{ext} = 470 nm) of residual DOX obtained after 20, 50, and 100-min incubations of a PIPES solution of $^{CL}NC_{GTP/GTP*}\supset$DOX with 1 mM GTP, followed by ultrafiltration. Red bars represent mean values ± SD from three different samples.

Guest encapsulation into $^{CL}NC_{GTP/GTP*}$

How to stably encapsulate guests inside nanocarriers is one of the important subjects for drug delivery. By using gold nanoparticles (NP_{Au}; 14 pM, diameter 50 nm) as a guest, we succeeded in obtaining NP_{Au}-encapsulated $^{CL}NC_{GTP/GTP*}$ by adding Glue^{CO2-} (100 μM) to a PIPES buffer solution of a mixture of $NS_{GTP/GTP*}$ (13 μg ml^{-1}) and NP_{Au} at 37 °C. After 30-min incubation, the resulting mixture was exposed for 2 min to UV light (300 nm) for crosslinking. Using TEM (Figure 4.19f) and asymmetric field flow fractionation analysis (reported in the Appendix in Supplementary Fig. S4.55), we confirmed that $^{CL}NC_{GTP/GTP*}$ encapsulated NP_{Au} ($^{CL}NC_{GTP/GTP*}\supset NP_{Au}$) in its hollow sphere. We also confirmed that $^{CL}NC_{GTP/GTP*}$, when treated with GTP, indeed released its preloaded guest. For this purpose, we first prepared FITC-labeled THD_{GDP} with a mixture of GTP and GTP* (GTP* content: 83 mol%) in PIPES buffer, and further incubated the resulting fluorescent $NS_{GTP/GTP*}$ with Glue^{CO2-} in the presence of doxorubicin (DOX) for 30 min. Then, the mixture was exposed for 2 min to UV light (300 nm) for transforming $NC_{GTP/GTP*}\supset$DOX into $^{CL}NC_{GTP/GTP*}\supset$DOX, which was confirmed by confocal laser scanning microscopy (CLSM) to carry both FITC and DOX dyes (reported in the Appendix in Supplementary Fig. S4.56, green and red, respectively). When $^{CL}NC_{GTP/GTP*}\supset$DOX was incubated with 1 mM GTP in PIPES buffer for 100 min, DOX, as observed by CLSM, became much less fluorescent, indicating the disruption of $^{CL}NC_{GTP/GTP*}$ to release DOX (Figure 4.19g, (i)–(iii), lower panel). Upon incubation for 20 min, 50 min, and 100 min, the residues obtained by ultrafiltration (cutoff molecular weight = 5000) of the reaction mixtures contained 73%, 53%, and 21% of the total amount of preloaded DOX, respectively (Figure 4.19h), while in the absence of GTP, DOX was not released (Figure 4.19g, (i)–(iii), upper panel).

Intracellular drug delivery with $^{CL}NC_{GTP/GTP*}$

As a proof-of-concept study, we investigated whether FITC-labeled $^{CL}NC_{GTP/GTP*}$ can be taken up by human hepatocellular carcinoma Hep3B cells (Figure 4.20a). The cells were incubated in Eagle's minimum essential medium (EMEM) containing $^{CL}NC_{GTP/GTP*}$ (0.5 μg ml–1) for 2.5 h, rinsed with Dulbecco's phosphate-buffered saline (D-PBS), and further incubated in EMEM containing 10% fetal bovine serum (FBS) for 1.5 h. CLSM (Figure 4.20b (i), left panel) together with flow cytometry analysis (Figure 4.20c) revealed that most of the cells took up FITC-labeled $^{CL}NC_{GTP/GTP*}$. Upon subsequent incubation for 21.5 h in EMEM (10% FBS), the entire cytoplasm eventually became fluorescent (Figure 4.20b (ii), right panel) as a possible consequence of the collapse of incorporated $^{CL}NC_{GTP/GTP*}$. In sharp contrast, FITC-labeled THD_{GDP} and $NS_{GTP/GTP*}$, the intermediates for constructing $^{CL}NC_{GTP/GTP*}$, were scarcely taken up into Hep3B cells (see Appendix, Supplementary Figs. S4.57 and S4.58).

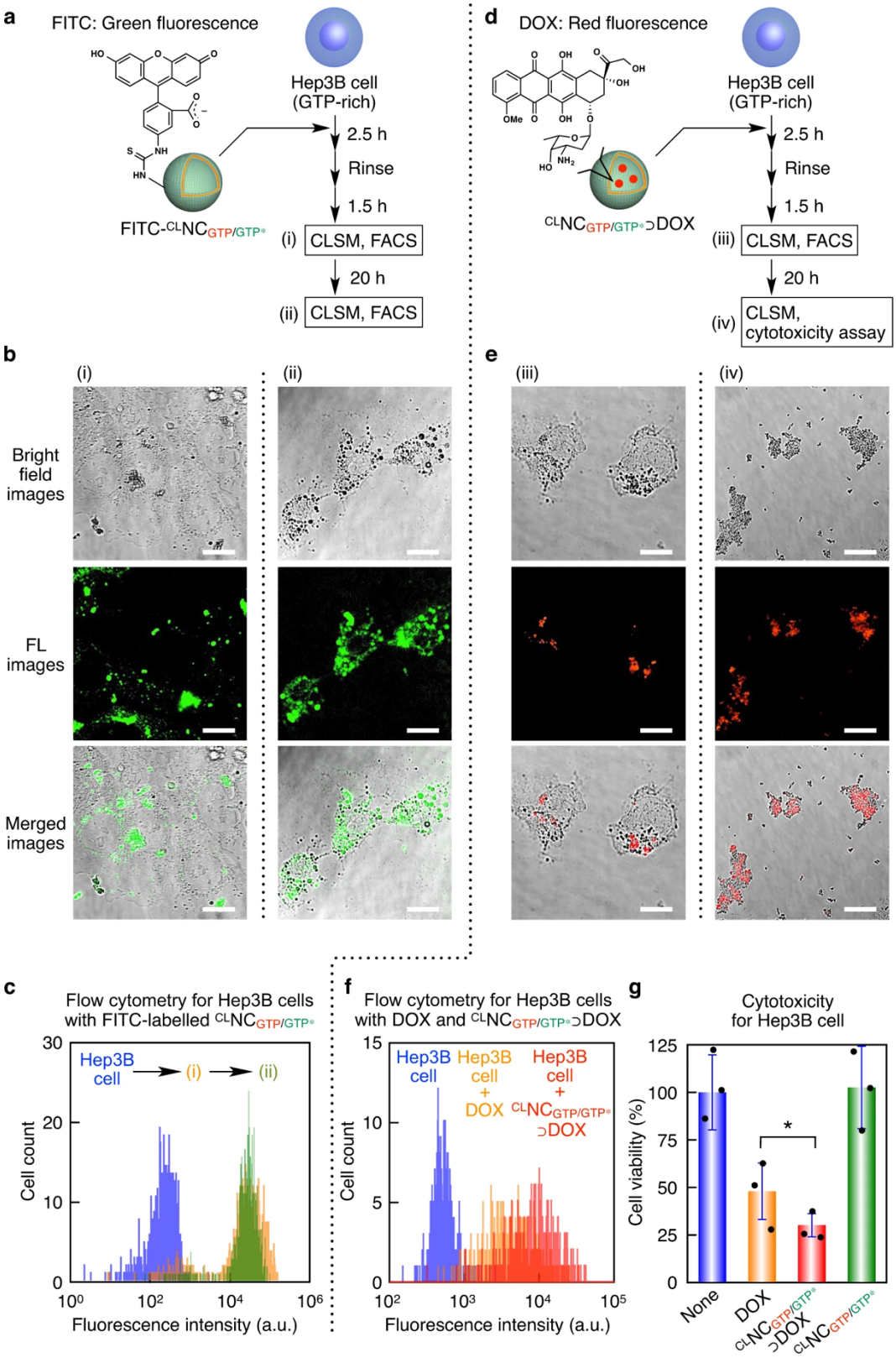
a
FITC: Green fluorescence
Hep3B cell (GTP-rich)
2.5 h
Rinse
1.5 h
(i) CLSM, FACS
20 h
(ii) CLSM, FACS
FITC-CLNCGTP/GTP*
d
DOX: Red fluorescence
Hep3B cell (GTP-rich)
2.5 h
Rinse
1.5 h
(iii) CLSM, FACS
20 h
(iv) CLSM, cytotoxicity assay
CLNCGTP/GTP*⊃DOX
b
e
(i)
(ii)
(iii)
(iv)
Bright field images
FL images
Merged images
c
Flow cytometry for Hep3B cells with FITC-labelled CLNCGTP/GTP*
Hep3B cell
(i)
(ii)
Cell count
Fluorescence intensity (a.u.)
f
Flow cytometry for Hep3B cells with DOX and CLNCGTP/GTP*⊃DOX
Hep3B cell
Hep3B cell + DOX
Hep3B cell + CLNCGTP/GTP* ⊃DOX
Cell count
Fluorescence intensity (a.u.)
g
Cytotoxicity for Hep3B cell
Cell viability (%)
*
None
DOX
CLNCGTP/GTP* ⊃DOX
CLNCGTP/GTP*

Figure 4.20. Intracellular drug delivery using $^{CL}NC_{GTP/GTP*}$.a Schematic illustration of the uptake of FITC-labeled $^{CL}NC_{GTP/GTP*}$ into Hep3B cells. b Bright field (upper row) and CLSM images displaying FITC (middle row, green) in Hep3B cells and their merged images (lower row). The cells were incubated in EMEM containing $^{CL}NC_{GTP/GTP*}$ (0.5 μg ml–1) for 2.5 h, rinsed with D-PBS, and further incubated in EMEM (10% FBS) for 1.5 h (i) and 21.5 h (ii). Scale bars, 20 μm. c Flow cytometry profiles showing FITC fluorescence of Hep3B cells (n > 660) incubated without (blue) and with FITC-labeled $^{CL}NC_{GTP/GTP*}$ for 2.5 h, rinsed with D-PBS, and further incubated in EMEM (10% FBS) for 1.5 h (i, orange) and 21.5 h (ii, green). d Schematic illustration of the cellular uptake of $^{CL}NC_{GTP/GTP*}$⊃DOX. e Bright field (upper row) and CLSM images displaying DOX (middle row, red) in Hep3B cells and their merged images (lower row). The cells were incubated in EMEM containing $^{CL}NC_{GTP/GTP*}$⊃DOX ([$^{CL}NC_{GTP/GTP*}$] = 2.6 μg ml^{-1}, [DOX] = 2 μM) for 2.5 h, rinsed with D-PBS, and further incubated in EMEM (10% FBS) for 1.5 h (iii) and 21.5 h (iv). Scale bars, 20 μm. f, g Flow cytometry profiles (f) showing DOX fluorescence of Hep3B cells (n > 390) and their normalized viabilities (g) determined using Cell Counting Kit-8 (n = 3). The cells were incubated without (blue) and with DOX (2 μM; orange), and $^{CL}NC_{GTP/GTP*}$⊃DOX ([$^{CL}NC_{GTP/GTP*}$] = 2.6 μg ml^{-1}, [DOX] = 2 μM; red) for 2.5 h in EMEM, and then rinsed with D-PBS, followed by incubation in EMEM (10% FBS) for 21.5 h. Statistical significance was examined by two-sided Student's t test (*p = 0.0094 < 0.01). Bars represent mean values ± SD from three different samples.

The high intracellular uptake of FITC-labeled $^{CL}NC_{GTP/GTP*}$ is possibly due to a salt-bridge interaction between the Gu^+ groups in adhering $Glue^{CO2-}$ and cell-surface oxyanionic groups[384]. We confirmed that the intracellular uptake was little affected by the presence of endocytosis inhibitor NaN_3[378], suggesting that the incorporation of $^{CL}NC_{GTP/GTP*}$ into Hep3B cells was caused via an endocytosis-independent direct pathway (Appendix, Supplementary Fig. S4.59). For the drug delivery application of $^{CL}NC_{GTP/GTP*}$, we conducted a cell viability assay with $^{CL}NC_{GTP/GTP*}$⊃DOX. When treated with $^{CL}NC_{GTP/GTP*}$⊃DOX ([$^{CL}NC_{GTP/GTP*}$]= 2.6 μg ml^{-1}, [DOX] = 2 μM) in EMEM (Figure 4.20d) for 2.5 h, Hep3B cells took up DOX as observed by CLSM after a subsequent incubation in EMEM (10% FBS) for 1.5 h (Figure 4.20e (iii), left panel), and then died within next 21.5 h to form an ill-defined agglomerate (Figure 4.20e (iv), right panel). We also confirmed that Hep3B cells took up a larger amount of DOX in $^{CL}NC_{GTP/GTP*}$ (Figure 4.20f, red) than DOX alone (Figure 4.20f, orange). Accordingly, $^{CL}NC_{GTP/GTP*}$⊃DOX successfully lowered the cell viability to 30 ± 6% (Figure 4.20g, red), whereas that caused by DOX alone was only 48 ± 15% (Figure 4.20g, orange). As expected, the cell viability decreased as the concentration of $^{CL}NC_{GTP/GTP*}$⊃DOX was increased (Appendix, Supplementary Fig. S4.60), while the viability upon incubation with $^{CL}NC_{GTP/GTP*}$⊃DOX did not substantially increase when the incubation time was shortened from 2.5 h to 1.0 h (Appendix, Supplementary Fig. S4.61). This is likely caused by the GTP-selective

collapse of $^{CL}NC_{GTP/GTP*}$. The intracellular delivery of $^{CL}NC_{GTP/GTP*}\supset$DOX was also successful with other cell lines such as A549 cell and HeLa cell (Supplementary Fig. S4.62 in the Appendix). We also confirmed that neither the coexistence of THD_{GDP} nor $THD_{GDP/GlueCO2-}$ enhanced the efficacy of DOX (Appendix, Supplementary Fig. S4.63). Together with the noncytotoxic nature of $^{CL}NC_{GTP/GTP*}$ (Figure 4.20g, green) and its stability in a range of pH at tumor tissue (Figure 4.17h)[377], these results allow us to expect that $^{CL}NC_{GTP/GTP*}$ may have the potential to deliver preloaded drugs into cancer cells using GTP as an endogenous reporter.

4.4.5 Discussion and Conclusions

Here, we have documented the successful reconstitution of MT_{GTP} into a GTP-responsive nanocarrier. MT_{GTP} is depolymerized into THD_{GDP}, which is incubated with a mixture of GTP* and GTP (content of GTP*: 70–85 mol%), thereby facilitating the in situ coassembly of the resulting THD_{GTP*} and THD_{GTP} monomers to form $NS_{GTP/GTP*}$. Subsequently, $NS_{GTP/GTP*}$ is treated with molecular glue $Glue^{CO2-}$ to be transformed into spherical $NC_{GTP/GTP*}$, followed by UV exposure to afford crosslinked $^{CL}NC_{GTP/GTP*}$ capable of stably encapsulating guests. In GTP-rich environments, $^{CL}NC_{GTP/GTP*}$ collapses and releases preloaded guests through the transformation of $^{CL}NC_{GTP/GTP*}$ into $^{CL}NC_{GTP}$ followed by the hydrolysis of its bound GTP into GDP, analogous to the depolymerization of MT_{GTP}. Using $^{CL}NC_{GTP/GTP*}$, we successfully delivered DOX into cancer cells that overexpress GTP, and caused cell death more efficiently than DOX alone. Most importantly, $^{CL}NC_{GTP/GTP*}$ is a drug carrier that can selectively collapse in response to GTP rather than ATP that is abundant in normal cells. Since cells infected with RNA viruses such as coronavirus produce a large amount of GTP in their self-replication process, GTP is an endogenous reporter for RNA virus-infected cells. In vivo utilization of $^{CL}NC_{GTP/GTP*}$ for curing RNA virus-induced diseases such as COVID-19 is one of the interesting subjects worthy of further investigation.

Chapter V

Conclusions and future perspectives

5.1 Concluding remarks

Molecular modelling constitutes a very powerful toolbox to mechanistically explore the interactions of small molecules and selected biomolecular targets, both of weak (e.g. Van-der-Waals and hydrophobic interactions) and of strong (e.g. between charged molecules) nature. Using all-atom molecular dynamics simulations, one can obtain crucial insights into the biophysical interactions of the investigated systems with resolutions in time and in space that are largely inaccessible to experimental methods. As such, computational methodologies such as those described in this work should be thought of as a support to experimental evidence, i.e. to assist researchers in better understanding and exploiting the molecular mechanisms through which small molecules exert their effects, in contexts such as medicinal chemistry, enhanced drug delivery and materials science.

At the same time however, not every computational approach is suitable for any molecular system. This means that the final choice of the specific *in-silico* methodology to apply remains demanded to the experience of the modeler. From static approaches such as molecular docking, to plain and enhanced-sampling molecular dynamics simulations and even to most recent machine learning methods, the choice might seem overwhelming. As exemplified through the research works reported herein, the choice of the method depends on the characteristics of the molecular system being investigated, as well as on the

experimental evidence at hand and timescale of the phenomena to be observed or predicted. The following paragraph is intended to serve as a concise reference handbook to provide starting points for modelling the interaction between small molecules, such as drugs, and biomolecular targets of interest, including proteins and membranes.

5.2 Best practices for molecular modelling of *specific* and *aspecific* modulation mechanisms

5.2.1 *Specific* small-molecule / target interactions

Whenever for a given small molecule an exact interaction site is known, e.g. from an experimentally solved 3D structure deposited in the PDB database, or by experimental findings such as mutagenesis, the ligand-target interaction can be said to be *specific*. This usually means that this exact binding site(s) must be found by the ligand, and must be able to properly accommodate the latter, for it to exert its therapeutic (or toxic) action. In the context of molecular simulations, this warrants a detailed preliminary study of the location, biophysical characteristic and accessibility of the target binding site, which might demand extended or even enhanced-sampling molecular dynamics simulations to ensure the availability of a sufficient ensemble of conformations. Furthermore, the computational investigation of how a given small molecule acts on such a specific binding site heavily depends on the initial conditions of the simulations, i.e. on where and how the ligand is placed on the target. In the case of a lack of an experimentally solved structure for the system under investigation, e.g. when key interacting residues are known from experiments but the crystal structure of complex is not yet solved, a valid strategy can be to perform the initial placement of the small molecule by means of molecular docking, thereby generating an ensemble of biophysically sensible and energetically similar binding poses. These shall be evaluated carefully and manually whenever possible, to ensure that conformations contrasting with the chemical/physical characteristics of the binding environment or that are incoherent with experimental findings are discarded. This docking-based strategy is in most cases computationally inexpensive, allowing for the generation of many putative binding conformations for up to millions of ligands, at the cost of a sub-optimal accuracy warranting extensive post-processing. Other, more refined approaches exist which are based on combinations of molecular dynamics simulations with enhanced sampling techniques, such as Funnel Metadynamics[385], but these are usually targeted towards binding free energy calculations and rarely used to obtain

starting conformations in computational drug discovery pipelines, due to their significant computational cost.

However the initial placement of the ligand is obtained, if possible, the generated starting poses should be analyzed by an expert biophysicist or medicinal chemist, who can further help with the extraction of realistic or plausible binding poses based on experience.

Once the initial ligand placement is obtained, the effects of the presence of the ligand in a given binding site can be explored through plain or enhanced-sampling molecular dynamics simulations, depending on the timescales at which the ligand exerts its downstream cascade of molecular events. Starting from the less computationally demanding approaches, plain molecular dynamics simulations of the ligand-target complex spanning time scales of up to tens of microseconds, depending on the size of the system, can be employed to analyze the conformational events triggered by the ligand, e.g. through cluster analysis of the MD trajectories or dimensionality reduction techniques such as PCA[386] or FMA[387]. Motions and conformational biases can be compared between simulations with and without the ligand placed in the binding site, or even against simulations where specific binding site residues are mutated, to obtain useful insights into the molecular events triggered by the ligand. If the sampling provided by classic molecular dynamics is insufficient, enhanced sampling techniques can be employed, such as metadynamics. This latter approach is particularly useful if some information regarding the conformational rearrangements caused by the ligand is known, so that the most suitable set of collective variables can be chosen. This can bias the MD simulation towards the exploration of states that are along or near the pathway of target activation, so as to explore this region of the phase space more effectively, at the expense of an increase in the computational cost and in the complexity of setting up the simulation. Lastly, plain and enhanced sampling MD simulations can provide useful data to estimate the binding energy between the ligand and the target, starting from simple (and arguably rough[41,46,388]) approaches such as MM/GBSA and MM/PBSA[389,390] all the way to more refined methodologies such as funnel metadynamics[385], free energy perturbation[391] or thermodynamic integration[392], depending on the needs and on the availability of computational resources. Docking scores should generally be avoided as absolute estimates of binding free energies, since the scoring functions are tailored towards the enrichment of libraries of candidate compounds rather than towards the accurate estimation of the free energy of binding, in line with the simplifications and approximations of this method.

5.2.2 *Aspecific* small-molecule / target interactions

Molecular modelling strategies can also be proficiently applied in the case of systems where small molecules interact *aspecifically* with their target. Aspecific binding herein refers to molecular assemblies where the binding between a ligand and its target is not restricted to a well-defined binding site, which might be also characterized by a preferential reciprocal ligand-target orientation. Rather, there also exist scenarios in which:

a. the formation of a complex between a macromocule and one (or many) ligand(s) can take place in various, energetically equivalent binding locations, with no unique binding pocket;

b. the investigation is focused on molecular assemblies involving small molecules such as gases or solvents, whose binding energy is difficult to quantify using a static approach;

c. molecular transporters such as nanoparticles are being investigated, which usually do not present a single well-defined binding site but rather an ensemble of anchor points for the cargo;

d. the interest lies in dynamic processes, such as diffusion, e.g. in the case of the permeation of ligands through the cell membrane.

In similar scenarios, which we might define *one-vs-many* or *many-vs-many* interaction studies, conventional strategies such as those described in paragraph 5.2.1 might not be adequate to perform a proper sampling of the interaction. Indeed, since these *aspecific binding scenarios* are conceptually different from the previous example of a ligand binding within its specific binding site, relying entirely on strategies such as docking, which usually requires an *a priori* definition of the binding site, might yield inconclusive results regarding the binding process, on top of the already discussed limitations regarding the estimation of the binding free energy using static approaches (see paragraph 2.3). Thus, a different computational strategy should be employed, which would ideally account not only for the presence of multiple interaction locations, but also for the dynamic nature thereof, given that multiple binding and unbinding events might occur, especially with low-affinity ligands. One feasible strategy in this context is to rely on the intrinsically dynamic information provided by MD to be able to sample the time evolution of ligand binding and unbinding processes. The difference with respect to the specific binding studies described in section 5.2.1 is that instead of considering a single ligand instance that is initialized in or near a putative binding site, the approach

should consider an ensemble of ligands – e.g. a predefined concentration – which are simulated together with the target and initialized randomly at a given concentration in the solvent at the beginning of the simulation. This approach, sometimes referred to as flooding molecular dynamics[393,394], allows for an extensive exploration of the interaction surface of the target by the ligands in solution, which can then be used to reconstruct the probability density of the ligand and thus high-probability regions of interactions on the target. This ligand occupancy map can finally not only highlight preferential anchor points when there is no information regarding the binding site location[393], but also shed light on the nature of the noncovalent interaction between ligand and receptor. In the case of low-affinity ligands with reduced molecular weights, e.g. the volatile anesthetics investigated in chapter 3, such an approach can provide valuable information regarding the stability of the binding events as well as the conformational consequences of the presence of a given solute at specific concentrations on the receptor. It also represents a valuable strategy to assess the permeability of cell membranes to specific ligands, as well as the effect of the latter on membrane stability, shape and mechanics, as shown in the research described in paragraphs 3.4 and 4.2. Lastly, it represents an effective approach to study the interaction between strong ionic ligands to carriers such as nanoparticles, as discussed in paragraphs 4.3 and 4.4.

5.3 Conclusions and future perspectives

In summary, computational molecular modelling represents a rich toolbox which can improve our understanding of how biological systems behave at the microscopic scale. The scope of molecular modelling nowadays spans a large amount of subfields ranging from materials science to drug design and discovery, covering a vast amount of (bio)molecular assemblies and mechanisms, from detailed protein-ligand binding studies to massive virtual screening campaigns, from the study of the dynamics of carbohydrates to computational lipidomics.

As highlighted in the present dissertation, the choice of a specific methodological approach is highly dependent on the system under investigation. In the context of bioengineering, the combination of molecular docking and molecular dynamics can provide key insights into how small molecules influence their surroundings, which can not only drive the development of improved drugs and drug delivery systems, but also shed light on the mechanistic underpinnings of specific molecular events. The computational study of the interaction between small molecules and their targets can be *predictive*, meaning that it is deployed to estimate

quantitative features such as e.g. the binding affinity prior to performing experiments, or *explanatory*, indicating the use of computational models to explain the macroscopic observations of experimental settings. The research reported herein provides examples of both these aims, highlighting how both in the case of *weak* and of *strong* binding events appropriate computational protocols can be developed and deployed to obtain new knowledge, by exploiting the remarkably high spatial and temporal accuracy of all-atom models. Provided that rational modelling choices are made, meaning that the theoretical requirements and assumptions of the employed methods are satisfied by the system under investigation (see sections 2.3, 5.2.1, and 5.2.2), molecular modelling greatly improves our understanding of the mechanisms of action of small molecules and helps in the design of novel chemical formulations able to overcome current limitations and drawbacks in a variety of scenarios. It is thus entirely reasonable to expect computational molecular modelling to play a fundamental role in the future of personalized medicine and healthcare, at the intersection between bioengineering, physics, (medicinal) chemistry, computer science, and medicine.

Chapter VI

Portfolio

6.1 Peer-reviewed Scientific Publications

(1)

Sztandera, K.; Gorzkiewicz, M.; **Zizzi, E. A.**; Dybczak, N.; Poltorak, L.; Deriu, M. A.; Klajnert-Maculewicz, B. Cellular Uptake of Rose Bengal Is Mediated by OATP1B1/1B3 Transporters. *Bioelectrochemistry* **2023**, *152*, 108449. https://doi.org/10.1016/j.bioelechem.2023.108449.

(2)

Kalra, A. P.; Benny, A.; Travis, S. M.; **Zizzi, E. A**.; Morales-Sanchez, A.; Oblinsky, D. G.; Craddock, T. J. A.; Hameroff, S. R.; MacIver, M. B.; Tuszyński, J. A.; Petry, S.; Penrose, R.; Scholes, G. D. Electronic Energy Migration in Microtubules. *ACS Cent. Sci.* **2023**, acscentsci.2c01114. https://doi.org/10.1021/acscentsci.2c01114.

(3)

Zizzi, E. A.; Cavaglià, M.; Tuszynski, J. A.; Deriu, M. A. Alteration of Lipid Bilayer Mechanics by Volatile Anesthetics: Insights from Ms-Long Molecular Dynamics Simulations. *iScience* **2022**, *25* (3), 103946. https://doi.org/10.1016/J.ISCI.2022.103946/ATTACHMENT/2A3FBAAF-AD50-4195-B199-06838EFE2870/MMC1.PDF.

(4)

Uchida, N.; Kohata, A.; Okuro, K.; Cardellini, A.; Lionello, C.; **Zizzi, E. A**.; Deriu, M. A.; Pavan, G. M.; Tomishige, M.; Hikima, T.; Aida, T. Reconstitution of Microtubule into GTP-Responsive Nanocapsules. *Nature Communications 2022 13:1* **2022**, *13* (1), 1–11. https://doi.org/10.1038/s41467-022-33156-5.

(5)

Cavaglià, M.; **Zizzi, E. A.**; Dombrowski, S.; Deriu, M. A.; Tuszynski, J. A. Alteration of Consciousness by Anaesthetics: A Multiscale Modulation from the Molecular to the Systems Level. *Journal of Consciousness Studies* **2022**, *29* (5), 21–49. https://doi.org/10.53765/20512201.29.5.021.

(6)

Brigante, G.; Lazzaretti, C.; Paradiso, E.; Nuzzo, F.; Sitti, M.; Tüttelmann, F.; Moretti, G.; Silvestri, R.; Gemignani, F.; Försti, A.; Hemminki, K.; Elisei, R.; Romei, C.; **Zizzi, E. A.;** Deriu, M. A.; Simoni, M.; Landi, S.; Casarini, L. Genetic Signature of Differentiated Thyroid Carcinoma Susceptibility: A Machine Learning Approach. *European Thyroid Journal* **2022**, *11* (5). https://doi.org/10.1530/ETJ-22-0058.

(7)

Aminpour, M.; Cannariato, M.; Preto, J.; Safaeeardebili, M. E.; Moracchiato, A.; Doria, D.; Donato, F.; **Zizzi, E. A.;** Deriu, M. A.; Scheim, D. E.; Santin, A. D.; Tuszynski, J. A. In Silico Analysis of the Multi-Targeted Mode of Action of Ivermectin and Related Compounds. *Computation 2022, Vol. 10, Page 51* **2022**, *10* (4), 51. https://doi.org/10.3390/COMPUTATION10040051.

(8)

Zizzi, E. A.; Cavaglià, M.; Tuszynski, J. A.; Deriu, M. A. Insights into the Interaction Dynamics between Volatile Anesthetics and Tubulin through Computational Molecular Modelling. *Journal of Biomolecular Structure and Dynamics* **2021**, 1–15. https://doi.org/10.1080/07391102.2021.1897044.

(9)

Sztandera, K.; Gorzkiewicz, M.; Dias Martins, A. S.; Pallante, L.; **Zizzi, E. A**.; Miceli, M.; Bątal, M.; Reis, C. P.; Deriu, M. A.; Klajnert-Maculewicz, B. Noncovalent Interactions with PAMAM and PPI Dendrimers Promote the Cellular Uptake and Photodynamic Activity of Rose Bengal: The Role of the

Dendrimer Structure. *Journal of Medicinal Chemistry* **2021**, *64* (21), 15758–15771. https://doi.org/10.1021/acs.jmedchem.1c01080.

(10)

Gaetani, R.; **Zizzi, E. A.;** Deriu, M. A.; Morbiducci, U.; Pesce, M.; Messina, E. When Stiffness Matters: Mechanosensing in Heart Development and Disease. *Frontiers in Cell and Developmental Biology* **2020**, *8*. https://doi.org/10.3389/fcell.2020.00334.

6.2 Scientific Awards

2023 **Cover Art:** ACS Central Science, Vol. 9 Issue 3, related to the publication "Electronic Energy Migration in Microtubules"

2021 **Cover Art:** Journal of Medicinal Chemistry, Vol. 64 N. 21, related to the publication "Noncovalent Interactions with PAMAM and PPI Dendrimers Promote the Cellular Uptake and Photodynamic Activity of Rose Bengal: The Role of the Dendrimer Structure"

6.3 Teaching Activity

The teaching activities listed below were carried out within the master's degree course in Biomedical Engineering at Politecnico di Torino.

6.3.1 Academic Year 2020/2021

01RXKMV Biomechanical Design (ENG) – 14.5 hrs.

6.3.2 Academic Year 2021/2022

01UCBMV Rational Drug Design: Principles and Applications (ENG) – 10.5 hrs.

01RXKMV Biomechanical Design (ENG) – 8.5 hrs.

01UQUMV Biomeccanica Multiscala (IT) – 9 hrs.

6.3.3 Academic Year 2022/2023

01UCBMV Rational Drug Design: Principles and Applications (ENG) – 1.5 hrs.

01UQUMV Biomeccanica Multiscala (IT) – 13 hrs.

6.3.4 Undergraduate student supervision

Supervision of 14 B.Sc. final projects and 1 M.Sc. thesis

6.4 PhD Courses

6.4.1 Acquired Hard Skills

Course Name	Year	Hours
Computing@PoliTO Workshop	2020	4
Multiscale modelling and coarse-graining for flow and transport PDEs	2020	12
ICTP-SISSA-CECAM Workshop on Molecular Dynamics and its Applications to Biological Systems	2020	20
BioExcel Winter School	2020	30
VIRTUOUS Transfer of Knowledge – Omics, Machine Learning and Molecular Modelling Targeting Taste and Nutrition	2020	12
Planning, management, and analysis of chemical and laboratory research	2021	15
Meccanica Statistica non Estensiva	2021	10

6.4.2 Acquired Soft Skills

Course Name	Year	Hours
Enterpreneurial Finance	2021	5
L'uso delle risorse e dei servizi digitali UniTo per la ricerca bibliografica in campo umanistico	2020	6
Project Management	2020	5

Responsible research and innovation, the impact on social challenges	2021	5
Research Integrity	2021	5
Thinking Out of the Box	2022	1
Personal Branding	2022	1
Design Thinking, Processes and Methods	2022	2
Communication	2022	5
Public Speaking	2022	5

6.5 International Conferences and Workshops

Event	Contribution	Year
ICTP-SISSA-CECAM Workshop on Molecular Dynamics and its Applications to Biological Systems	Attendee	2020
First VIRTUOUS Transfer of Knowledge Workshop	Oral Pres.	2020
Second VIRTUOUS Trasfer of Knowledge Worskhop	Attendee	2022
CANCERTO - Nanoscience In Cancer Immunotherapy 2021	Poster	2021
BioExcel Winter School on Biomolecular Simulations	Poster	2020
III Annual Symposium: L'era delle 3R: modelli in silico, in vitro e in vivo per promuovere la ricerca traslazionale	Poster	2021
8th Annual CCPBioSim Conference - Frontiers in Biomolecular Simulation 2022	Poster	2022
AIDD 2022 Spring School	Attendee	2022
The TWCF Banff Workshop - Experimental Testing of the Orch OR Theory of Consciousness	Oral Pres.	2022
26th Congress of the European Society of Biomechanics	Poster	2021

6.6 International Exchange Periods

Period	Host Instituion	Country
02/2020 – 03/2020	MissingTech Sagl.	Switzerland
10/2020 – 12/2020	InSyBio PC	Greece
05/2022 – 06/2022	MissingTech Sagl.	Switzerland
02/2023 – 04/2023	University of Ottawa	Canada

References

1. Grandbois, M., Beyer, M., Rief, M., Clausen-Schaumann, H. & Gaub, H. E. How Strong Is a Covalent Bond? *Science* **283**, 1727–1730 (1999).

2. Beyer, M. K. The mechanical strength of a covalent bond calculated by density functional theory. *J. Chem. Phys.* **112**, 7307–7312 (2000).

3. Haase, F. *et al.* Tuning the stacking behaviour of a 2D covalent organic framework through non-covalent interactions. *Materials Chemistry Frontiers* **1**, 1354–1361 (2017).

4. N. Johnson, S. *et al.* Probing non-covalent interactions driving molecular assembly in organo-electronic building blocks. *CrystEngComm* **21**, 3151–3157 (2019).

5. Su, Z. *et al.* The role of architectural engineering in macromolecular self-assemblies via non-covalent interactions: A molecular LEGO approach. *Progress in Polymer Science* **103**, 101230 (2020).

6. Hollingsworth, S. A. & Dror, R. O. Molecular Dynamics Simulation for All. *Neuron* **99**, 1129–1143 (2018).

7. Leach, A. R. *Molecular modelling: Principles and applications*. (Adison Wesley Longman, 1996). doi:https://doi.org/10.1016/S0097-8485(96)00029-0.

8. Bayly, C. I., Cieplak, P., Cornell, W. & Kollman, P. A. A well-behaved electrostatic potential based method using charge restraints for deriving atomic charges: the RESP model. *J. Phys. Chem.* **97**, 10269–10280 (1993).

9. Jakalian, A., Jack, D. B. & Bayly, C. I. Fast, efficient generation of high-quality atomic charges. AM1-BCC model: II. Parameterization and validation. *Journal of Computational Chemistry* **23**, 1623–1641 (2002).

10. Mulliken, R. S. Electronic Population Analysis on LCAO–MO Molecular Wave Functions. I. *J. Chem. Phys.* **23**, 1833–1840 (1955).

11. Gasteiger, J. & Marsili, M. A new model for calculating atomic charges in molecules. *Tetrahedron Letters* **19**, 3181–3184 (1978).

12. Eisenschitz, R. & London, F. Über das Verhältnis der van der Waalsschen Kräfte zu den homöopolaren Bindungskräften. *Z. Physik* **60**, 491–527 (1930).

13. Liptrot, D. J. & Power, P. P. London dispersion forces in sterically crowded inorganic and organometallic molecules. in *Nature Reviews Chemistry* vol. 1 0004 (2017).

14. Howard, J. & Hyman, A. A. Dynamics and mechanics of the microtubule plus end. *Nature* **422**, 753–758 (2003).

15. Tilney, L. G. *et al.* Microtubules: evidence for 13 protofilaments. *J Cell Biol* **59**, 267–275 (1973).

16. Chaaban, S. & Brouhard, G. J. A microtubule bestiary: structural diversity in tubulin polymers. *Mol Biol Cell* **28**, 2924–2931 (2017).

17. Erickson, H. P. & O'Brien, E. T. Microtubule Dynamic Instability and GTP Hydrolysis. *Annu. Rev. Biophys. Biomol. Struct* **21**, 145–166 (1992).

18. Nogales, E., Wolf, S. G. & Downing, K. H. Structure of the ab tubulin dimer by electron crystallography. *Nature* **391**, 199–204 (1998).

19. Löwe, J., Li, H., Downing, K. H. & Nogales, E. Refined structure of αβ-tubulin at 3.5 Å resolution. *Journal of Molecular Biology* **313**, 1045–1057 (2001).

20. Lu, Y.-M. & Zheng, C. The Expression and Function of Tubulin Isotypes in Caenorhabditis elegans. *Front Cell Dev Biol* **10**, 860065 (2022).

21. Craddock, T. J. A., Tuszynski, J. A. & Hameroff, S. Cytoskeletal signaling: Is memory encoded in microtubule lattices by CaMKII phosphorylation? *PLoS Computational Biology* **8**, (2012).

22. van Meer, G., Voelker, D. R. & Feigenson, G. W. Membrane lipids: where they are and how they behave. *Nat Rev Mol Cell Biol* **9**, 112–124 (2008).

23. van Meer, G. & de Kroon, A. I. P. M. Lipid map of the mammalian cell. *Journal of Cell Science* **124**, 5–8 (2011).

24. Op den Kamp, J. A. F. Lipid Asymmetry in Membranes. *Annual Review of Biochemistry* **48**, 47–71 (1979).

25. Lyman, E., Hsieh, C.-L. & Eggeling, C. From Dynamics to Membrane Organization: Experimental Breakthroughs Occasion a "Modeling Manifesto". *Biophysical Journal* **115**, 595–604 (2018).

26. Schmidt, T., Schütz, G. J., Baumgartner, W., Gruber, H. J. & Schindler, H. Imaging of single molecule diffusion. *Proceedings of the National Academy of Sciences* **93**, 2926–2929 (1996).

27. Sezgin, E., Levental, I., Mayor, S. & Eggeling, C. The mystery of membrane organization: composition, regulation and roles of lipid rafts. *Nat Rev Mol Cell Biol* **18**, 361–374 (2017).

28. Schwille, P., Haupts, U., Maiti, S. & Webb, W. W. Molecular Dynamics in Living Cells Observed by Fluorescence Correlation Spectroscopy with One- and Two-Photon Excitation. *Biophysical Journal* **77**, 2251–2265 (1999).

29. Marrink, S. J. *et al.* Computational Modeling of Realistic Cell Membranes. *Chemical Reviews* **119**, 6184–6226 (2019).

30. Bottaro, S. & Lindorff-Larsen, K. Biophysical experiments and biomolecular simulations: A perfect match? *Science* **361**, 355–360 (2018).

31. Schlick, T., Collepardo-Guevara, R., Halvorsen, L. A., Jung, S. & Xiao, X. Biomolecular modeling and simulation: a field coming of age. *Quarterly Reviews of Biophysics* **44**, 191–228 (2011).

32. Hait, W. N. Anticancer drug development: the grand challenges. *Nat Rev Drug Discov* **9**, 253–254 (2010).

33. Abbasi, E. *et al.* Dendrimers: synthesis, applications, and properties. *Nanoscale Res Lett* **9**, 247 (2014).

34. Jorgensen, W. L. & Tirado-Rives, J. Monte Carlo vs Molecular Dynamics for Conformational Sampling. *J. Phys. Chem.* **100**, 14508–14513 (1996).

35. Berman, H. M. *et al.* The protein data bank. *Acta Crystallographica Section D: Biological Crystallography* **58**, 899–907 (2002).

36. Waterhouse, A. *et al.* SWISS-MODEL: Homology modelling of protein structures and complexes. *Nucleic Acids Research* **46**, W296–W303 (2018).

37. Hetényi, C. & van der Spoel, D. Blind docking of drug-sized compounds to proteins with up to a thousand residues. *FEBS Letters* **580**, 1447–1450 (2006).

38. Corso, G., Stärk, H., Jing, B., Barzilay, R. & Jaakkola, T. DiffDock: Diffusion Steps, Twists, and Turns for Molecular Docking. Preprint at https://doi.org/10.48550/arXiv.2210.01776 (2023).

39. Zheng, Z. & Merz, K. M. Jr. Development of the Knowledge-Based and Empirical Combined Scoring Algorithm (KECSA) To Score Protein–Ligand Interactions. *J. Chem. Inf. Model.* **53**, 1073–1083 (2013).

40. Trott, O. & Olson, A. J. AutoDock Vina: improving the speed and accuracy of docking with a new scoring function, efficient optimization and multithreading. *J Comput Chem* **31**, 455–461 (2010).

41. Genheden, S. & Ryde, U. The MM/PBSA and MM/GBSA methods to estimate ligand-binding affinities. *Expert Opin Drug Discov* **10**, 449–461 (2015).

42. Gentile, F. *et al.* Deep Docking: A Deep Learning Platform for Augmentation of Structure Based Drug Discovery. *ACS Central Science* **6**, 939–949 (2020).

43. Gentile, F. *et al.* Artificial intelligence–enabled virtual screening of ultra-large chemical libraries with deep docking. *Nature Protocols* **17**, 672–697 (2022).

44. Shirts, M. R., Mobley, D. L. & Chodera, J. D. Chapter 4 Alchemical Free Energy Calculations: Ready for Prime Time? in *Annual Reports in Computational Chemistry* (eds. Spellmeyer, D. C. & Wheeler, R.) vol. 3 41–59 (Elsevier, 2007).

45. Zhu, T. *et al.* Fragment-Based Drug Discovery Using a Multidomain, Parallel MD-MM/PBSA Screening Protocol. *J. Chem. Inf. Model.* **53**, 560–572 (2013).

46. Hou, T., Wang, J., Li, Y. & Wang, W. Assessing the Performance of the MM/PBSA and MM/GBSA Methods. 1. The Accuracy of Binding Free Energy Calculations Based on Molecular Dynamics Simulations. *J. Chem. Inf. Model.* **51**, 69–82 (2011).

47.Craddock, T. J. A., Hameroff, S. R., Ayoub, A. T., Klobukowski, M. & Tuszynski, J. A. Anesthetics act in quantum channels in brain microtubules to prevent consciousness. *Current Topics in Medicinal Chemistry* **15**, 523–533 (2015).

48.Chalmers, D. The Hard Problem of Consciousness. *The Blackwell Companion to Consciousness* 223–235 (2007) doi:10.1002/9780470751466.CH18.

49.Baijpai, R. P. Biophotonic Route for Understanding Mind, Brain and the World. *Cosmos and History: The Journal of Natural and Social Philosophy* **11**, 189–200 (2015).

50.Craddock, T. J. A. *et al.* Anesthetic Alterations of Collective Terahertz Oscillations in Tubulin Correlate with Clinical Potency: Implications for Anesthetic Action and Post-Operative Cognitive Dysfunction. *Scientific Reports* **7**, (2017).

51.Meyer, K. H. Contributions to the theory of narcosis. *Transactions of the Faraday Society* **33**, 1062–1064 (1937).

52.Franks, N. P. & Lieb, W. R. Do general anaesthetics act by competitive binding to specific receptors? *Nature 1984 310:5978* **310**, 599–601 (1984).

53.Franks, N. P. & Lieb, W. R. Molecular and cellular mechanisms of general anaesthesia. *Nature 1994 367:6464* **367**, 607–614 (1994).

54.Campagna, J. A., Miller, K. W. & Forman, S. A. Mechanisms of Actions of Inhaled Anesthetics. *New England Journal of Medicine* **348**, 2110–2124 (2003).

55.Fütterer, C. D. *et al.* Alterations in Rat Brain Proteins after Desflurane Anesthesia. *Anesthesiology* (2004) doi:10.1097/00000542-200402000-00019.

56.Pan, J. Z., Xi, J., Eckenhoff, M. F. & Eckenhoff, R. G. Inhaled anesthetics elicit region-specific changes in protein expression in mammalian brain. *Proteomics* **8**, 2983–2992 (2008).

57.Kalenka, A., Feldmann, R. E., Kuschinsky, W., Waschke, K. F. & Maurer, M. H. The Effects of Sevoflurane Anesthesia on Rat Brain Proteins : A Proteomic Time-Course Analysis. **104**, 1129–1135 (2007).

58.Hameroff, S. & Penrose, R. Consciousness in the universe: A review of the 'Orch OR' theory. *Physics of Life Reviews* Preprint at https://doi.org/10.1016/j.plrev.2013.08.002 (2014).

59.Tobias, J. W., Eckenhoff, M. F., Xi, J., Eckenhoff, R. G. & Pan, J. Z. Halothane Binding Proteome in Human Brain Cortex. *Journal of Proteome Research* **6**, 582–592 (2006).

60.Avidan, M. S. & Evers, A. S. Review of clinical evidence for persistent cognitive decline or incident dementia attributable to surgery or general anesthesia. *Journal of Alzheimer's Disease* Preprint at https://doi.org/10.3233/JAD-2011-101680 (2011).

61.Monk, T. G. *et al.* Predictors of cognitive dysfunction after major noncardiac surgery. *Anesthesiology* (2008) doi:10.1097/01.anes.0000296071.19434.1e.

62.Lømo, T. The discovery of long-term potentiation. *Philosophical Transactions of the Royal Society B: Biological Sciences* Preprint at https://doi.org/10.1098/rstb.2002.1226 (2003).

63.Bliss, T. V. P., Collingridge, G. L. & Morris, R. G. M. Long-term potentiation: Enhancing neuroscience for 30 years - Introduction. *Philosophical Transactions of the Royal Society B: Biological Sciences* Preprint at https://doi.org/10.1098/rstb.2003.1282 (2003).

64.Clugnet, M. C. & LeDoux, J. E. Synaptic plasticity in fear conditioning circuits: Induction of LTP in the lateral nucleus of the amygdala by stimulation of the medial geniculate body. *Journal of Neuroscience* (1990) doi:10.1523/jneurosci.10-08-02818.1990.

65.Conde, C. & Cáceres, A. Microtubule assembly, organization and dynamics in axons and dendrites. *Nature Reviews Neuroscience* **10**, 319–332 (2009).

66.Kapitein, L. C. & Hoogenraad, C. C. Building the Neuronal Microtubule Cytoskeleton. *Neuron* **87**, 492–506 (2015).

67.Hameroff, S., Nip, A., Porter, M. & Tuszynski, J. Conduction pathways in microtubules, biological quantum computation, and consciousness. *Bio Systems* **64**, 149–168 (2002).

68.HAMEROFF, S. R., CRADDOCK, T. J. A. & TUSZYNSKI, J. A. 'MEMORY BYTES' — MOLECULAR MATCH FOR CaMKII PHOSPHORYLATION ENCODING OF MICROTUBULE LATTICES . *Journal*

of Integrative Neuroscience **09**, 253–267 (2010).

69. Craddock, T. J. A., Friesen, D., Mane, J., Hameroff, S. & Tuszynski, J. A. The feasibility of coherent energy transfer in microtubules. *Journal of the Royal Society Interface* **11**, 2–10 (2014).

70. Tang, J., Eckenhoff, M. F. & Eckenhoff, R. G. Anesthesia and the old brain. *Anesthesia and Analgesia* (2010) doi:10.1213/ANE.0b013e3181b80939.

71. Fodale, V., Ritchie, K., Rasmussen, L. S. & Mandal, P. K. Anesthetics and Alzheimer's disease: Background and research. *Journal of Alzheimer's Disease* Preprint at https://doi.org/10.3233/JAD-2010-100809 (2010).

72. Bowdle, T. A., Knutsen, L. J. S. & Williams, M. Local and Adjunct Anesthesia. in *Comprehensive Medicinal Chemistry II* 351–367 (Elsevier, 2007). doi:10.1016/B0-08-045044-X/00175-9.

73. Livingston, A. & Vergara, G. A. Effects of halothane on microtubules in the sciatic nerve of the rat. *Cell and Tissue Research* (1979) doi:10.1007/BF00234841.

74. Telser, A. The inhibition of flagellar regeneration in Chlamydomonas reinhardii by inhalational anesthetic halothane. *Experimental Cell Research* (1977) doi:10.1016/0014-4827(77)90406-2.

75. Riazi, S. & Ibarra Moreno, C. A. *Pharmacology and Physiology for Anesthesia*. *Anesthesia & Analgesia* vol. 129 (Elsevier, 2013).

76. Mazze, R. I. Renal Dysfunction Associated With Methoxyflurane Anesthesia. *JAMA* **216**, 278 (1971).

77. Porter, K. M., Dayan, A. D., Dickerson, S. & Middleton, P. M. The role of inhaled methoxyflurane in acute pain management. *Open Access Emergency Medicine* **Volume 10**, 149–164 (2018).

78. Hinkley, R. E. Microtubule—macrotubule transformations induced by volatile anesthetics. Mechanism of macrotubule assembly. *Journal of Ultrastructure Research* **57**, 237–250 (1976).

79. Miller, R. D. *et al.* Ethylene--halothane anesthesia: addition or synergism? *Anesthesiology* (1969) doi:10.1097/00000542-196910000-00002.

80.Bernardi, R. C., Melo, M. C. R. & Schulten, K. Enhanced sampling techniques in molecular dynamics simulations of biological systems. *Biochimica et Biophysica Acta* **1850**, 872–877 (2015).

81.Lu, D. *et al.* The role of molecular modeling in bionanotechnology. *Physical biology* **3**, S40--53 (2006).

82.Hollingsworth, S. A. & Dror, R. O. Molecular Dynamics Simulation for All. *Neuron* **99**, 1129–1143 (2018).

83.Grasso, G. *et al.* Conformational fluctuations of the AXH monomer of Ataxin-1. *Proteins: Structure, Function and Bioinformatics* **84**, 52–59 (2016).

84.Grasso, G. *et al.* Cell Penetrating Peptide Adsorption on Magnetite and Silica Surfaces: A Computational Investigation. *Journal of Physical Chemistry B* **119**, 8239–8246 (2015).

85.Apicella, A. *et al.* A Hydrophobic Gold Surface Triggers Misfolding and Aggregation of the Amyloidogenic Josephin Domain in Monomeric Form, While Leaving the Oligomers Unaffected. *PLoS ONE* **8**, (2013).

86.Grasso, G. *et al.* Cell penetrating peptide modulation of membrane biomechanics by Molecular dynamics. *Journal of Biomechanics* **73**, 137–144 (2018).

87.Deriu, M. A. M. A. *et al.* Investigation of the Josephin Domain Protein-Protein Interaction by Molecular Dynamics. *PLoS ONE* **9**, e108677 (2014).

88.Huzil, J. T., Ludueña, R. F. & Tuszynski, J. Comparative modelling of human $β$ tubulin isotypes and implications for drug binding. *Nanotechnology* **17**, S90--S100 (2006).

89.Carpenter, E. J., Huzil, J. T., Ludueña, R. F. & Tuszynski, J. a. Homology modeling of tubulin: influence predictions for microtubule's biophysical properties. *European biophysics journal* **36**, 35–43 (2006).

90.Leandro-García, L. J. *et al.* Tumoral and tissue-specific expression of the major human β-tubulin isotypes. *Cytoskeleton* **67**, 214–223 (2010).

91.Alushin, G. M. *et al.* High-resolution microtubule structures reveal the structural transitions in $α$$β$-tubulin upon GTP hydrolysis. *Cell* **157**, 1117–1129

(2014).

92. Pettersen, E. F. *et al.* UCSF Chimera?A visualization system for exploratory research and analysis. *Journal of Computational Chemistry* **25**, 1605–1612 (2004).

93. Martì-Renom, M. A., Stuart, A. C., Roberto, S., Melo, F. & Andrej, S. COMPARATIVE PROTEIN STRUCTURE MODELING OF GENES AND GENOMES. *Annu. Rev. Biophys. Biomol. Struct* **29**, 291–325 (2000).

94. Laskowski, R. A., MacArthur, M. W., Moss, D. S. & Thornton, J. M. PROCHECK: a program to check the stereochemical quality of protein structures. *Journal of Applied Crystallography* **26**, 283–291 (1993).

95. Hooft RW, Vriend G, Sander C & Abola EE. Errors in Protein structures. *Nature* **381**, 272 (1996).

96. Colovos, C. & Yeates, T. O. Verification of protein structures: patterns of nonbonded atomic interactions. *Protein science : a publication of the Protein Society* **2**, 1511–1519 (1993).

97. Eisenberg, D., Lüthy, R. & Bowie, J. U. VERIFY3D: Assessment of protein models with three-dimensional profiles. *Methods in Enzymology* **277**, 396–404 (1997).

98. Benkert, P., Tosatto, S. C. E. & Schomburg, D. QMEAN: A comprehensive scoring function for model quality assessment. *Proteins: Structure, Function and Genetics* **71**, 261–277 (2008).

99. Benkert, P., Biasini, M. & Schwede, T. Toward the estimation of the absolute quality of individual protein structure models. *Bioinformatics* **27**, 343–350 (2011).

100. Morris, G. M. *et al.* AutoDock4 and AutoDockTools4: Automated Dockingwith Selective Receptor Flexibility. *Journal of Computational Chemistry* **30**, 2786–2791 (2009).

101. Trott, O. & Olson, A. J. Software News and UpdateAutoDock Vina: Improving the Speed and Accuracy ofDocking with a New Scoring Function, EfficientOptimization, and Multithreading. *Journal of Computational Chemistry* **31**, 455–461 (2010).

102. Craddock, T. J. A. *et al.* Computational predictions of volatile anesthetic interactions with the microtubule cytoskeleton: Implications for side effects of general anesthesia. *PLoS ONE* **7**, (2012).

103. Chau, P. L. New insights into the molecular mechanisms of general anaesthetics. *British Journal of Pharmacology* **161**, 288–307 (2010).

104. Guo, J. *et al.* Comparison of subarachnoid anesthetic effect of emulsified volatile anesthetics in rats. *International Journal of Clinical and Experimental Pathology* **7**, 8748–8755 (2014).

105. Humphrey, W., Dalke, A. & Schulten, K. VMD: visual molecular dynamics. *Journal of molecular graphics* **14**, 27-28,33-38 (1996).

106. Abraham, M. J. *et al.* GROMACS: High performance molecular simulations through multi-level parallelism from laptops to supercomputers. *SoftwareX* **1–2**, 19–25 (2015).

107. Lindorff-Larsen, K. *et al.* Improved side-chain torsion potentials for the Amber ff99SB protein force field. *Proteins* **78**, 1950–1958 (2010).

108. Wishart, D. S. DrugBank: a comprehensive resource for in silico drug discovery and exploration. *Nucleic Acids Research* **34**, D668–D672 (2006).

109. Wang, J., Wang, W., Kollman, P. A. & Case, D. A. Automatic atom type and bond type perception in molecular mechanical calculations. *Journal of Molecular Graphics and Modelling* **25**, 247–260 (2006).

110. Jakalian, A., Jack, D. B. & Bayly, C. I. Fast, efficient generation of high-quality atomic charges. AM1-BCC model: II. Parameterization and validation. *Journal of Computational Chemistry* **23**, 1623–1641 (2002).

111. Berendsen, H. J. C. J. C., Postma, J. P. M., Van Gunsteren, W. F., DiNola, A. & Haak, J. R. Molecular dynamics with coupling to an external bath. *The Journal of chemical physics* **81**, 3684–3690 (1984).

112. Parrinello, M. & Rahman, A. Polymorphic transitions in single crystals: A new molecular dynamics method. *Journal of Applied Physics* **52**, 7182–7190 (1981).

113. Ewald, P. Die Berechnung optischer und elektrostatischer

Gitterpotentiale. *Annalen der Physik* (1921).

114. Touw, W. G. *et al.* A series of PDB-related databanks for everyday needs. *Nucleic Acids Research* **43**, D364–D368 (2015).

115. Gowers, R. *et al.* MDAnalysis: A Python Package for the Rapid Analysis of Molecular Dynamics Simulations. *Proceedings of the 15th Python in Science Conference* 98–105 (2016) doi:10.25080/majora-629e541a-00e.

116. Naveen, M.-A., Denning, E. J., Woolf, T. B. & Beckstein, O. MDAnalysis: A toolkit for the analysis of molecular dynamics simulations. *Journal of Computational Chemistry* **32**, (2011).

117. Kollman, P. A. *et al.* Calculating structures and free energies of complex molecules: combining molecular mechanics and continuum models. *Accounts of Chemical Research* **33**, 889–897 (2000).

118. Case, D. A. *et al.* AMBER 2020. Preprint at (2020).

119. Molecular Operating Environment (MOE) 2019.01. Preprint at (2019).

120. Webb, B. & Sali, A. Comparative Protein Structure Modeling Using MODELLER. *Current Protocols in Bioinformatics* **54**, 5.6.1-5.6.37 (2016).

121. Pantsar, T. & Poso, A. Binding Affinity via Docking: Fact and Fiction. *Molecules (Basel, Switzerland)* **23**, 1–11 (2018).

122. Eckenhoff, R. G. & Johansson, J. S. Molecular interactions between inhaled anesthetics and proteins. *Pharmacological reviews* **49**, 343–367 (1997).

123. Sahni, P. Tubulin Conformation and Anaesthetic Interaction - An Experimental Study. *Biochemistry & Analytical Biochemistry* **s3**, 1–7 (2016).

124. De Planque, M. R. R. & Killian, J. A. Protein-lipid interactions studied with designed transmembrane peptides: Role of hydrophobic matching and interfacial anchoring (Review). *Molecular Membrane Biology* **20**, 271–284 (2003).

125. Mouritsen, O. G. & Bloom, M. Models of Lipid-Protein Interactions in Membranes. *Annual Review of Biophysics and Biomolecular Structure* **22**, 145–171 (1993).

126. Dumas, F., Lebrun, M. C. & Tocanne, J. F. Is the protein/lipid hydrophobic matching principle relevant to membrane organization and functions? *FEBS Letters* **458**, 271–277 (1999).

127. Lingwood, D. & Simons, K. Lipid rafts as a membrane-organizing principle. *Science* **327**, 46–50 (2010).

128. Allen, J. A., Halverson-Tamboli, R. A. & Rasenick, M. M. Lipid raft microdomains and neurotransmitter signalling. *Nature Reviews Neuroscience 2007 8:2* **8**, 128–140 (2006).

129. Levental, I., Grzybek, M. & Simons, K. Raft domains of variable properties and compositions in plasma membrane vesicles. *Proceedings of the National Academy of Sciences* **108**, 11411–11416 (2011).

130. Moon, S. *et al.* Spectrally Resolved, Functional Super-Resolution Microscopy Reveals Nanoscale Compositional Heterogeneity in Live-Cell Membranes. *Journal of the American Chemical Society* **139**, 10944–10947 (2017).

131. Cantor, R. S. Lipid Composition and the Lateral Pressure Profile in Bilayers. *Biophysical Journal* **76**, 2625–2639 (1999).

132. Cantor, R. S. The Lateral Pressure Profile in Membranes: A Physical Mechanism of General Anesthesia. *Biochemistry* **36**, 2339–2344 (1997).

133. Huang, P. & Bertaccini, E. Molecular dynamics simulation of anesthetic-phospholipid bilayer interactions. *Journal of Biomolecular Structure and Dynamics* **12**, 725–754 (1995).

134. Gray, E., Karslake, J., Machta, B. B. & Veatch, S. L. Liquid general anesthetics lower critical temperatures in plasma membrane vesicles. *Biophysical Journal* **105**, 2751–2759 (2013).

135. Lee, A. G. Model for action of local anaesthetics. *Nature 1976 262:5569* **262**, 545–548 (1976).

136. Lerner, R. A. A hypothesis about the endogenous analogue of general anesthesia. *Proceedings of the National Academy of Sciences* **94**, 13375–13377 (1997).

137. Pavel, M. A., Petersen, E. N., Wang, H., Lerner, R. A. & Hansen, S.

B. Studies on the mechanism of general anesthesia. *Proceedings of the National Academy of Sciences* **117**, 13757–13766 (2020).

138. Zhuang, X., Makover, J. R., Im, W. & Klauda, J. B. A systematic molecular dynamics simulation study of temperature dependent bilayer structural properties. *Biochimica et Biophysica Acta - Biomembranes* **1838**, 2520–2529 (2014).

139. Grasso, G. *et al.* Cell penetrating peptide modulation of membrane biomechanics by Molecular dynamics. *Journal of Biomechanics* **73**, 137–144 (2018).

140. Tang, P. & Xu, Y. Large-scale molecular dynamics simulations of general anesthetic effects on the ion channel in the fully hydrated membrane: The implication of molecular mechanisms of general anesthesia. *Proceedings of the National Academy of Sciences* **99**, 16035–16040 (2002).

141. Dickson, C. J., Rosso, L., Betz, R. M., Walker, R. C. & Gould, I. R. GAFFlipid: A General Amber Force Field for the accurate molecular dynamics simulation of phospholipid. *Soft Matter* **8**, 9617–9627 (2012).

142. Pluhackova, K. *et al.* A Critical Comparison of Biomembrane Force Fields: Structure and Dynamics of Model DMPC, POPC, and POPE Bilayers. *Journal of Physical Chemistry B* **120**, 3888–3903 (2016).

143. Jämbeck, J. P. M. & Lyubartsev, A. P. Derivation and Systematic Validation of a Refined All-Atom Force Field for Phosphatidylcholine Lipids. *The Journal of Physical Chemistry B* **116**, 3164–3179 (2012).

144. Dickson, C. J. *et al.* Lipid14: The amber lipid force field. *Journal of Chemical Theory and Computation* **10**, 865–879 (2014).

145. Klauda, J. B. *et al.* Update of the CHARMM All-Atom Additive Force Field for Lipids: Validation on Six Lipid Types. *The Journal of Physical Chemistry B* **114**, 7830–7843 (2010).

146. Ingólfsson, H. I. *et al.* Computational Lipidomics of the Neuronal Plasma Membrane. *Biophysical Journal* **113**, 2271–2280 (2017).

147. Taylor, D. M., Eger, E. I. & Bickler, P. E. Halothane, But Not the

Nonimmobilizers Perfluoropentane and 1,2-Dichlorohexafluorocyclobutane, Depresses Synaptic Transmission in Hippocampal CA1 Neurons in Rats. *Anesthesia & Analgesia* **89**, 1040 (1999).

148. Perouansky, M., Hentschke, H., Perkins, M. & Pearce, R. A. Amnesic Concentrations of the Nonimmobilizer 1,2-Dichlorohexafluorocyclobutane (F6, 2N) and Isoflurane Alter Hippocampal θ Oscillations In Vivo. *Anesthesiology* **106**, 1168–1176 (2007).

149. Eger, E. I. *et al.* The convulsant and anesthetic properties of cis-trans isomers of 1,2-dichlorohexafluorocyclobutane and 1,2-dichloroethylene. *Anesthesia and Analgesia* **93**, 922–927 (2001).

150. Róg, T., Pasenkiewicz-Gierula, M., Vattulainen, I. & Karttunen, M. Ordering effects of cholesterol and its analogues. *Biochimica et Biophysica Acta (BBA) - Biomembranes* **1788**, 97–121 (2009).

151. Leftin, A., Molugu, T. R., Job, C., Beyer, K. & Brown, M. F. Area per Lipid and Cholesterol Interactions in Membranes from Separated Local-Field 13C NMR Spectroscopy. *Biophysical Journal* **107**, 2274–2286 (2014).

152. Needham, D. & Nunn, R. S. Elastic deformation and failure of lipid bilayer membranes containing cholesterol. *Biophysical Journal* **58**, 997–1009 (1990).

153. Zachowski, A. Phospholipids in animal eukaryotic membranes: Transverse asymmetry and movement. *Biochemical Journal* **294**, 1–14 (1993).

154. Klähn, M. & Zacharias, M. Transformations in plasma membranes of cancerous cells and resulting consequences for cation insertion studied with molecular dynamics. *Physical Chemistry Chemical Physics* **15**, 14427–14441 (2013).

155. Shahane, G., Ding, W., Palaiokostas, M. & Orsi, M. Physical properties of model biological lipid bilayers: insights from all-atom molecular dynamics simulations. *Journal of Molecular Modeling* **25**, 1–13 (2019).

156. Wu, E. L. *et al.* CHARMM-GUI Membrane Builder toward realistic biological membrane simulations. *Journal of Computational Chemistry* **35**, 1997–2004 (2014).

157. Jo, S., Lim, J. B., Klauda, J. B. & Im, W. CHARMM-GUI Membrane Builder for Mixed Bilayers and Its Application to Yeast Membranes. *Biophysical Journal* **97**, 50–58 (2009).

158. Jo, S., Kim, T. & Im, W. Automated Builder and Database of Protein/Membrane Complexes for Molecular Dynamics Simulations. *PLoS ONE* **2**, e880 (2007).

159. Jo, S., Kim, T., Iyer, V. G. & Im, W. CHARMM-GUI: A web-based graphical user interface for CHARMM. *Journal of Computational Chemistry* **29**, 1859–1865 (2008).

160. Abraham, M. J. *et al.* Gromacs: High performance molecular simulations through multi-level parallelism from laptops to supercomputers. *SoftwareX* **1–2**, 19–25 (2015).

161. Arvayo-Zatarain, J. A., Favela-Rosales, F., Contreras-Aburto, C., Urrutia-Bañuelos, E. & Maldonado, A. Molecular dynamics simulation study of the effect of halothane on mixed DPPC/DPPE phospholipid membranes. *Journal of Molecular Modeling* **25**, 1–10 (2019).

162. Mojumdar, E. H. & Lyubartsev, A. P. Molecular dynamics simulations of local anesthetic articaine in a lipid bilayer. *Biophysical Chemistry* **153**, 27–35 (2010).

163. Koubi, L., Tarek, M., Klein, M. L. & Scharf, D. Distribution of Halothane in a Dipalmitoylphosphatidylcholine Bilayer from Molecular Dynamics Calculations. *Biophysical Journal* **78**, 800–811 (2000).

164. McCarthy, N. L. C. *et al.* A combined X-ray scattering and simulation study of halothane in membranes at raised pressures. *Chemical Physics Letters* **671**, 21–27 (2017).

165. Franks, N. P. & Lieb, W. R. The structure of lipid bilayers and the effects of general anaesthetics: An X-ray and neutron diffraction study. *Journal of Molecular Biology* **133**, 469–500 (1979).

166. Berendsen, H. J. C., Postma, J. P. M., Van Gunsteren, W. F., DiNola, A. & Haak, J. R. Molecular dynamics with coupling to an external bath. *Journal of Chemical Physics* **81**, (1984).

167. Nosé, S. A unified formulation of the constant temperature molecular dynamics methods. *The Journal of Chemical Physics* **81**, 511 (1998).

168. Hess, B., Bekker, H., Berendsen, H. J. C. & Fraaije, J. G. E. M. LINCS: A Linear Constraint Solver for Molecular Simulations. *J Comput Chem* **18**, 14631472 (1997).

169. Shahane, G., Ding, W., Palaiokostas, M., Azevedo, H. S. & Orsi, M. Interaction of Antimicrobial Lipopeptides with Bacterial Lipid Bilayers. *Journal of Membrane Biology* **252**, 317–329 (2019).

170. Michaud-Agrawal, N., Denning, E. J., Woolf, T. B. & Beckstein, O. MDAnalysis: A toolkit for the analysis of molecular dynamics simulations. *Journal of Computational Chemistry* **32**, 2319–2327 (2011).

171. Van Rossum, G. & Drake, F. L. Python 3 Reference Manual. Preprint at (2009).

172. Piggot, T. J., Allison, J. R., Sessions, R. B. & Essex, J. W. On the Calculation of Acyl Chain Order Parameters from Lipid Simulations. *Journal of Chemical Theory and Computation* **13**, 5683–5696 (2017).

173. Khelashvili, G., Kollmitzer, B., Heftberger, P., Pabst, G. & Harries, D. Calculating the bending modulus for multicomponent lipid membranes in different thermodynamic phases. *Journal of Chemical Theory and Computation* **9**, 3866–3871 (2013).

174. Khelashvili, G., Pabst, G. & Harries, D. Cholesterol Orientation and Tilt Modulus in DMPC Bilayers. *The Journal of Physical Chemistry B* **114**, 7524–7534 (2010).

175. Watson, M. C., Penev, E. S., Welch, P. M. & Brown, F. L. H. Thermal fluctuations in shape, thickness, and molecular orientation in lipid bilayers. *The Journal of Chemical Physics* **135**, 244701 (2011).

176. Fošnarič, M., Iglič, A. & May, S. Influence of rigid inclusions on the bending elasticity of a lipid membrane. *Physical Review E* **74**, 051503 (2006).

177. Johner, N., Harries, D. & Khelashvili, G. Implementation of a methodology for determining elastic properties of lipid assemblies from molecular dynamics simulations. *BMC Bioinformatics* **17**, 1–11 (2016).

178. Biasini, M. *et al.* OpenStructure: An integrated software framework for computational structural biology. *Acta Crystallographica Section D: Biological Crystallography* **69**, 701–709 (2013).

179. Flyvbjerg, H. & Petersen, H. G. Error estimates on averages of correlated data. *The Journal of Chemical Physics* **91**, 461–466 (1989).

180. Nicholls, A. Confidence limits, error bars and method comparison in molecular modeling. Part 1: The calculation of confidence intervals. *Journal of Computer-Aided Molecular Design* **28**, 887–918 (2014).

181. Grossfield, A. *et al.* Best Practices for Quantification of Uncertainty and Sampling Quality in Molecular Simulations [Article v1.0]. *Living Journal of Computational Molecular Science* **1**, 1–24 (2019).

182. Grossfield, A. & Zuckerman, D. M. Chapter 2 Quantifying Uncertainty and Sampling Quality in Biomolecular Simulations. *Annual Reports in Computational Chemistry* **5**, 23–48 (2009).

183. Saeedimasine, M., Montanino, A., Kleiven, S. & Villa, A. Role of lipid composition on the structural and mechanical features of axonal membranes: a molecular simulation study. *Scientific Reports 2019 9:1* **9**, 1–12 (2019).

184. Maulik, P. R. & Shipley, G. G. Interactions of N-stearoyl sphingomyelin with cholesterol and dipalmitoylphosphatidylcholine in bilayer membranes. *Biophysical Journal* **70**, 2256–2265 (1996).

185. Li, L. B., Vorobyov, I. & Allen, T. W. The role of membrane thickness in charged protein–lipid interactions. *Biochimica et Biophysica Acta (BBA) - Biomembranes* **1818**, 135–145 (2012).

186. TJ, M. The effect of cholesterol on the structure of phosphatidylcholine bilayers. *Biochimica et biophysica acta* **513**, 43–58 (1978).

187. Hofsäß, C., Lindahl, E. & Edholm, O. Molecular Dynamics Simulations of Phospholipid Bilayers with Cholesterol. *Biophysical Journal* **84**, 2192 (2003).

188. Meyer, F. de & Smit, B. Effect of cholesterol on the structure of a phospholipid bilayer. *Proceedings of the National Academy of Sciences* **106**, 3654–

3658 (2009).

189. Pickholz, M., Saiz, L. & Klein, M. L. Concentration effects of volatile anesthetics on the properties of model membranes: A coarse-grain approach. *Biophysical Journal* **88**, 1524–1534 (2005).

190. Tu, K., Tarek, M., Klein, M. L. & Scharf, D. Effects of Anesthetics on the Structure of a Phospholipid Bilayer: Molecular Dynamics Investigation of Halothane in the Hydrated Liquid Crystal Phase of Dipalmitoylphosphatidylcholine. *Biophysical Journal* **75**, 2123–2134 (1998).

191. Vauquelin, G. & Packeu, A. Ligands, their receptors and ... plasma membranes. *Molecular and Cellular Endocrinology* **311**, 1–10 (2009).

192. Yamamoto, E. *et al.* Diffusive nature of xenon anesthetic changes properties of a lipid bilayer: Molecular dynamics simulations. *Journal of Physical Chemistry B* **116**, 8989–8995 (2012).

193. Tsuchiya, H. & Mizogami, M. Interaction of local anesthetics with biomembranes consisting of phospholipids and cholesterol: Mechanistic and clinical implications for anesthetic and cardiotoxic effects. *Anesthesiology Research and Practice* **2013**, (2013).

194. Bennett, W. F. D., MacCallum, J. L., Hinner, M. J., Marrink, S. J. & Tieleman, D. P. Molecular view of cholesterol flip-flop and chemical potential in different membrane environments. *Journal of the American Chemical Society* **131**, 12714–12720 (2009).

195. Pohorille, A., Cieplak, P. & Wilson, M. A. Interactions of anesthetics with the membrane-water interface. *Chemical Physics* **204**, 337–345 (1996).

196. Pohorille, A., Wilson, M. A., New, M. H. & Chipot, C. Concentrations of anesthetics across the water–membrane interface; the Meyer–Overton hypothesis revisited. *Toxicology Letters* **100–101**, 421–430 (1998).

197. Christophe Chipot, †, §, Michael A. Wilson, †, ‡ and & Andrew Pohorille*, †, ‡. Interactions of Anesthetics with the Water−Hexane Interface. A Molecular Dynamics Study. *Journal of Physical Chemistry B* **101**, 782–791 (1997).

198. Herold, K. F., Sanford, R. L., Lee, W., Andersen, O. S. & Hemmings, H. C. Clinical concentrations of chemically diverse general anesthetics

minimally affect lipid bilayer properties. *Proceedings of the National Academy of Sciences of the United States of America* **114**, 3109–3114 (2017).

199. Seeman, P. The Membrane Actions of Anesthetics and Tranquilizers. *Pharmacological Reviews* **24**, 583–655 (1972).

200. Subczynski, W. K., Pasenkiewicz-Gierula, M., Widomska, J., Mainali, L. & Raguz, M. High cholesterol/low cholesterol: Effects in biological membranes Review. *Cell biochemistry and biophysics* **75**, 369 (2017).

201. Pontes, B. *et al.* Membrane Elastic Properties and Cell Function. *PLoS ONE* **8**, e67708 (2013).

202. Herold, K. F. & Hemmings, H. C. Sodium channels as targets for volatile anesthetics. *Frontiers in Pharmacology* **3 MAR**, 50 (2012).

203. Bertaccini, E. J. The molecular mechanisms of anesthetic action: Updates and cutting edge developments from the field of molecular modeling. *Pharmaceuticals* vol. 3 2178–2196 Preprint at https://doi.org/10.3390/ph3072178 (2010).

204. Bertaccini, E. J., Yoluk, O., Lindahl, E. R. & Trudell, J. R. Assessment of Homology Templates and an Anesthetic Binding Site within the γ-Aminobutyric Acid Receptor. *Anesthesiology* **119**, 1087–1095 (2013).

205. Yamakura, T., Bertaccini, E., Trudell, J. R. & Harris, R. A. Anesthetics and Ion Channels: Molecular Models and Sites of Action1. *http://dx.doi.org/10.1146/annurev.pharmtox.41.1.23* **41**, 23–51 (2003).

206. Mascia, M. P., Trudell, J. R. & Harris, R. A. Specific binding sites for alcohols and anesthetics on ligand-gated ion channels. *Proceedings of the National Academy of Sciences* **97**, 9305–9310 (2000).

207. John Mihic, S. *et al.* Sites of alcohol and volatile anaesthetic action on GABA(A) and glycine receptors. *Nature* **389**, 385–389 (1997).

208. Koblin, D. D. *et al.* Are convulsant gases also anesthetics? *Anesthesia and Analgesia* **60**, 464–470 (1981).

209. Modica, P. A., Templehoff, R. & White, P. F. Pro- and anticonvulsant effects of anesthetics (Part II). *Anesthesia and Analgesia* **70**, 433–

444 (1990).

210. Sztandera, K., Gorzkiewicz, M. & Klajnert-Maculewicz, B. Nanocarriers in photodynamic therapy—in vitro and in vivo studies. *Wiley Interdisciplinary Reviews: Nanomedicine and Nanobiotechnology* **12**, 1–24 (2020).

211. Demartis, S., Obinu, A., Gavini, E., Giunchedi, P. & Rassu, G. Nanotechnology-based rose Bengal: A broad-spectrum biomedical tool. *Dyes and Pigments* vol. 188 109236 Preprint at https://doi.org/10.1016/j.dyepig.2021.109236 (2021).

212. Demartis, S., Obinu, A., Gavini, E., Giunchedi, P. & Rassu, G. Nanotechnology-based rose Bengal: A broad-spectrum biomedical tool. *Dyes and Pigments* **188**, 109236 (2021).

213. Sztandera, K. *et al.* pH-stable polymersome as nanocarrier for post-loaded rose bengal in photodynamic therapy. *Colloids and Surfaces B: Biointerfaces* **217**, 112662 (2022).

214. Sztandera, K. *et al.* Triazine–Carbosilane Dendrimersomes Enhance Cellular Uptake and Phototoxic Activity of Rose Bengal in Basal Cell Skin Carcinoma Cells. *International Journal of Nanomedicine* **17**, 1139–1154 (2022).

215. Dabrzalska, M. *et al.* Cationic Phosphorus Dendrimer Enhances Photodynamic Activity of Rose Bengal against Basal Cell Carcinoma Cell Lines. *Molecular Pharmaceutics* **14**, 1821–1830 (2017).

216. Sztandera, K. *et al.* Noncovalent Interactions with PAMAM and PPI Dendrimers Promote the Cellular Uptake and Photodynamic Activity of Rose Bengal: The Role of the Dendrimer Structure. *Journal of Medicinal Chemistry* **64**, 15758–15771 (2021).

217. Buck, S. T. G. *et al.* Photodynamic Efficiency of Xanthene Dyes and Their Phototoxicity against a Carcinoma Cell Line: A Computational and Experimental Study. *Journal of Chemistry* **2017**, (2017).

218. Alberts, B. *et al.* Principles of Membrane Transport. in *Molecular Biology of the Cell* vol. 54 1392 (2007).

219. Roth, M., Obaidat, A. & Hagenbuch, B. OATPs, OATs and OCTs: The organic anion and cation transporters of the SLCO and SLC22A gene

superfamilies. *British Journal of Pharmacology* **165**, 1260–1287 (2012).

220. Tuerkova, A. *et al.* Data-Driven Ensemble Docking to Map Molecular Interactions of Steroid Analogs with Hepatic Organic Anion Transporting Polypeptides. *Journal of Chemical Information and Modeling* **61**, 3109–3127 (2021).

221. Abraham, M. J. *et al.* Gromacs: High performance molecular simulations through multi-level parallelism from laptops to supercomputers. *SoftwareX* **1–2**, 19–25 (2015).

222. Huang, J. & Mackerell, A. D. CHARMM36 all-atom additive protein force field: Validation based on comparison to NMR data. *Journal of Computational Chemistry* **34**, 2135–2145 (2013).

223. Humphrey, W., Dalke, A. & Schulten, K. VMD: Visual molecular dynamics. *Journal of Molecular Graphics* **14**, 33–38 (1996).

224. Klähn, M. & Zacharias, M. Transformations in plasma membranes of cancerous cells and resulting consequences for cation insertion studied with molecular dynamics. *Physical Chemistry Chemical Physics* **15**, 14427–14441 (2013).

225. Shahane, G., Ding, W., Palaiokostas, M. & Orsi, M. Physical properties of model biological lipid bilayers: insights from all-atom molecular dynamics simulations. *Journal of Molecular Modeling* **25**, 1–13 (2019).

226. Zizzi, E. A., Cavaglià, M., Tuszynski, J. A. & Deriu, M. A. Alteration of lipid bilayer mechanics by volatile anesthetics: Insights from μs-long molecular dynamics simulations. *iScience* **25**, 103946 (2022).

227. Jo, S., Lim, J. B., Klauda, J. B. & Im, W. CHARMM-GUI membrane builder for mixed bilayers and its application to yeast membranes. *Biophysical Journal* **97**, 50–58 (2009).

228. Wu, E. L. *et al.* CHARMM-GUI membrane builder toward realistic biological membrane simulations. *Journal of Computational Chemistry* **35**, 1997–2004 (2014).

229. Jo, S., Kim, T., Iyer, V. G. & Im, W. CHARMM-GUI: A web-based

graphical user interface for CHARMM. *Journal of Computational Chemistry* **29**, 1859–1865 (2008).

230. Klauda, J. B. *et al.* Update of the CHARMM All-Atom Additive Force Field for Lipids: Validation on Six Lipid Types. *Journal of Physical Chemistry B* **114**, 7830–7843 (2010).

231. Vanommeslaeghe, K. *et al.* CHARMM general force field: A force field for drug-like molecules compatible with the CHARMM all-atom additive biological force fields. *Journal of Computational Chemistry* **31**, 671–690 (2010).

232. Yu, W., He, X., Vanommeslaeghe, K. & MacKerell, A. D. Extension of the CHARMM general force field to sulfonyl-containing compounds and its utility in biomolecular simulations. *Journal of Computational Chemistry* **33**, 2451–2468 (2012).

233. Parrinello, M. & Rahman, A. Polymorphic transitions in single crystals: A new molecular dynamics method. *Journal of Applied Physics* **52**, 7182–7190 (1981).

234. Nosé, S. A unified formulation of the constant temperature molecular dynamics methods. *The Journal of Chemical Physics* **81**, 511–519 (1984).

235. Ewald, P. P. Die Berechnung optischer und elektrostatischer Gitterpotentiale. *Annalen der Physik* **369**, 253–287 (1921).

236. Hess, B., Bekker, H., Berendsen, H. J. C. & Fraaije, J. G. E. M. LINCS: A Linear Constraint Solver for molecular simulations. *Journal of Computational Chemistry* **18**, 1463–1472 (1997).

237. Miller, B. R. I. *et al.* MMPBSA.py: An Efficient Program for End-State Free Energy Calculations. *J. Chem. Theory Comput.* **8**, 3314–3321 (2012).

238. Valdés-Tresanco, M. S., Valdés-Tresanco, M. E., Valiente, P. A. & Moreno, E. gmx_MMPBSA: A New Tool to Perform End-State Free Energy Calculations with GROMACS. *J. Chem. Theory Comput.* **17**, 6281–6291 (2021).

239. Her Choong, F. & Keat Yap, B. Cell-Penetrating Peptides: Correlation between Peptide-Lipid Interaction and Penetration Efficiency. *ChemPhysChem* **22**, 493–498 (2021).

240. Kakiuchi, T., Takasu, Y. & Senda, M. Voltage-Scan Fluorometry of Rose Bengal Ion at the 1, 2-Dichloroethane-Water Interface. *Analytical Chemistry* **64**, 3096–3100 (1992).

241. Nishi, N., Izawa, K., Yamamoto, M. & Kakiuchi, T. AC-modulated voltfluorometric study of the transient adsorption of rose bengal dianions in the transfer across the 1,2-dichloroethane|water interface. *Journal of Physical Chemistry B* **105**, 8162–8169 (2001).

242. Poltorak, L., Sudhölter, E. J. R. & de Smet, L. C. P. M. Effect of charge of quaternary ammonium cations on lipophilicity and electroanalytical parameters: Task for ion transfer voltammetry. *Journal of Electroanalytical Chemistry* **796**, 66–74 (2017).

243. Herzog, G., Kam, V., Berduque, A. & Arrigan, D. W. M. Detection of food additives by voltammetry at the liquid-liquid interface. *Journal of Agricultural and Food Chemistry* **56**, 4304–4310 (2008).

244. Batistela, V. R. *et al.* PKa determinations of xanthene derivates in aqueous solutions by multivariate analysis applied to UV-Vis spectrophotometric data. *Spectrochimica Acta - Part A: Molecular and Biomolecular Spectroscopy* **79**, 889–897 (2011).

245. Gobry, V. *et al.* Generalization of ionic partition diagrams to lipophilic compounds and to biphasic systems with variable phase volume ratios. *Journal of the American Chemical Society* **123**, 10684–10690 (2001).

246. Reymond, F., Steyaert, G., Carrupt, P. A., Testa, B. & Girault, H. Ionic partition diagrams: A potential-pH representation. *Journal of the American Chemical Society* **118**, 11951–11957 (1996).

247. Reymond, F. *et al.* Ionic partition diagrams of ionisable drugs: pH-lipophilicity profiles, transfer mechanisms and charge effects on solvation. *Journal of Electroanalytical Chemistry* **462**, 235–250 (1999).

248. Samec, Z. Electrochemistry at the interface between two immiscible electrolyte solutions (IUPAC technical report). *Pure Appl. Chem.* **76**, 2147–2180 (2004).

249. Kuc-Ciepluch, D. *et al.* The effect of surface modification of

dendronized gold nanoparticles on activation and release of pyroptosis-inducing pro-inflammatory cytokines in presence of bacterial lipopolysaccharide in monocytes. *Colloids and Surfaces B: Biointerfaces* **217**, 112652 (2022).

250. Marczak, A. Fluorescence anisotropy of membrane fluidity probes in human erythrocytes incubated with anthracyclines and glutaraldehyde. *Bioelectrochemistry* **74**, 236–239 (2009).

251. Maulik, P. R. & Shipley, G. G. Interactions of N-stearoyl sphingomyelin with cholesterol and dipalmitoylphosphatidylcholine in bilayer membranes. *Biophysical Journal* **70**, 2256–2265 (1996).

252. Saeedimasine, M., Montanino, A., Kleiven, S. & Villa, A. Role of lipid composition on the structural and mechanical features of axonal membranes: a molecular simulation study. *Scientific Reports* **9**, (2019).

253. Yoguim, M. I. *et al.* Studies on the Interaction of Rose Bengal with the Human Serum Albumin Protein under Spectroscopic and Docking Simulations Aspects in the Characterization of Binding Sites. *Chemosensors* **10**, 440 (2022).

254. Sztandera, K. *et al.* In search of a phosphorus dendrimer-based carrier of rose bengal: Tyramine linker limits fluorescent and phototoxic properties of a photosensitizer. *International Journal of Molecular Sciences* **21**, 1–20 (2020).

255. Kucinska, M. *et al.* Phthalocyanine derivatives possessing 2-(morpholin-4-yl)ethoxy groups as potential agents for photodynamic therapy. *Journal of Medicinal Chemistry* **58**, 2240–2255 (2015).

256. Olivo, M., Bhuvaneswari, R., Lucky, S. S., Dendukuri, N. & Thong, P. S. P. Targeted therapy of cancer using photodynamic therapy in combination with multi-faceted anti-tumor modalities. *Pharmaceuticals* **3**, 1507–1529 (2010).

257. Dos Santos, A. F., De Almeida, D. R. Q., Terra, L. F., Baptista, M. S. & Labriola, L. Photodynamic therapy in cancer treatment - an update review. *Journal of Cancer Metastasis and Treatment* **5**, 25 (2019).

258. Redmond, R. W. & Gamlin, J. N. A compilation of singlet oxygen yields from biologically relevant molecules. *Photochemistry and Photobiology* **70**, 391–475 (1999).

259. Master, A., Livingston, M. & Sen Gupta, A. Photodynamic

nanomedicine in the treatment of solid tumors: Perspectives and challenges. *Journal of Controlled Release* **168**, 88–102 (2013).

260. Qidwai, A. *et al.* Role of nanocarriers in photodynamic therapy. *Photodiagnosis and Photodynamic Therapy* **30**, 101782 (2020).

261. Ghaffari, M. *et al.* Co-delivery of curcumin and Bcl-2 siRNA by PAMAM dendrimers for enhancement of the therapeutic efficacy in HeLa cancer cells. *Colloids and Surfaces B: Biointerfaces* **188**, 110762 (2020).

262. Duncan, R. & Izzo, L. Dendrimer biocompatibility and toxicity. *Advanced Drug Delivery Reviews* **57**, 2215–2237 (2005).

263. Tripathi, P. K. & Tripathi, S. Dendrimers for anticancer drug delivery. *Pharmaceutical Applications of Dendrimers* 131–150 (2019).

264. Gorzkiewicz, M. & Klajnert-Maculewicz, B. Chapter 10 in Dendrimers for Drug Delivery. in *Dendrimers as Nanocarriers for Anticancer Drugs* (eds. Sharma, A. K. & Keservan, R. K.) 327–374 (Apple Academic Press, 2018).

265. Agarwal, A., Gupta, U., Asthana, A. & Jain, N. K. Dextran conjugated dendritic nanoconstructs as potential vectors for anti-cancer agent. *Biomaterials* **30**, 3588–3596 (2009).

266. Patri, A. K., Kukowska-Latallo, J. F. & Baker, J. R. Targeted drug delivery with dendrimers: Comparison of the release kinetics of covalently conjugated drug and non-covalent drug inclusion complex. *Advanced Drug Delivery Reviews* **57**, 2203–2214 (2005).

267. Karthikeyan, K., Babu, A., Kim, S. J., Murugesan, R. & Jeyasubramanian, K. Enhanced photodynamic efficacy and efficient delivery of Rose Bengal using nanostructured poly(amidoamine) dendrimers: Potential application in photodynamic therapy of cancer. *Cancer Nanotechnology* **2**, 95–103 (2011).

268. Kojima, C., Toi, Y., Harada, A. & Kono, K. Preparation of poly (ethylene glycol)-attached dendrimers encapsulating photosensitizers for application to photodynamic therapy. *Bioconjugate Chemistry* **18**, 663–670 (2007).

269. Gorzkiewicz, M. *et al.* Effect of the Structure of Therapeutic Adenosine Analogues on Stability and Surface Electrostatic Potential of their Complexes with Poly(propyleneimine) Dendrimers. *Macromolecular Rapid Communications* **40**, 1900181 (2019).

270. Gorzkiewicz, M. *et al.* Poly(propyleneimine) glycodendrimers non-covalently bind ATP in a pH- and salt-dependent manner – model studies for adenosine analogue drug delivery. *International Journal of Pharmaceutics* **544**, 83–90 (2018).

271. Maingi, V., Jain, V., Bharatam, P. V. & Maiti, P. K. Dendrimer building toolkit: Model building and characterization of various dendrimer architectures. *Journal of Computational Chemistry* **33**, 1997–2011 (2012).

272. Wang, J., Wolf, R. M., Caldwell, J. W., Kollman, P. A. & Case, D. A. Development and testing of a general Amber force field. *Journal of Computational Chemistry* **25**, 1157–1174 (2004).

273. Jain, V., Maingi, V., Maiti, P. K. & Bharatam, P. V. Molecular dynamics simulations of PPI dendrimer-drug complexes. *Soft Matter* **9**, 6482–6496 (2013).

274. Gupta, S. & Biswas, P. Effect of pH on Size and Internal Structure of Poly(propylene imine) Dendrimers: A Molecular Dynamics Simulation Study. *Journal of Physical Chemistry B* **122**, 9250–9263 (2018).

275. Ramos, M. C., Horta, V. A. C. & Horta, B. A. C. Molecular Dynamics Simulations of PAMAM and PPI Dendrimers Using the GROMOS-Compatible 2016H66 Force Field. *Journal of Chemical Information and Modeling* **59**, 1444–1457 (2019).

276. Koper, G. J. M. *et al.* Protonation mechanism of poly(propylene imine) dendrimers and some associated oligo amines. *Journal of the American Chemical Society* **119**, 6512–6521 (1997).

277. Van Duijvenbode, R. C., Borkovec, M. & Koper, G. J. M. Acid-base properties of poly(propylene imine) dendrimers. *Polymer* **39**, 2657–2664 (1998).

278. Jakalian, A., Jack, D. B. & Bayly, C. I. Fast, efficient generation of high-quality atomic charges. AM1-BCC model: II. Parameterization and validation.

Journal of Computational Chemistry **23**, 1623–1641 (2002).

279. Wang, J., Wang, W., Kollman, P. A. & Case, D. A. Automatic atom type and bond type perception in molecular mechanical calculations. *Journal of Molecular Graphics and Modelling* **25**, 247–260 (2006).

280. Sousa Da Silva, A. W. & Vranken, W. F. ACPYPE - AnteChamber PYthon Parser interfacE. *BMC Research Notes* **5**, 367 (2012).

281. Mark, P. & Nilsson, L. Structure and dynamics of the TIP3P, SPC, and SPC/E water models at 298 K. *Journal of Physical Chemistry A* **105**, 9954–9960 (2001).

282. Bussi, G., Donadio, D. & Parrinello, M. Canonical sampling through velocity rescaling. *Journal of Chemical Physics* **126**, 014101 (2007).

283. Berendsen, H. J. C., Postma, J. P. M., Van Gunsteren, W. F., Dinola, A. & Haak, J. R. Molecular dynamics with coupling to an external bath. *The Journal of Chemical Physics* **81**, 3684–3690 (1984).

284. Darden, T., York, D. & Pedersen, L. Particle mesh Ewald: An N·log(N) method for Ewald sums in large systems. *The Journal of Chemical Physics* **98**, 10089–10092 (1993).

285. Kavyani, S., Amjad-Iranagh, S., Dadvar, M. & Modarress, H. Hybrid Dendrimers of PPI(core)-PAMAM(shell): A Molecular Dynamics Simulation Study. *Journal of Physical Chemistry B* **120**, 9564–9575 (2016).

286. Rudnick, J. & Gaspari, G. The aspherity of random walks. *Journal of Physics A: General Physics* **19**, L191–L193 (1986).

287. Maiti, P. K., Çağin, T., Wang, G. & Goddard, W. A. Structure of PAMAM dendrimers: Generations 1 through 11. *Macromolecules* **37**, 6236–6254 (2004).

288. Deriu, M. A., Popescu, L. M., Ottaviani, M. F., Danani, A. & Piticescu, R. M. Iron oxide/PAMAM nanostructured hybrids: combined computational and experimental studies. *Journal of Materials Science* **51**, 1996–2007 (2016).

289. Baker, N. A., Sept, D., Joseph, S., Holst, M. J. & McCammon, J. A.

Electrostatics of nanosystems: Application to microtubules and the ribosome. *Proceedings of the National Academy of Sciences of the United States of America* **98**, 10037–10041 (2001).

290. Chen, C. & Pettitt, B. M. The binding process of a nonspecific enzyme with DNA. *Biophysical Journal* **101**, 1139–1147 (2011).

291. Klajnert, B. & Bryszewska, M. The interaction of tryptophan and ANS with PAMAM dendrimers. *Cellular and Molecular Biology Letters* **7**, 1087–1094 (2002).

292. Huang, C. Y. Determination of binding stoichiometry by the continuous variation method: The job plot. *Methods in Enzymology* **87**, 509–525 (1982).

293. Hong, S. *et al.* Interaction of polycationic polymers with supported lipid bilayers and cells: Nanoscale hole formation and enhanced membrane permeability. *Bioconjugate Chemistry* **17**, 728–734 (2006).

294. Honary, S. & Zahir, F. Effect of zeta potential on the properties of nano-drug delivery systems - A review (Part 1 and 2). *Tropical Journal of Pharmaceutical Research* **12**, 255–264 (2013).

295. Basset-Seguin, N. & Herms, F. Update on the management of basal cell carcinoma. *Acta Dermato-Venereologica* vol. 100 284–290 Preprint at (2020).

296. Di Stefani, A. & Chimenti, S. Basal cell carcinoma: clinical and pathological features. *Giornale Italiano di Dermatologia e Venereologia* **150**, 385–391 (2015).

297. Tanis, I. & Karatasos, K. Molecular dynamics simulations of polyamidoamine dendrimers and their complexes with linear poly(ethylene oxide) at different pH conditions: Static properties and hydrogen bonding. *Physical Chemistry Chemical Physics* **11**, 10017–10028 (2009).

298. Kono, K. *et al.* Temperature sensitivity control of alkylamide-terminated poly(amidoamine) dendrimers induced by guest molecule binding. *Journal of the American Chemical Society* **129**, 7222–7223 (2007).

299. Jansen, J. F. G. A., Meijer, E. W. & de Brabander-van den Berg, E. M. M. The Dendritic Box: Shape-Selective Liberation of Encapsulated Guests.

Journal of the American Chemical Society vol. 117 4417–4418 Preprint at (1995).

300. Tamaki, M., Fukushima, D. & Kojima, C. Dual pH-sensitive and UCST-type thermosensitive dendrimers: Phenylalanine-modified polyamidoamine dendrimers with carboxyl termini. *RSC Advances* **8**, 28147–28151 (2018).

301. Haba, Y., Harada, A., Takagishi, T. & Kono, K. Synthesis of biocompatible dendrimers with a peripheral network formed by linking of polymerizable groups. *Polymer* **46**, 1813–1820 (2005).

302. Dabrzalska, M., Zablocka, M., Mignani, S., Majoral, J. P. & Klajnert-Maculewicz, B. Phosphorus dendrimers and photodynamic therapy. Spectroscopic studies on two dendrimer-photosensitizer complexes: Cationic phosphorus dendrimer with rose bengal and anionic phosphorus dendrimer with methylene blue. *International Journal of Pharmaceutics* **492**, 266–274 (2015).

303. Dabrzalska, M. *et al.* Fourier transform infrared spectroscopy (FTIR) characterization of the interaction of anti-cancer photosensitizers with dendrimers. *Analytical and Bioanalytical Chemistry* **408**, 535–544 (2016).

304. Opitz, A. W. & Wagner, N. J. Structural investigations of poly(amido amine) dendrimers in methanol using molecular dynamics. *Journal of Polymer Science, Part B: Polymer Physics* **44**, 3062–3077 (2006).

305. Barraza, L. F., Zuñiga, M., Alderete, J. B., Arbeloa, E. M. & Jiménez, V. A. Effect of pH on Eosin Y/PAMAM interactions studied from absorption spectroscopy and molecular dynamics simulations. *Journal of Luminescence* **199**, 258–265 (2018).

306. Caballero, J., Poblete, H., Navarro, C. & Alzate-Morales, J. H. Association of nicotinic acid with a poly(amidoamine) dendrimer studied by molecular dynamics simulations. *Journal of Molecular Graphics and Modelling* **39**, 71–78 (2013).

307. Kanchi, S., Gosika, M., Ayappa, K. G. & Maiti, P. K. Dendrimer Interactions with Lipid Bilayer: Comparison of Force Field and Effect of Implicit vs Explicit Solvation. *Journal of Chemical Theory and Computation* **14**, 3825–3839 (2018).

308. Lee, I., Athey, B. D., Wetzel, A. W., Meixner, W. & Baker, J. R.

Structural molecular dynamics studies on polyamidoamine dendrimers for a therapeutic application: Effects of pH and generation. *Macromolecules* **35**, 4510–4520 (2002).

309. Porcar, L. *et al.* Structural investigation of PAMAM dendrimers in aqueous solutions using small-angle neutron scattering: Effect of generation. *Journal of Physical Chemistry B* **112**, 14772–14778 (2008).

310. Rathgeber, S., Monkenbusch, M., Kreitschmann, M., Urban, V. & Brulet, A. Dynamics of star-burst dendrimers in solution in relation to their structural properties. *Journal of Chemical Physics* **117**, 4047–4062 (2002).

311. Liu, Y., Bryantsev, V. S., Diallo, M. S. & Goddard, W. A. PAMAM dendrimers undergo pH responsive conformational changes withoutswelling. *Journal of the American Chemical Society* **131**, 2798–2799 (2009).

312. Maiti, P. K., Çağin, T., Lin, S. T. & Goddard, W. A. Effect of solvent and pH on the structure of PAMAM dendrimers. *Macromolecules* **38**, 979–991 (2005).

313. Topp, A., Bauer, B. J., Tomalia, D. A. & Amis, E. J. Effect of solvent quality on the molecular dimensions of PAMAM dendrimers. *Macromolecules* **32**, 7232–7237 (1999).

314. Scherrenber, R. *et al.* The molecular characteristics of poly(propyleneimine) dendrimers as studied with small-angle neutron scattering, viscosimetry, and molecular dynamics. *Macromolecules* **31**, 456–461 (1998).

315. Prosa, T. J., Bauer, B. J., Amis, E. J., Tomalia, D. A. & Scherrenberg, R. A SAXS study of the internal structure of dendritic polymer systems. *Journal of Polymer Science, Part B: Polymer Physics* **35**, 2913–2924 (1997).

316. Wu, C. PH response of conformation of poly(propylene imine) dendrimer in water: A molecular simulation study. *Molecular Simulation* **36**, 1164–1172 (2010).

317. Gorzkiewicz, M., Buczkowski, A., Pałecz, B. & Klajnert-Maculewicz, B. PAMAM and PPI Dendrimers in Biophysical and Thermodynamic Studies on the Delivery of Therapeutic Nucleotides, Nucleosides and Nucleobase Derivatives for Anticancer Applications. in 183–243 (2019). doi:10.1007/978-981-

13-0989-2_7.

318. Miklis, P., Çağin, T. & Goddard, W. A. Dynamics of Bengal Rose Encapsulated in the Meijer Dendrimer Box. *J. Am. Chem. Soc* **119**, 7458–7462 (1997).

319. Liang, X., Wang, K. K. & Zhu, T. C. Singlet oxygen dosimetry modeling for photodynamic therapy. in *Optical Methods for Tumor Treatment and Detection: Mechanisms and Techniques in Photodynamic Therapy XXI* vol. 8210 82100T (2012).

320. Kashyap, A., Ramasamy, E., Ramalingam, V. & Pattabiraman, M. Supramolecular Control of Singlet Oxygen Generation. *Molecules* **26**, 2673 (2021).

321. Allison, R. R. *et al.* Photosensitizers in clinical PDT. *Photodiagnosis and Photodynamic Therapy* **1**, 27–42 (2004).

322. Zhang, D. & Nettles, C. B. A generalized model on the effects of nanoparticles on fluorophore fluorescence in solution. *Journal of Physical Chemistry C* **119**, 7941–7948 (2015).

323. Zhai, W., Wang, C., Yu, P., Wang, Y. & Mao, L. Single-layer MnO2 nanosheets suppressed fluorescence of 7-hydroxycoumarin: Mechanistic study and application for sensitive sensing of ascorbic acid in vivo. *Analytical Chemistry* **86**, 12206–12213 (2014).

324. Killig, F., Stark, G. & Apell, H. J. Photodynamic inactivation of the Na,K-ATPase occurs via different pathways. *Journal of Membrane Biology* **200**, 133–144 (2004).

325. Nishiyama, N., Morimoto, Y., Jang, W. D. & Kataoka, K. Design and development of dendrimer photosensitizer-incorporated polymeric micelles for enhanced photodynamic therapy. *Advanced Drug Delivery Reviews* **61**, 327–338 (2009).

326. Hirakawa, K., Hirano, T., Nishimura, Y., Arai, T. & Nosaka, Y. Dynamics of singlet oxygen generation by DNA-binding photosensitizers. *Journal of Physical Chemistry B* **116**, 3037–3044 (2012).

327. Gorzkiewicz, M. *et al.* Fludarabine-Specific Molecular Interactions

with Maltose-Modified Poly(propyleneimine) Dendrimer Enable Effective Cell Entry of the Active Drug Form: Comparison with Clofarabine. *Biomacromolecules* **20**, 1429–1442 (2019).

328. Fox, L. J., Richardson, R. M. & Briscoe, W. H. PAMAM dendrimer - cell membrane interactions. *Advances in Colloid and Interface Science* vol. 257 1–18 Preprint at (2018).

329. Kochevar, I. E. & Redmond, R. W. Photosensitized production of singlet oxygen. *Methods in Enzymology* **319**, 20–28 (2000).

330. Kutner, N., Kunduru, K. R., Rizik, L. & Farah, S. Recent Advances for Improving Functionality, Biocompatibility, and Longevity of Implantable Medical Devices and Deliverable Drug Delivery Systems. *Advanced Functional Materials* **31**, 2010929 (2021).

331. Kim, M. W., Kwon, S.-H., Choi, J. H. & Lee, A. A Promising Biocompatible Platform: Lipid-Based and Bio-Inspired Smart Drug Delivery Systems for Cancer Therapy. *International Journal of Molecular Sciences* **19**, 3859 (2018).

332. Chen, W., Zhou, S., Ge, L., Wu, W. & Jiang, X. Translatable High Drug Loading Drug Delivery Systems Based on Biocompatible Polymer Nanocarriers. *Biomacromolecules* **19**, 1732–1745 (2018).

333. Sawyers, C. Targeted cancer therapy. *Nature* **432**, 294–297 (2004).

334. Srinivasarao, M. & Low, P. S. Ligand-targeted drug delivery. *Chem. Rev* **117**, 12133–12164 (2017).

335. Biswas, S. Biomolecular robotics for chemomechanically driven guest delivery fuelled by intracellular ATP. *Nat. Chem* **5**, 613–620 (2013).

336. Naito, M. A phenylboronate-functionalized polyion complex micelle for ATP-triggered release of siRNA. *Angew. Chem. Int. Ed* **51**, 10751–10755 (2012).

337. Jie, D. & Andreas, W. ATP-responsive and ATP-fueled self-assembling systems and materials. *Adv. Mater* **32**, 2002629 (2020).

338. Mishra, A., Dhiman, S. & George, S. J. ATP-driven synthetic

supramolecular assemblies: from ATP as a template to fuel. *Angew. Chem. Int. Ed* **60**, 2740–2756 (2021).

339. Liao, W. C. Adenosine triphosphate-triggered release of macromolecular and nanoparticle loads from aptamer/DNA-crosslinked microcapsules. *ACS Nano* **9**, 9078–9086 (2015).

340. Mu, J., Lin, J., Huang, P. & Chen, X. Development of endogenous enzyme-responsive nanomaterials for theranostics. *Chem. Soc. Rev* **47**, 5554–5573 (2018).

341. Karimi, M. Smart micro/nanoparticles in stimulus-responsive drug/gene delivery systems. *Chem. Soc. Rev* **45**, 1457–1501 (2016).

342. Zhou, Y. Intracellular ATP levels are a pivotal determinant of chemoresistance in colon cancer cells. *Cancer Res* **72**, 304–314 (2012).

343. Gribble, F. M. A novel method for measurement of submembrane ATP concentration. *J. Biol. Chem* **275**, 30046–30049 (2000).

344. Shaw, R. J. & Cantley, L. C. R. PI(3)K and mTOR signalling controls tumour cell growth. *Nature* **441**, 424–430 (2006).

345. Hsu, N. Y. Viral reorganization of the secretory pathway generates distinct organelles for RNA replication. *Cell* **141**, 799–811 (2010).

346. Meshkini, A. Fine-tuning of the cellular signaling pathways by intracellular GTP levels. *Cell Biochem. Biophys* **70**, 27–32 (2014).

347. Mitchinson, T. & Kirschner, M. Dynamic Instability of Microtubule Growth. *Nature* **312**, 237–241 (1984).

348. Aldaz, H., Rice, L. M., Stearns, T. & Agard, D. A. Insights into microtubule nucleation from the crystal structure of human γ- tubulin. *Nature* **435**, 523–527 (2005).

349. Kerssemakers, J. W. J. Assembly dynamics of microtubules at molecular resolution. *Nature* **442**, 709–712 (2006).

350. Hoenger, A., Sablin, E. P., Vale, R. D., Fletterick, R. J. & Milligan, R. A. Three–dimensional structure of a tubulin–motor–protein complex. *Nature*

376, 271–274 (1995).

351. Avila, J. Microtubule functions. *Life Sci* **50**, 327–334 (1991).

352. Dogterom, M. & Yurke, B. Measurement of the force-velocity relation for growing microtubules. *Science* **278**, 856–860 (1997).

353. Kruse, A. C. Activation and allosteric modulation of a muscarinic acetylcholine receptor. *Nature* **504**, 101–106 (2013).

354. Kobilka, B. K. G protein coupled receptor structure and activation. *Biochim. Biophys. Acta* **1768**, 794–807 (2007).

355. Carter, A. P. Functional insights from the structure of the 30S ribosomal subunit and its interactions with antibiotics. *Nature* **407**, 340–348 (2000).

356. Lin, J., Gagnon, M. G., Bulkley, D. & Steitz, T. A. Conformational changes of elongation factor G on the ribosome during tRNA translocation. *Cell* **160**, 219–227 (2015).

357. Cherfils, J. & Zeghouf, M. Regulation of small GTPases by GEFs, GAPs, and GDIs. *Physiol. Rev* **93**, 269–309 (2013).

358. Dijk, A. A. & Makeyev, E. V. Initiation of viral RNA-dependent RNA polymerization. *J. Gen. Virol* **85**, 1077–1093 (2004).

359. Walsh, D. & Mohr, I. Viral subversion of the host protein synthesis machinery. *Nat. Rev. Microbiol* **9**, 860–875 (2011).

360. Kumar, M. Crystallographic and biochemical analysis of rotavirus NSP2 with nucleotides reveals a nucleoside diphosphate kinase-like activity. *J. Virol* **81**, 12272–12284 (2007).

361. Hu, B., Guo, H., Zhou, P. & Shi, Z.-L. Characteristics of SARS-CoV-2 and COVID-19. *Nat. Rev. Microbiol* **19**, 141–154 (2020).

362. Inaoka, T. & Ochi, K. RelA protein is involved in induction of genetic competence in certain Bacillus subtilis strains by moderating the level of intracellular GTP. *J. Bacteriol* **184**, 3923–3930 (2002).

363. Otero, A. S. NM23/nucleoside diphosphate kinase and signal

transduction. *J. Bioenerg. Biomembr* **32**, 269–275 (2000).

364. Smee, D. F. Intracellular metabolism of favipiravir (T-705) in uninfected and influenza A (H5N1) virus-infected cells. *J. Antimicrob. Chemother* **64**, 741–746 (2009).

365. Smethurst, P. A. & Griffin, M. Measurement of tissue transglutaminase activity in a permeabilized cell system: its regulation by Ca2+ and nucleotides. *Biochem. J* **313**, 803–808 (1996).

366. Desai, A. & Mitchison, T. J. Microtubule polymerization dynamics. *Annu. Rev. Cell Dev. Biol* **13**, 83–117 (1997).

367. Yajima, H. Conformational changes in tubulin in GMPCPP and GDP-taxol microtubules observed by cryoelectron microscopy. *J. Cell Biol* **198**, 315–322 (2012).

368. Gonen, S., DiMaio, F., Gonen, T. & Baker, D. Design of ordered two-dimensional arrays mediated by noncovalent protein-protein interfaces. *Science* **348**, 1365–1368 (2015).

369. Suzuki, Y. Self-assembly of coherently dynamic, auxetic, two-dimensional protein crystals. *Nature* **533**, 369–373 (2016).

370. Mogaki, R., Hashim, P. K., Okuro, K. & Aida, T. Guanidinium-based “molecular glues” for modulation of biomolecular functions. *Chem. Soc. Rev* **46**, 6480–6491 (2017).

371. Uchida, N. Photoclickable dendritic molecular glue: noncovalent-to-covalent photochemical transformation of protein hybrids. *J. Am. Chem. Soc* **135**, 4684–4687 (2013).

372. Wang, Q. High-water-content mouldable hydrogel by mixing clay and dendritic molecular binder. *Nature* **463**, 339–343 (2010).

373. Tacar, O., Sriamornsak, P. & Dass, C. R. Doxorubicin: an update on anticancer molecular action, toxicity and novel drug delivery sys- tems. *J. Pharm. Pharmacol* **65**, 157–170 (2013).

374. Jurrus, E. *et al.* Improvements to the APBS biomolecular solvation software suite. *Protein Science* **27**, 112–128 (2018).

375. Hyman, A. Preparation of modified tubulins. *Meth. Enzymol* **196**, 478–485 (1990).

376. Wang, H.-W., Long, S., Finley, K. R. & Nogales, E. Assembly of GMPCPP-bound tubulin into helical ribbons and tubes and effect of colchicine. *Cell Cycle* **4**, 1157–1160 (2005).

377. Kim, S. H. Synthesis of PEG-iodine-capped gold nanoparticles and their contrast enhancement in in vitro and in vivo for X-ray/CT. *J. Nanomater* (2012) doi:10.1155/2012/504026.

378. Grillaud, M., Russier, J. & Bianco, A. Polycationic adamantane-based dendrons of different generations display high cellular uptake without triggering cytotoxicity. *J. Am. Chem. Soc* **136**, 810–819 (2014).

379. Melki, R., Fievez, S. & Carlier, M.-F. Continuous monitoring of Pi release following nucleotide hydrolysis in actin or tubulin assembly using 2-amino-6-mercapto-7-methylpurine ribonucleoside and purine-nucleoside phosphorylase as an enzyme-linked assay. *Biochemistry* **35**, 12038–12045 (1996).

380. Zhang, R., Alushin, G. M., Brown, A. & Nogales, E. Mechanistic origin of microtubule dynamic instability and its modulation by EB pro- teins. *Cell* **162**, 849–859 (2015).

381. Garzoni, M., Okuro, K., Ishii, N., Aida, T. & Pavan, G. M. Structure and shape effects of molecular glue on supramolecular tubulin assemblies. *ACS Nano* **8**, 904–914 (2014).

382. Pavan, G. M. Modeling the interaction between dendrimers and nucleic acids: a molecular perspective through hierarchical scales. *ChemMedChem* **9**, 2623–2631 (2014).

383. Walker, D. A., Kowalczyk, B., Cruz, M. O. & Grzybowski, B. A. Elec- trostatics at the nanoscale. *Nanoscale* **3**, 1316–1344 (2011).

384. Herce, H. D., Garcia, A. E. & Cardoso, M. C. Fundamental molecular mechanism for the cellular uptake of guanidinium-rich molecules. *J. Am. Chem. Soc* **136**, 17459–17467 (2014).

385. Limongelli, V., Bonomi, M. & Parrinello, M. Funnel metadynamics as accurate binding free-energy method. *Proceedings of the National Academy of*

Sciences of the United States of America **110**, 6358–6363 (2013).

386. Palma, J. & Pierdominici-Sottile, G. On the Uses of PCA to Characterise Molecular Dynamics Simulations of Biological Macromolecules: Basics and Tips for an Effective Use. *ChemPhysChem* **24**, e202200491 (2023).

387. Hub, J. S. & Groot, B. L. de. Detection of Functional Modes in Protein Dynamics. *PLOS Computational Biology* **5**, e1000480 (2009).

388. Tuccinardi, T. What is the current value of MM/PBSA and MM/GBSA methods in drug discovery? *Expert Opinion on Drug Discovery* **16**, 1233–1237 (2021).

389. Fogolari, F. *et al.* MM/PBSA analysis of molecular dynamics simulations of bovine beta-lactoglobulin: free energy gradients in conformational transitions? *Proteins* **59**, 91–103 (2005).

390. Kuhn, B., Gerber, P., Schulz-Gasch, T. & Stahl, M. Validation and use of the MM-PBSA approach for drug discovery. *Journal of Medicinal Chemistry* **48**, 4040–4048 (2005).

391. Zwanzig, R. W. High-Temperature Equation of State by a Perturbation Method. I. Nonpolar Gases. *J. Chem. Phys.* **22**, 1420–1426 (1954).

392. Straatsma, T. P. & Berendsen, H. J. C. Free energy of ionic hydration: Analysis of a thermodynamic integration technique to evaluate free energy differences by molecular dynamics simulations. *J. Chem. Phys.* **89**, 5876–5886 (1988).

393. Stock, L., Cirqueira, L. & Treptow, W. Dilute vs Non-Dilute Flooding Molecular Dynamics Simulations - Where do We Draw the Line. *Biophysical Journal* **118**, 48a (2020).

394. Cirqueira, L., Stock, L. & Treptow, W. Improved Flooding Molecular Dynamics Analysis. *Biophysical Journal* **118**, 141a (2020).

Appendix

Appendix to Chapter 3

Molecular modelling and simulation of anesthetics

3.1 Elucidating the interaction between volatile anesthetics and human tubulin assemblies

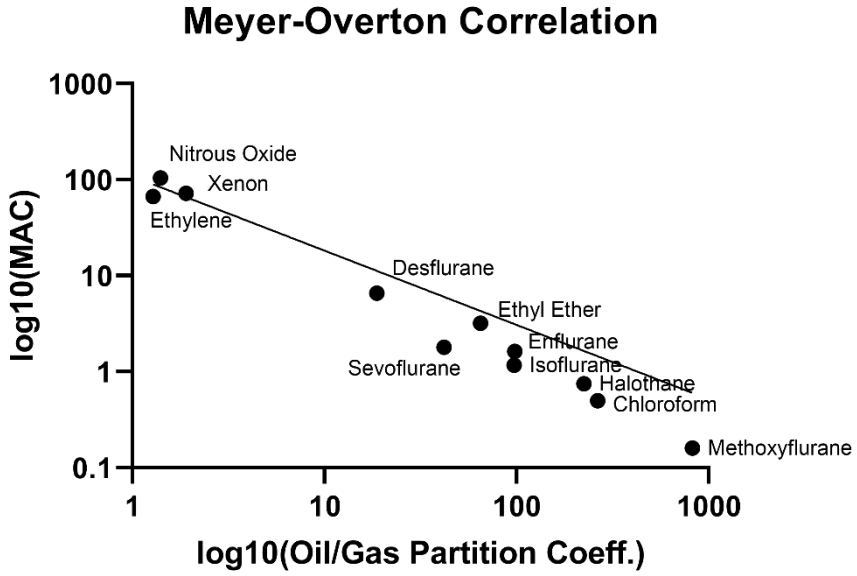

Supplementary Figure S3.1 The Meyer-Overton correlation, highlighting the strict relationship between anesthetic potency (in terms of Minimum Alveolar Concentration) and solubility in olive-oil-like, lipid media.

3.1.1 Detailed Docking Protocol and Results

For blind docking, snapshots of the tubulin dimers were extracted from the molecular dynamics simulations with the respective ligands every 10ns in the last 50ns of the simulations. Blind docking was performed in Autodock-Vina after preparing the dimer snapshots and the ligands in AutoDockTools, adding Gasteiger charges, and saving them in pdbqt format, using the prepare_receptor4.py and prepare_ligand4.py scripts, respectively. For each isotype-anesthetic pair, the

search box was centered at the center of mass of the given snapshot and was built to encompass the whole dimer, including the C-terminal tails. Docking was performed with the exhaustiveness set to 64, and with the default setting of 9 maximum generated poses per run. For each anesthetic-isotype pair, all sampled poses were analyzed to obtain an average estimate of the binding energies, which is reported in the main text. The binding sites which were most frequently found by blind docking, as well as the ones with highest mean predicted affinity were further validated using a second set of local docking runs, carried out as follows: for each isotype-anesthetic pair, the dominant conformations have been extracted from the cluster analysis of each of the three 100-ns MD simulations, excluding the highly-fluctuating C-terminal tails; clustering was performed with an RMSD cutoff of 0.15 nm using GROMACS, and resulted in one dominant tubulin conformation for each individual simulation, i.e. three conformations for each isotype-anesthetic pair. Extracted conformations were converted into pdbqt with the same methodology used for blind docking, assigning Gasteiger charges, again using the prepare_receptor4.py script included in AutoDockTools, and used as targets for docking. For each isotype-anesthetic pair, on each of the aforementioned targets, the grid box has been iteratively centered to encompass the residues forming the binding sites found from blind docking runs (most frequent and highest avg. affinity sites). To achieve this, the optimal grid box geometry was determined dynamically using the AutoGridFR program[1] by supplying the list of residues forming the site, with the grid spacing set to 1.0 Å as required by Autodock-Vina, and with an additional padding of 2 Å. Local docking was again carried out in Autodock-Vina, with the same settings as for the blind docking runs (except for the grid box geometry), namely a maximum of 9 generated poses per run, with exhaustiveness set to 64. Finally, the best conformation for each anesthetic on each isotype has been extracted, along with the predicted affinity, which is reported in table ST1 below.

Supplementary Table ST3.1. Predicted binding affinities in kcal/mol with each anesthetic after local docking validation. The affinity of the best overall binding pose is reported.

	Isotype		
	αβVI (kcal/mol)	**αβIIa (kcal/mol)**	**αβIVa (kcal/mol)**
Ethylene	-2.1	-2.5	-2.2
Desflurane	-5.6	-5.5	-5.9
Halothane	-4.4	-4.3	-4.8
Methoxyflurane	-4.4	-4.8	-4.6

Local docking validation confirmed that Ethylene is consistently predicted to interact with a considerably lower affinity to all three isotypes with respect to the other three compounds, completing docking runs at -2.5 kcal/mol at best on isotype αβIIa, in the cleft formed by αTRP388, αMET203, αPHE267, αALA201, αPHE202 and αPRO173. For the other three anesthetics, the trends provided by the blind docking estimates were confirmed: the highest-affinity pose for Desflurane was located on isotype αβIVa in the cleft formed by αTHR239, αLEU136, αPHE138 and αPHE135 . Halothane and Methoxyflurane showed again comparable predicted affinities, with the best poses scoring both -4.8 kcal/mol, on isotype αβIVa in the case of Halothane and isotype αβIIa for Methoxyflurane. Overall, the local docking runs confirmed the results obtained from blind docking, and further underlined how the docking approach on its own is not sufficient to provide insights into the interaction mechanism. This is expected, due to the low predicted affinity and the lack of classical lock-and-key mechanism, with a single, strong binding site in the systems under investigation. Rather, the possible simultaneous interactions of multiple ligand molecules in multiple binding sites on the tubulin dimer and the weak nature of the interactions themselves justify the investigation through Molecular Dynamics and contact probability analysis, which provides a more in-depth understanding on where and how much interaction occurs on the dimer, and yields more robust quantitative data in this scenario.

3.1.2 Homology Models

In detail, the three simulated isotypes βVI, βIIa and βIVa featured 94.9%, 94.7% and 95.0% residues in those regions, respectively. Since it is agreed upon[2] that a fair quality model should feature more than 90% of residues in most favoured regions, the models generated in the present work are of good quality. For comparison, the 3J6F template used for modelling showed 91.4% of residues in the most favoured regions and 0.1% in generally disallowed regions.

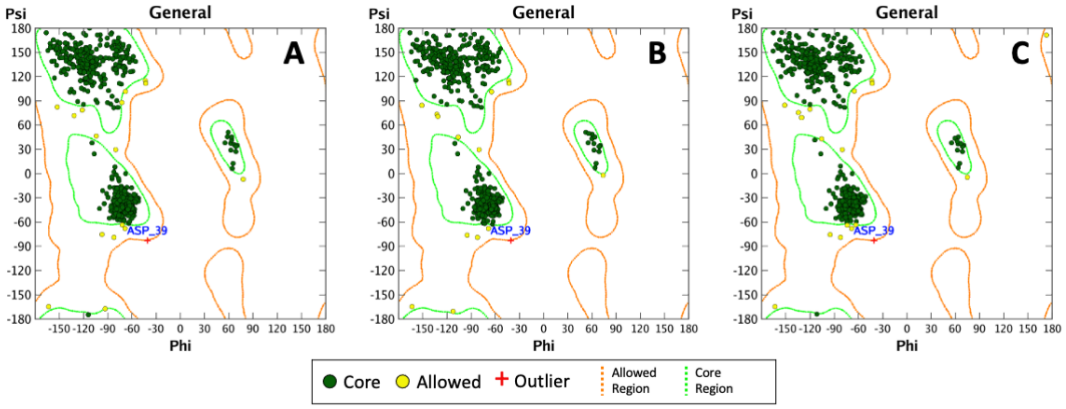

Supplementary Figure S3.2. Ramachandran plots for the modeled dimers αβVI (A), αβIIA (B) and αβIVa (C).

The Verify-3D analysis reported an averaged 3D-1D score higher than 0.2 for every isotype modeled, which means the models passed the Verify-3D test. Dimers with isotypes βVI, βIIa and βIVa specifically showed 94.12%, 96.09% and 94.97% of residues with scores greater than 0.2 respectively, with only the highly variable C-terminal regions partly falling below that threshold.

The WHAT_CHECK verification confirmed the goodness of the models, reporting a Ramachandran Z-score of 0.869, 1.120 and 0.917 for the three studied dimers αβVI, αβIIA, αβIVa along with normal bond length and angle variations.

Finally, the ERRAT quality factors were compared with thresholds indicative of good quality models[3]. The results consisted of quality factors above 88 for every α-tubulin isotype and above 90 for every modeled β-tubulin isotype. The three subsequently simulated dimers αβVI, αβIIa, αβIVa scored respectively 88.86, 91.36 and 90.18 for their α chains and 90.18, 90.18 and 92.49 for their β chains, hence confirming high model quality.

3.1.3 Molecular Dynamics

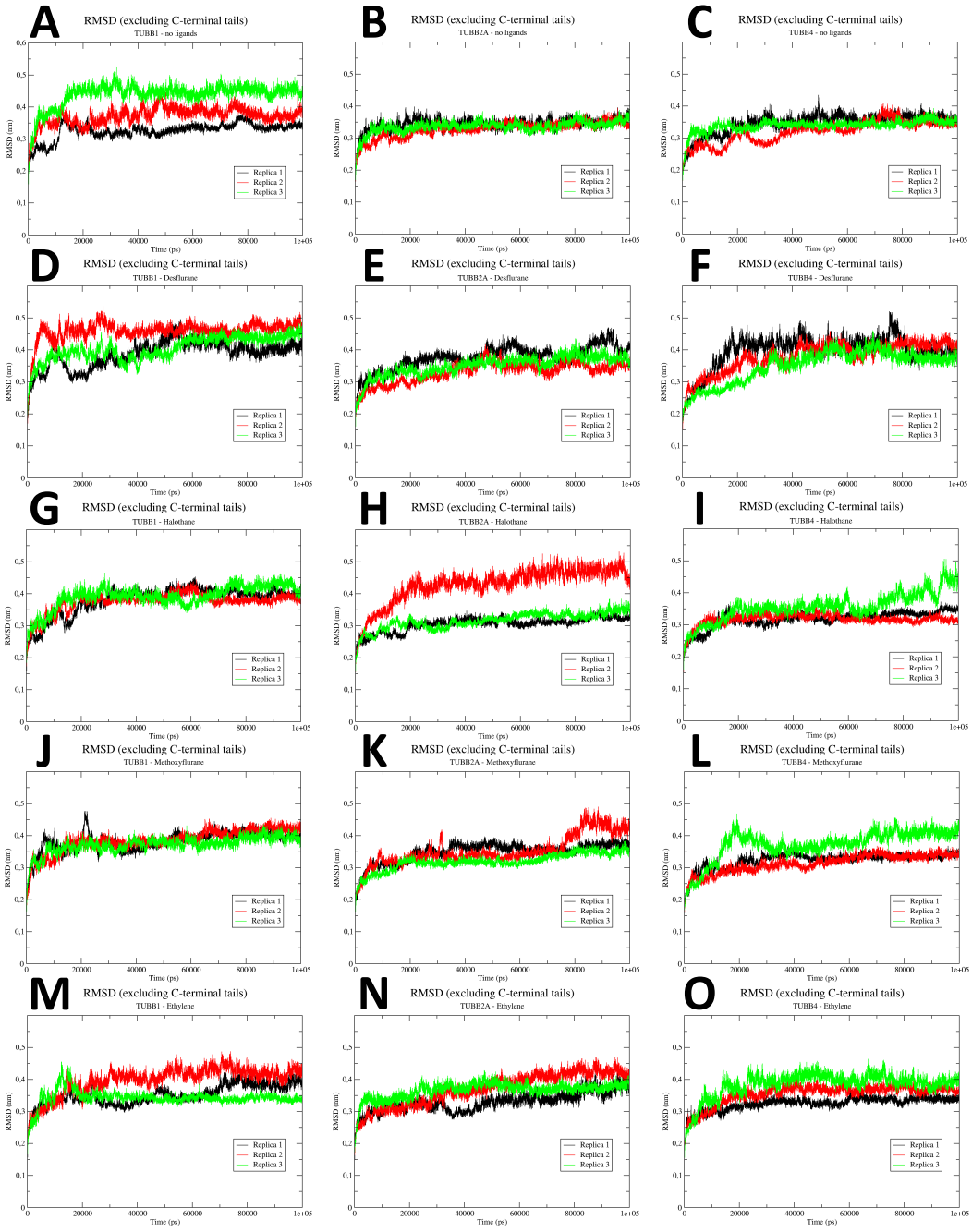

Supplementary Figure S3.3. RMSD plots for each individual replica of all simulated systems. Black line = replica 1, red line = replica 2, green line = replica 3. Columns represent isotypes, starting on the left with αβVI: a) without ligands, d) with Desflurane, g) with Halothane, j) with methoxyflurane, m) with Ethylene. Middle column is isotype αβIIa b) without ligands, e) with Desflurane, h) with Halothane, k) with methoxyflurane, n) with

Ethylene. Right column is isotype αβIVa c) without ligands, f) with Desflurane, i) with Halothane, l) with methoxyflurane, o) with Ethylene.

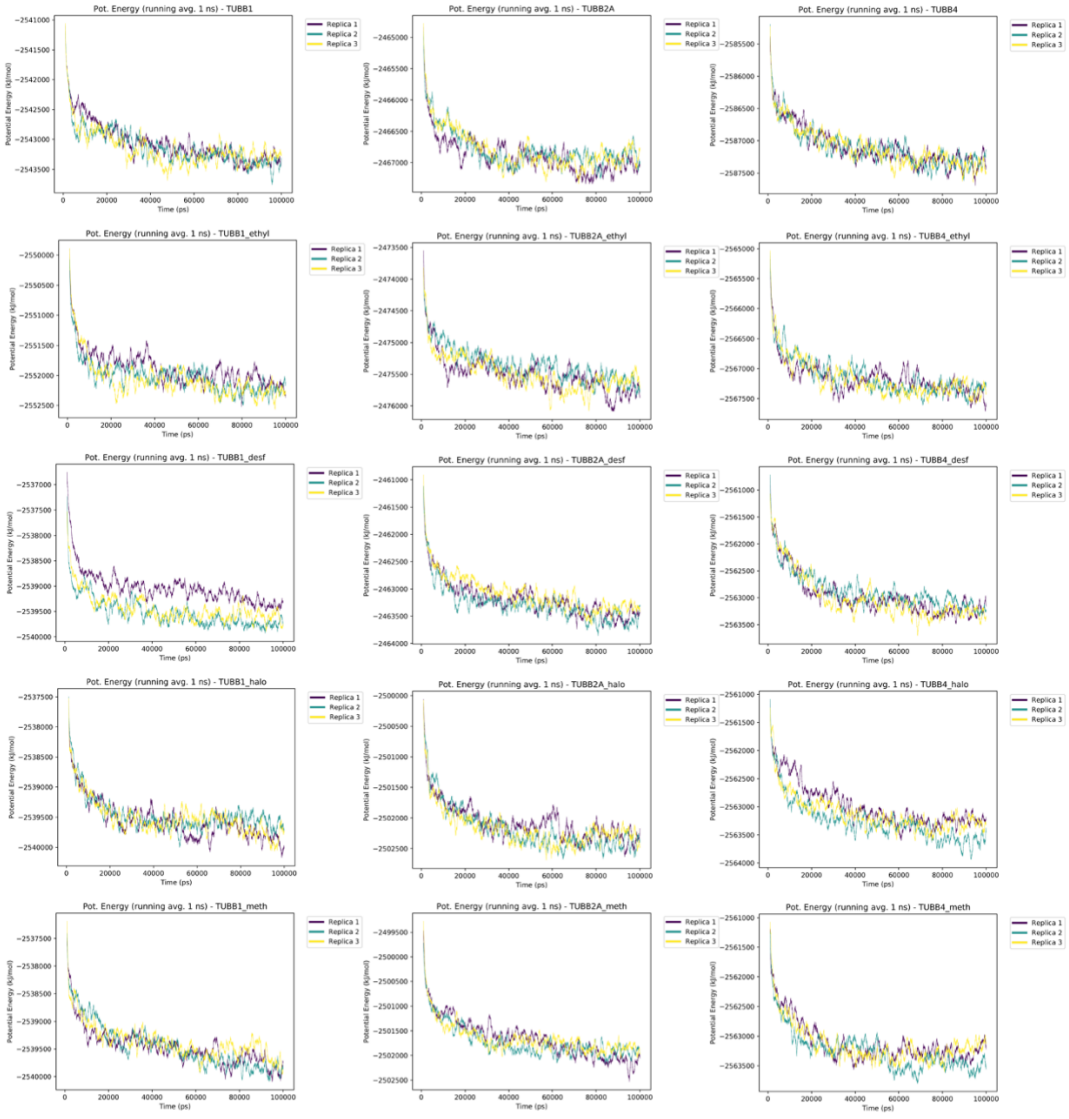

Supplementary Figure S3.4. Potential Energy plots for each individual replica of all simulated systems. Columns represent simulations of different isotypes, starting on the left with αβVI, middle column is isotype αβIIa, right column is isotype αβIVa. Rows correspond to simulations with different ligands (top to bottom): without ligands; with ethylene, with desflurane, with halothane and with methoxyflurane.

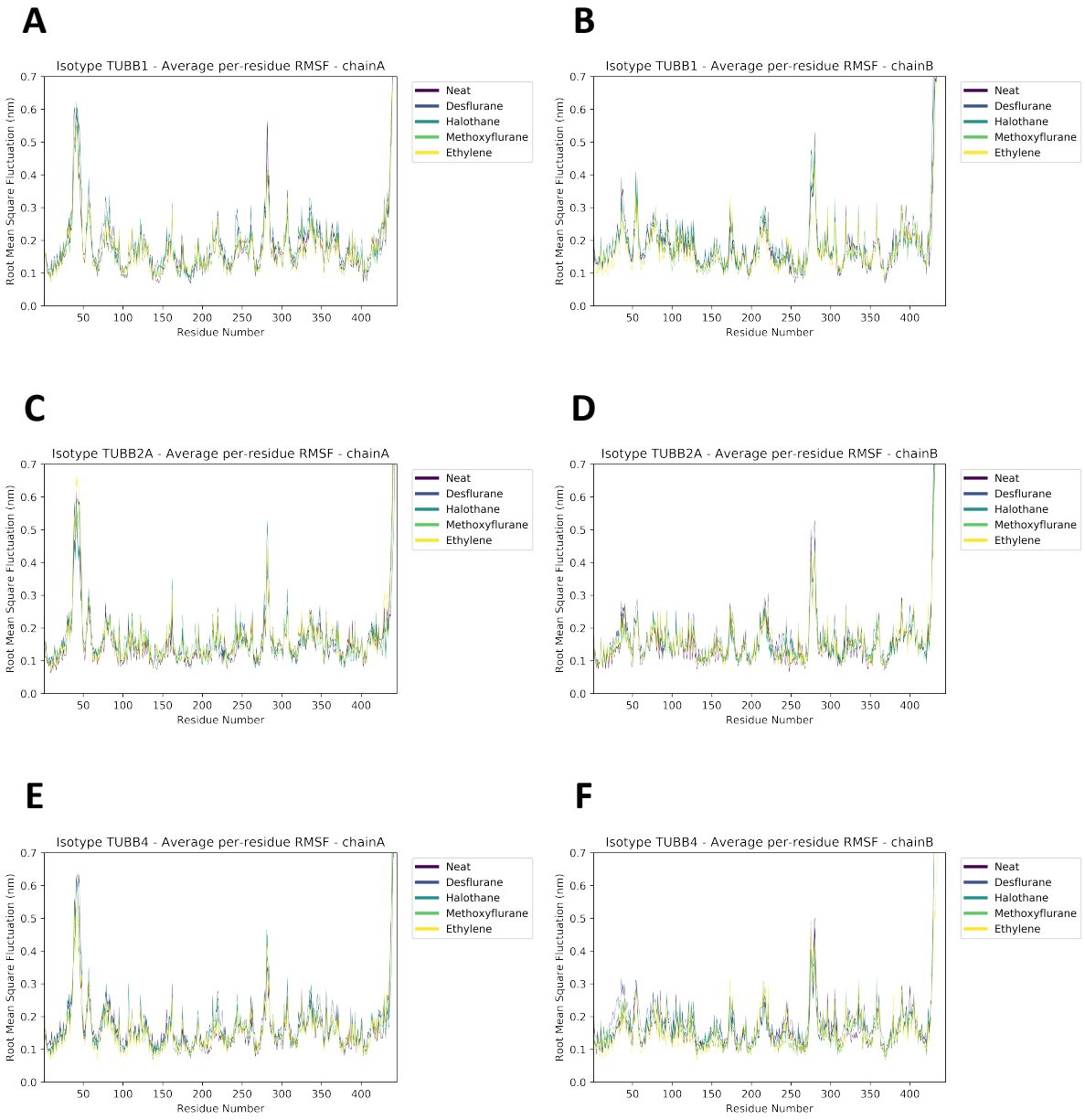

Supplementary Figure S3.5. RMSF plots for each simulated isotype with and without anesthetics. Panels are as follows: A: αβVI dimer, chain alpha, B: αβVI dimer, chain beta, C: αβIIa dimer, chain alpha, D: αβIIa dimer, chain beta, E: αβIVa dimer, chain alpha, F: αβIVa dimer, chain beta.

3.1.4 Per-residue contact probabilities

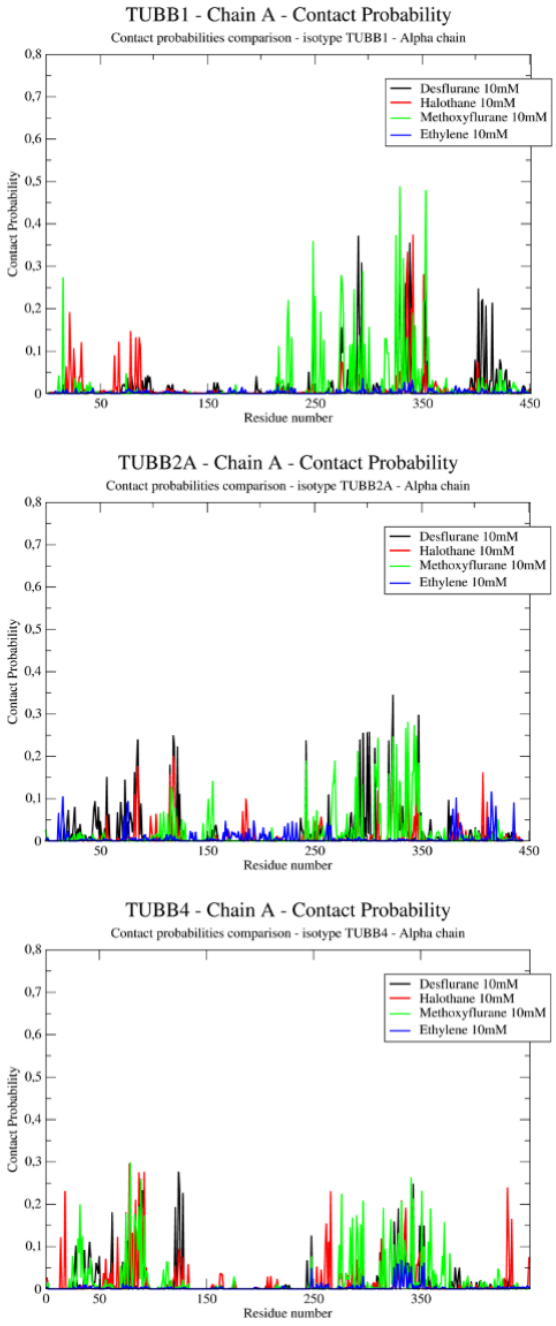

Supplementary Figure S3.6. Per-residue contact probability for chain A of each isotype. Each plot reports contact probabilities with desflurane (black), halothane (red), methoxyflurane (green) and ethylene (blue). The latter shows the lowest overall contact probabilities, consistent with notably lower potency as a general anesthetic. Desflurane has an exclusive area of interaction on isotype αβVI between residues 390 and 420. Single-

residue contact probabilities are comparable among the first three anesthetics, with methoxyflurane showing more ubiquitous interactions on this subunit.

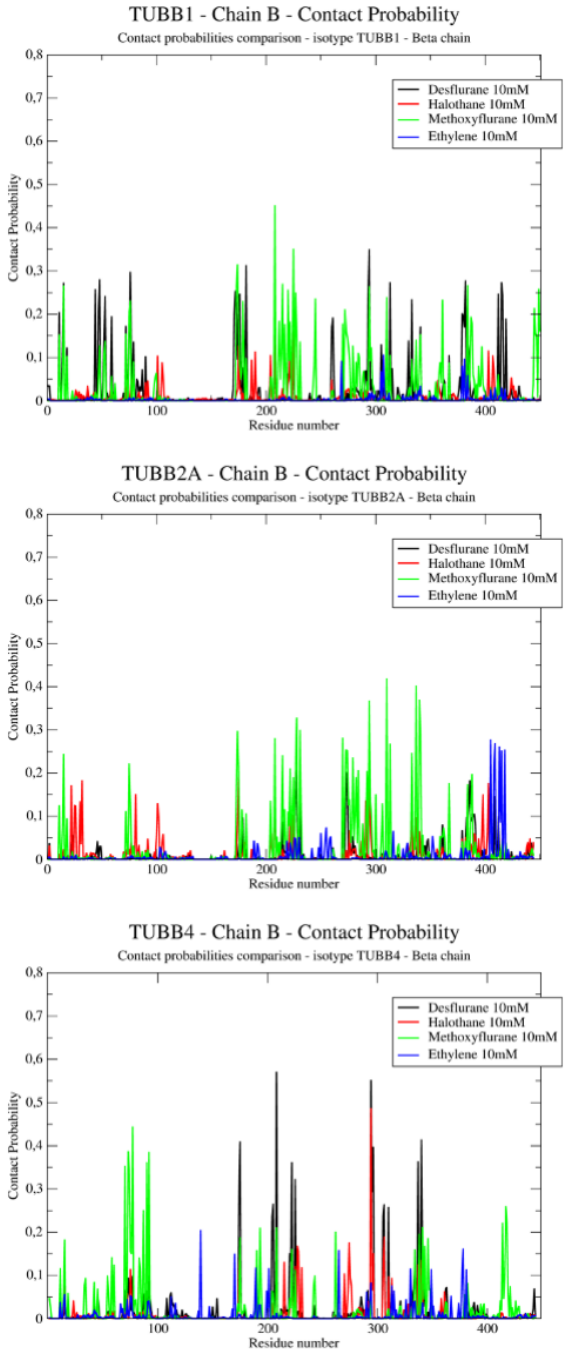

Supplementary Figure S3.7. Per-residue contact probability for chain B of each isotype. Each plot reports contact probabilities with desflurane (black), halothane (red),

methoxyflurane (green) and ethylene (blue). The latter shows the lowest overall contact probabilities, consistent with notably lower potency as a general anesthetic, with a single spike in contact probability only on isotype αβIIa around residues 400 to 410. Single-residue contact probabilities are comparable among the first three anesthetics, with methoxyflurane showing more ubiquitous interactions on the beta chain of subunits αβVI and αβIIa. Isotype αβIVa interestingly has peak contact probabilities of above 0.4 for desflurane, halothane and methoxyflurane, the latter having exclusive areas of interaction on all three tested isotypes.

3.1.5 Proximity of Tryptophan residues

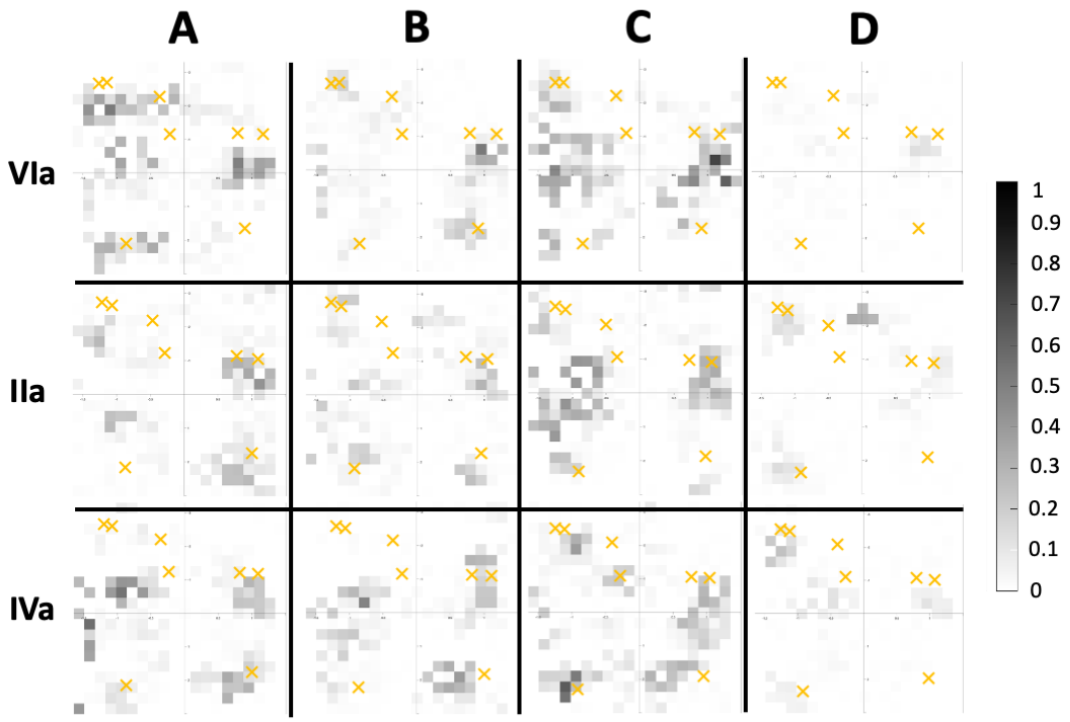

Supplementary Figure S3.8. Sectorized contact probability heatmaps for each simulated isotype (rows) with each anesthetic (columns). A: desflurane. B: halothane. C: methoxyflurane. D: ethylene. Tryptophan residue locations highlighted as orange crosses on the heatmaps. Color scale is 0 to 1 contact probability.

3.1.6 Binding Clefts

Supplementary Table ST3.2. Frequent binding clefts for isotypes αβVI and αβIIa

	Ligand	Cleft	Residues
αβVI	Desflurane	C_D1	αPRO325, αVAL328, αASN329, αILE332, αLYS352, αVAL353, αALA247
		C_D2	αGLU290, αTHR292, αASN293, αALA331, αTHR334, αILE335, αLYS338

		C_D3	βGLU412, βASN413, βASP417, βVAL419, βGLU383, βSER382, βARG380, βASN379
		C_D4	βVAL175, βGLU181, βPRO182, βALA185, βMET170, βPRO171, βSER172, βPRO173, βASP203, βGLU205, βARG380, βHIS384
		C_D5	βSER78, βSER79, βILE76, βTHR72, βGLN11, βASN14, βGLN15, βALA18
	Halothane	C_H1	αPRO325, αVAL328, αASN329, αILE332, αLYS352, αVAL353, αALA247
		C_H2	βLYS174, βVAL175, βASP177, βTHR219, βPRO220, βTHR221, βTYR222
		C_H3	αPHE87, αLEU86, αTYR83, αTRP21, αGLU22, αCYS25
	Methoxy-flurane	C_M1	αPRO325, αVAL328, αASN329, αILE332, αLYS352, αVAL353, αALA247
		C_M2	αPRO274, αVAL275, αILE276, αGLU290, αILE291, αALA294, αCYS295, αALA299
		C_M3	βALA275, βGLY360, βPRO358, βLEU228, βHIS227
		C_M4	βGLU288, βLEU289, βSER285, βLEU284, βALA283
		C_M5	βPRO173, βVAL175, βSER176, βASP177, βTHR178, βHIS384, βMET388, βALA387
	Ethylene	C_E1	βARG307, βARG306, βVAL381, βASN379
αβIIa	Desflurane	C_D1	αLYS326, αASP327, αASN329, αALA330, αALA333, αGLY354, αLYS352
		C_D2	αALA65, αVAL66, αARG64, αGLN91, αLEU92, αILE122, αLEU125
		C_D3	βGLU383, βTHR386, βPHE389, βSER413, βGLU412, βTHR409
		C_D4	βALA231, βSER230, βLEU228, βHIS227, βLEU361, βLEU273, βTHR274
	Halothane	C_H1	αLYS326, αASP327, αASN329, αALA330, αALA333, αGLY354, αLYS352
		C_H2	αGLU90, αGLN91, αLEU92, αLEU125
		C_H3	βSER78, βGLY79, βASP74, βGLY71, βPHE92, βGLY93, βPHE90
		C_H4	βMET403, βGLY400, βTHR399, βTYR398
	Methoxy-flurane	C_M1	αLYS326, αASN329, αALA330, αALA333, αLYS336, αTHR337, αASN356, αGLY354, αLYS352, αPHE351, αGLY350, αLEU317, αGLN342, αVAL344
		C_M2	βGLY308, βASN337, βTYR340, βVAL333, βASP295, βSER296, βPHE294
		C_M3	βHIS227, βLEU228, βSER230, βALA231, βSER275, βTHR274, βLEU273, βARG276
	Ethylene	C_E1	βTHR409, βGLU410

3.1.7 MM/PBSA Binding Energy Decomposition maps

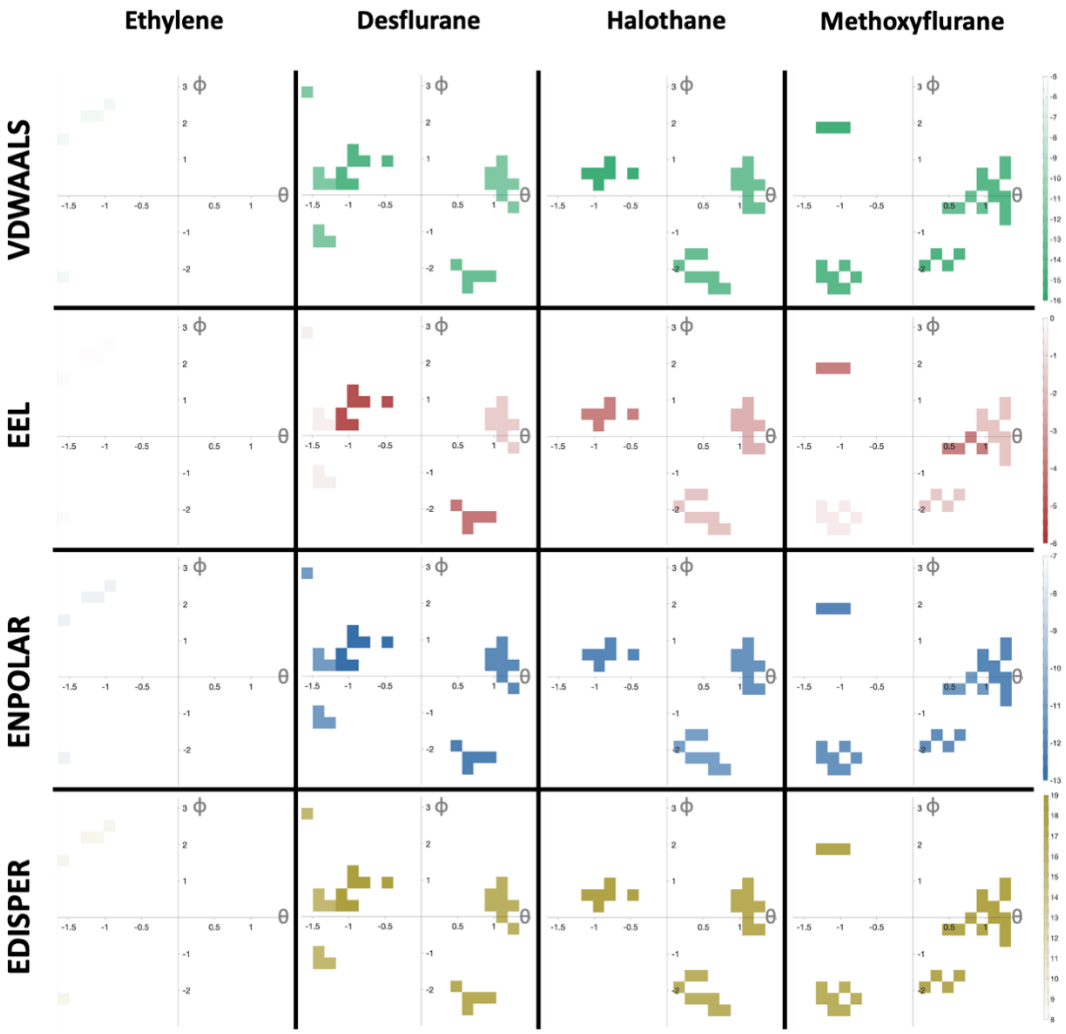

Supplementary Figure S3.9. MM/PBSA binding energy decomposition into the four main components for isotype αβIVa with all simulated ligands. VDWAALS represents the Van der Waals interaction not including 1-4 terms; EEL are electrostatic interactions not including 1-4 terms; ENPOLAR and EDISPER are the non-polar contributions.

3.1.8 Frequent Docking Interactions

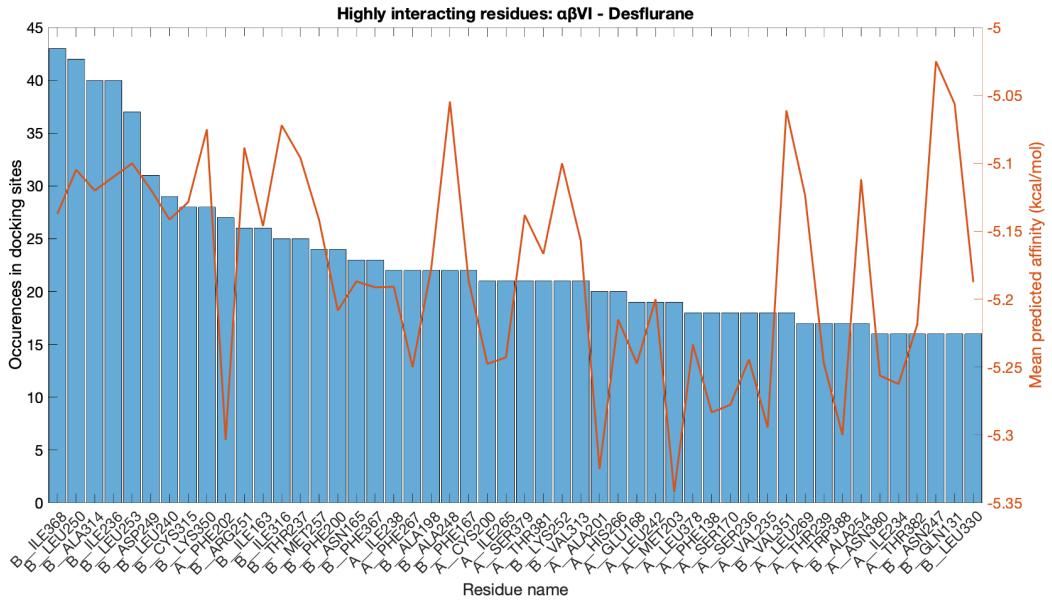

Supplementary Figure S3.10. Residue occurrence across all calculate docking poses, calculated as residues within 6 Å of each docked desflurane pose on the αβVI dimer (bars). Corresponding mean predicted affinity of all binding poses where the given residue was within 6 Å reported as a red line.

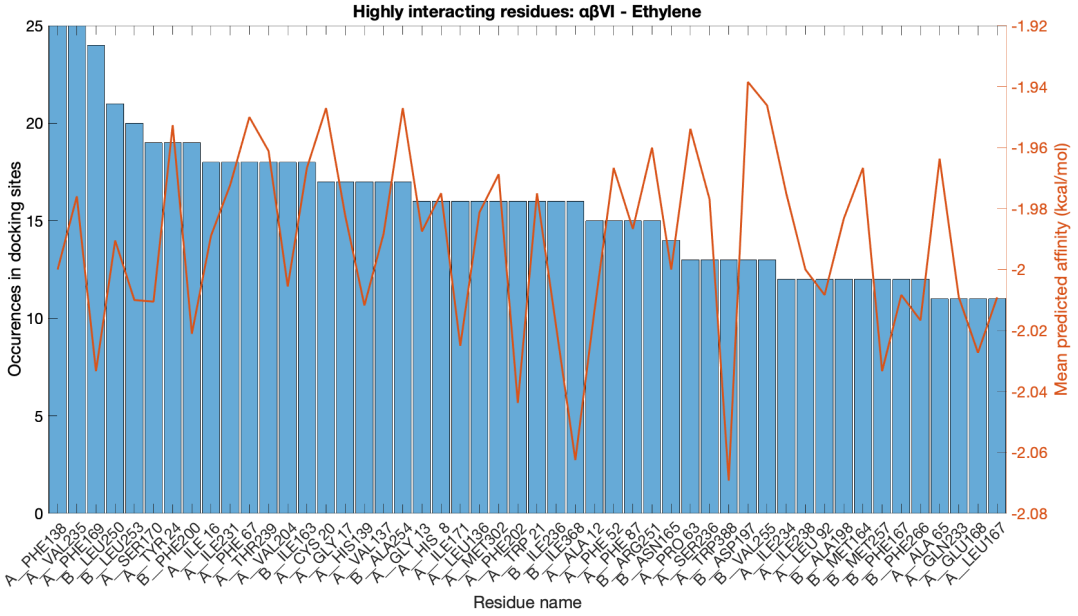

Supplementary Figure S3.11. Residue occurrence across all calculate docking poses, calculated as residues within 6 Å of each docked ethylene pose on the αβVI dimer (bars). Corresponding mean predicted affinity of all binding poses where the given residue was within 6 Å reported as a red line.

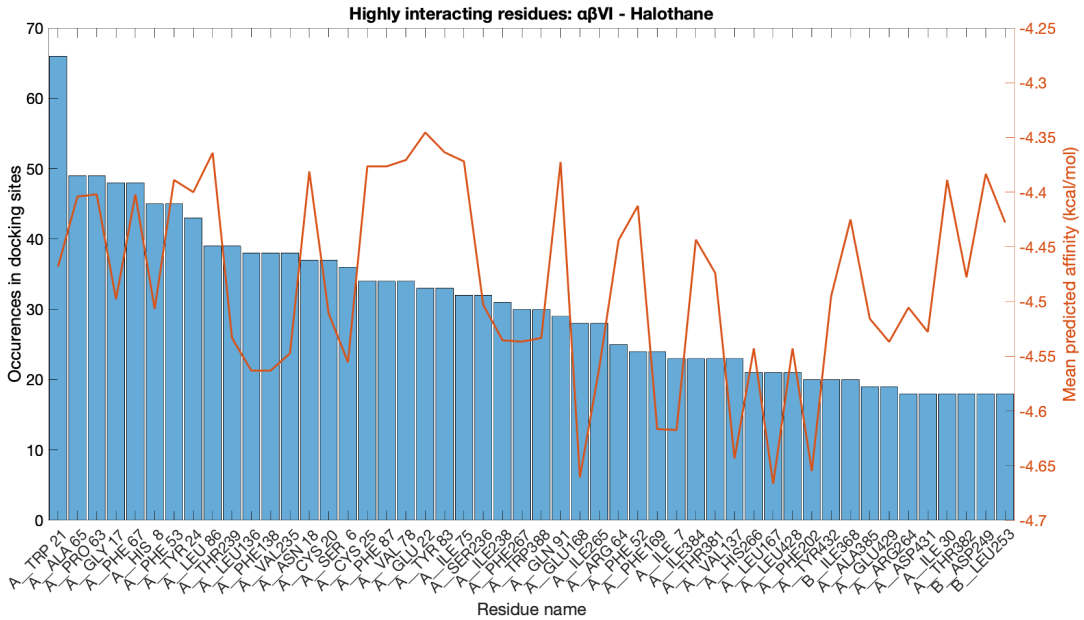

Supplementary Figure S3.12. Residue occurrence across all calculate docking poses, calculated as residues within 6 Å of each docked halothane pose on the αβVI dimer (bars).

Corresponding mean predicted affinity of all binding poses where the given residue was within 6 Å reported as a red line.

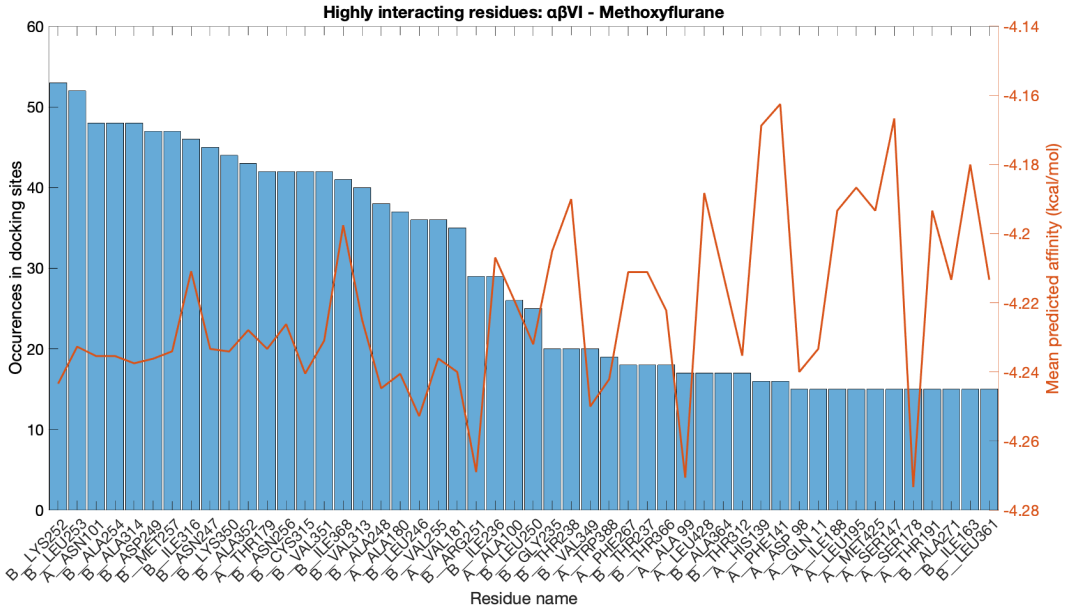

Supplementary Figure S3.13. Residue occurrence across all calculate docking poses, calculated as residues within 6 Å of each docked methoxyflurane pose on the αβVI dimer (bars). Corresponding mean predicted affinity of all binding poses where the given residue was within 6 Å reported as a red line.

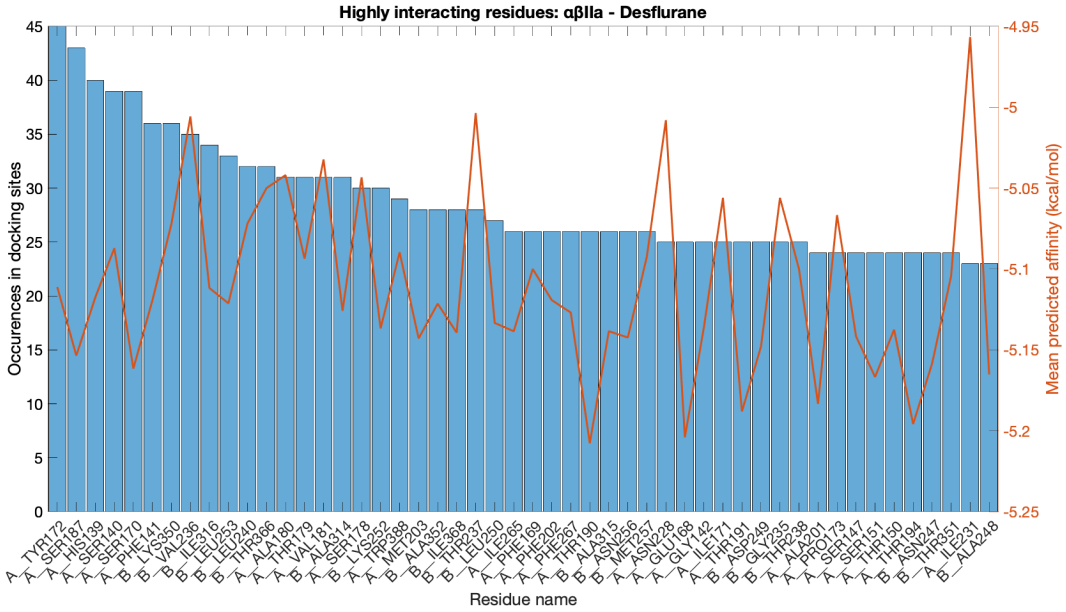

Supplementary Figure S3.14. Residue occurrence across all calculated docking poses, calculated as residues within 6 Å of each docked desflurane pose on the αβIIa dimer (bars). Corresponding mean predicted affinity of all binding poses where the given residue was within 6 Å reported as a red line.

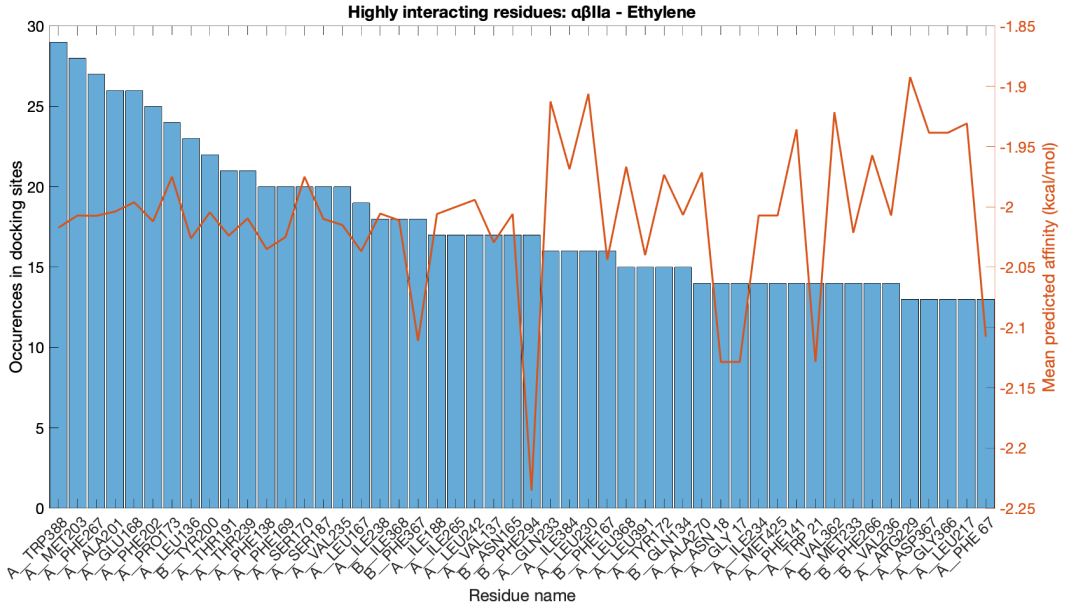

Supplementary Figure S3.15. Residue occurrence across all calculate docking poses, calculated as residues within 6 Å of each docked ethylene pose on the αβIIa dimer (bars). Corresponding mean predicted affinity of all binding poses where the given residue was within 6 Å reported as a red line.

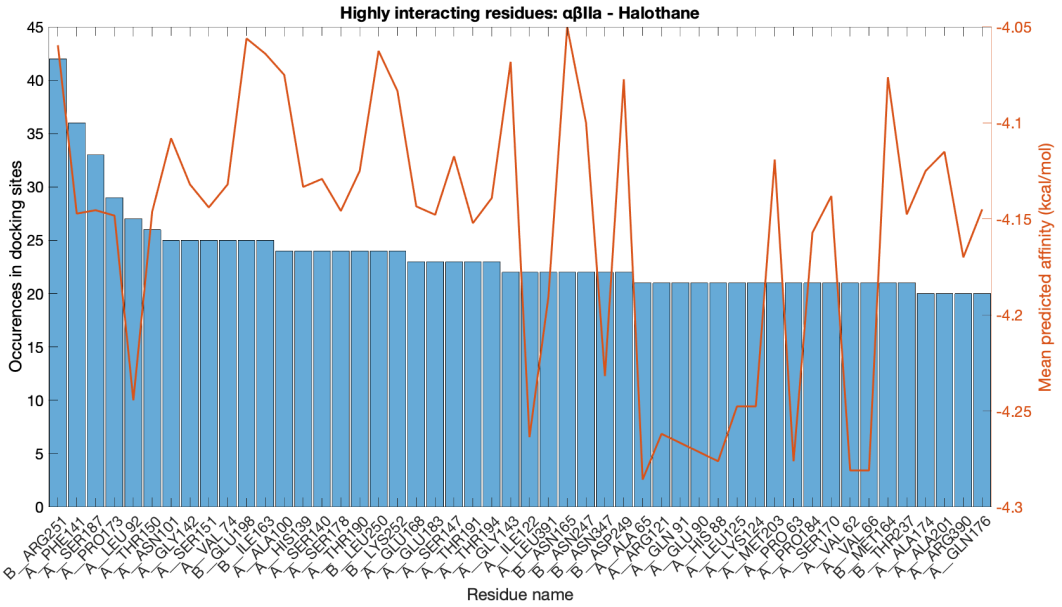

Supplementary Figure S3.16. Residue occurrence across all calculate docking poses, calculated as residues within 6 Å of each docked halothane pose on the αβIIa dimer (bars). Corresponding mean predicted affinity of all binding poses where the given residue was within 6 Å reported as a red line.

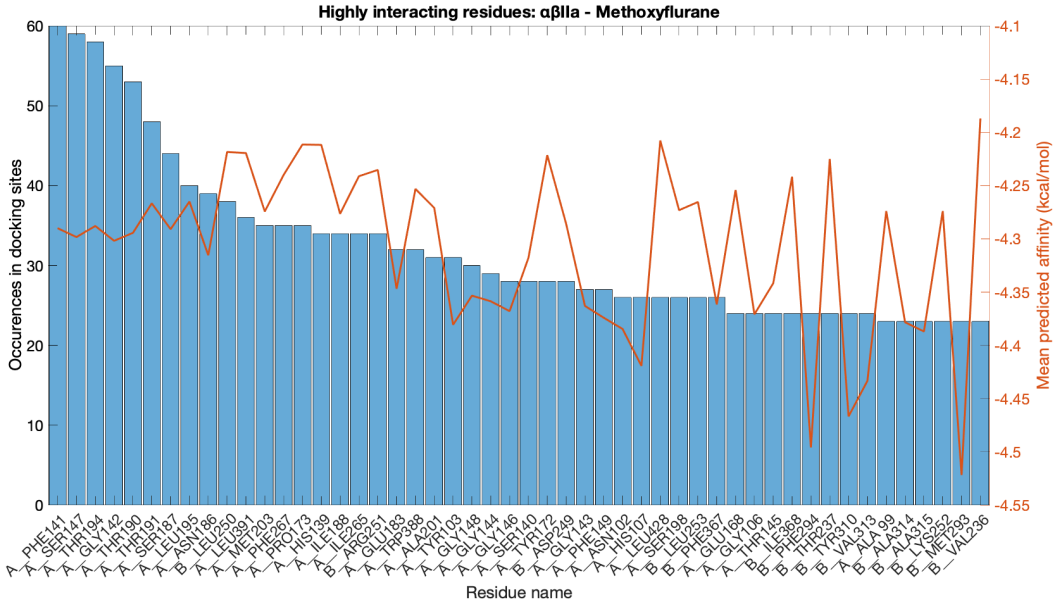

Supplementary Figure S3.17. Residue occurrence across all calculate docking poses, calculated as residues within 6 Å of each docked methoxyflurane pose on the αβIIa dimer

(bars). Corresponding mean predicted affinity of all binding poses where the given residue was within 6 Å reported as a red line.

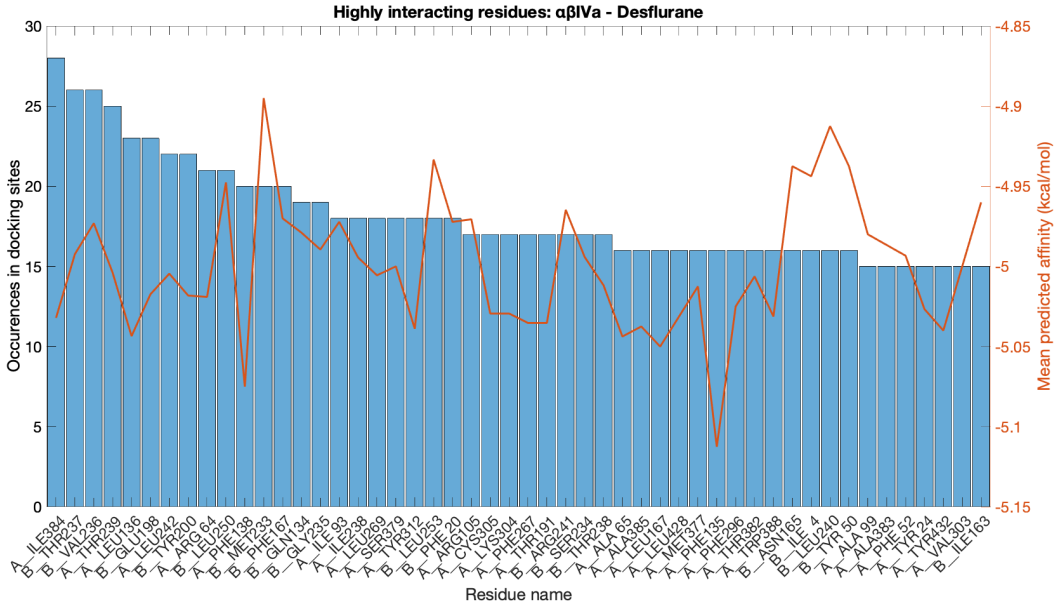

Supplementary Figure S3.18. Residue occurrence across all calculate docking poses, calculated as residues within 6 Å of each docked desflurane pose on the αβIVa dimer (bars). Corresponding mean predicted affinity of all binding poses where the given residue was within 6 Å reported as a red line.

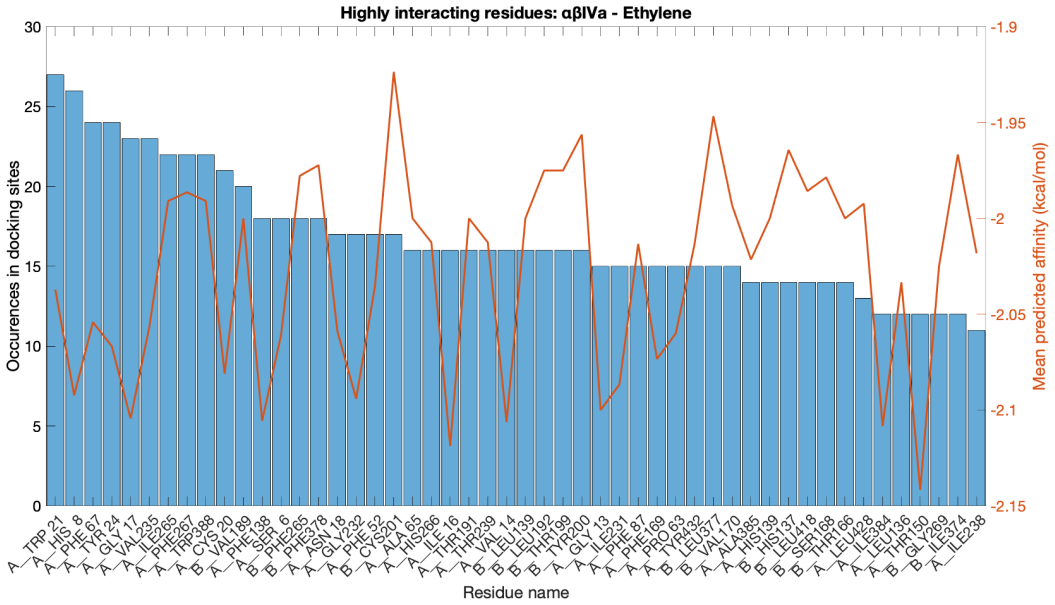

Supplementary Figure S 3.19. Residue occurrence across all calculate docking poses, calculated as residues within 6 Å of each docked ethylene pose on the αβIVa dimer (bars). Corresponding mean predicted affinity of all binding poses where the given residue was within 6 Å reported as a red line.

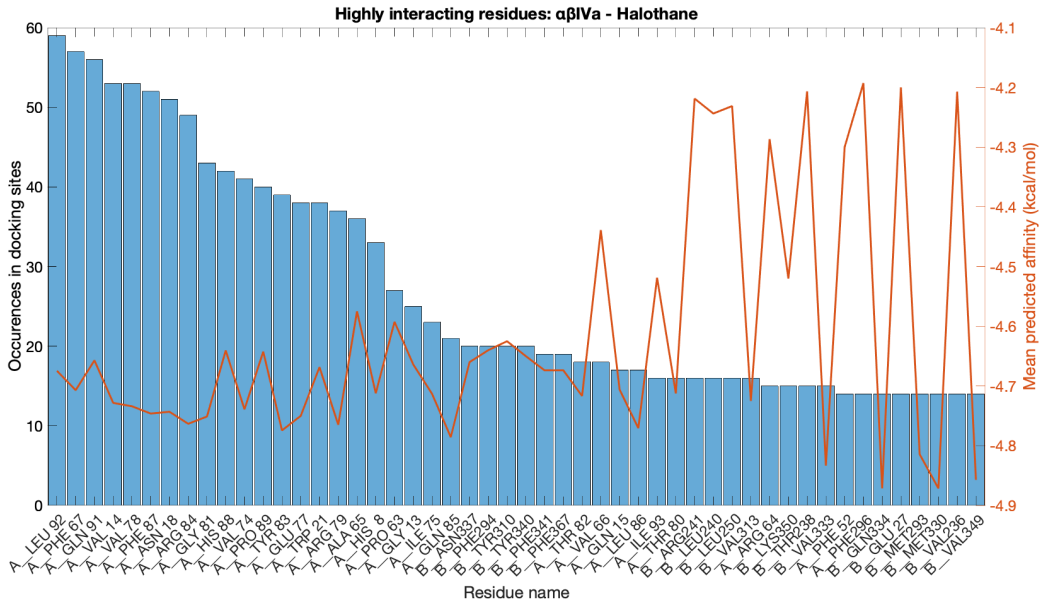

Supplementary Figure S3.20. Residue occurrence across all calculate docking poses, calculated as residues within 6 Å of each docked halothane pose on the αβIVa dimer (bars).

Corresponding mean predicted affinity of all binding poses where the given residue was within 6 Å reported as a red line.

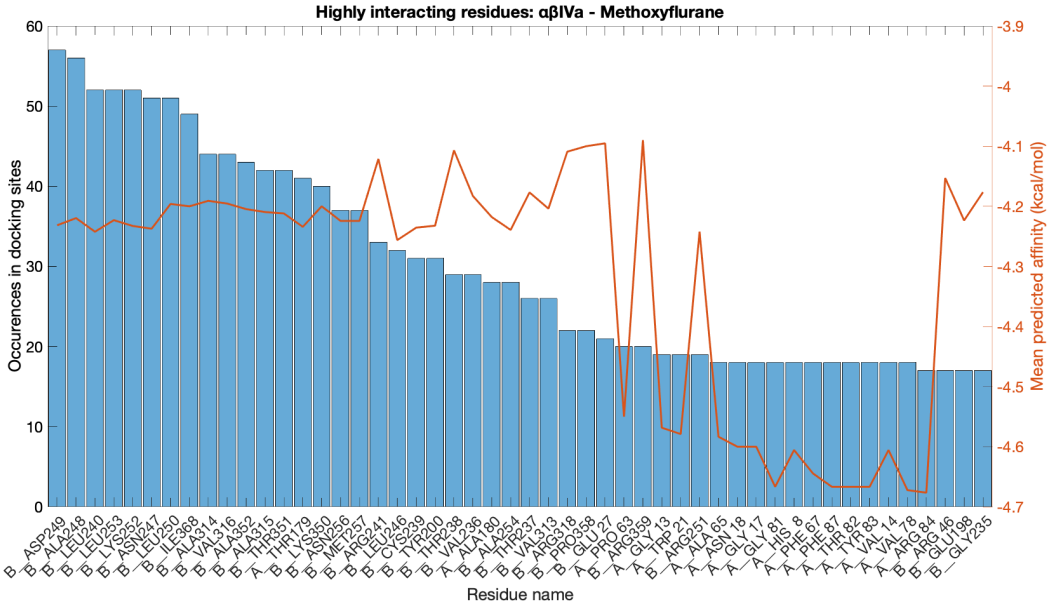

Supplementary Figure S3.21. Residue occurrence across all calculate docking poses, calculated as residues within 6 Å of each docked methoxyflurane pose on the αβIVa dimer (bars). Corresponding mean predicted affinity of all binding poses where the given residue was within 6 Å reported as a red line.

3.1.9 Comparison with avg. residence times

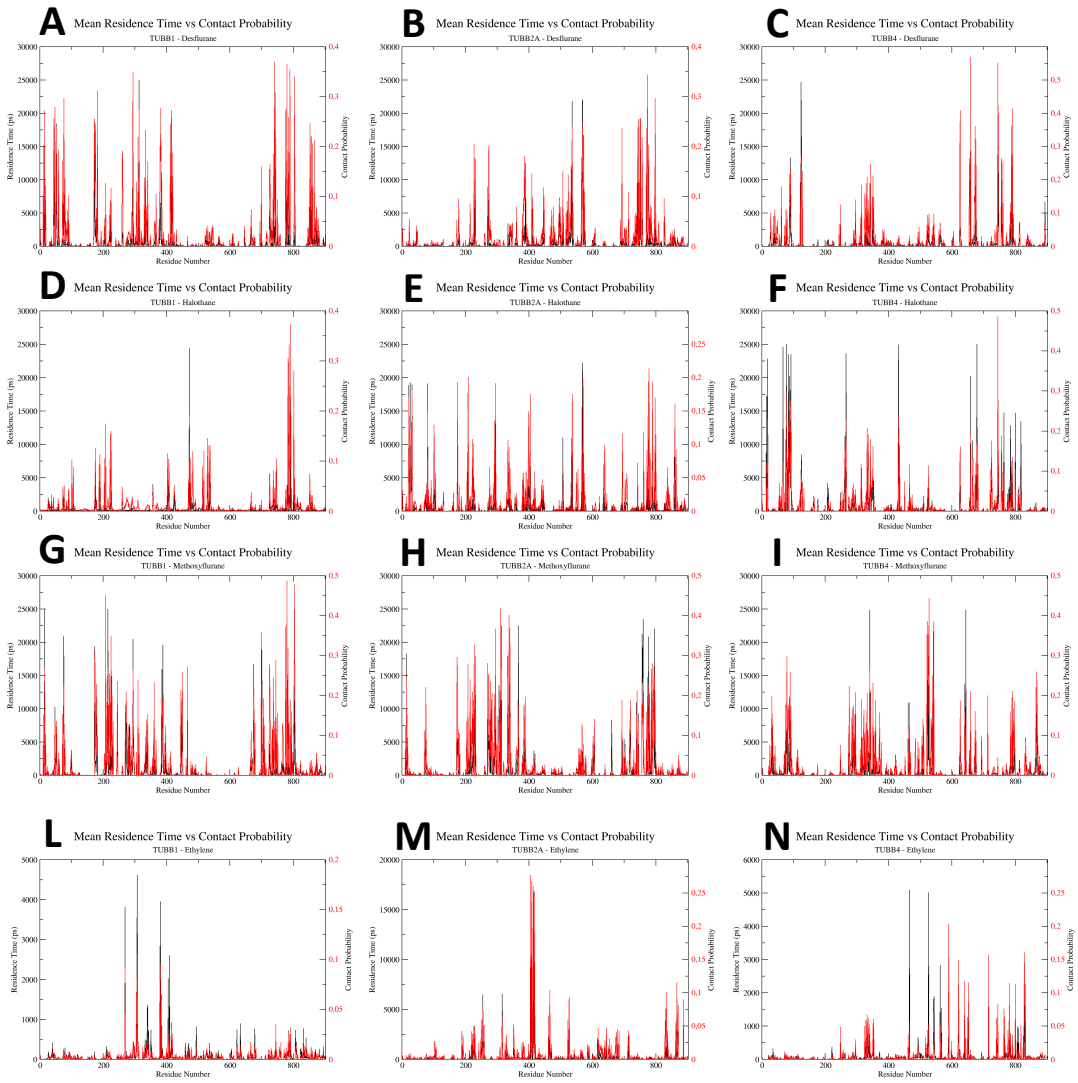

Supplementary Figure S7.22. Comparison between per-residue average residence times (solid black line) and contact probabilities (solid red line). First column refers to isotype αβVI with Desflurane (A), Halothane (D), Methoxyflurane (G) and Ethylene (L). Second column refers to isotype αβIIa with Desflurane (B), Halothane (E), Methoxyflurane (H) and Ethylene (M). Last column is isotype αβIVa with Desflurane (C), Halothane (F), Methoxyflurane (I) and Ethylene (N).

3.2 Characterization of the modulation of cell membrane mechanics by volatile anesthetics

3.2.1 Density Profiles

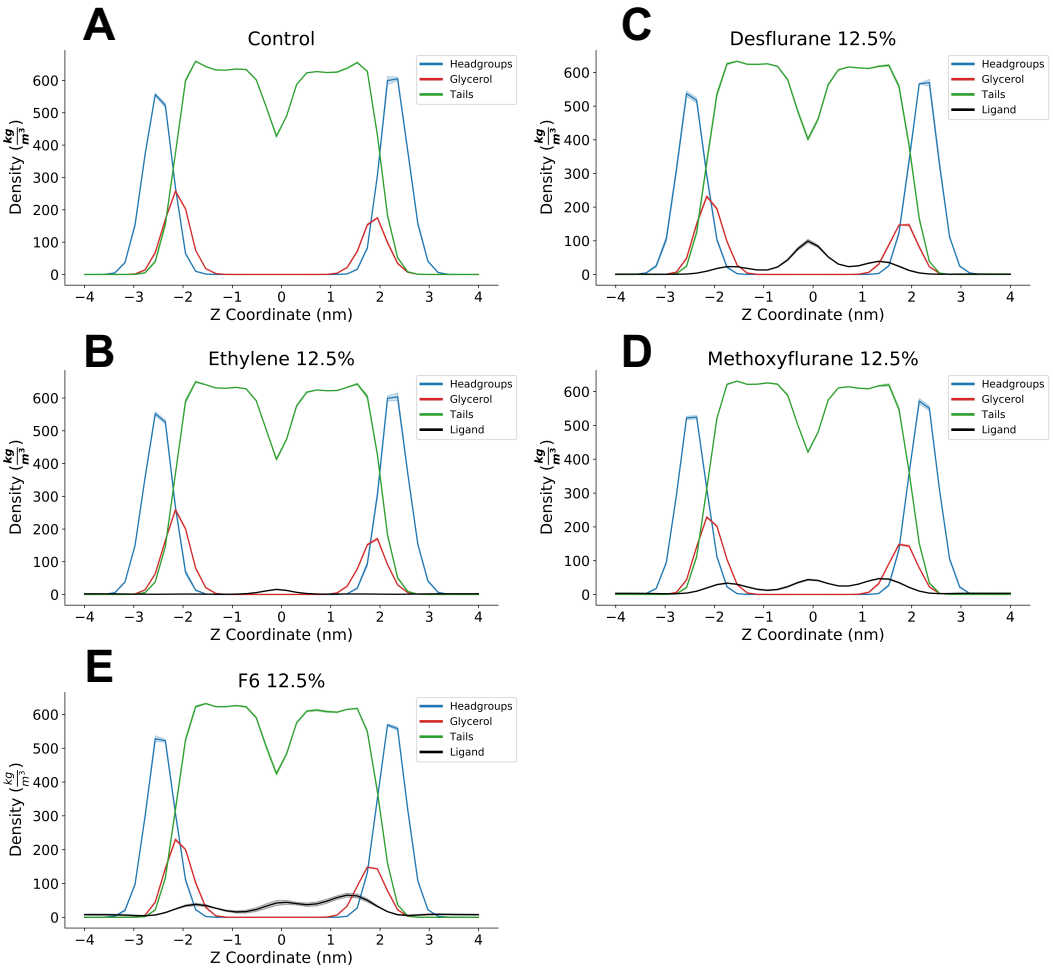

Supplementary Figure S3.23. Density profiles of control simulations (A) and ligands at 12.5% molar ratio: (B) Ethylene; (C) Desflurane; (D) Methoxyflurane; (E) F6. Densities of lipid headgroups, glycerol groups, hydrophobic lipid tails and ligands are highlighted. Shaded areas represent 95% confidence intervals.

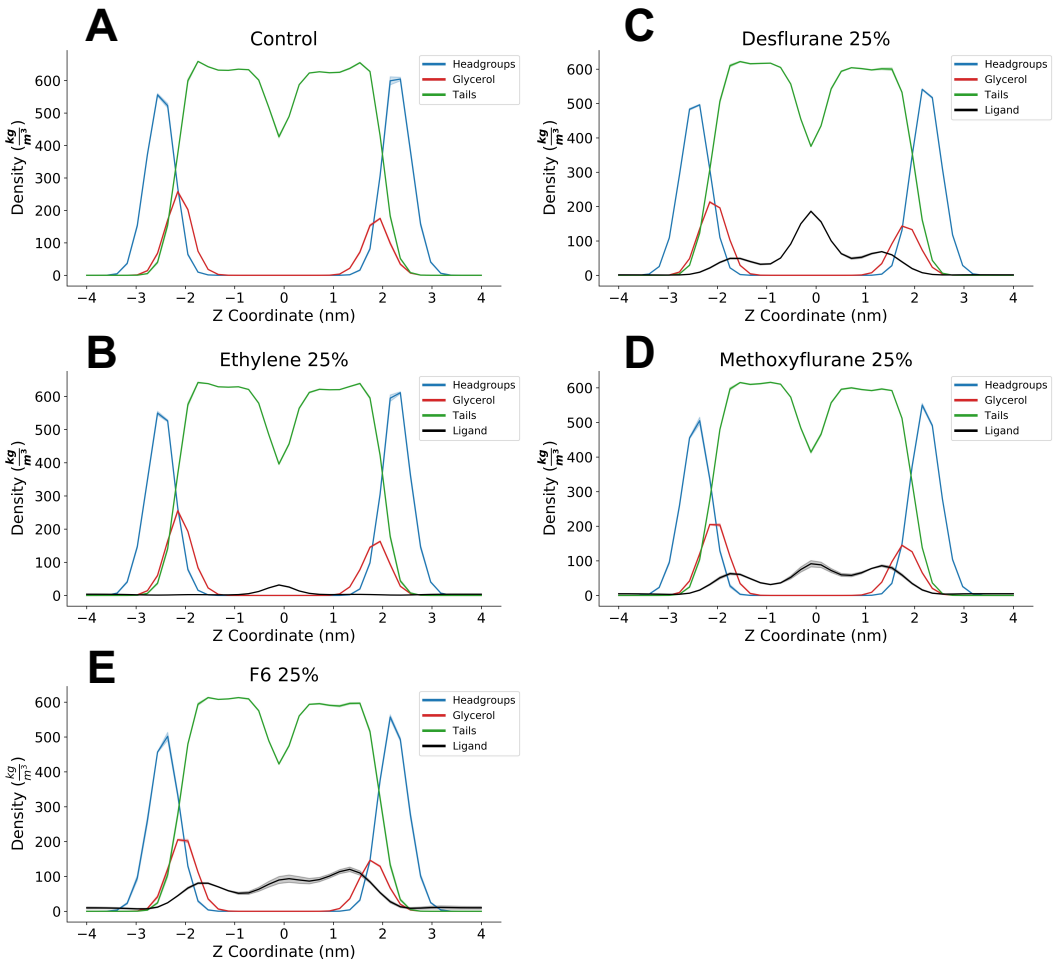

Supplementary Figure S3.24. Density profiles of control simulations (A) and ligands at 25% molar ratio: (B) ethylene; (C) desflurane; (D) methoxyflurane; (E) F6. Densities of lipid headgroups, glycerol groups, hydrophobic lipid tails and ligands are highlighted. Shaded areas represent 95% confidence intervals.

3.2.2 Order Parameters

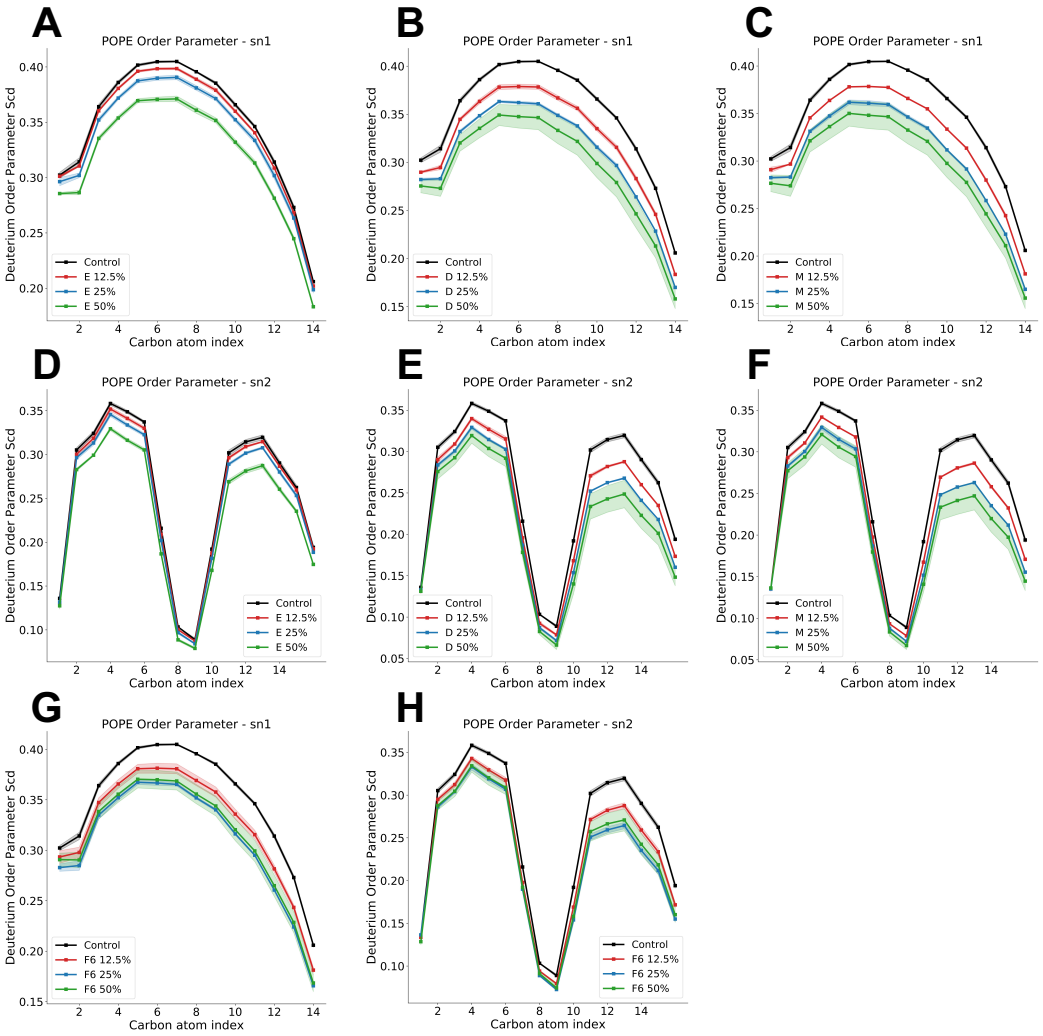

Supplementary Figure S3.25. Lipid tail order parameters for POPE sn1 and sn2 chains, with different ligands: (A) and (D) ethylene; (B) and (E) desflurane; (C) and (F) methoxyflurane; (G) and (H) F6. Shaded intervals correspond to 95% confidence intervals.

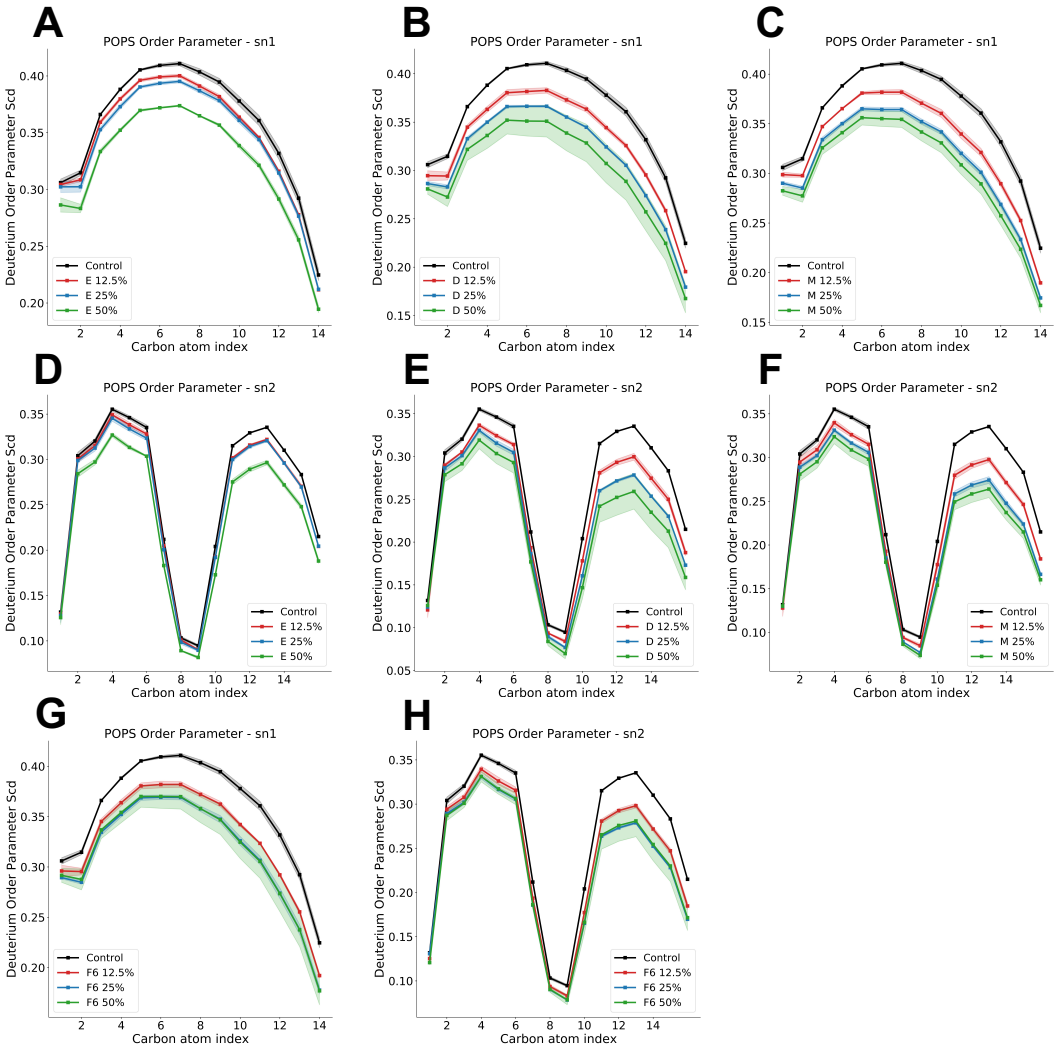

Supplementary Figure S3.26. Lipid tail order parameters for POPS sn1 and sn2 chains, with different ligands: (A) and (D) ethylene; (B) and (E) desflurane; (C) and (F) methoxyflurane; (G) and (H) F6. Shaded intervals correspond to 95% confidence intervals.

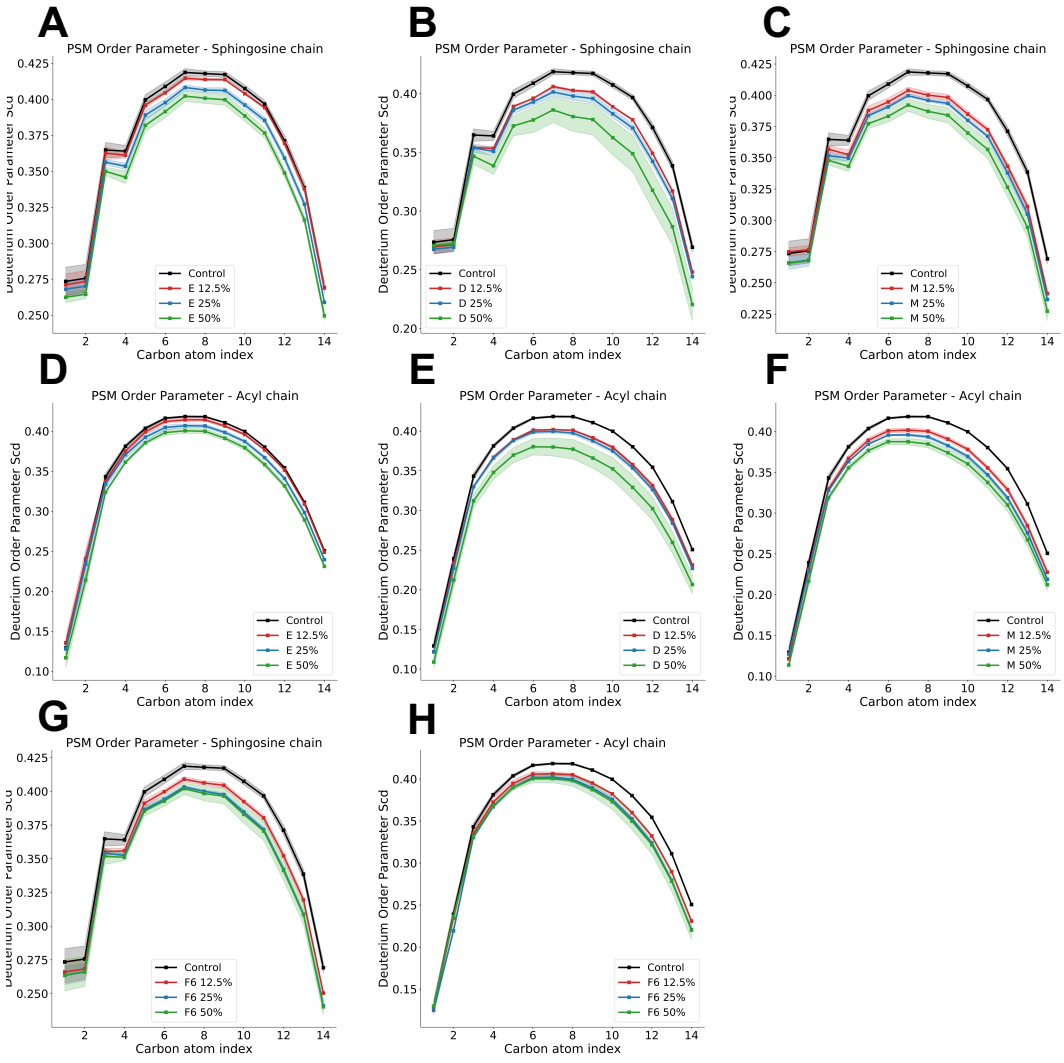

Supplementary Figure S3.27. Lipid tail order parameters for PSM sphingosine chain and acyl chain, with different ligands: (A) and (D) ethylene; (B) and (E) desflurane; (C) and (F) methoxyflurane;(G) and (H) F6. Shaded intervals correspond to 95% confidence intervals.

Appendix to Chapter 4

Investigation of non-covalent molecular assemblies for drug delivery using molecular simulations

4.1 Dendrimeric nanoparticles as candidate nanocarriers for Rose Bengal

4.1.1 Experimental Materials and Methods

Materials

RB, fetal bovine serum (FBS), penicillin/streptomycin solution, trypsin-EDTA solution, ABDA probe [9,10-antherachenediyl-bis(methylene) dimalonic acid], MTT [3-(4,5-dimethyl-2-thiazolyl)-2,5-diphenyl-2H-tetrazolium bromide], and HEPES (4-(2-hydroxyethyl)-1-piperazineethanesulfonic acid) were purchased from Sigma-Aldrich (Taufkirchen, Germany). Dulbecco's phosphate buffered saline without calcium and magnesium (DPBS) was purchased from Biowest (Nuaillé, France). HBSS (Hanks' Balanced Salt Solution) and 154 CF culture medium were obtained from Gibco/ThermoFisher Scientific (Waltham, MA, USA). Chelex 100 Resin was obtained from Bio-Rad (Hercules, CA, USA). H_2DCFDA (2′,7′ dichlorodihydrofluorescein diacetate) was purchased from Invitrogen/ThermoFisher Scientific. Dimethyl sulfoxide (DMSO) was purchased from POCH (Gliwice, Poland). Murine basal cell carcinoma lines (AsZ, BsZ, CsZ) were provided by Dr. Ervin Epstein (Children's Oakland Research Institute, Oakland, CA, USA).

Poly(propyleneimine) (PPI) dendrimers of the 3rd and 4th generation* with 32 or 64 primary amino surface groups, respectively, were obtained from Symo-Chem (Eindhoven, the Netherlands). Poly(amidoamine) (PAMAM) dendrimers of the 3rd

and 4th generation with 32 and 64 primary amino surface groups, respectively, were obtained from Sigma-Aldrich.

*According to [4] the nomenclature for Tomalia-type PAMAM dendrimers can be used for PPI dendrimers. Hence, we adopted the suggested classification, describing commercially available PPI dendrimer of the 5th generation (DAB-Am-64) as 4th generation, and 4th generation (DAB-Am-32) as 3rd generation.

Methods

Spectrofluorimetric and zeta potential studies on the interaction between PAMAM or PPI dendrimers and RB

Fluorescence (F) emission spectra were obtained on an LS 55 fluorescence spectrometer (PerkinElmer, Waltham, MA, USA) at a constant temperature of 25°C. All samples were prepared in HEPES buffer (10 mM, pH 7.4) and measured in quartz cuvettes. The excitation wavelength was set to 525 nm, and spectra were recorded between 540 and 650 nm. Excitation and emission slits were 5 and 7.5 nm, respectively. RB solution in a constant concentration of 1 μM was titrated with dendrimer solutions in concentrations ranging from 0.02 to 1 μM in order to maintain the molar ratio of dendrimer:RB complexes between 1:50 and 1:1. The experiments were performed in three independent replicates. To determine the stoichiometry of the polymer:dye complexes, plots of F_{564}/F_{575} vs. RB:dendrimer molar ratio were evaluated using Job's method.

Zeta potential measurements were performed using electrophoretic mobility assays on a Zetasizer Nano ZS (Malvern Instruments Ltd., Malvern, UK) at a constant temperature of 25°C. All samples were prepared in HEPES buffer (10 mM, pH 7.4). Dendrimer solutions of constant concentration (10 μM) were placed in DTS 1070 folded capillary cells, and their zeta potentials were measured. The solutions were subsequently titrated with RB solution to obtain final RB concentrations ranging from 10 to 500 μM, corresponding to dendrimer:RB molar ratios of 1:1 to 1:50. The experiments were performed in three independent replicates. Analysis of the titration curves for all studied systems enabled the evaluation of the stoichiometry of complexes as follows: decreasing dependence of dendrimer zeta potential on dendrimer:RB mixture stoichiometry was extrapolated to the intersection with the eventual zeta potential value of fully saturated dendrimer, and binding stoichiometry was determined from the intersection point (Job's method).

Preparation of complexes for further in vitro studies

Dendrimers were dissolved in double-distilled water to a final concentration of 40 μM. Dendrimer solutions were prepared fresh and used on the same day. RB (dissolved in double-distilled water) was added to the dendrimer solutions in a dendrimer:RB molar ratio of 1:10 (to a final RB concentration of 400 μM). This molar ratio ensures complete complexation of RB molecules by all tested dendrimers. The mixtures were stirred for 0.5 h at ambient temperature. Stock solutions were prepared just before the experiments.

Singlet oxygen generation assay

The singlet oxygen generation was studied using the ABDA probe (final concentration: 5 μM) as an indicator. Solutions of RB, PAMAM G3:RB, PAMAM G4:RB, PPI G3:RB, PPI G4:RB, and free dendrimers in the highest concentration used for complex formation (0.1 μM) were prepared in 10 mM HEPES. The complexes were prepared at RB concentrations of 0.125, 0.25, 0.5, 0.75, and 1 μM. Upon sample preparation, 100 μL of each solution was transferred to a 96-well black plate. All measurements were performed on a fluorescence microplate reader (Fluoroskan Ascent FL, ThermoFisher Scientific) at an excitation wavelength of 355 nm and an emission wavelength of 430 nm. Samples were mixed before each measurement. The first measurement was recorded without ABDA probe to determine whether RB, dendrimers, or their complexes exhibit any fluorescence in this range. Following the first measurement, ABDA was added to each well, and the fluorescence of the probe without irradiation was measured. Next, the plate was immediately placed under a Q.Light Pro Unit lamp (Q.Light, Rorschach, Switzerland) equipped with a filter emitting visible light in the wavelength range 385−780 nm. Fluorescence was measured in 5 min intervals during irradiation for 5–60 min. The experiments were performed in four independent replicates. The slopes of the fluorescence curves were considered to be a measurement of singlet oxygen generation. The results were presented as percentages of the singlet oxygen generation in the control sample (HEPES buffer irradiated with probe).

Cell culture

AsZ, BsZ, and CsZ (murine basal cell carcinoma) cell lines were cultured in 154 CF medium with 5% penicillin/streptomycin, 0.05 mM calcium, and 2% Chelex-purified, heat-inactivated FBS. Cells were cultured in T-75 culture flasks at 37°C/5% CO_2 and subcultured every 2 or 3 days. Cells were harvested using 0.25% (w/v) trypsin/0.03% (w/v) EDTA. The number of viable cells was determined by Trypan blue exclusion assay on a Countess Automated Cell Counter (Invitrogen, Carlsbad, CA, USA).

Cytotoxicity studies

AsZ, BsZ, and CsZ cells were seeded in 96-well transparent plates at a density of 3×10^4 cells per well in 90 µL medium and incubated for 24 h before experiments. Then, using stock solutions (according to 2.2.2), the samples (PAMAM G3:RB, PAMAM G4:RB, PPI G3:RB PPI G4:RB, and free RB solutions) were prepared in HEPES buffer and added to the cells to obtain final RB concentrations of 0.25, 0.5, 0.75, and 1 µM. Cytotoxicity of free dendrimers was also evaluated at the highest concentration used for the preparation of complexes. Cells were incubated with tested compounds for 5 h (37°C, 5% CO_2). The medium was replaced with DPBS, and the cells were irradiated with visible light using the Q.Light Pro Unit lamp (Q.Light) for 30 min. Immediately after irradiation, DPBS was replaced with fresh culture medium, and the cells were incubated for 24 h (post-PDT incubation). So-called “dark” toxicity (without irradiation) was evaluated in parallel.

The cell viability was measured by MTT assay. MTT was added to the wells at a final concentration of 0.5 mg/mL, and the plates were incubated for 2 h (37°C, 5% CO_2). After incubation, formazan crystals were dissolved in DMSO, and the absorbance was read at 570 nm using the PowerWave HT Microplate Spectrophotometer (BioTek, Winooski, VT, USA). Experiments were performed in six independent replicates. Cell viabilities are presented as percentages of the viability in the untreated control.

ROS generation assay

An H_2DCFDA probe was used to investigate the intracellular production of ROS. For this purpose, AsZ cells were seeded in 96-well black plates at a density of 1×10^4 cells per well in 90 µL medium. After incubation for 24 h, the samples (PAMAM G3:RB, PAMAM G4:RB, PPI G3:RB PPI G4:RB, and free RB solutions) were prepared in HEPES buffer and added to the cells to obtain final RB

concentrations of 0.25, 0.50, 1, or 2 μM. ROS-generating activity of free dendrimers was also evaluated at the highest concentration used for preparation of complexes. Cells were incubated with tested compounds for 5 h (37°C, 5% CO_2). Medium containing the tested compounds was removed, a 2 μM solution of H_2DCFDA in HBSS was added to each well, and the plates were incubated for the next 20 min in the dark (37°C, 5% CO_2). Next, the cells were washed with HBSS, and background fluorescence (excitation: 485 nm; emission: 530 nm) of nonirradiated cells submerged in 100 μL HBSS was measured on a PowerWave HT Microplate reader (BioTek). The cells were then irradiated using Q.Light Pro Unit lamp (Q.Light Pro Unit) for 30 min, and 2',7'-dichlorofluorescein (DCF) fluorescence was measured. The experiments were performed in four independent replicates. ROS level was calculated as DCF fluorescence intensity and was presented as a percentage of the ROS production in control samples (without treatment). Each measurement was corrected by subtraction of the background fluorescence intensity (before irradiation).

Cellular uptake assay

AsZ cells were seeded into 24-well plates at a density of 1×10^5 cells per well and incubated for 24 h (37ºC, 5% CO_2). Next, RB, PAMAM G3:RB, PAMAM G4:RB, PPI G3:RB, and PPI G4:RB (5 μM final concentration of RB) were added to each well, and the cells were incubated with the compounds for up to 4 h. Following incubation, the compounds were removed, and the cells were washed with DPBS and detached using trypsin-EDTA solution. Fresh culture medium was added to the cells, and the samples were gently mixed and collected for measurements. To estimate cellular uptake, the fluorescence of the samples was measured using flow cytometry (LSRII, Becton Dickinson, Franklin Lakes, NJ, USA). The excitation and emission filters were 520 and 570 nm, respectively. The experiments were performed in five independent replicates. The results are presented as the percentage of cells in the population that internalized RB.

Statistical analysis

Statistical significance was tested using two-way ANOVA for concentrations and compound series followed by post-hoc Tukey's test for pairwise difference testing. In all tests, p-values < 0.05 were considered statistically significant. Data were

collected from at least three independent experiments and presented as arithmetic means ± SD.

4.2 Mechanisms for cellular uptake of Rose Bengal

4.2.1 Experimental Materials and Methods

Materials

RB, fetal bovine serum, penicillin/streptomycin solution, trypsin-EDTA solution, MTT (3-(4,5-dimethyl-2-thiazolyl)-2,5-diphenyl-2H-tetrazolium bromide), lipopolysaccharides from Escherichia coli O111:B4 (LPS), cyclosporin A, rifampicin, budesonide, pravastatin, naringin, taurocholic acid, allura red, and ritonavir were purchased from Sigma-Aldrich (Taufkirchen, Germany). Dulbecco's phosphate buffered saline with no calcium and magnesium (DPBS) was purchased from Biowest (France). DMEM and RPMI culture media was obtained from Gibco, Thermo Fisher Scientific (Waltham, Massachusetts, USA). Dimethyl sulfoxide (DMSO) was purchased from POCH (Gliwice, Poland). Cell lines (HepG2, Hep3B, HT-29, and Caco-2) were obtained from ATCC. For the experiments involving the electrified liquid-liquid interface, the aqueous phase was a solution of 10 mM NaCl (analytical grade, POCH) or Britton-Robinson buffer (mixture of phosphoric acid, boric acid, and acetic acid, at equimolar concentrations of 10 mM), which was pH adjusted with 1 M HCl or 1 M NaOH. The organic phase solvent was 1,2-dichloroethane (1,2-DCE, 99%, Sigma). Bis(triphenylphosphoranylidene)ammonium tetrakis(4-chlorophenyl)borate was used as the organic phase background electrolyte salt, was synthesized from bis(triphenylphosphoranylidene)ammonium chloride (BTPPACl; 97%, Sigma-Aldrich) and potassium tetrakis(4-chlorophenyl)borate (>98%, Sigma-Aldrich); its concentration was maintained at 5 mM in all measurements.

Electrified liquid-liquid interface

The behavior of RB at the electrified liquid-liquid interface was studied in a traditional four-electrode cell (glass tube equipped with two Luggin capillaries) with the Autolab 302n potentiostat. Two reference (Ag/AgCl wires) and two counter (Pt wires) electrodes were used to measure the interfacial potential drop and impose interfacial potential difference, respectively. The organic phase reference electrode was additionally immersed in the 10 mM BTPPACl and 10 mM NaCl aqueous solution placed into the longer Luggin capillary. The organic phase counter electrode was insulated with the glass within the section remaining in direct contact with the aqueous phase. Potentiostatic cyclic voltammetry was employed as the electroanalytical tool. The experiential scan rate was 20 mV/s unless indicated

otherwise. The recorded ionic current corresponded to the following: transfer of the anion from the aqueous to the organic phase (negative current); transfer of the anion from the organic to the aqueous phase (positive current); transfer of the cation from the organic to the aqueous phase (negative current); and transfer of the cation from the aqueous to the organic phase (positive current).

Hydrodynamic diameter measurements

Measurements of hydrodynamic diameter were performed by the Dynamic Light Scattering method (DLS) on a Zetasizer Nano ZS instrument (Malvern Instruments Ltd, Malvern, UK). LPS (from *E. coli*) was dissolved in PBS (10 mM, pH 7.4) to a final concentration of 100 μg/mL. The solutions were placed in low volume sizing cuvettes (ZEN0112, Malvern Instruments Ltd., Malvern, UK) and the size of the formed micelles was measured. RB solution was then added to obtain given concentrations and the hydrodynamic diameter was measured immediately. The data were analyzed using Malvern software.

Cell culture

The Caco-2, HepG2, and Hep3B cell lines were cultured in DMEM medium, and the HT-29 cell line was cultured in RPMI medium. Both media contained 1% penicillin/streptomycin and 10% heat-inactivated FBS. Cells were cultured in T-75 culture flasks at 37 °C/5% CO_2 and sub-cultured every 3 days. Cells were harvested using 0.25% (w/v) trypsin-0.03% (w/v) EDTA. The number of viable cells was determined with the Trypan blue exclusion assay on a Countess Automated Cell Counter (Invitrogen, Carlsbad, CA, USA).

Fluorescence anisotropy

HT-29, Caco-2, HepG2, and Hep3B cells were used to analyze changes in fluorescence anisotropy. Following trypsinization, 1×10^6 cells in PBS (10 mM, pH 7.4) were placed in quartz cuvettes. Next, 1,6-diphenyl-1,3,5-hexatriene (DPH) and 1-(4-(trimethyloamino)phenyl)-6-phenylhexa-1,3,5-triene (TMA-DPH) were added to the cells at final concentration of 2.5 μM and incubated for 30 min at 37 °C. The fluorescence anisotropy of DPH and TMA-DPH was measured using a PerkinElmer LS-50B spectrofluorometer (Waltham, Massachusetts, USA). Measurements were performed in PBS (10 mM, pH 7.4) at 37 °C. The excitation and emission wavelengths were set to 348 and 426 nm for DPH and 358 and 428 for TMA-DPH. Increasing concentrations of RB dissolved in HBSS (10 mM, pH

7.4) was added to the sample, and the anisotropy of fluorescence was measured again.

Fluorescence anisotropy was calculated using Perkin Elmer software and Jablonski's equation:

$$r = (I_{VV} - GI_{VH})/(I_{VV} + GI_{VH})$$

where r is fluorescence anisotropy, and I_{VV} and I_{VH} are the vertical and horizontal fluorescence intensities, respectively, to the vertical polarization of the excitation light beam. $G = I_{VH}/I_{VV}$ (grating correction factor) corrects the polarization effects of the monochromator.

Intracellular uptake inhibition assay

Cells were seeded into 24-well plates at a density of 1×10^5 cells/well and incubated for 24 h (37 ºC, 5% CO_2). Next, the cells were treated with RB (5 μM final concentration) for up to 3 h. For the inhibition assay, cells were pre-incubated with inhibitors (50 μM final concentration) for 1 h. Following incubation, the compounds were removed, and the cells were washed with DPBS and detached using trypsin-EDTA solution. Following the addition of fresh culture medium, samples were gently mixed and collected for measurements. To estimate cellular uptake, fluorescence was measured using flow cytometry (LSRII, Becton Dickinson, Franklin Lakes, NJ, USA). The excitation and emission filters were 520 and 570 nm, respectively. The results are presented as the percentage of cells in the population that internalized RB.

Confocal microscopy

Caco-2, HT-29, HepG2, and Hep3B cells were seeded into black 96-well plates with a transparent glass bottom at a density of 1×10^4 cells/well followed by 24 h of incubation in standard conditions. The medium was replaced with 100 μL fresh culture medium containing RB (5 μM) and plates were incubated for 4 h in the dark (37 ºC, 5% CO_2). Cells were subsequently washed with DPBS and fixed with 4% formaldehyde solution for 15 min. Phalloidin–Atto 633 (1:400) was then added to each well for 20 min to stain F-actin in the cell membrane. Cells were washed with DPBS and 5 μM Hoechst 33342 was added to the cells for an additional 15 min to stain nuclear DNA. Following incubation, cells were washed with DPBS and submerged in 100 μL of fresh DPBS. Images were taken with a Leica TCS SP8 confocal microscope.

Cytotoxicity studies

Caco-2, HepG2, Hep3B, and HT-29 cells were seeded into 96-well plates at a density of 1.5×10^4 cells/well. After 24 h of incubation (37 °C, 5% CO_2), 100 µL of fresh culture medium containing different concentrations of RB was added to the cells and incubated for 5 h (37 ºC, 5% CO_2). The medium was then replaced with DPBS, and cells were irradiated for 30 min (2.4 J/cm^2/min) with the Q. Light Pro Unit lamp. Immediately after irradiation, DPBS was replaced with fresh culture medium, and cells were incubated for 24 h as a post-photodynamic therapy incubation. Additionally, the "dark" toxicity (without irradiation) and cytotoxicity of inhibitors were evaluated.

Cell viability was measured using the MTT assay. MTT was added to the wells (final concentration 0.5 mg/mL) and the plates were incubated for 2 h (37 ºC, 5% CO_2). After incubation, formazan crystals were dissolved in DMSO, and the absorbance was read at 570 nm using a PowerWave HT Microplate Spectrophotometer (BioTek, USA).

In silico analysis

Amino acid sequences were analyzed with Jalview software. Sequences obtained from the Protein Bank (NCBI) were used for the analysis. Tertiary protein structures were compared using the Swiss PDB viewer; the structures used for these comparisons were obtained from UniProt.

Western blot analysis

Cells were lysed in RIPA buffer (with PMSF and PIC) and the lysates were separated using SDS-PAGE electrophoresis and transferred to a nitrocellulose membrane (Amersham™ Protran®). After blocking with milk, the membrane was stained with primary antibodies (PA5106753- OATP1B1/1B3 (1:1000) and PA516914- beta-actin (1:10000) - Thermo Fisher Scientific, Waltham, MA, USA) at 4 °C overnight. After incubation, membranes were washed with PBS-Tween, and HRP-conjugated secondary antibodies were added (Goat anti-Rabbit IgG (H+L) Secondary Antibody, HRP (1:200000) Thermo Fisher Scientific, Waltham, MA, USA). Protein bands bound to HRP-conjugated secondary antibodies were visualized using the SuperSignal™ West Pico chemiluminescent substrate (Thermo Fisher Scientific, Waltham, MA, USA) and images were acquired with the ChemiDoc-IT2 (UVP, Meranco, Poznan, Poland). Beta-actin was used as the loading control.

4.2.2 Results

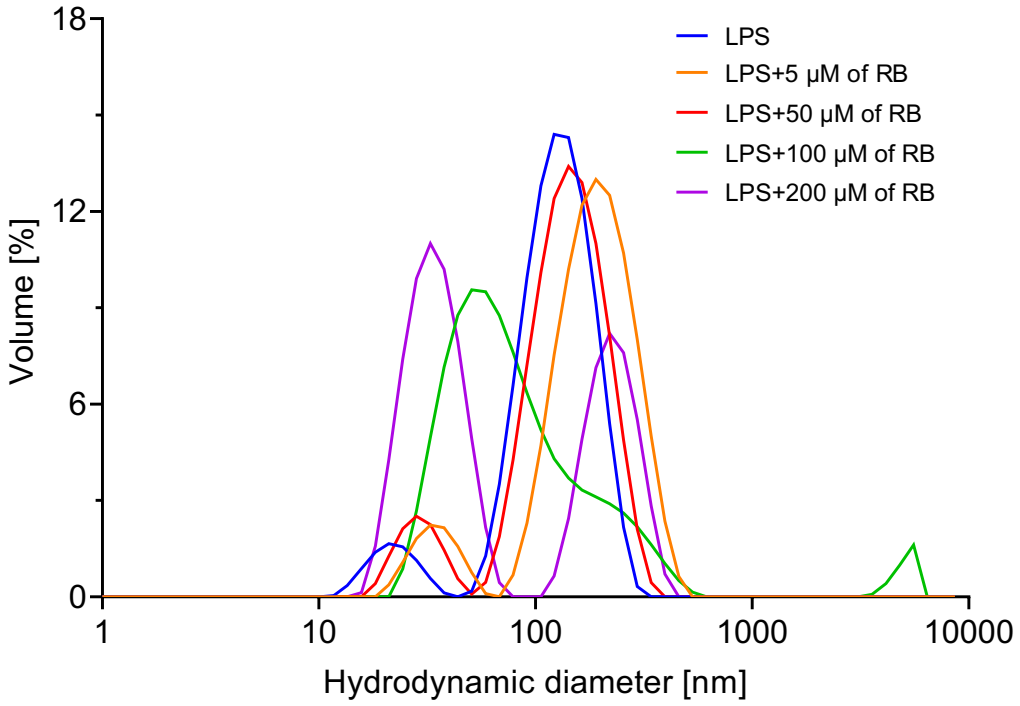

Supplementary Figure S4.28. Dissociation of LPS (E. coli) micelles by different concentrations of rose bengal.

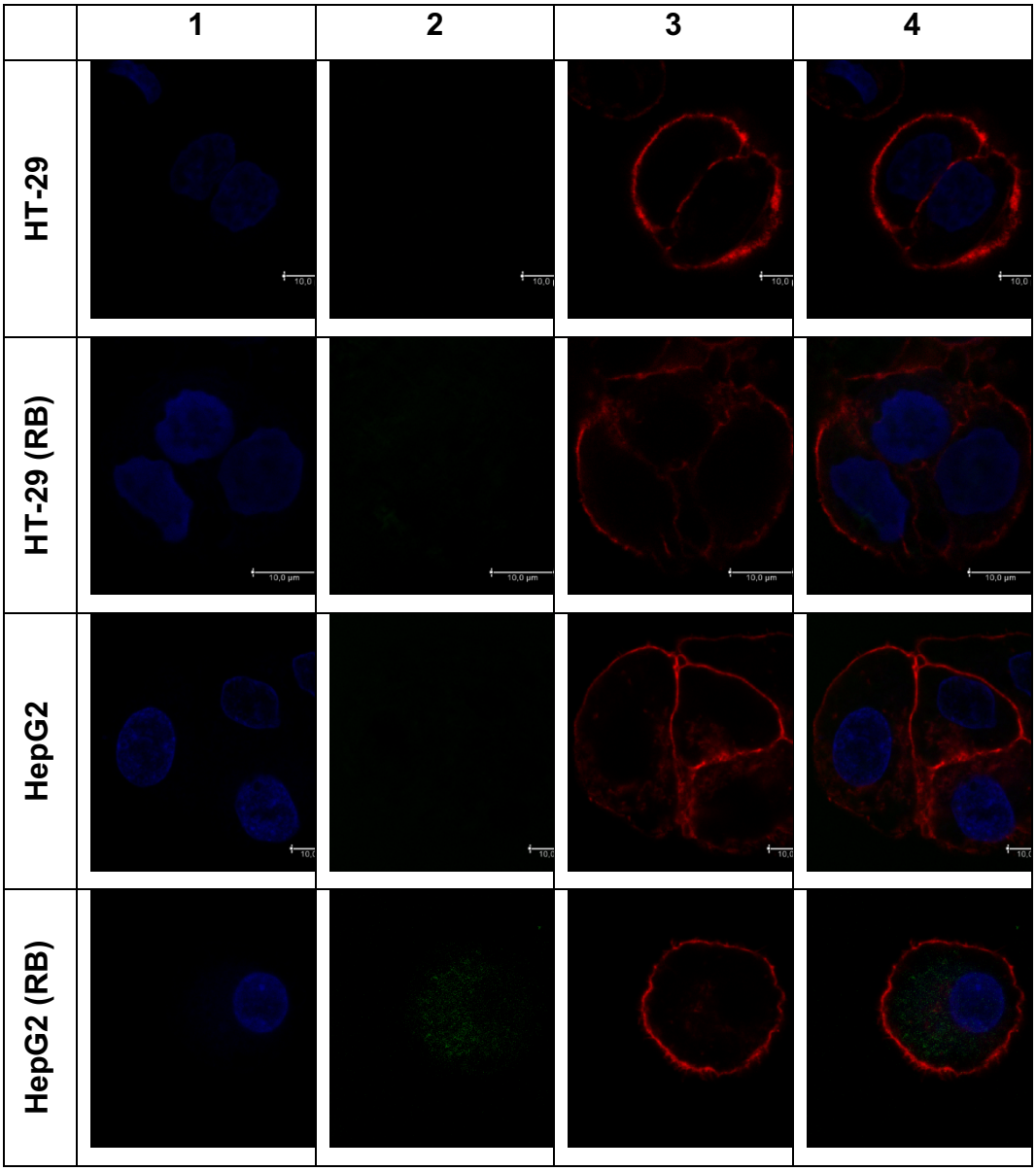

Supplementary Figure S4.29. Confocal micrographs of Caco-2 and HepG2 cell lines: (1) Hoechst 33342 (2) rose bengal (3) Phalloidin–Atto 633; (4) merge of channels 1, 2, and 3. Scale bar represents 10 µm.

Supplementary Table ST4.3. Comparison of IC50 values for evaluated cell lines

Cell line	IC50 [µM]
HepG2	5.03
Hep3B	2.75

Caco-2	19.84
HT-29	20.64

Supplementary Table ST4.4. Statistically significant difference at $p < 0.05$ between the uptake of RB on nontreated cells and after treatment with each inhibitor

	HepG2	Allura red	Taurocholic acid	Rifampicin	Prawastatin	Budesonide	Naringin	Cyclosporin A	Ritonavir
0.5 h	RB	*	*	*	*	*	*	*	*
1 h		*	*	*	*	*	*	*	*
2 h		*	*	*	*	*	*	*	*
3 h		*	*	*	*	*	*	*	*
	Hep3B	Allura red	Taurocholic acid	Rifampicin	Prawastatin	Budesonide	Naringin	Cyclosporin A	Ritonavir
0.5 h	RB	*			*				
1 h		*		*	*	*		*	
2 h		*	*	*	*	*		*	
3 h		*	*		*	*			*

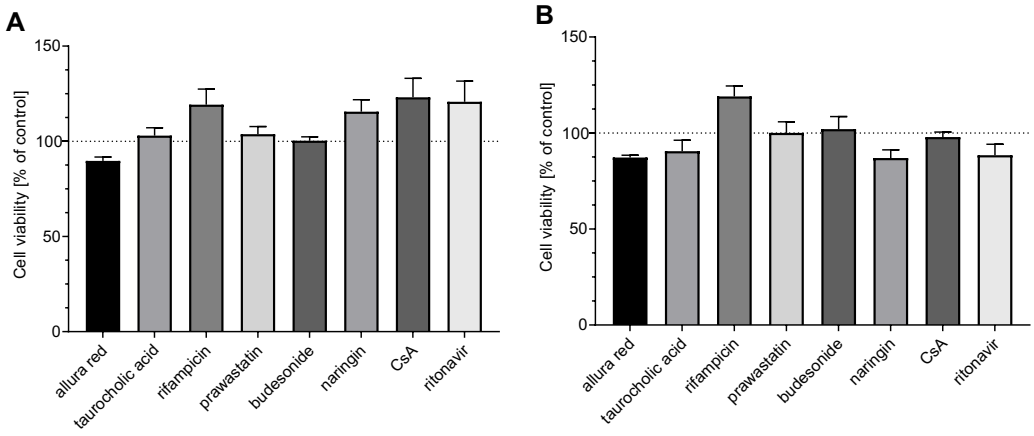

Supplementary Figure S4.30. Cytotoxic effect of selected inhibitors (50 μM) in (A) HepG2 and (B) Hep3B cell lines. Cell viability was determined using MTT assay. Data are presented as percentages of the viability of control (untreated) cells; means ± SD; n = 3.

>NP_006437.3 solute carrier organic anion transporter family member 1B1 [Homo sapiens]

MDQNQHLNKTAEAQPSENKKTRYCNGLKMFLAALSLSFIAKTLGAIIMKSSIIHIERRFEISSSLV
GFIDGSFEIGNLLVIVFVSYFGSKLHRPKLIGIGCFIMGIGGVLTALPHFFMGYYRYSKETNINSS
ENSTSTLSTCLINQILSLNRASPEIVGKGCLKESGSYMWIYVFMGNMLRGIGETPIVPLGLSYIDD
FAKEGHSSLYLGILNAIAMIGPIIGFTLGSLFSKMYVDIGYVDLSTIRITPTDSRWVGAWWLNFLV
SGLFSIISSIPFFFLPQTPNKPQKERKASLSLHVLETNDEKDQTANLTNQGKNITKNVTGFFQSFK
SILTNPLYVMFVLLTLLQVSSYIGAFTYVFKYVEQQYGQPSSKANILLGVITIPIFASGMFLGGYI
IKKFKLNTVGIAKFSCFTAVMSLSFYLLYFFILCENKSVAGLTMTYDGNNPVTSHRDVPLSYCNSD
CNCDESQWEPVCGNNGITYISPCLAGCKSSSGNKKPIVFYNCSCLEVTGLQNRNYSAHLGECPRDD
ACTRKFYFFVAIQVLNLFFSALGGTSHVMLIVKIVQPELKSLALGFHSMVIRALGGILAPIYFGAL
IDTTCIKWSTNNCGTRGSCRTYNSTSFSRVYLGLSSMLRVSSLVLYIILIYAMKKKYQEKDINASE
NGSVMDEANLESLNKNKHFVPSAGADSETHC

>NP_062818.1 solute carrier organic anion transporter family member 1B3 isoform 1 [Homo sapiens]

MDQHQHLNKTAESASSEKKKTRRCNGFKMFLAALSFSYIAKALGGIIMKISITQIERRFDISSSLA
GLIDGSFEIGNLLVIVFVSYFGSKLHRPKLIGIGCLLMGTGSILTSLPHFFMGYYRYSKETHINPS
ENSTSSLSTCLINQTLSFNGTSPEIVEKDCVKESGSHMWIYVFMGNMLRGIGETPIVPLGISYIDD
FAKEGHSSLYLGSLNAIGMIGPVIGFALGSLFAKMYVDIGYVDLSTIRITPKDSRWVGAWWLGFLV
SGLFSIISSIPFFFLPKNPNKPQKERKISLSLHVLKTNDDRNQTANLTNQGKNVTKNVTGFFQSLK
SILTNPLYVIFLLLTLLQVSSFIGSFTYVFKYMEQQYGQSASHANFLLGIITIPTVATGMFLGGFI
IKKFKLSLVGIAKFSFLTSMISFLFQLLYFPLICESKSVAGLTLTYDGNNSVASHVDVPLSYCNSE
CNCDESQWEPVCGNNGITYLSPCLAGCKSSSGIKKHTVFYNCSCVEVTGLQNRNYSAHLGECPRDN

TCTRKFFIYVAIQVINSLFSATGGTTFILLTVKIVQPELKALAMGFQSMVIRTLGGILAPIYFGAL
IDKTCMKWSTNSCGAQGACRIYNSVFFGRVYLGLSIALRFPALVLYIVFIFAMKKKFQGKDTKASD
NERKVMDEANLEFLNNGEHFVPSAGTDSKTCNLDMQDNAAAN

Supplementary Figure S 4.31. Amino acid sequences of (A) OATP1B1 and (B) OATP1B3 transporters used in the alignment.

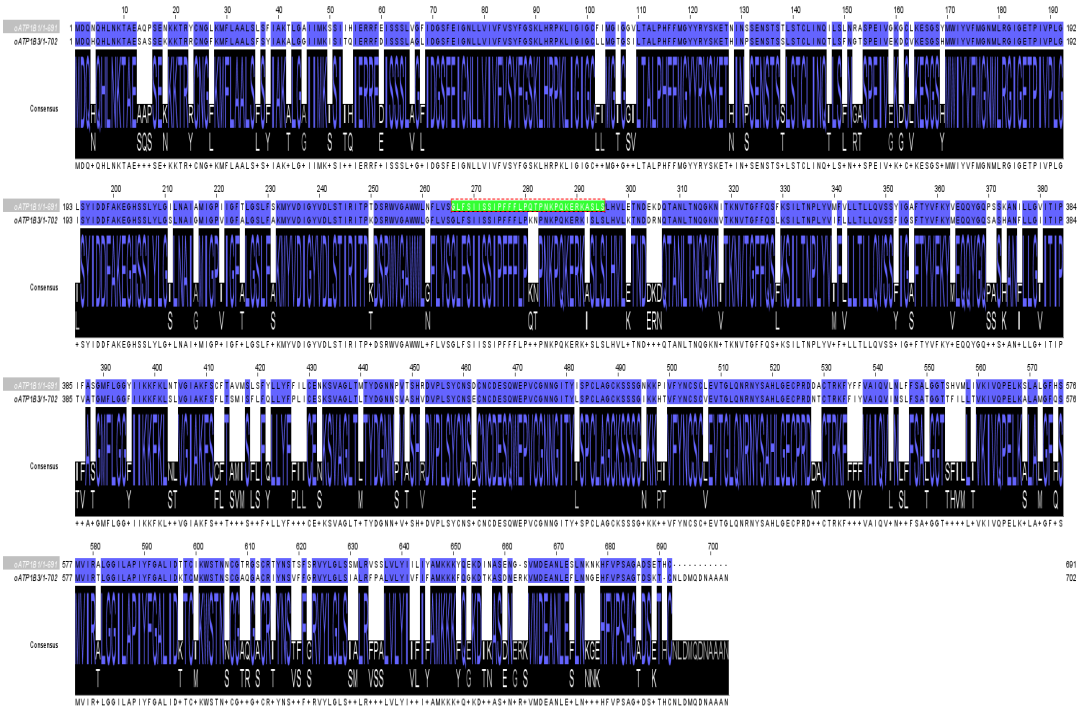

Supplementary Figure S4.32. Alignment of amino acid sequences of OATP1B1 and OATP1B3 transporters.

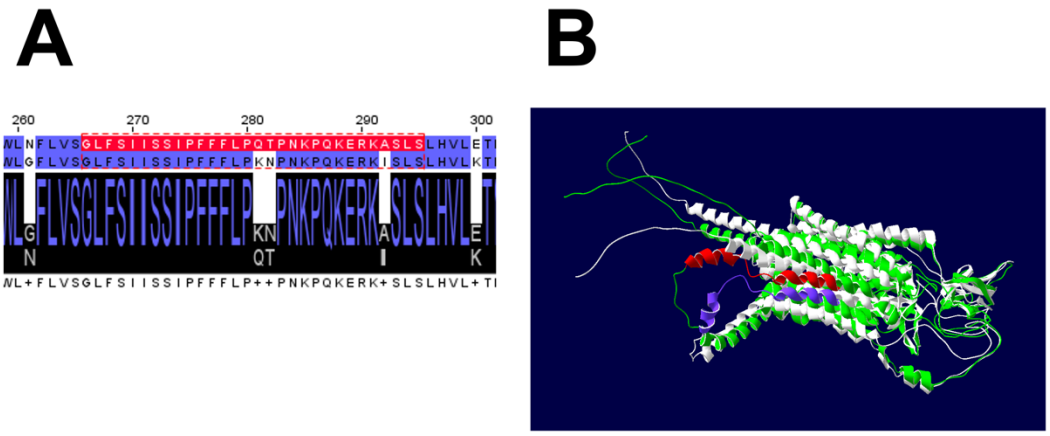

Supplementary Figure S4.33. Alignment of amino acid sequence of OATP1B1 and OATP1B3 recognized by the antibody used for Western blotting (red). (B) Predicted OATP structure based on the amino acid sequence of OATP1B1 (white) and OATP1B3 (green). The domain recognized by the applied antibody is marked for OATP1B1 in purple and OATP1B3 for in red.

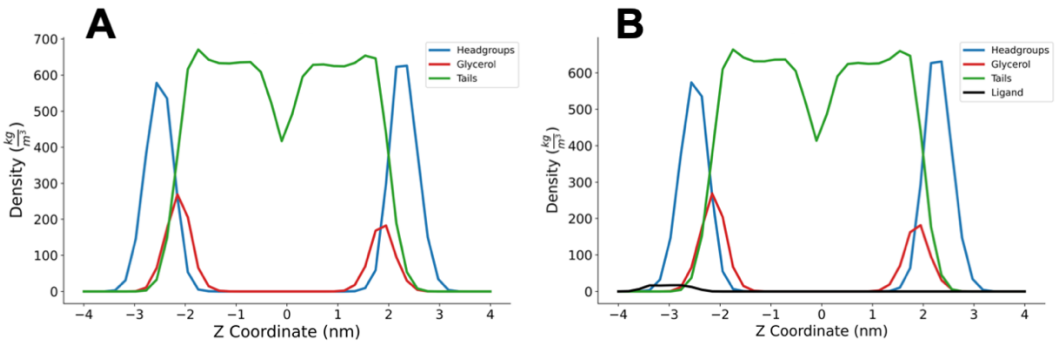

Supplementary Figure S4.34. Density profiles of lipid head groups (blue), glycerol groups (red), lipid tails (green) and RB (black) with respect to the bilayer center (z=0) for the control simulation (A) and the simulation with 1 RB molecule (B).

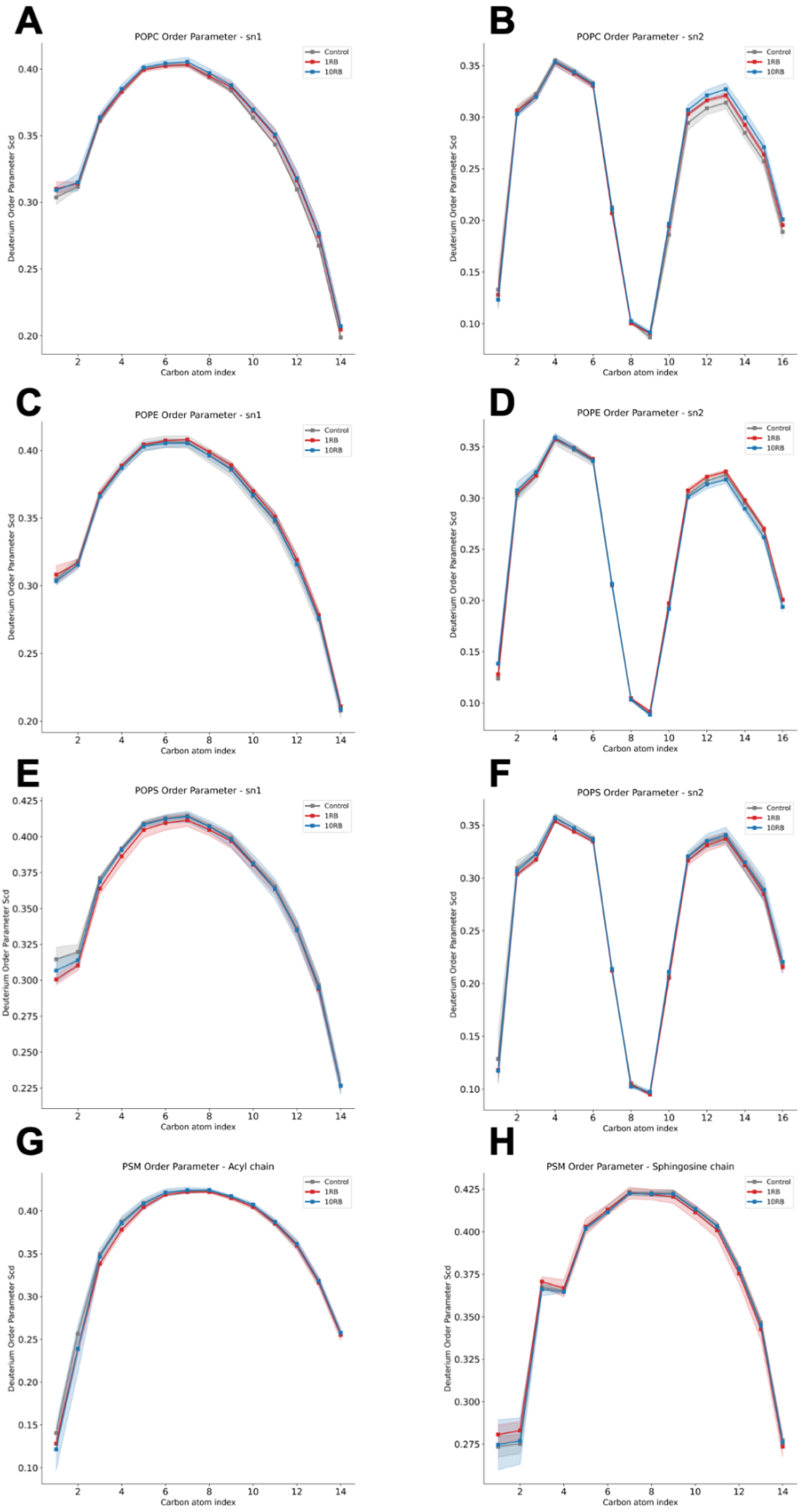
A
POPC Order Parameter - sn1
B
POPC Order Parameter - sn2
C
POPE Order Parameter - sn1
D
POPE Order Parameter - sn2
E
POPS Order Parameter - sn1
F
POPS Order Parameter - sn2
G
PSM Order Parameter - Acyl chain
H
PSM Order Parameter - Sphingosine chain
Control
1RB
10RB
Deuterium Order Parameter Scd
Carbon atom index

Supplementary Figure S 4.35. Deuterium order parameters, SCD, f the sn1 (left column) and sn2 (right column) chains of POPC (A and B), POPE (C and D), POPS (E and F) and PSM (G and H). Each plot reports the order parameters as a function of the carbon atom index for the control simulation (grey), the simulation with 1 RB (red) and the simulation with 10 RB molecules (blue). Shaded colors represent the 95% confidence interval for each series calculated after block-averaging.

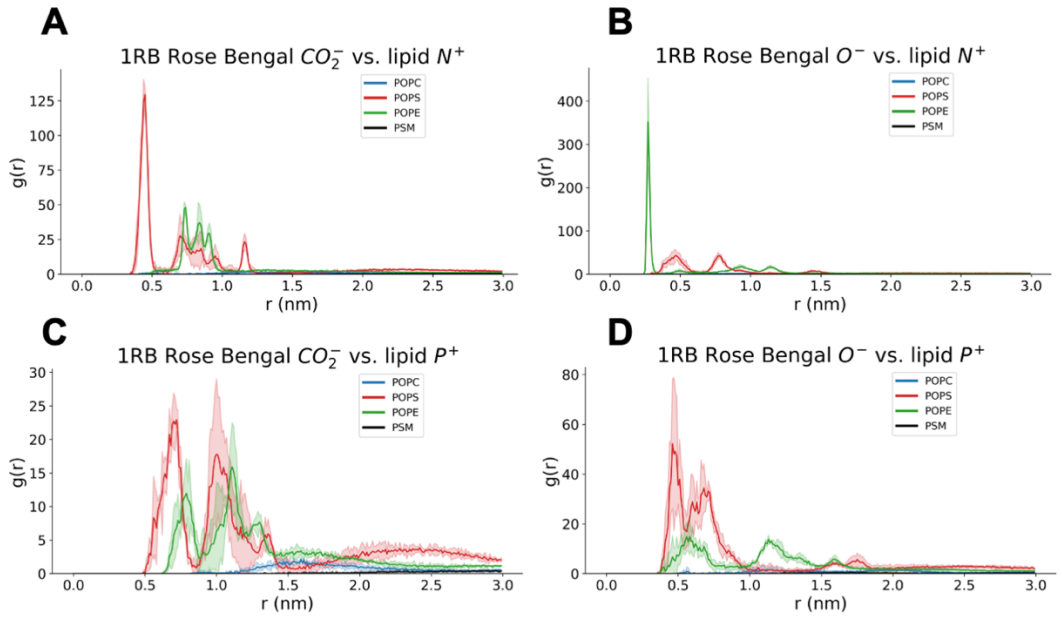

Supplementary Figure S4.36. Radial distribution functions from the simulation with 1 RB molecule, highlighting the distances between RB CO2- groups and lipid head nitrogen atoms (A) and phosphorus (C) atoms, and the distances between RB O- groups and lipid head nitrogen (B) and phosphorus (D) atoms. Shaded intervals represent 95% confidence intervals calculated from block averaging.

4.3 Dendrimeric nanoparticles as candidate nanocarriers for Rose Bengal

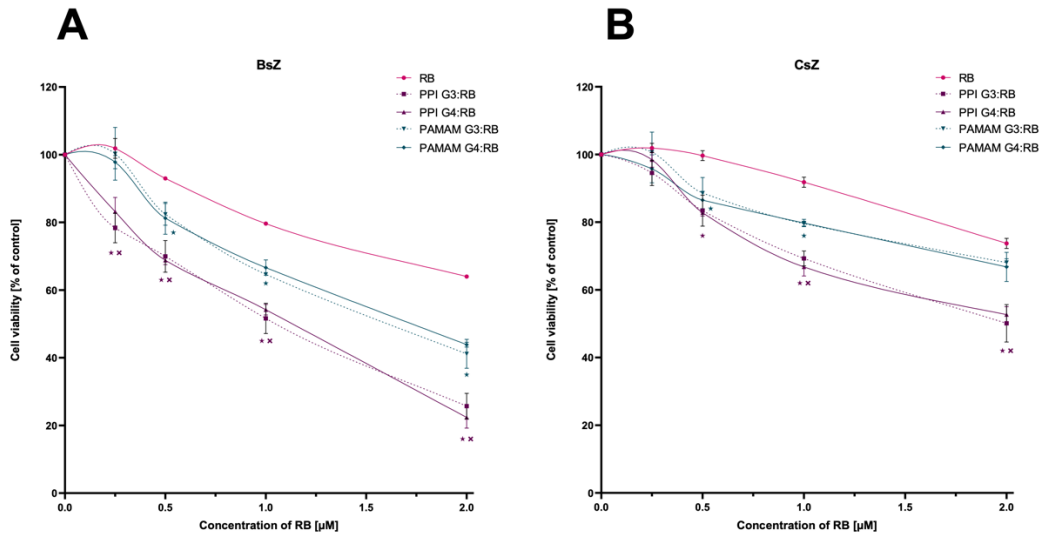

Supplementary Figure S4.37. Phototoxic effect of RB and dendrimer:RB complexes in 1:10 molar ratio, in BsZ and CsZ cells. The viability of cells was determined using MTT assay. Data are presented as percentage of viability of control (untreated) cells; mean ± SD; n = 6. *Statistically significant difference vs. free RB; $p < 0.05$. ×Statistically significant difference vs. dendrimers of different type, regardless of generation; $p < 0.05$.

Supplementary Table ST4.5. Statistically significant differences (*$p < 0.05$) in intracellular uptake of the tested compounds at the indicated time points.

		RB	PPI G3:RB	PPI G4:RB	PAMAM G3:RB	PAMAM G4:RB
0.25 h	RB	-			*	
	PPI G3:RB		-	*		
	PPI G4:RB			-		
	PAMAM G3:RB				-	
	PAMAM G4:RB					-
0.5 h	RB	-		*		
	PPI G3:RB		-	*		
	PPI G4:RB			-	*	*
	PAMAM G3:RB				-	

	PAMAM G4:RB					-
1 h	**RB**	-	*	*		*
	PPI G3:RB		-	*	*	
	PPI G4:RB			-	*	*
	PAMAM G3:RB				-	*
	PAMAM G4:RB					-
2 h	**RB**	-	*	*	*	*
	PPI G3:RB		-	*	*	
	PPI G4:RB			-	*	*
	PAMAM G3:RB				-	*
	PAMAM G4:RB					-
3 h	**RB**	-	*	*	*	*
	PPI G3:RB		-	*	*	
	PPI G4:RB			-	*	
	PAMAM G3:RB				-	*
	PAMAM G4:RB					-
4 h	**RB**	-	*	*	*	*
	PPI G3:RB		-	*	*	
	PPI G4:RB			-	*	
	PAMAM G3:RB				-	*
	PAMAM G4:RB					-

Supplementary Table ST4.6. Comparison of RoG values obtained in the present work with previously published computational and experimental data.

		Literature (MD)			**Experimental**	
System	**This work**	**GAFF**	**CHARMM**	**Other**	**SANS**	**SAXS**
PAMAM G3	1.460 ± 0.058	1.578 ± 0.029[5] 1.21[6] 1.52[7]	1.533[8] 1.408[9]	1.61 ± 0.01[10] 1.454[11] 1.97[12] 1.619[9]	1.666[13]	1.509[14]

PAMAM G4	1.859 ± 0.064	2.064 ± 0.022[5] 1.49[6]	2.104[8]	2.06 ±0.01[10] 2.143 ± 0.01[15] 2.17 ± 0.001[12] 1.848[11] 1.7[16] 2.67[12]	2.129[13]	1.860[14]
PPI G3	1.284 ± 0.024			1.16 ± 0.007[10] 1.342[11]	1.24[17] 1.16[18]	1.33[19]
PPI G4	1.590 ± 0.020	1.601 ± 0.011[5] 1.577 ± 0.021[20]		1.40 ± 0.007[10] 1.648[11] 1.59[21] 1.577 ± 0.021[20]	1.56[17] 1.39[18]	1.43[19]

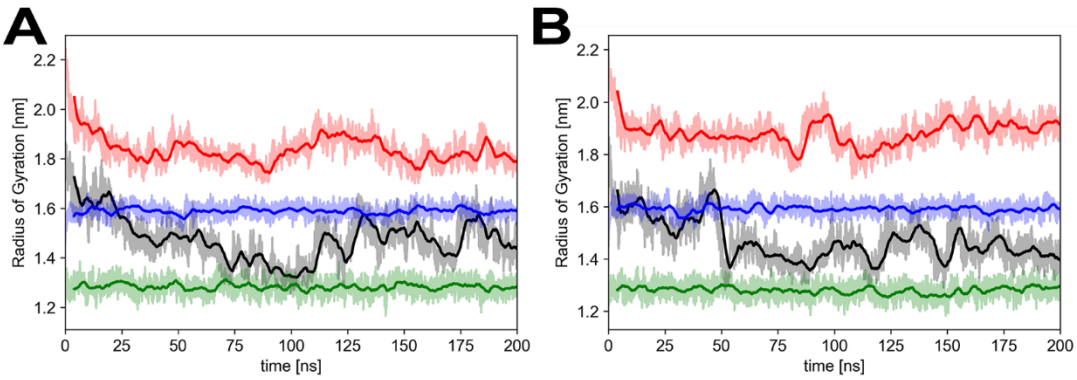

Supplementary Figure S4.38. Radius of gyration (RoG) during the first (A) and second (B) 200 ns replicates of the dendrimer systems. PAMAM G3 is presented in black, PAMAM G4 in red, PPI G3 in green, and PPI G4 in blue. Shaded colors show data from all processed trajectories, whereas solid colors represent moving averages.

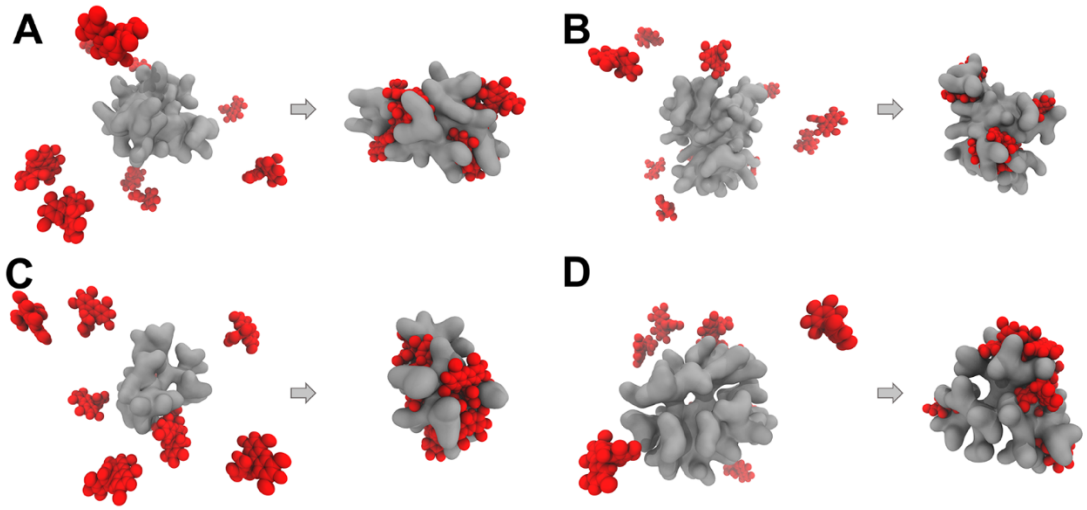

Supplementary Figure S 4.39. Starting and final snapshots of the MD simulation from the first replica for (A) PAMAM G3, (B) PAMAM G4, (C) PPI G3 and (D) PPI G4 with 10 RB molecules.

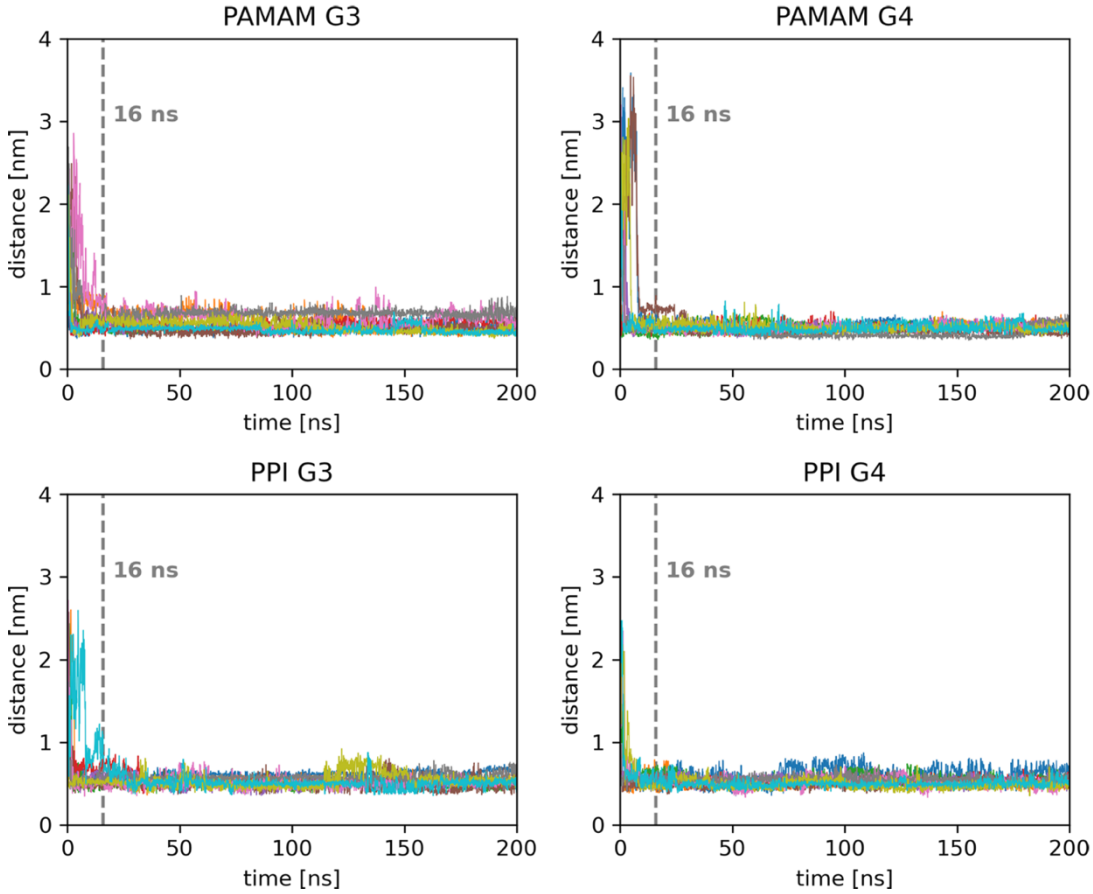

Supplementary Figure S 4.40. Distances of the centers of mass of the 10 RB molecules with respect to the center of mass of each dendrimer during the first MD replica. Each RB molecule is represented with a different color.

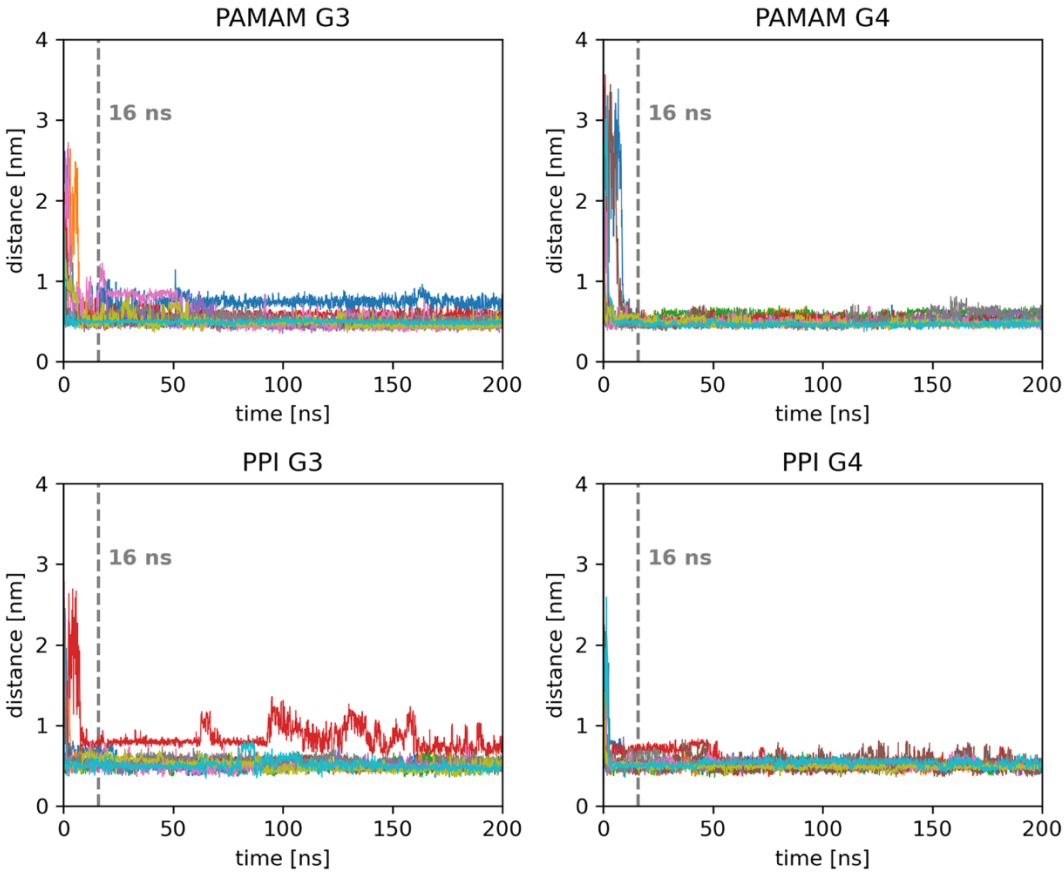

Supplementary Figure S4.41. Distances of the centers of mass of the 10 RB molecules with respect to the center of mass of each dendrimer during the second MD replica. Each RB molecule is represented with a different color.

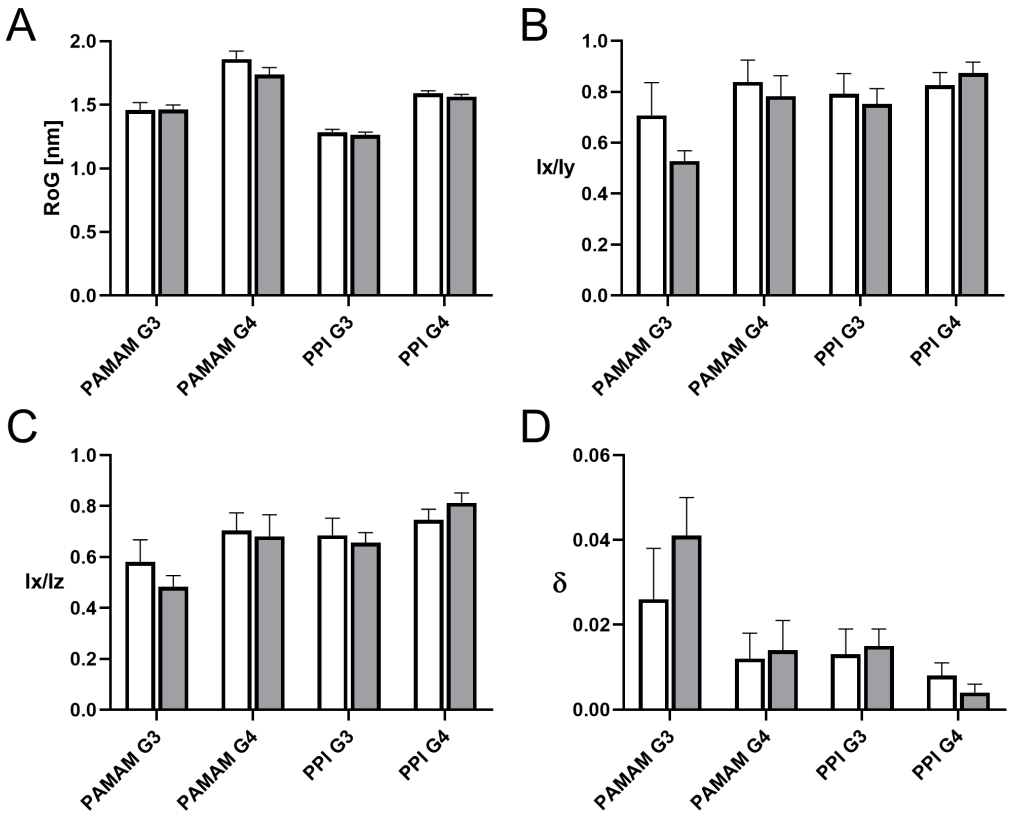

Supplementary Figure S4.42. Comparison of average values (± SD) of geometrical descriptors in the presence (gray) and absence (white) of RB. (A) Radius of gyration (RoG), (B, C) aspect ratios, and (D) asphericity. Data were obtained by averaging over the last 50 ns of simulation from two MD replicas, with snapshots taken every 2 ps.

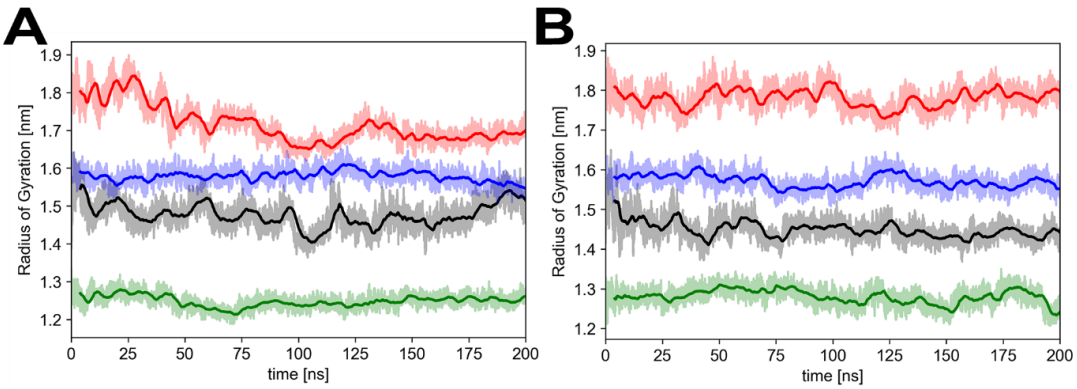

Supplementary Figure S4.43. Radius of gyration (RoG) during the first (A) and second (B) 200 ns replicates of the dendrimer:RB complexes. PAMAM G3:RB complex is presented

in black, PAMAM G4:RB in red, PPI G3:RB in green, and PPI G4:RB in blue. Shaded colors show data from all processed trajectories, whereas solid colors represent moving averages.

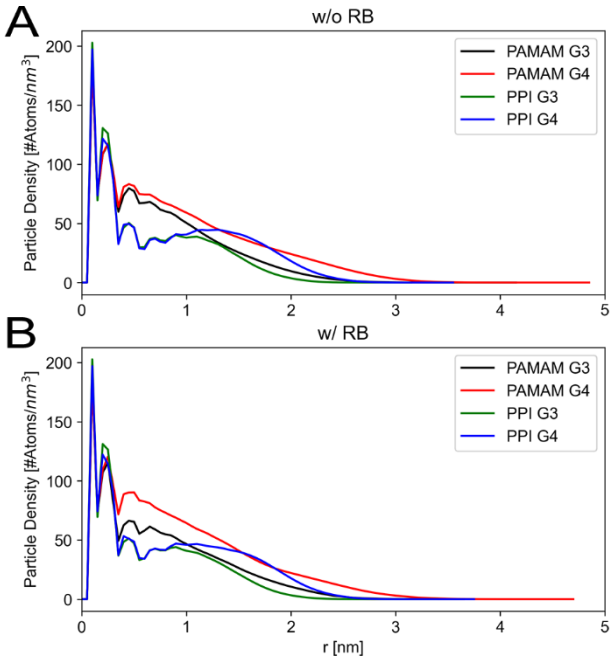

Supplementary Figure S4.44. Particle density (number of atoms per unit volume) of the investigated dendrimers with respect to the dendrimer central core in the (A) presence and (B) absence of RB

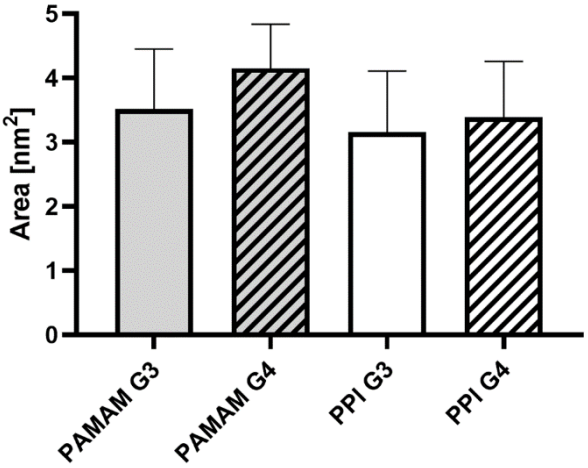

Supplementary Figure S4.45. Average (± SD) of the interaction area between dendrimers and RB molecules during the last 50 ns of the two independent MD replicates.

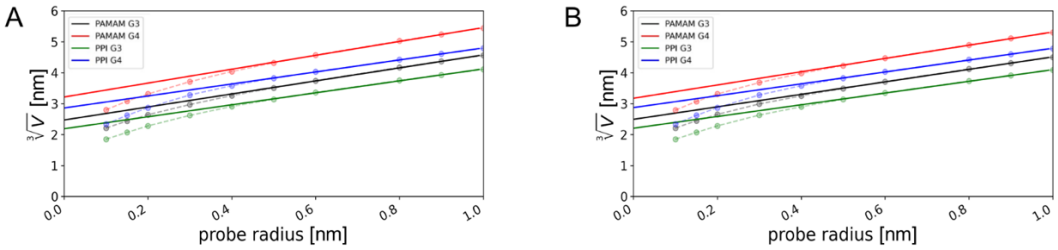

Supplementary Figure S4.46. Linear regression to calculate the volumes of internal cavities for (A) dendrimer-only systems and (B) dendrimer:RB complexes.

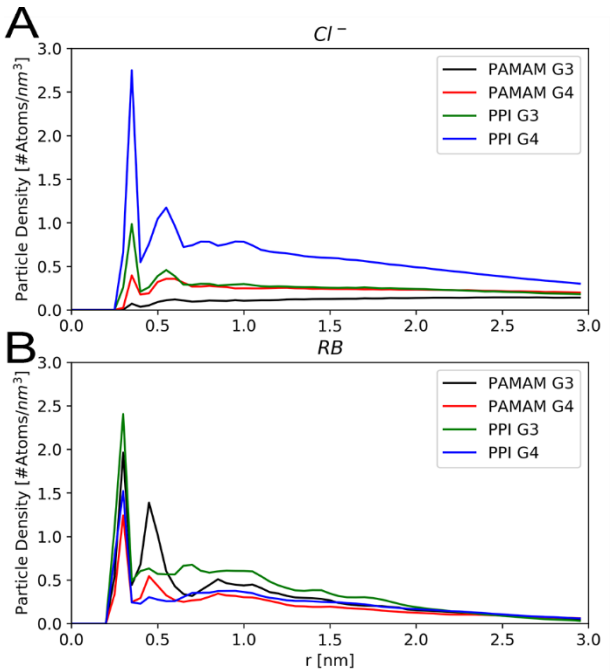

Supplementary Figure S4.47. RDF of (A) the CL- ions and (B) RB molecules with respect to the positively charged amines of the simulated dendrimers during the concatenated equilibrium trajectory (last 50 ns of each MD replica).

Multiple-dendrimer systems

Snapshots of each of the simulated dendrimers at structural equilibrium were extracted from previously described MD simulations and used to build multiple-dendrimer systems as follows: two copies of each dendrimer configuration were juxtaposed to obtain two-dendrimer systems with an inter-dendrimer distance of 2 nm. The obtained configuration was inserted into a dodecahedral box, and 20 RB

molecules were added in random positions around the dendrimer to obtain a 1:10 dendrimer:RB molar ratio. The systems were solvated, neutralized, and simulated following the protocols described in the Materials and Methods.

During this set of simulations, G3 dendrimers exhibited a marked tendency to interact with each other, whereas G4 dendrimers either interacted on longer time scales or were unable to interact (Supplementary Figure S4.48). We are well aware that the complete characterization of such processes requires a more thorough sampling. Accordingly, we wish to emphasize that these results are complementary to surface potential data derived from APBS, with more neutral complexes of G3 dendrimers interacting with each other, and complexes of G4 dendrimers (with more positive surface potential) showing only marginal to no interaction. Such preliminary data provide be a suitable starting point for future developments aimed at a thorough characterization of dendrimer–dendrimer interaction and cell internalization mechanisms.

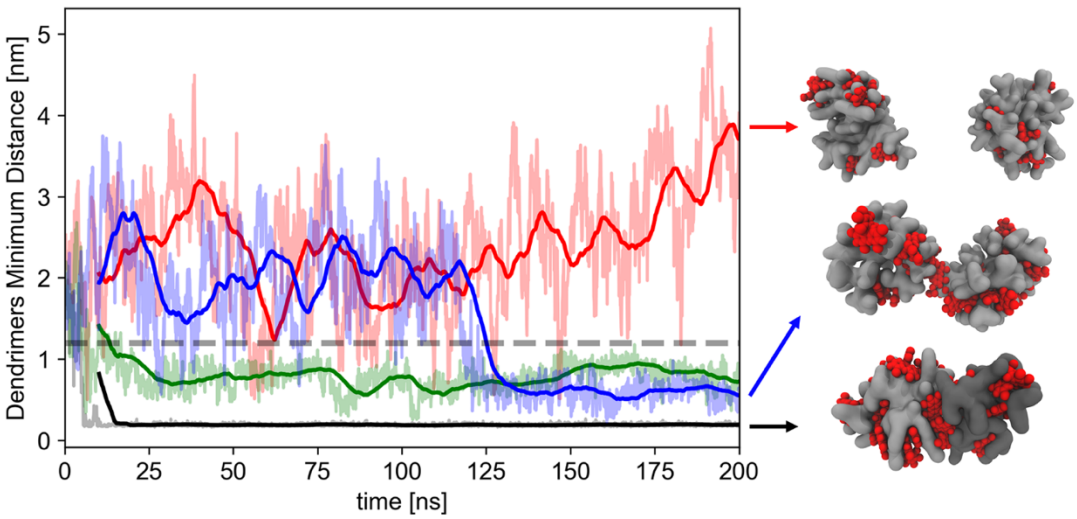

Supplementary Figure S4.48. Dendrimer–dendrimer minimum distance during the 200 ns MD simulation: G3 dendrimers interact after a few ns of simulation, whereas G4 dendrimers interact on longer time scales (PPI) or are not able to interact with each other (PAMAM). PAMAM G3 is presented in black, PAMAM G4 in red, PPI G3 in green, and PPI G4 in blue. Shaded colors show data from all processed trajectories, whereas solid colors represent moving averages. On the right, representative snapshots of the structural stability are presented for PAMAM G3, PPI G4, and PAMAM G4.

Hydrodynamic diameter measurement

The solutions of complexes prepared as described in the point 4.2.2 of the Experimental Section were diluted in HEPES to a final dendrimer concentration of

10 μM and placed in the low volume sizing cuvettes (ZEN0112, Malvern Instruments Ltd., Malvern, UK). Measurements were performed at 25°C. The data were analyzed using the Malvern software. The particle size distribution was determined using a multimodal peak analysis, with individual peaks analyzed by number. Data were presented as mean ± SD, n = 3 (8 measurements each) (Supplementary Table ST4.7).

Supplementary Table ST4.7. Hydrodynamic diameters of dendrimer:RB complexes. Data presented as average ± SD, n = 3 (8 measurements each)

	Hydrodynamic diameter [nm]	Polydispersity index (PDI)
PAMAM G3:RB	232.52 ± 10.11	0.30 ± 0.06
PAMAM G4:RB	6.20 ± 2.42	0.28 ± 0.10
PPI G3:RB	311.50 ± 39.95	0.56 ± 0.18
PPI G4:RB	373.87 ± 59.28	0.60 ± 0.16

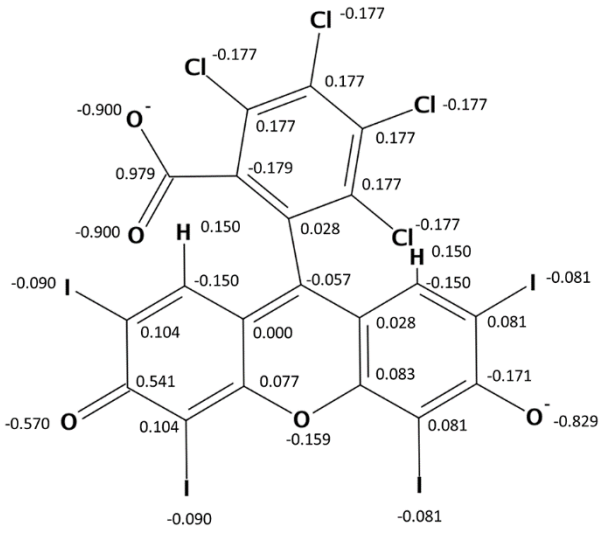

Supplementary Figure S4.49. Rose bengal (RB) structure with partial charges assigned using the AM1-BCC charge method

4.4 Tailoring tubulin assemblies as GTP-responsive drug delivery nanocapsules

4.4.1 Materials and Methods

Materials

Unless indicated otherwise, all commercial reagents were used as received. Bovine serum albumin (BSA), doxorubicin hydrochloride (DOX), uridine-5'-triphosphate trisodium salt (UTP), cytidine-5'-triphosphate disodium salt (CTP), guanosine-5'-triphosphate trisodium salt (GTP), guanosine-5'-diphosphate sodium salt (GDP), adenosine-5'-triphosphate disodium salt (ATP), and Dulbecco's phosphate-buffered saline (D-PBS) were purchased from Wako Pure Chemical Industries. Fluorescein isothiocyanate (FITC) and 1,4-piperazinediethanesulfonic acid (PIPES) were purchased from Tokyo Chemical Industry (TCI). Guanylyl 5'-α, β-methylenediphosphonate (GTP*) was purchased from Cosmobio. Foetal bovine serum (FBS) was purchased from Thermo Fisher Scientific. Eagle's minimal essential medium (EMEM) was purchased from Life Technologies. Polyacrylamide gel was purchased from Bio-Rad. Biomol GreenTM Reagent was purchased from Enzo Life Sciences. Cell Counting Kit-8 was purchased from Dojindo Laboratories. The human hepatocellular carcinoma Hep3B cell line (ATCC® HB-8064TM) was purchased from American Type Culture Collection (ATCC). α-Mercaptoethyl-ω-methoxy, polyoxyethylene (PEG-SH, Mw; 5 K) was purchased from NOF. Gold nanoparticles (50 nm in diameter) were purchased from Sigma–Aldrich. Polyoxyethylene sorbitan monolaurate (Tween 20) was purchased from Nacalai Tesque.

General Procedures

^{1}H NMR and ^{13}C NMR spectra were recorded on a JEOL model GSX-500 spectrometer, where chemical shifts (δ in ppm) were determined using $CHCl_3$ (δ 7.26), $CHD_2(CD_3)SO$ (δ 2.50), and HDO (δ 4.79) for ^{1}H NMR and $CDCl_3$ (δ 77.2) and $(CD_3)_2SO$ (δ 39.5) for ^{13}C NMR as internal references. Matrix-assisted laser desorption ionization time-of-flight (MALDI-TOF) mass spectrometry was performed with *a*-cyano-4-hydroxycinnamic acid (CCA), 2,5-dihydroxybenzoic acid (DHB), or sinapinic acid (SA) as a matrix and an Applied Biosystems Biospectrometry Workstation^{TM} model Voyager-DE^{TM} STR spectrometer or a

Bruker model Autoflex Speed™ spectrometer. A Horiba model AS-212 compact pH metre was used for pH measurements. Electronic absorption spectra were recorded with a Molecular Devices model SpectraMax Paradigm multimode microplate detection platform, a Thermo Scientific model NanoDrop 2000c spectrophotometer, or a JASCO Model V-570 spectrophotometer. Fluorescence spectra were recorded using a Molecular Devices model SpectraMax Paradigm multimode microplate detection platform. UV exposure for photoreaction was performed with a UVP model UVLM-28 UV lamp. Analyses of images of the acrylamide gels were performed using an Amersham Biosciences model Typhoon 9410 variable image analyser.

Recycling preparative gel permeation chromatography (GPC) was performed with a Japan Analytical Industry model LC908-C60 using a column set consisting of JAIGEL 1H-40 and 2H-40. Transmission electron microscopy (TEM) images were recorded using a JEOL model JEM-1400 electron microscope operating at an anode voltage of 120 kV. Samples were applied to an electron microscope specimen grid covered with a thin carbon support film that had been hydrophilized by ion bombardment. Then, the samples were negatively stained with a saturated uranyl acetate solution. Tapping-mode atomic force microscopy (AFM) of air-dried samples on a mica surface was performed using an SII Nano Technology model NanoNavi S-image. Small-angle X-ray scattering (SAXS) was carried out at BL45XU in SPring-8 (Hyogo, Japan) with a Dectris model Pilatus 3X 300K-W detector. Scattering vector q ($q = 4\pi\sin\theta/\lambda$; 2θ and λ are the scattering angle and wavelength of the incident X-ray beam [1.70 Å], respectively) and the position of an incident X-ray beam on the detector were calibrated using several orders of layer reflections from silver behenate (d = 58.380 Å). Dynamic light scattering (DLS) measurements were performed with a Malvern model Zetasizer μV light scattering spectrometer using an infrared laser (830 nm). Zeta potential measurements were performed using a Malvern model Zetasizer Nano ZSP zeta potential analyser. Confocal laser scanning microscopy (CLSM) was performed using a Leica model TCS SP8 microscope. Flow cytometry was performed using a BD model Accuri® C6 flow cytometer. Asymmetric field flow fractionation was performed using an Eclipse model AF4 separation system equipped with a JASCO model UV-2070*plus* variable-wavelength UV-Vis detector. A regenerated cellulose membrane with a 5 kD cut-off (Wyatt Technology) and 350 μm spacer to adjust the channel thickness was used in combination with PIPES buffer (10 mM PIPES and 1 mM $MgCl_2$, pH 6.8) as an eluent (detector-flow rate: 1.0 ml min^{-1} cross-flow rate: gradient from 0.5

ml min^{-1} to 0 ml min^{-1} for 180 min, transition time: 5 min). BSA was used as a standard for evaluating the concentrations of tubulin heterodimer (THD). Ultrafiltration was performed using cellulose-made centrifugal filters (Amicon® Ultra-0.5 ml 100K) with a molecular weight cut-off of 100 kDa. Concentrations of FITC molecules and gold nanoparticles were measured by determining the absorbance at 490 nm and 540 nm, respectively.

Synthesis of compounds

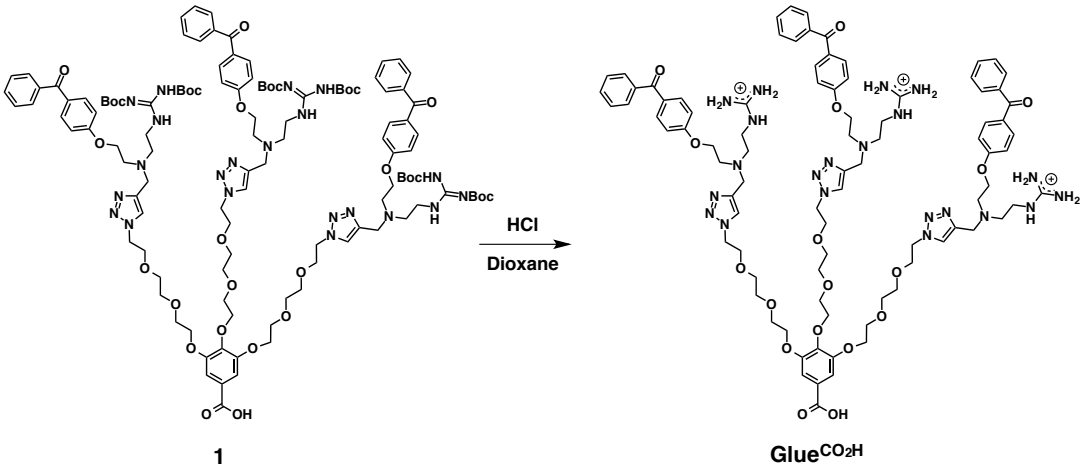

Supplementary Figure S4.50. GlueCO2H: To a 1,4-dioxane (10 ml) solution of HCl (4 M) was added 1 (99 mg, 42 µmol)6, and the mixture was stirred for 4 h at room temperature. Compound 1 (99 mg, 42 µmol) was added to a 1,4-dioxane (10 ml) solution containing HCl (4 M)6, and the mixture was stirred for 4 h at room temperature. Hexane (50 ml) was added to the reaction mixture, and the mixture was filtered. The insoluble fraction was dissolved in water and then reprecipitated with 1,4-dioxane to enable the isolation of GlueCO2H as a yellow solid at a 74% yield (58 mg). 1H NMR (500 MHz, DMSO-d6, 28 °C): δ (ppm) 3.34–4.64 (br, 66H), 7.17 (br, 6H), 7.53–7.73 (br, 22H), 8.16 (br, 2H), 8.46 (br, 2H), 11.64 (br, 3H). 13C NMR (125 MHz, DMSO-d6, 28 °C): δ (ppm) 35.7, 47.2, 49.6, 51.0, 51.4, 62.5, 68.5, 68.8, 69.5, 69.7, 71.7, 108.1, 114.4, 125.5, 127.8, 128.3, 129.1, 129.9, 131.9, 132.1, 135.6, 137.4, 141.3, 151.7, 157.0, 160.9, 166.6, 194.3. MALDI-TOF-MS m/z calculated for C88H112N21O17S [M – 3HCl + H]+; 1734.85, found; 1735.69.

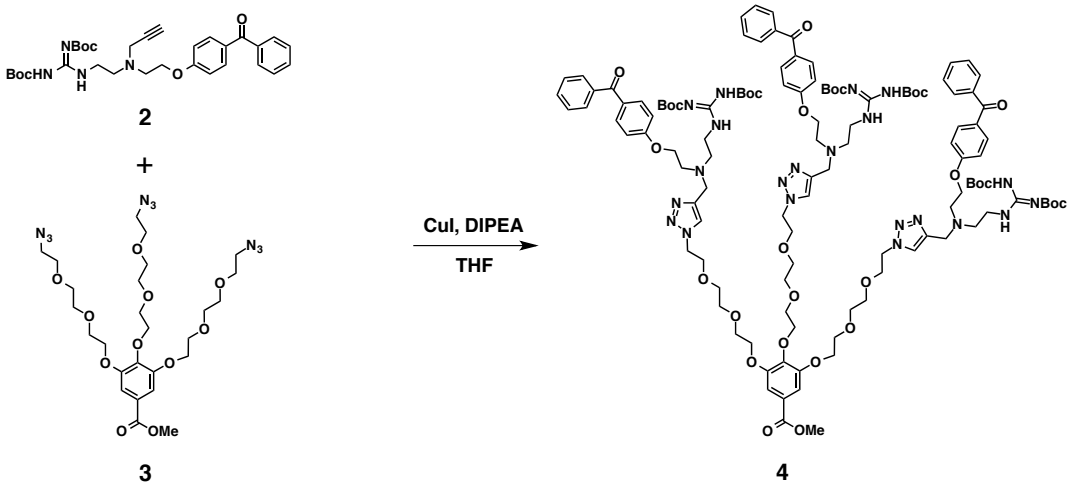

Supplementary Figure S4.51. Compound 4: To a THF (60 ml) solution of a mixture of 2 (470 mg, 832 μmol)6, 3 (136 mg, 208 μmol)7, and diisopropylethylamine (DIPEA, 181 μl, 1.7 mmol) was added copper iodide (158 mg, 832 μmol), and the mixture was stirred for 17 h at room temperature. Copper iodide (158 mg, 832 μmol) was added to a THF (60 ml) solution composed of a mixture of Compound 2 (470 mg, 832 μmol)6, Compound 3 (136 mg, 208 μmol)7, and diisopropylethylamine (DIPEA, 181 μl, 1.7 mmol), and the mixture was stirred for 17 h at room temperature. The reaction mixture was extracted with AcOEt, and washed with saturated aqueous NH4Cl and brine. A separated organic extract was dried over Na2SO4 and filtered off from an insoluble fraction. The filtrate was subjected to recycling preparative GPC using CHCl3 as an eluent to isolate Compound 4 as a green solid at a 21% yield (100 mg). 1H NMR (500 MHz, CDCl3, 24 °C): δ (ppm) 1.43–1.46 (s, 54H), 2.80–2.97 (br, 12H), 3.54–4.13 (br, 48H), 4.47 (br, 6H), 6.90–6.92 (br, 6H), 7.45–7.75 (br, 26H), 8.73 (s, 3H), 11.43 (br, 3H). 13C NMR (125 MHz, CDCl3, 24 °C): δ (ppm) 28.1, 28.4, 29.8, 38.7, 49.3, 50.3, 50.8, 52.2, 52.5, 66.9, 68.8, 69.6, 69.9, 70.5, 72.5, 79.5, 83.1, 108.9, 114.1, 124.1, 125.4, 128.3, 129.8, 130.2, 132.1, 132.6, 138.1, 138.3, 152.3, 153.0, 156.1, 162.0, 162.5, 163.4, 195.6. MALDI-TOF-MS m/z calculated for C89H114N21O17S [M – 6Boc + H]+; 1748.87, found; 1749.83.

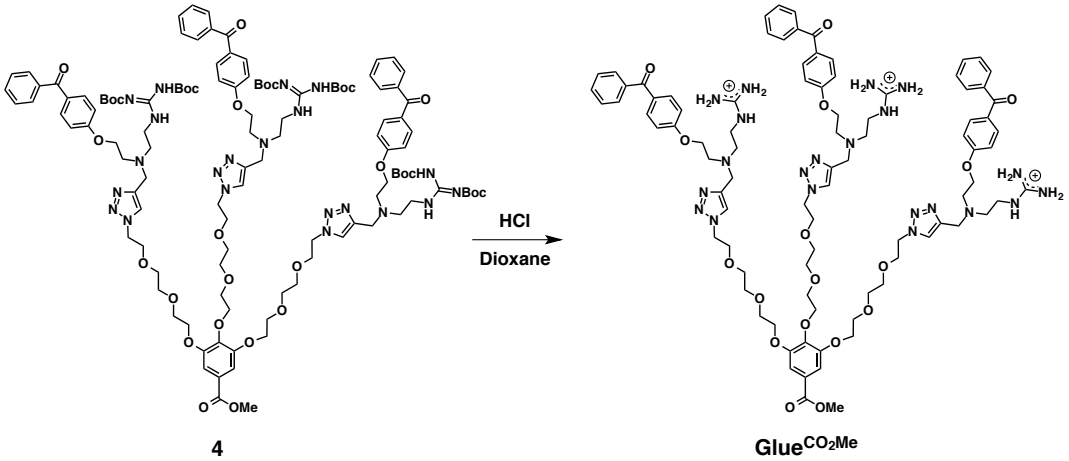

Supplementary Figure S4.52. GlueCO2Me: To a 1,4-dioxane/Et2O (1/1) solution (10 ml) of HCl (2 M) was added 4 (6.5 mg 2.8 µmol), and the mixture was stirred for 4.5 h at room temperature. Compound 4 (6.5 mg 2.8 µmol) was added to a 1,4-dioxane/Et2O (1/1) solution (10 ml) of HCl (2 M), and the mixture was stirred for 4.5 h at room temperature. Then, the reaction mixture was evaporated to dryness under reduced pressure. The residue was dissolved in water and then reprecipitated in 1,4-dioxane to isolate GlueCO2Me as a yellow solid with an 83% yield (4.3 mg). 1H NMR (500 MHz, D2O, 27 °C): δ (ppm) 3.54–3.97 (br, 57H), 4.31 (br, 6H), 4.66 (br, 6H), 6.88–6.90 (br, 8H), 7.49–7.62 (br, 22H), 8.29 (br, 2H). 13C NMR (125 MHz, DMSO-d6, 27 °C): δ (ppm) 48.0, 49.3, 49.7, 51.3, 52.3, 66.4, 68.4, 68.7, 69.5, 69.7, 71.9, 108.2, 114.3, 124.1, 124.4, 128.3, 128.3, 128.4, 129.2, 129.3, 132.1, 137.7, 141.7, 142.7, 151.9, 157.1, 162.0, 165.7, 194.3. MALDI- MALDI-TOF-MS m/z calculated for C89H114N21O17S [M – 3HCl + H]+; 1748.87, found; 1749.22.

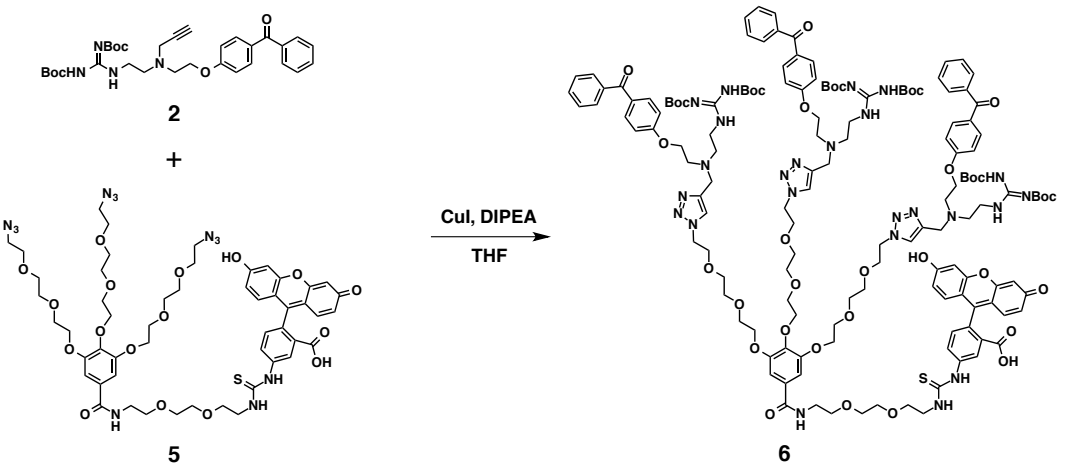

Supplementary Figure S4.53. Compound 6: To a THF (50 ml) solution of a mixture of 2 (215 mg, 380 µmol), 5 (110 mg, 95 µmol)6, and DIPEA (84 µl, 760 µmol) was added copper iodide (72 mg, 380 µmol), and the mixture was stirred overnight at room temperature. Copper iodide (72 mg, 380 µmol) to a THF (50 ml) solution composed of a

mixture of Compound 2 (215 mg, 380 µmol), Compound 5 (110 mg, 95 µmol)6, and DIPEA (84 µl, 760 µmol), and the mixture was stirred overnight at room temperature. The reaction mixture was extracted with AcOEt, and washed with saturated aqueous NH4Cl and brine. A separated organic extract was dried over Na2SO4 and filtered off from an insoluble fraction. The filtrate was subjected to recycling preparative GPC using CHCl3 as an eluent to isolate Compound 6 as a yellow solid with a 56% yield (151 mg). 1H NMR (500 MHz, DMSO-d6, 23 °C): δ (ppm) 1.35–1.39 (s, 54H), 2.67–2.84 (br, 12H), 3.50–4.13 (br, 60H), 4.46 (br, 6H), 6.58–6.67 (br, 5H), 7.01-7.17 (br, 9H), 7.52-7.64 (br, 23H), 7.97 (br, 4H), 8.48 (s, 3H), 10.13 (br, 1H), 11.43 (br, 3H). 13C NMR (125 MHz, CDCl3, 27 °C): δ (ppm) 28.1, 28.3, 29.7, 31.3, 38.7, 49.5, 50.4, 52.2, 52.5, 67.0, 69.3, 69.5, 70.6, 79.3, 82.9, 107.1, 114.1, 115.6, 124.0, 124.9, 128.3, 129.8, 130.1, 132.0, 132.6, 138.3, 140.6, 144.9, 152.2, 153.0, 156.0, 158.6, 162.1, 162.5, 163.5, 195.6. MALDI-TOF-MS m/z calculated for C115H137N24O23S [M – 6Boc + H]+; 2254.00, found; 2254.57.

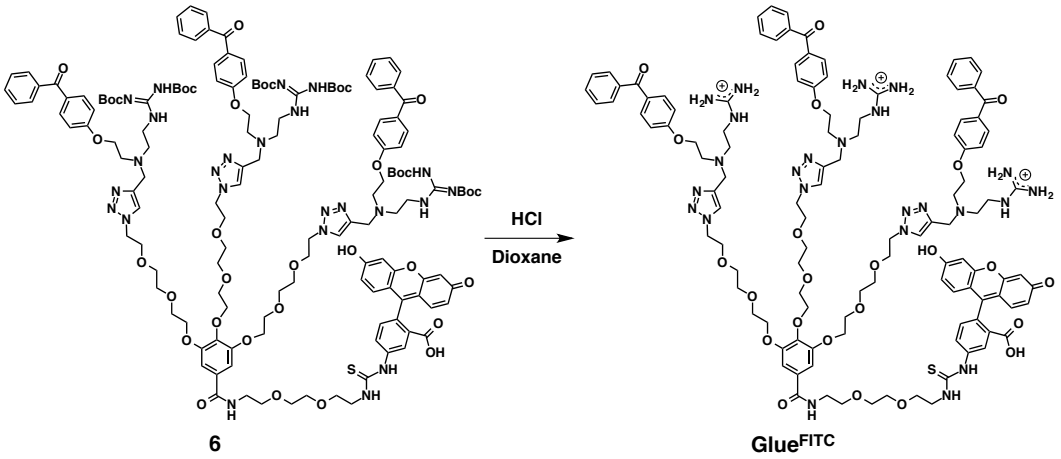

Supplementary Figure S4.54. GlueFITC: To a 1,4-dioxane (10 ml) solution of HCl (4 M) was added 6 (82 mg 29 µmol), and the mixture was stirred for 3 h at room temperature. Compound 6 (82 mg 29 µmol) was added to a 1,4-dioxane (10 ml) solution containing HCl (4 M), and the mixture was stirred for 3 h at room temperature. Then, the reaction mixture was evaporated to dryness under reduced pressure. The residue was dissolved in water and then reprecipitated in 1,4-dioxane to isolate GlueFITC as yellow a solid at a 61% yield (44 mg). 1H NMR (500 MHz, DMSO-d6, 24 °C): δ (ppm) 2.72–2.88 (br, 12H), 3.54–4.64 (br, 66H), 6.59–6.75 (br, 4H), 7.15–7.21 (br, 7H), 7.35 (br, 2H), 7.53–7.73 (br, 23H), 8.12 (br, 3H), 8.45 (br, 2H), 11.64 (br, 3H). 13C NMR (125 MHz, DMSO-d6, 24 °C): δ (ppm) 35.8, 47.2, 49.7, 51.1, 51.5, 60.1, 62.6, 68.3, 68.6, 68.9, 69.6, 69.7, 71.8, 102.2, 106.3, 112.8, 114.6, 127.9, 128.3, 128.4, 129.2, 130.0, 132.0, 132.2, 135.6, 137.5, 139.7, 151.6, 157.0, 161.0, 162.3, 165.5, 194.4. MALDI-TOF-MS m/z calculated for C115H136N24O22S [M – 3HCl – OH + H]+; 2238.01, found; 2238.04, C115H137N24O23S [M – 3HCl + H]+; 2254.00, found; 2253.30.

Analytical data

[1]H and [13]C NMR spectroscopy

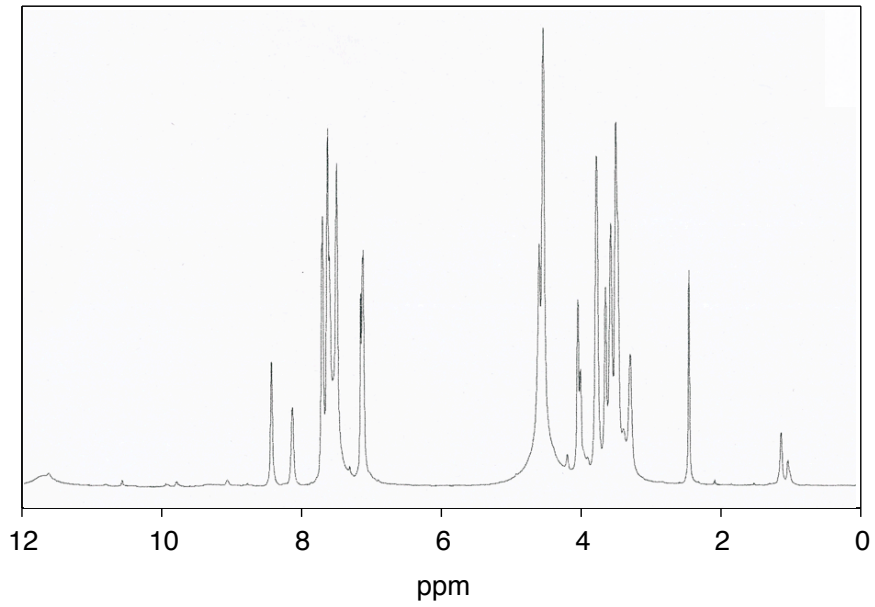

Supplementary Figure S 4.55. ^{1}H NMR spectrum (500 MHz) of Glue^{CO_2H} in DMSO-d_6 at 28 °C.

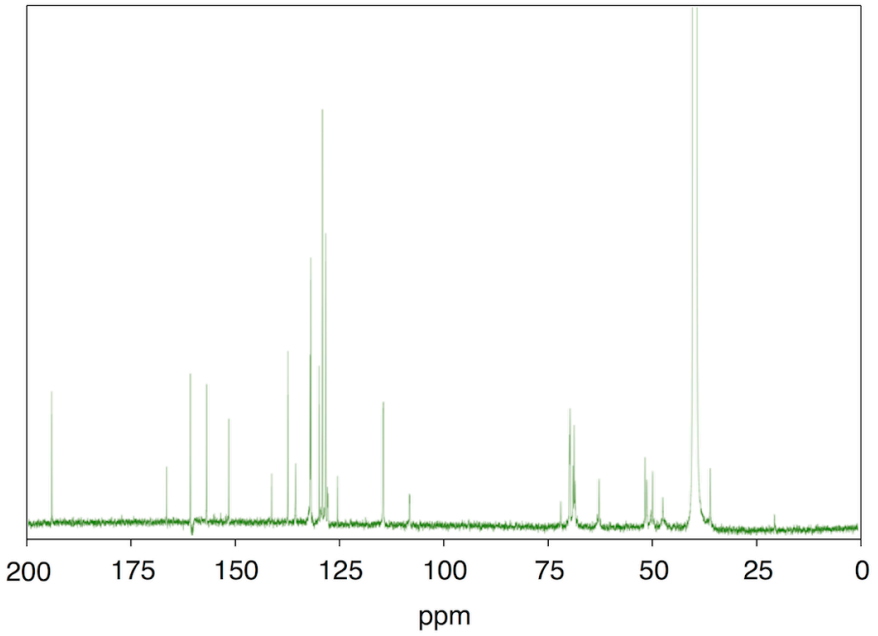

Supplementary Figure S 4.56. ^{13}C NMR spectrum (500 MHz) of Glue^{CO_2H} in DMSO-d_6 at 28 °C.

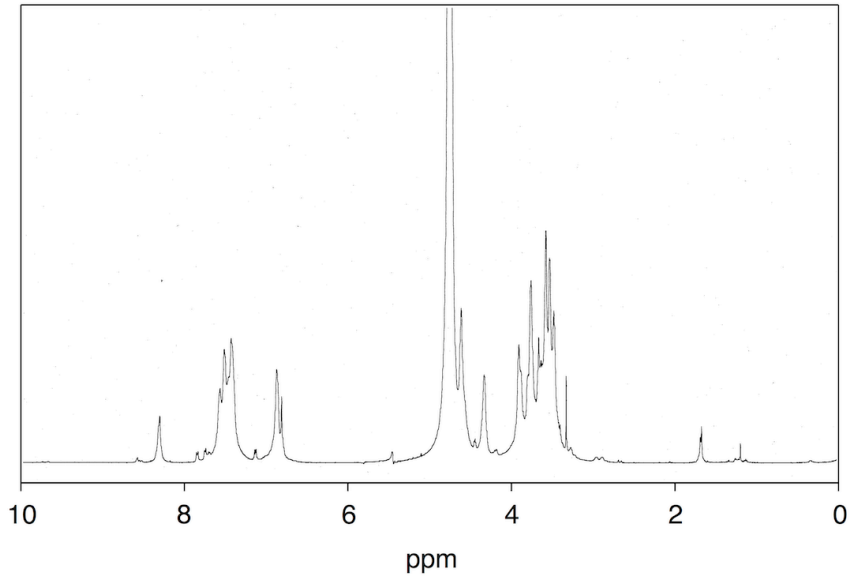

Supplementary Figure S 4.57. ^{1}H NMR spectrum (500 MHz) of Glue^{CO_2Me} in D_2O at 27 °C.

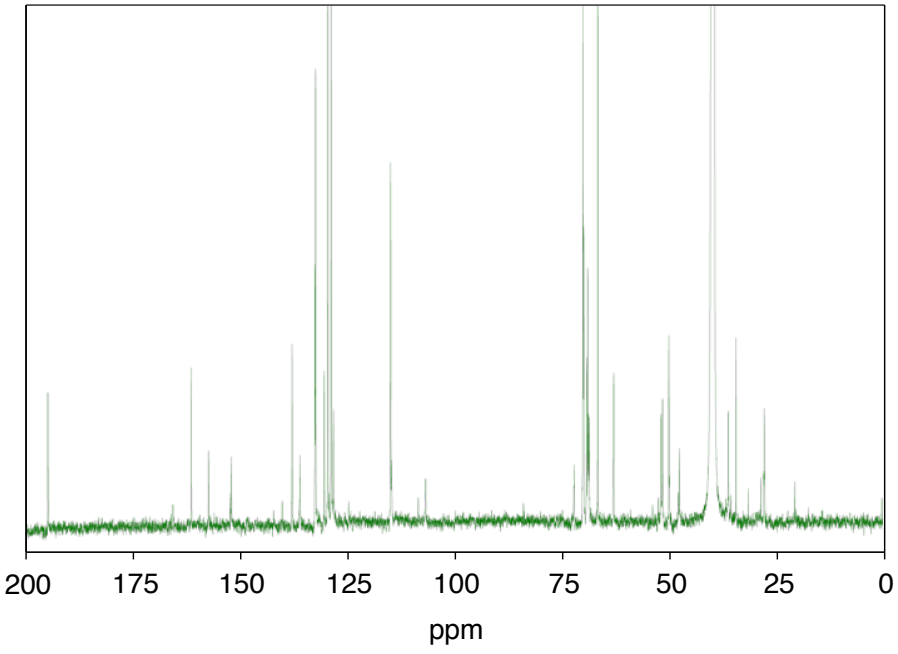

Supplementary Figure S 4.58. ^{13}C NMR spectrum (500 MHz) of Glue^{CO_2Me} in DMSO-d_6 at 27 °C.

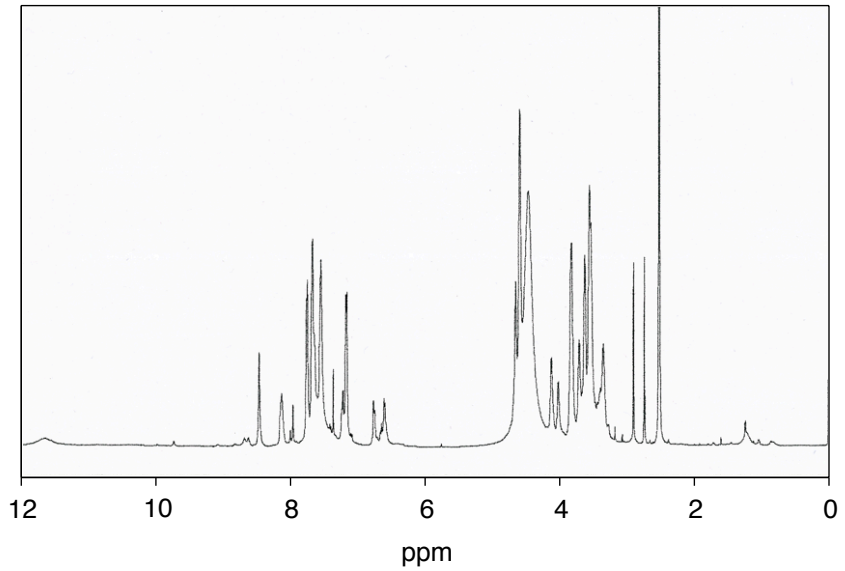

Supplementary Figure S 4.59. ^{1}H NMR spectrum (500 MHz) of Glue^{FITC} in DMSO-d_6 at 24 °C.

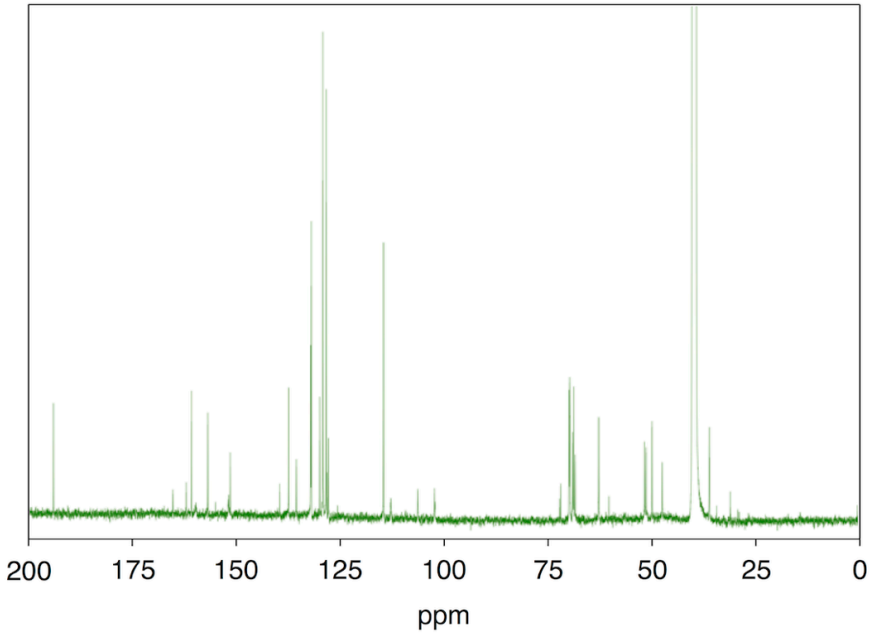

Supplementary Figure S 4.60. ^{13}C NMR spectrum (500 MHz) of Glue^{FITC} in DMSO-d_6 at 24 °C.

MALDI-TOF mass

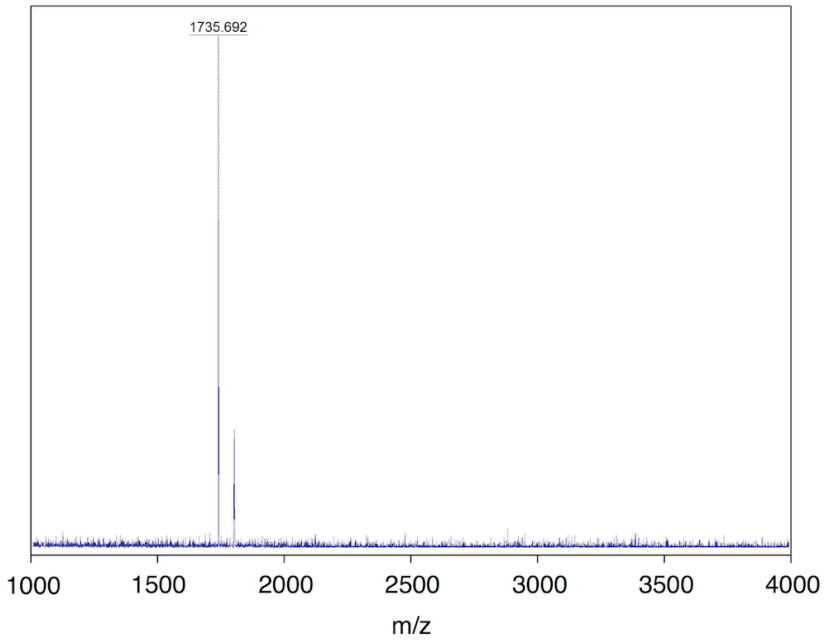

Supplementary Figure S4.61. MALDI-TOF mass spectrum of Glue^{CO_2H}.

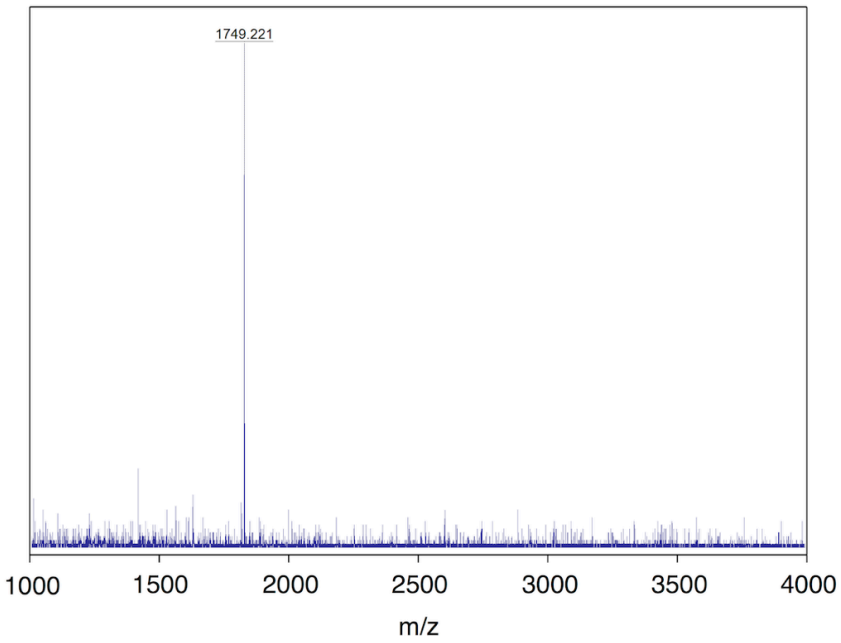

Supplementary Figure S4.62. MALDI-TOF mass spectrum of Glue^{CO_2Me}.

4.4.2 Results

Characterization of $NS_{GTP/GTP*}$

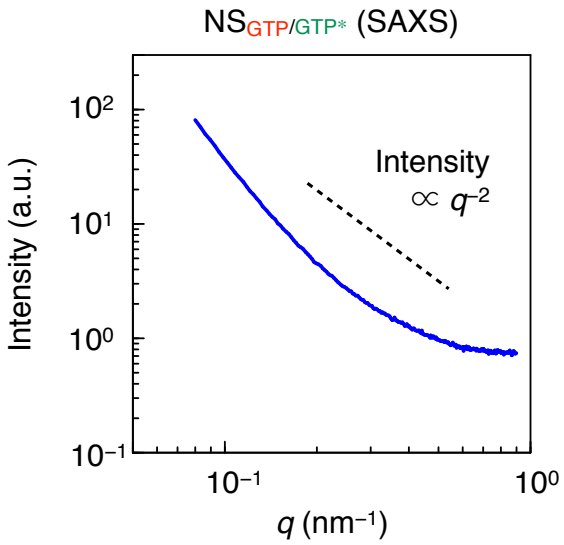

Supplementary Figure S4.63. SAXS profile of a solution of NSGTP/GTP* (0.3 mg ml–1) in PIPES buffer (100 mM PIPES, 1 mM MgCl2, 250 µM GTP*, and 50 µM GTP, pH 6.8). The scattering intensity was proportional to q–2 in the small-q region

*Self-assembly of THD in PIPES buffer containing a high mol% of GTP**

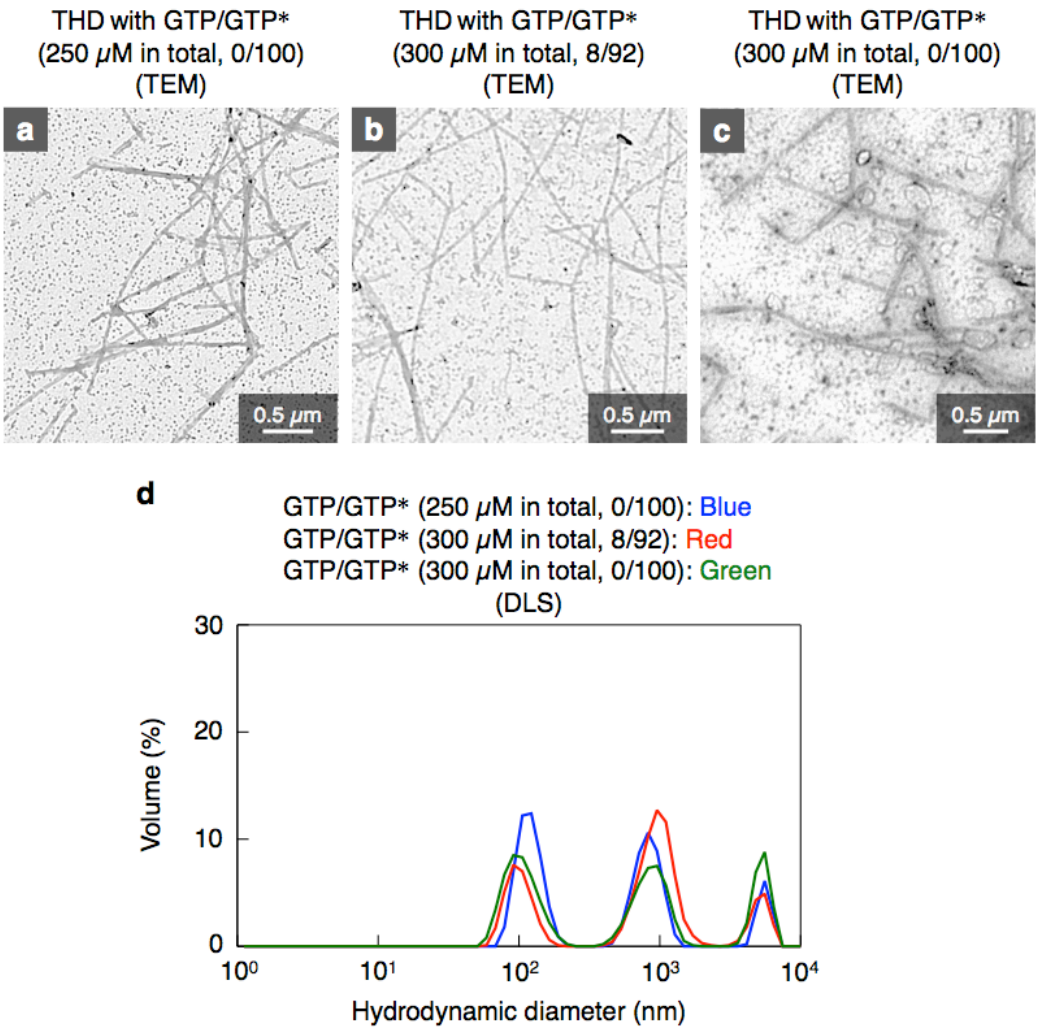

Supplementary Figure S 4.64. **a**–**c**, TEM images of a solution of THD_{GDP} (0.3 mg ml^{-1}) in PIPES buffer (100 mM PIPES and 1 mM $MgCl_2$, pH 6.8) after an incubation with GTP/GTP* (0/250 µM) (**a**), GTP/GTP* (25/275 µM) (**b**), or GTP/GTP* (0/300 µM) (**c**) at 37 °C for 30 min. **d**, DLS profiles of the THD samples incubated with (blue curve) GTP/GTP* (0/250 µM), (red curve) GTP/GTP* (25/275 µM), and (green curve) GTP/GTP* (0/300 µM).

*Self-assembly of THD in PIPES buffer containing a low mol% of GTP**

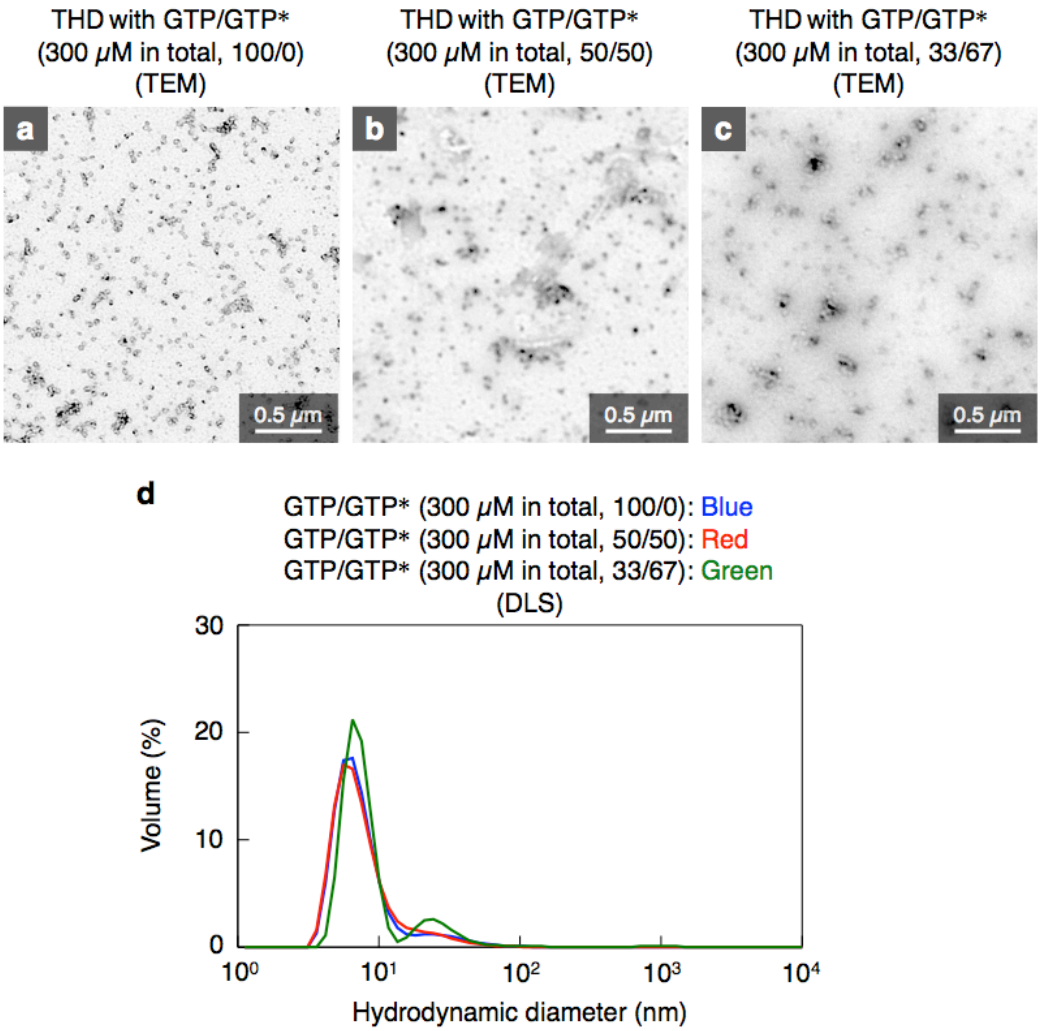

Supplementary Figure S 4.65. a–c, TEM images of a solution of THD (0.3 mg ml–1) in PIPES buffer (100 mM PIPES and 1 mM MgCl2, pH 6.8) after an incubation with GTP/GTP* (300/0 μM) (a), GTP/GTP* (150/150 μM) (b), or GTP/GTP* (100/200 μM) (c) at 37 °C for 30 min. d, DLS profiles of the THD samples incubated with (blue curve) GTP/GTP* (300/0 μM), (red curve) GTP/GTP* (150/150 μM), and (green curve) GTP/GTP* (100/200 μM).

NMR measurement of $NS_{GTP/GTP*}$

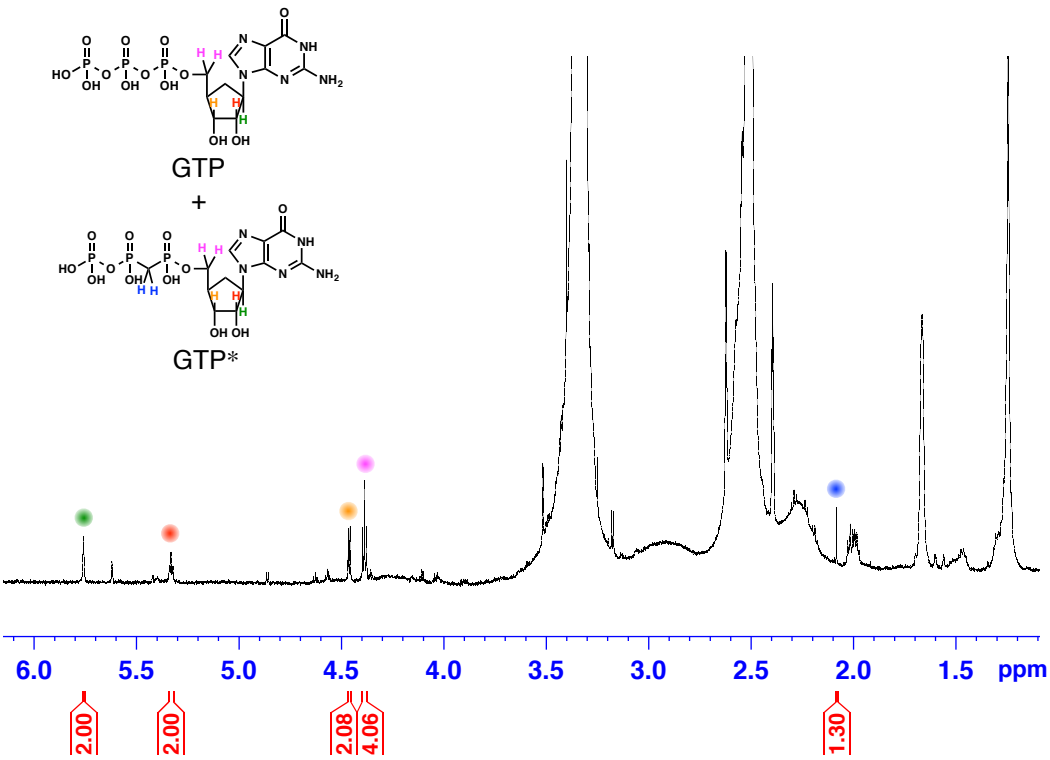

Supplementary Figure S4.66. 1H NMR spectrum (500 MHz) of NSGTP/GTP* in DMSO-d6 at 25 °C. Since two GTP molecules are hybridized to THDGTP, and one GTP and one GTP* molecule are hybridized to THDGTP*, the NMR results show that 65% of THDGTP* is contained in the NSGTP/GTP*. Signals marked with blue, magenta, orange, red, and green circles are assignable to protons in GTP and GTP*, which are highlighted in the corresponding colours.

*Self-assembly of THD in PIPES buffer containing a mixture of GTPγS and GTP**

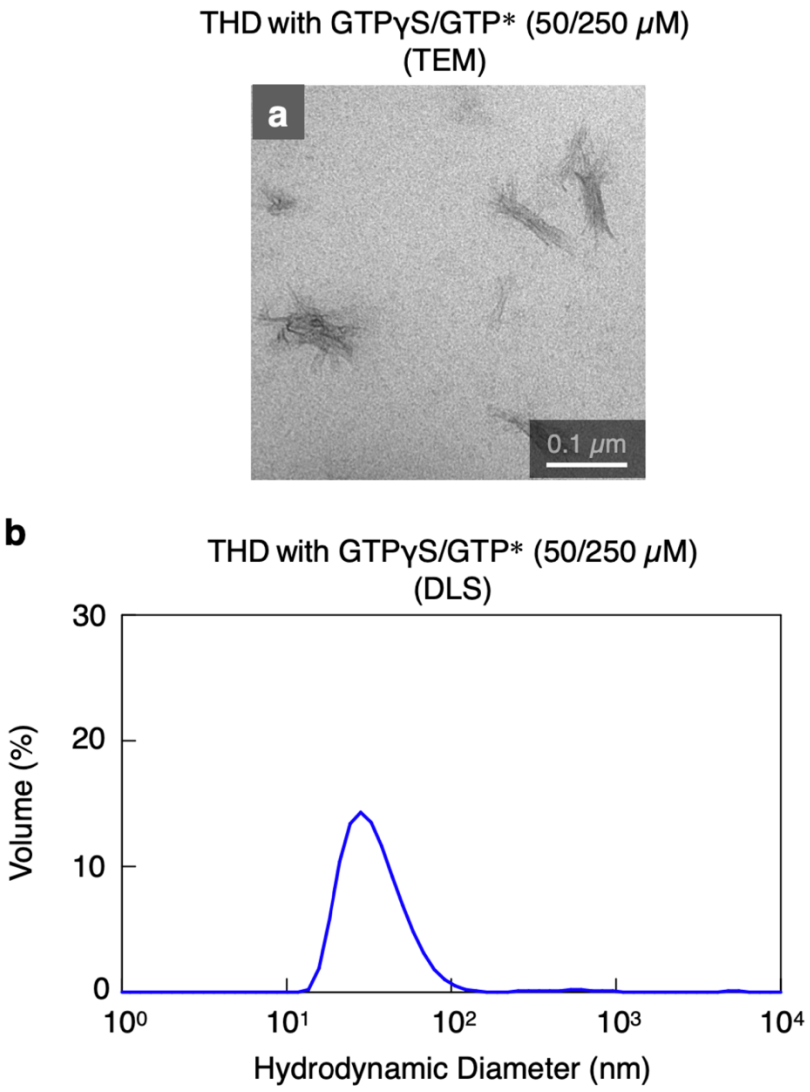

Supplementary Figure S 4.67. a, b, TEM image (a) and DLS profile (b) of THD (0.3 mg ml–1) after an incubation with GTPγS/GTP* (50/250 μM) at 37 °C for 30 min in PIPES buffer (100 mM PIPES and 1 mM MgCl2, pH 6.8).

Self-assembly of THD in PIPES buffer containing a mixture of GTP and GTPγS

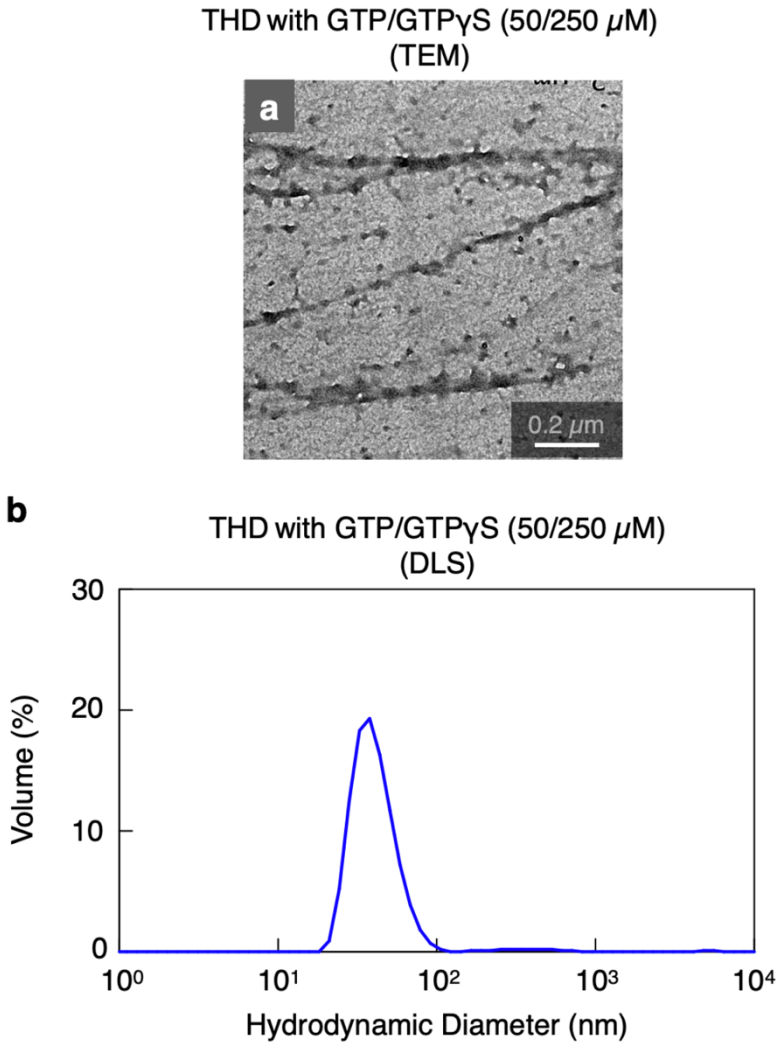

Supplementary Figure S 4.68. a, b, TEM image (a) and DLS profile (b) of THD (0.3 mg ml–1) after an incubation with GTP/GTPγS (50/250 μM) at 37 °C for 30 min in PIPES buffer (100 mM PIPES and 1 mM MgCl2, pH 6.8).

MTGTP treated with GlueCO2–*

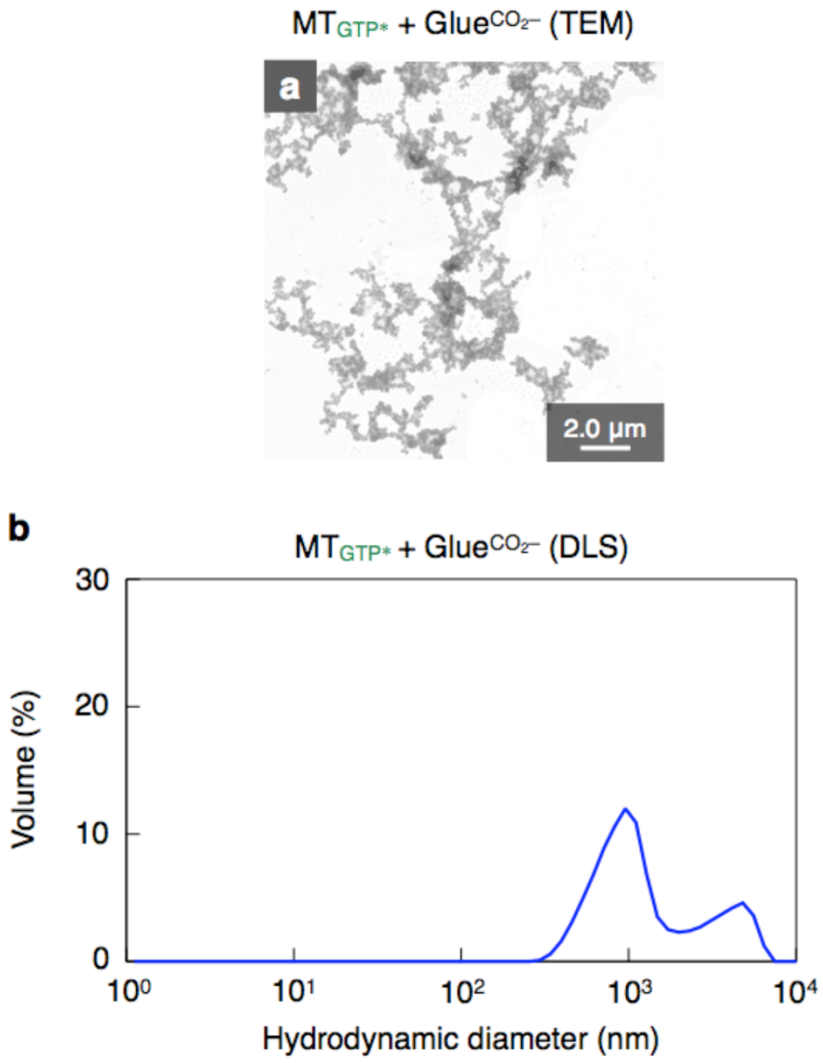

Supplementary Figure S 4.69. a, b, TEM image (a) and DLS profile (b) of MTGTP* (13 µg ml–1) in PIPES buffer (14 mM PIPES, 1 mM MgCl2, and 0.2 mM GTP*, pH 6.8) after an incubation with GlueCO2– (100 µM) at 37 °C for 30 min.

THDGDP treated with Glue^{CO2-}

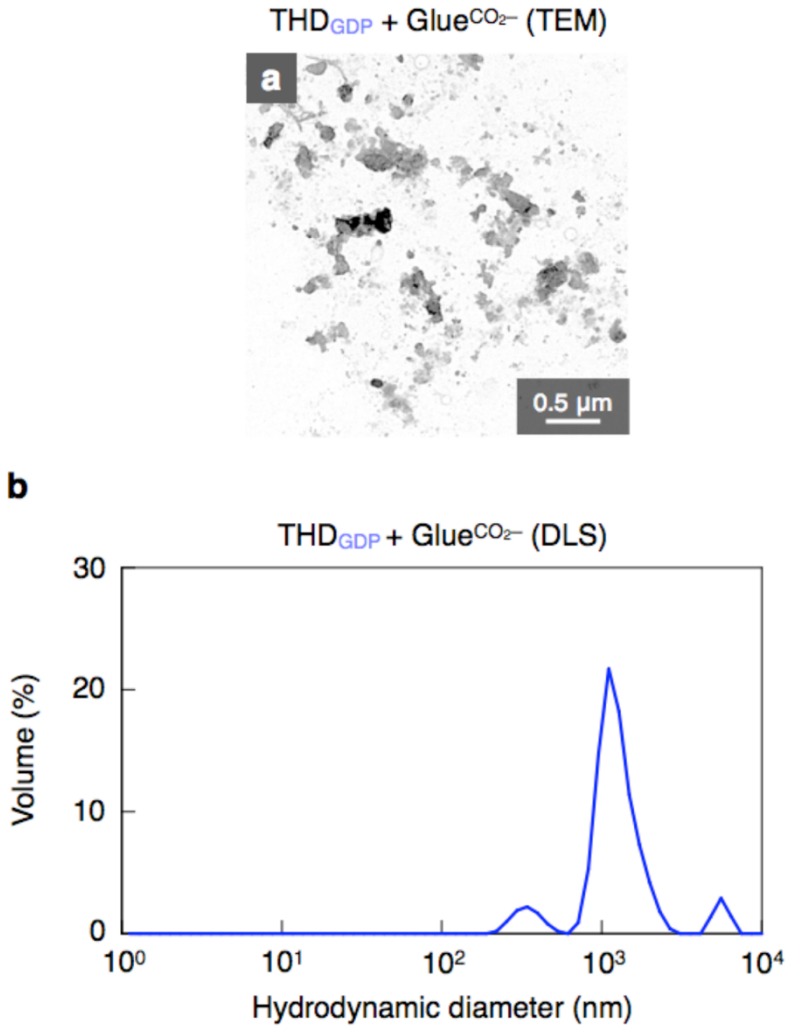

Supplementary Figure S4.70. a, b, TEM image (a) and DLS profile (b) of THDGDP (0.3 mg ml–1) in PIPES buffer (100 mM PIPES and 1 mM MgCl2, pH 6.8) after an incubation with GlueCO2– (100 µM) at 37 °C for 30 min.

Photo-induced covalent fixation of Glue^{FITC} onto THD$_{GDP}$

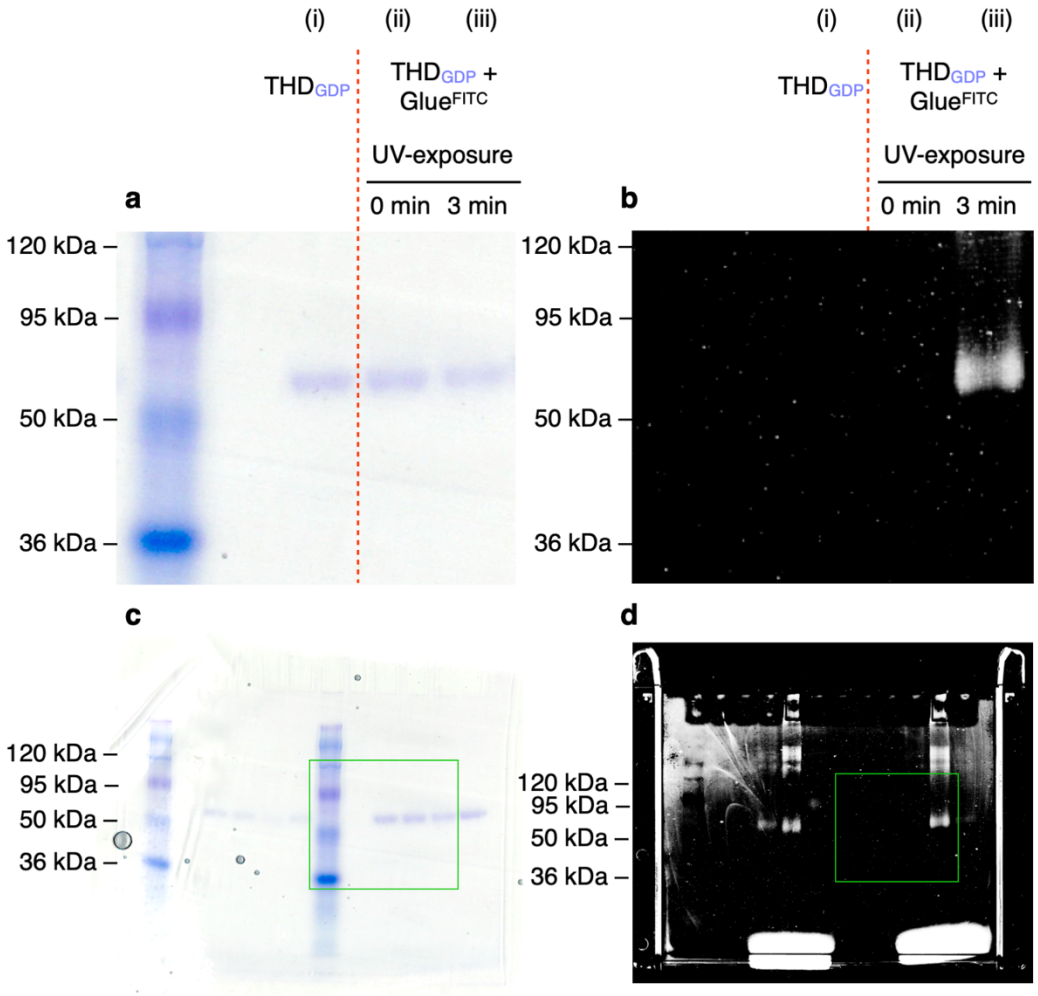

Supplementary Figure S4.71. a, b, Sodium dodecyl sulfate polyacrylamide gel electrophoresis (SDS– PAGE) analysis of THDGDP (0.15 mg ml–1; i) and a mixture of THDGDP (0.15 mg ml–1) and GlueFITC (10 μM) in PIPES buffer (20 mM PIPES, pH 6.8) before (ii) and after (iii) irradiation with 300-nm light for 3 min. The samples were visualized by staining with Coomassie Brilliant Blue (a) and by observing the fluorescence emission of FITC (λext = 488 nm, λobs = 526 nm; b). c, d, Uncropped version of gel images of a (c) and b (d), where green squares indicate cropped area.

AFM observation of $^{CL}NC_{GTP/GTP*}$

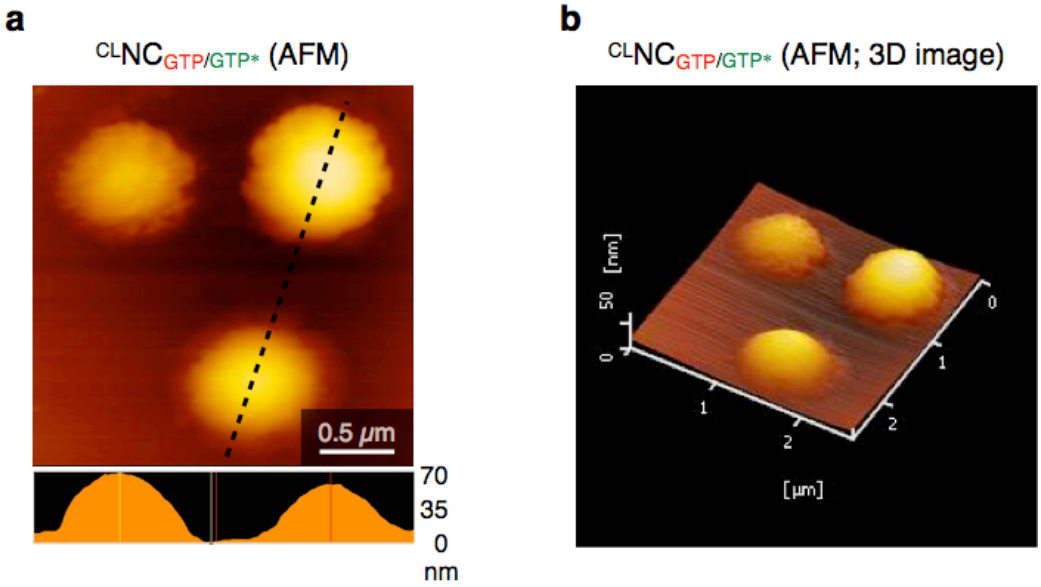

Supplementary Figure S4.72. a, b, 2D (a) and 3D (b) AFM images of a solution of CLNCGTP/GTP* (13 µg ml–1) in PIPES buffer (14 mM PIPES, 1 mM MgCl2, and 0.2 mM GTP*, pH 6.8).

Stability of $NC_{GTP/GTP*}$ and $^{CL}NC_{GTP/GTP*}$ in the presence of BSA

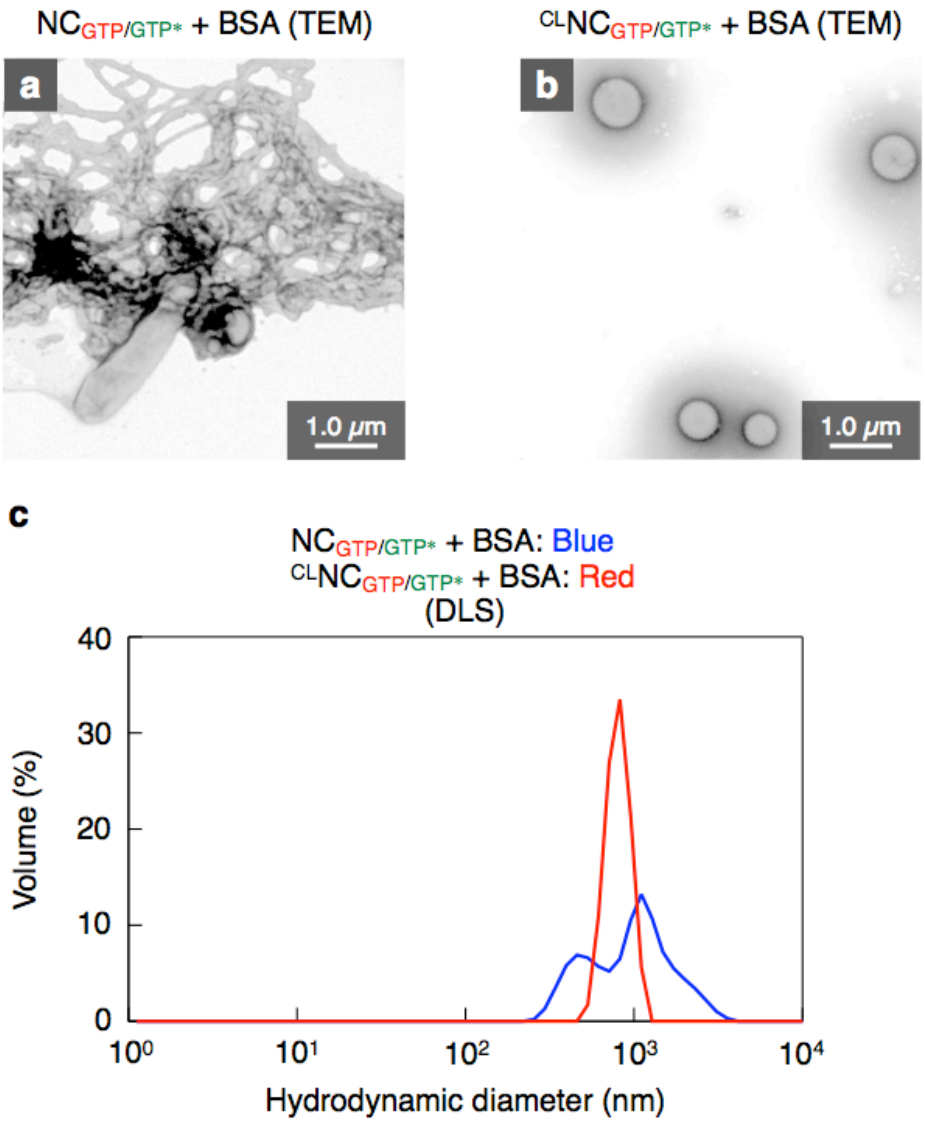

Supplementary Figure S4.73. a, b, TEM images of a solution of NCGTP/GTP* (13 μg ml–1; a) and CLNCGTP/GTP* (13 μg ml–1; b) in PIPES buffer (14 mM PIPES, 1 mM MgCl2, and 0.2 mM GTP*, pH 6.8) after an incubation with BSA (0.1 mg ml–1) at 37 °C for 30 min. c, DLS profiles of NCGTP/GTP* (blue) and CLNCGTP/GTP* (red) after the incubation with BSA.

Stability of $NC_{GTP/GTP*}$ and $^{CL}NC_{GTP/GTP*}$ in the presence of FBS

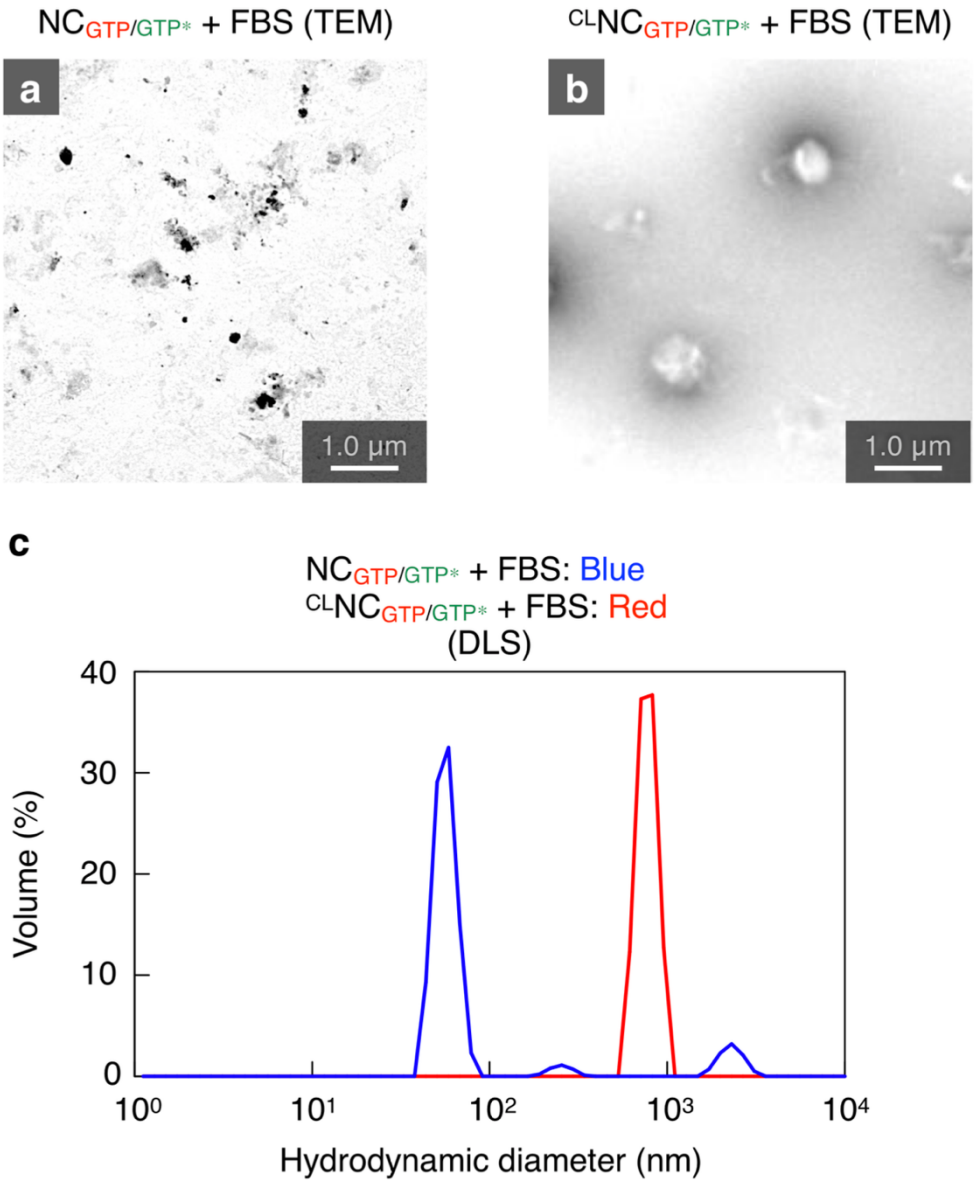

Supplementary Figure S4.74. a, b, TEM images of NCGTP/GTP* (13 μg ml–1; a) and CLNCGTP/GTP* (13 μg ml–1; b) after an incubation with FBS (0.01%) at 37 °C for 15 min in PIPES buffer (14 mM PIPES, 1 mM MgCl2, and 0.2 mM GTP*, pH 6.8). c, DLS profiles of NCGTP/GTP* (blue) and CLNCGTP/GTP* (red) after the incubation with FBS.

Formation of fluorescent $NC_{GTP/GTP*}$ and $^{CL}NC_{GTP/GTP*}$ using $Glue^{FITC}$

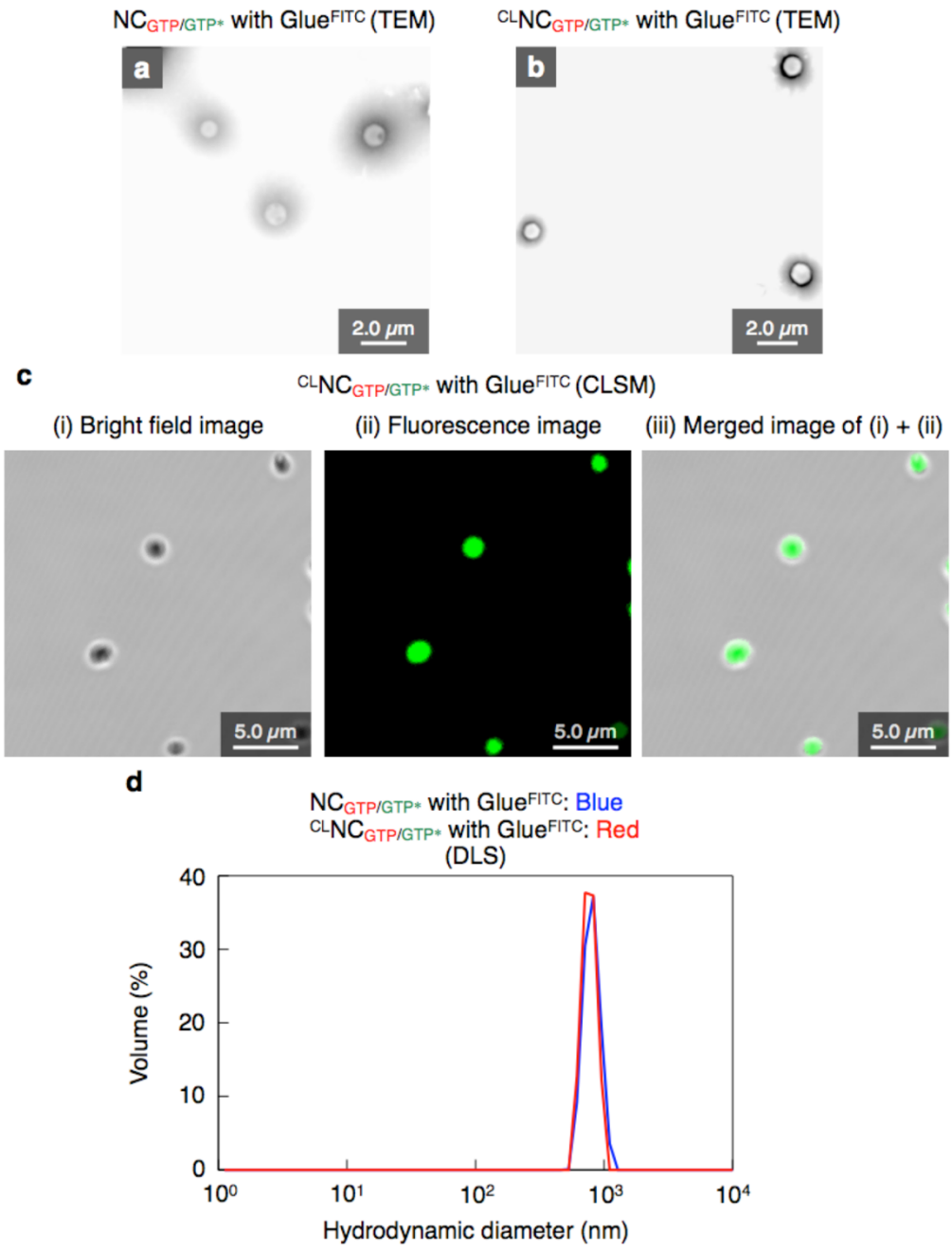

Supplementary Figure S4.75. a, b, TEM images of NCGTP/GTP* (13 μg ml–1; a) and CLNCGTP/GTP* (13 μg ml–1; b) prepared using GlueFITC (100 μM) in PIPES buffer (14 mM PIPES, 1 mM MgCl2, and 0.2 mM GTP*, pH 6.8). c, CLSM observation of CLNCGTP/GTP* prepared using GlueFITC (0.5 μg ml–1). (i) Bright field image, (ii) fluorescence image (λext = 488 nm, λobs = 505–565 nm), and (iii) a merged image of (i)

and (ii). d, DLS profiles of NCGTP/GTP* (blue curve) and CLNCGTP/GTP* (red curve) in PIPES buffer.

MD simulation of the folding of $Glue^{CO_2^-}$ *in aqueous solution*

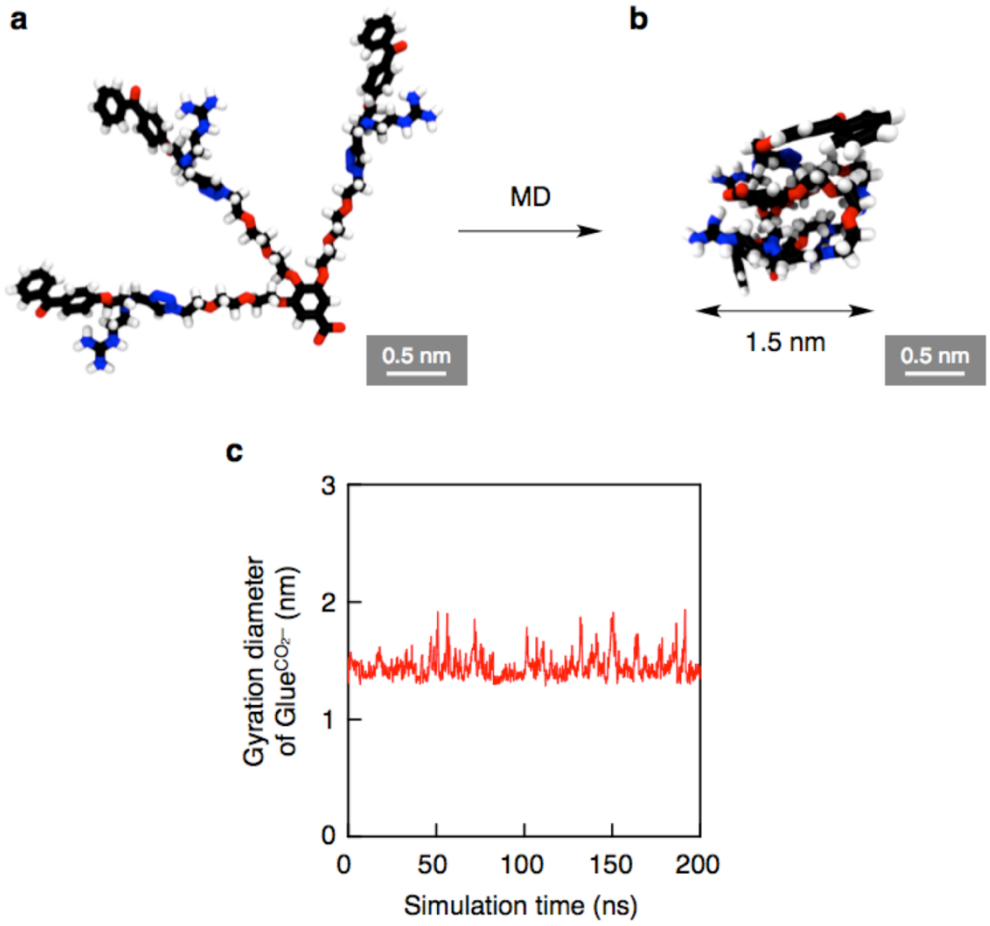

Supplementary Figure S4.76. a, b, Snapshot of Glue(CO2-) before (a) and after (b) the MD simulation. Nitrogen, oxygen, carbon, and hydrogen atoms of GlueCO2H are respectively coloured in blue, red, grey, and white. Water molecules and chloride anions are not shown explicitly and are the solution is represented in transparent blue for clarity. c, Gyration diameter of Glue(CO2-) calculated along 200 ns of MD simulation.

MD simulation of the adhesion of $Glue^{CO_2^-}$ onto THD_{GTP*}

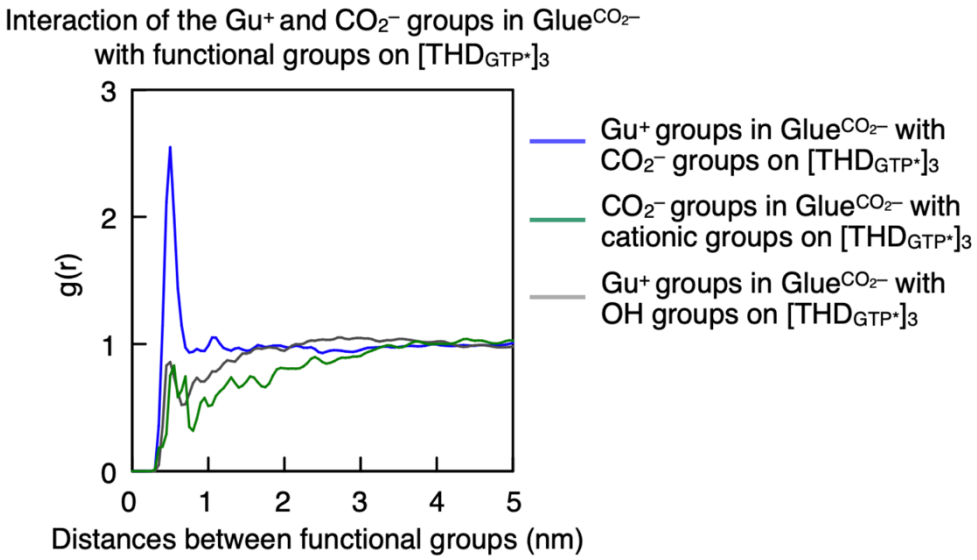

Supplementary Figure S4.77. Radial distribution functions g(r) of the Gu+ groups in GlueCO2– with CO2– groups (blue) and nonionic hydroxyl groups (grey) on [THDGTP*]3, and the CO2– group at the focal core of GlueCO2– with cationic groups on [THDGTP*]3 (green).

$NS_{GTP/GTP*}$ treated with $Glue^{CO2Me}$

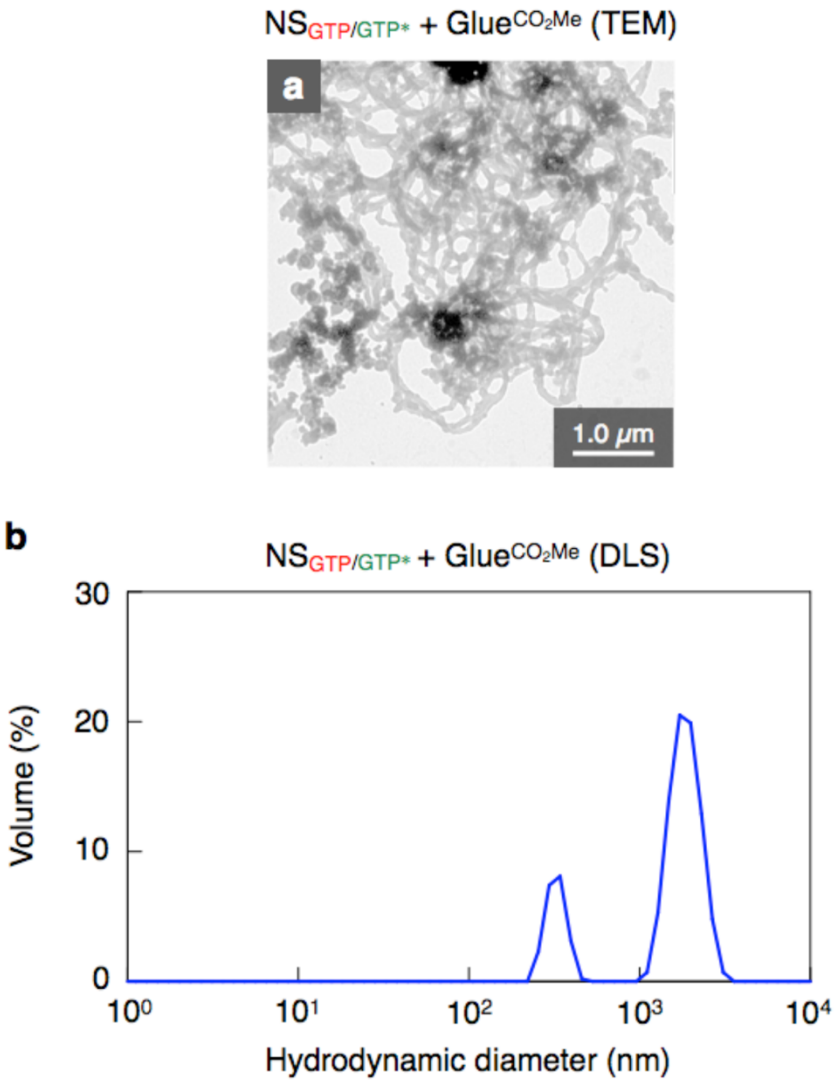

Supplementary Figure S 4.78. a, b, TEM image (a) and DLS profile (b) of NSGTP/GTP* (13 μg ml–1) in PIPES buffer (14 mM PIPES, 1 mM MgCl2, and 0.2 mM GTP*, pH 6.8) after an incubation with GlueCO2Me (100 μM) at 37 °C for 30 min.

*GTPase activity of THD depending on hybridization with GTP**

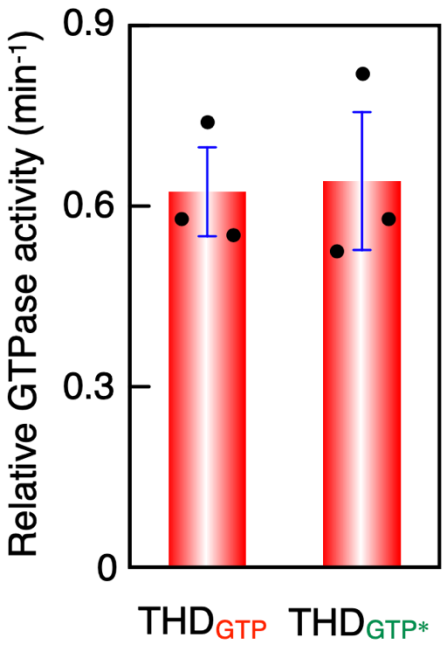

Supplementary Figure S4.79. GTPase activities of THDGTP (left) and THDGTP* (right) in PIPES buffer (14 mM PIPES, 1 mM MgCl2, pH 6.8). Red bars represent mean values ± SD from three different samples.

$^{CL}NC_{GTP/GTP*}$ treated with triphosphates

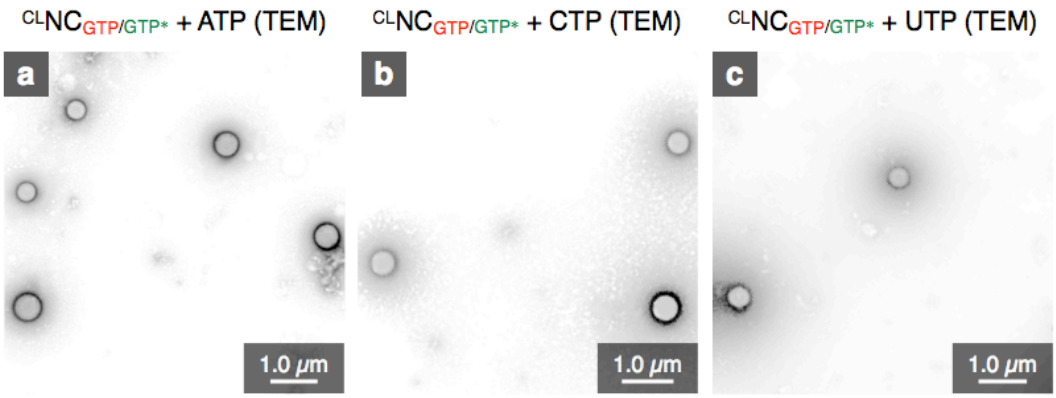

Supplementary Figure S4.80. a–c, TEM images of CLNCGTP/GTP* (9 µg ml–1) after an incubation with 0.5 mM of ATP (a), CTP (b), or UTP (c) at 37 °C for 100 min in PIPES buffer (13 mM PIPES, 0.7 mM MgCl2, and 0.1 mM GTP*, pH 6.8).

$^{CL}NC_{GTP/GTP*}$ without addition of GTP

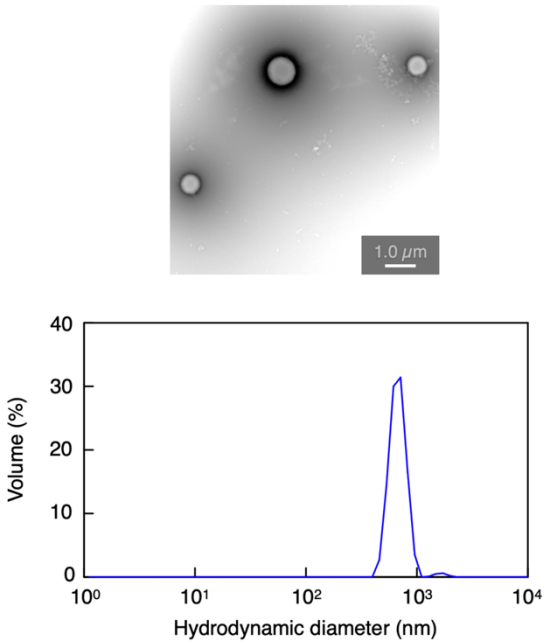

Supplementary Figure S4.81. a, b, TEM image (a) and DLS profile (b) of CLNCGTP/GTP* (9 μg ml–1) after an incubation at 37 °C for 100 min in PIPES buffer (13 mM PIPES, 0.7 mM MgCl2, and 0.1 mM GTP*, pH 6.8).

Encapsulation of NPAu into $^{CL}NC_{GTP/GTP*}$

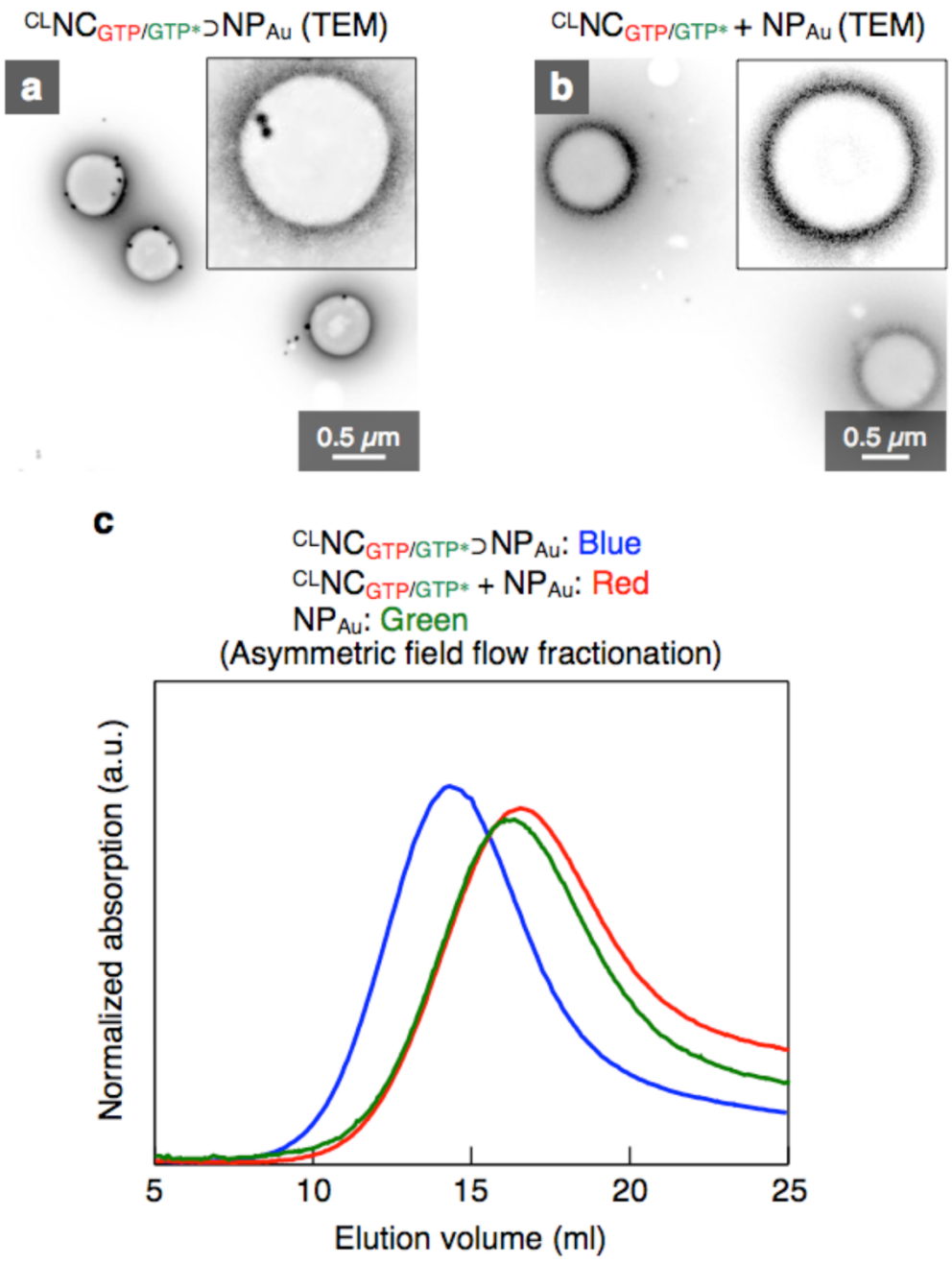

Supplementary Figure S4.82. a, b, TEM images of CLNCGTP/GTP*⊃NPAu ([CLNCGTP/GTP*] = 13 μg ml– 1, [NPAu] = 13 pM; a) and a mixture of CLNCGTP/GTP* (13 μg ml–1) and NPAu (13 pM; b). c, Elution profiles of

CLNCGTP/GTP*⊃NPAu (blue), the mixture of CLNCGTP/GTP* and NPAu (red), and NPAu (green) obtained using asymmetric field flow fractionation.

Encapsulation of DOX into $^{CL}NC_{GTP/GTP*}$

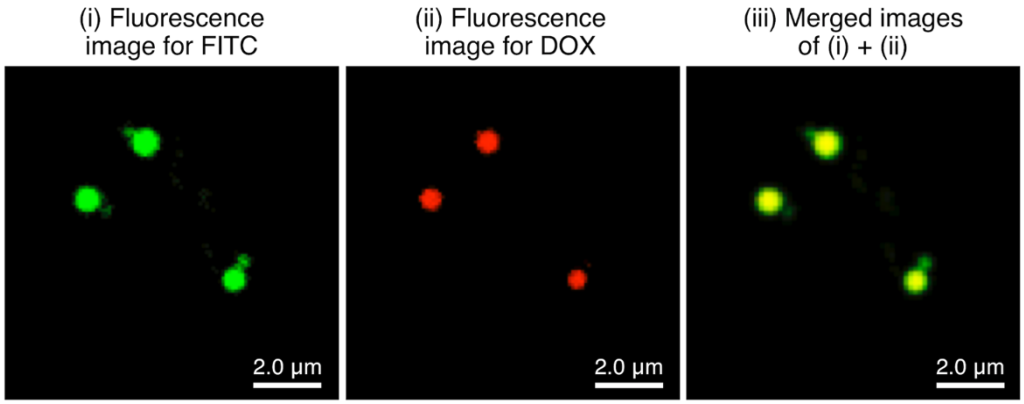

Supplementary Figure S4.83. CLSM observations of FITC-labelled CLNCGTP/GTP*⊃DOX. (i) λext = 488 nm, λobs = 505–520 nm for FITC, (ii) λext = 488 nm, λobs = 570–645 nm for DOX, and (iii) a merged image of (i) and (ii).

Uptake of FITC-labelled THD_{GDP} into Hep3B cells

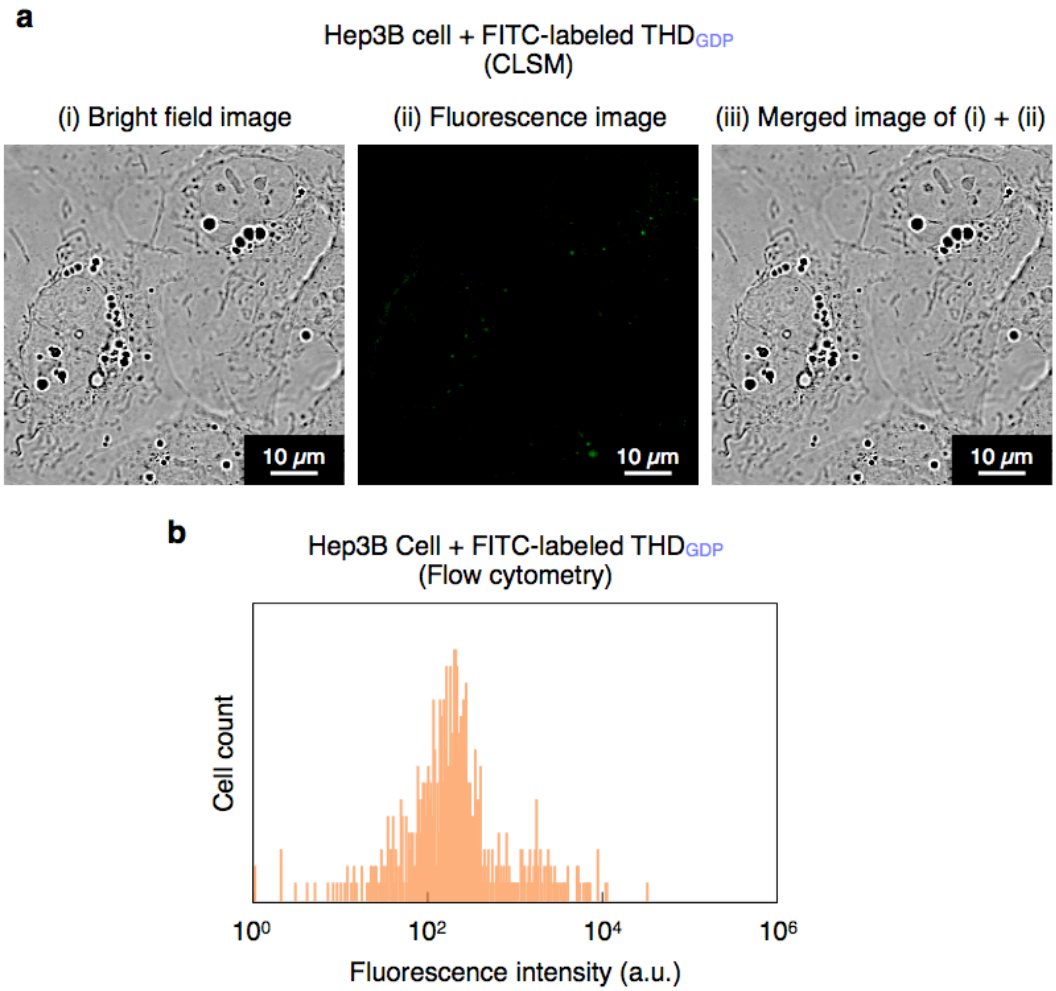

Supplementary Figure S4.84. a, CLSM images of Hep3B cells after 2.5-h incubation with FITC- labelled THDGDP (0.5 μg ml–1) at 37 °C in EMEM and rinsing with D-PBS, followed by 1.5-h incubation in EMEM (10% FBS). (i) Bright field image, (ii) fluorescence image (λext = 488 nm, λobs = 505–565 nm), and (iii) a merged image of (i) and (ii). b, Flow cytometry analysis of the Hep3B cell sample (n = 630).

Uptake of FITC-labelled $NS_{GTP/GTP*}$ into Hep3B cells

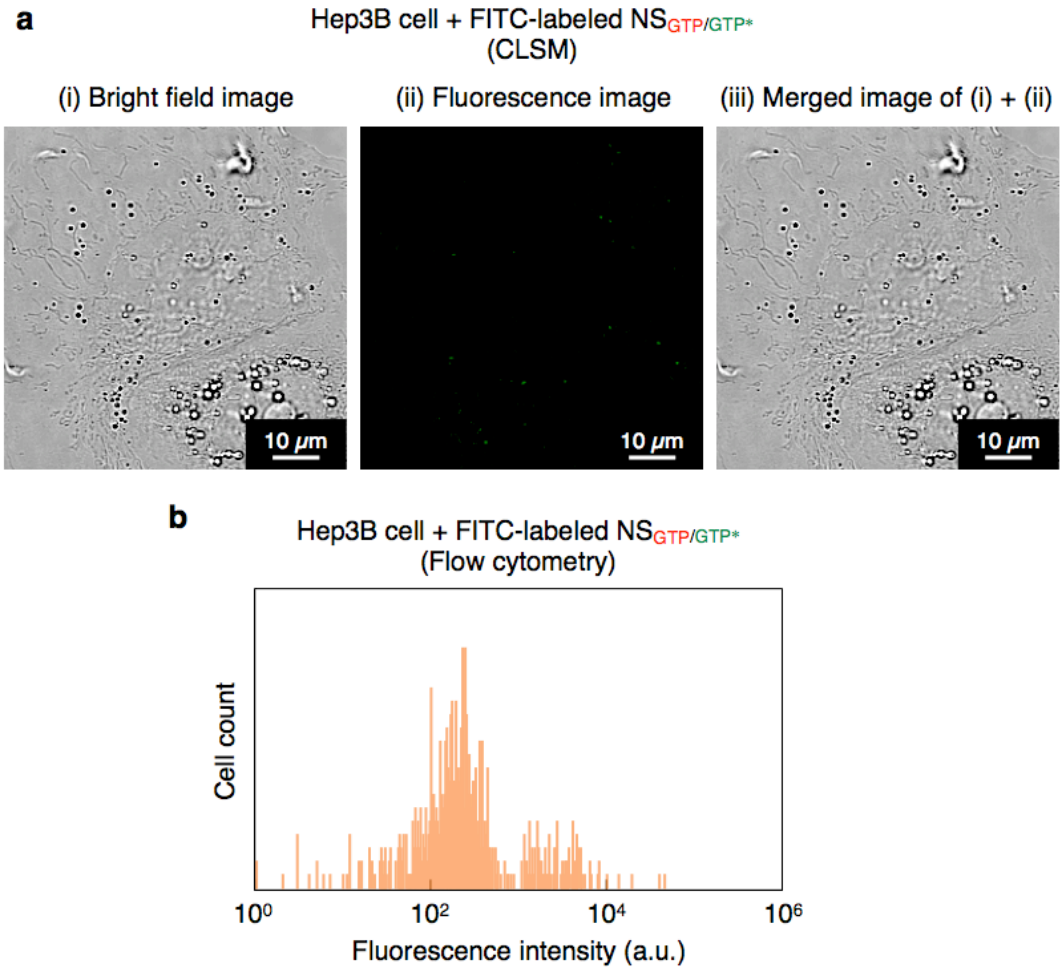

Supplementary Figure S 4.85. a, CLSM images of Hep3B cells after 2.5-h incubation with FITC- labelled NSGTP/GTP* (0.5 μg ml–1) at 37 °C in EMEM and rinsing with D-PBS, followed by 1.5-h incubation in EMEM (10% FBS). (i) Bright field image, (ii) fluorescence image (λext = 488 nm, λobs = 505–565 nm), and (iii) a merged image of (i) and (ii). b, Flow cytometry analysis of the Hep3B cell sample (n = 630).

Uptake of FITC-labelled $^{CL}NC_{GTP/GTP*}$ into Hep3B cells treated with an endocytosis inhibitor

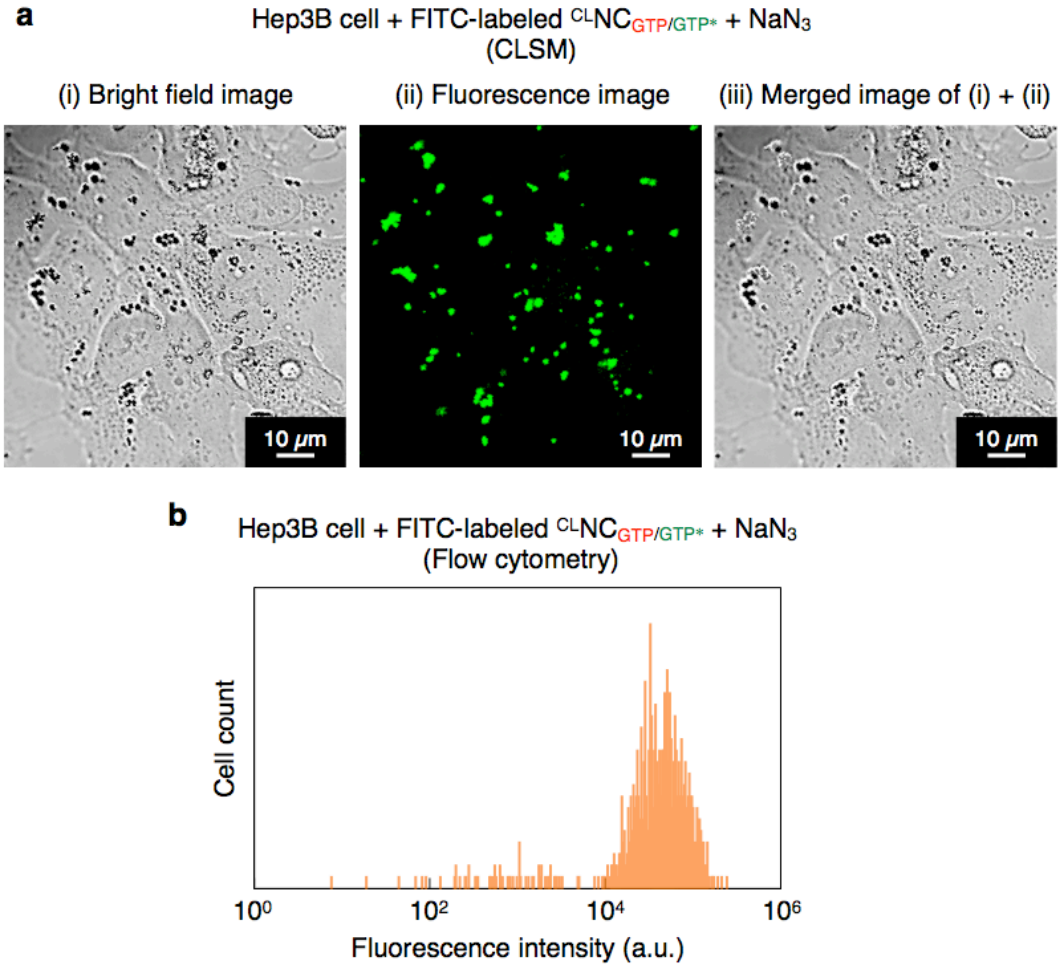

Supplementary Figure S 4.86. a, CLSM images of Hep3B cells after 2.5-h incubation with FITC- labelled CLNCGTP/GTP* (0.5 μg ml–1) in the presence of 5 mM of NaN3 (endocytosis inhibitor) at 37 °C in EMEM and rinsing with D-PBS, followed by 1.5-h incubation in EMEM (10% FBS). (i) Bright field image, (ii) fluorescence image (λext = 488 nm, λobs = 505–565 nm), and (iii) a merged image of (i) and (ii). b, Flow cytometry analysis of the Hep3B cell sample (n = 700).

Dose dependency on cytotoxicity of $^{CL}NC_{GTP/GTP*}\supset DOX$

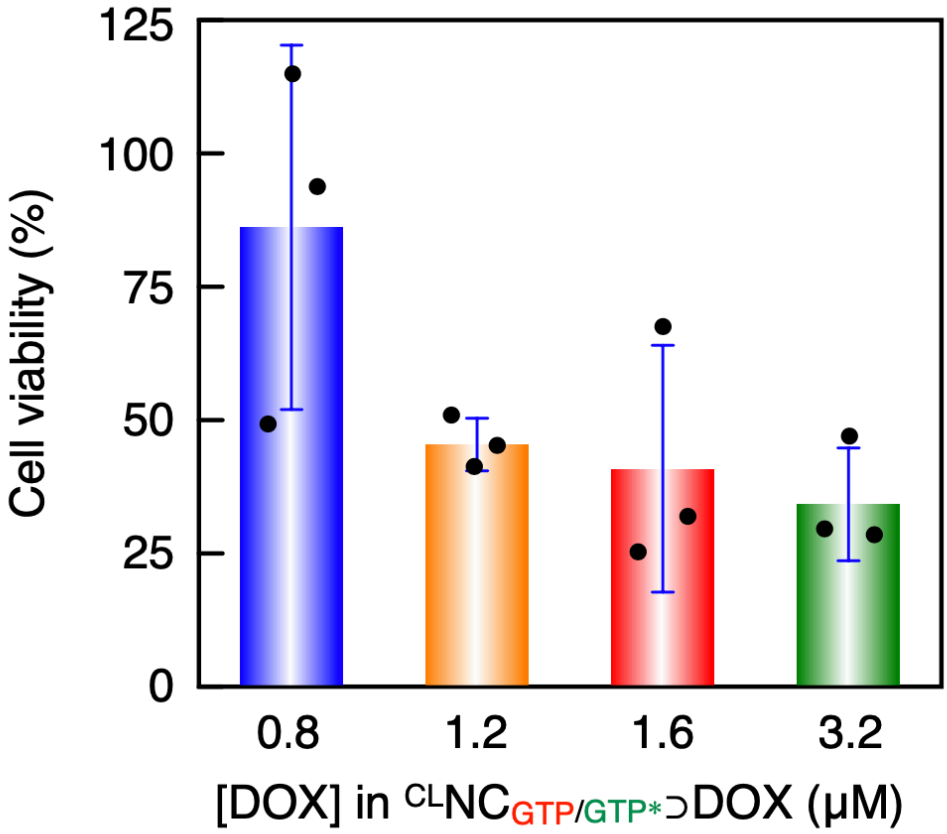

Supplementary Figure S4.87. Normalized viabilities of Hep3B cells determined using Cell Counting Kit-8. Hep3B cells were treated with four different concentrations of CLNCGTP/GTP* ⊃ DOX ([CLNCGTP/GTP*] = 1.0 μg ml–1, [DOX] = 0.8 μM; blue), ([CLNCGTP/GTP*] = 1.6 μg ml–1, [DOX] = 1.2 μM; orange), ([CLNCGTP/GTP*] = 2.1 μg ml–1, [DOX] = 1.6 μM; red), and ([CLNCGTP/GTP*] = 4.2 μg ml–1, [DOX] = 3.2 μM; green) for 2.5 h in EMEM, rinsed with D-PBS, and incubated in EMEM (10% FBS) for 21.5 h. Bars represent mean values ± SD from three different samples.

Incubation time dependency on cytotoxicity of $^{CL}NC_{GTP/GTP*}\supset DOX$

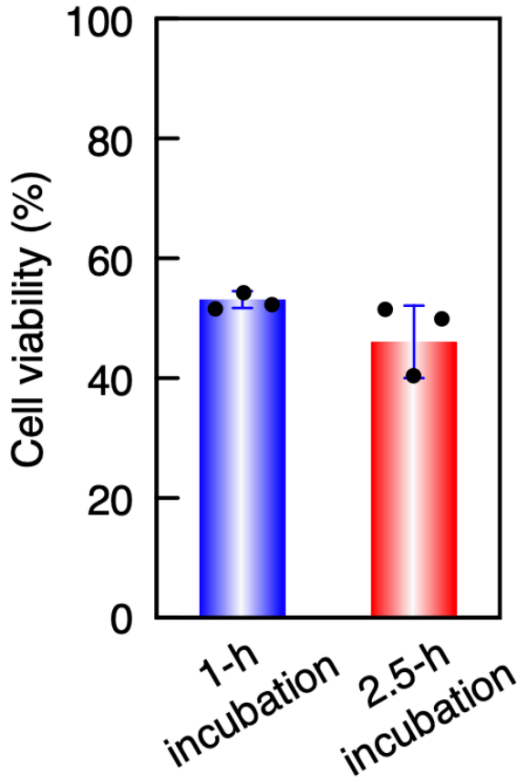

Supplementary Figure S4.88. Normalized viabilities of Hep3B cell determined using Cell Counting Kit-8. Hep3B cells were incubated in EMEM containing CLNCGTP/GTP*⊃DOX ([CLNCGTP/GTP*] = 1.6 μg ml–1, [DOX] = 1.2 μM) for 1 h (blue) or 2.5 h (red), rinsed with D-PBS, and further incubated in EMEM (10% FBS) for 21.5 h. Bars represent mean values ± SD from three different samples.

Cell line dependency on cytotoxicity of $^{CL}NC_{GTP/GTP*}\supset DOX$

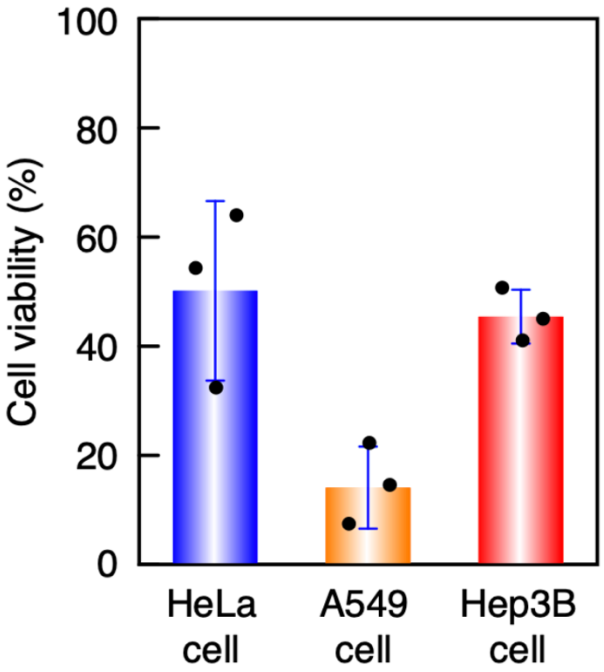

Supplementary Figure S4.89. Normalized viabilities of HeLa cell (blue), A549 cell (orange), and Hep3B cell (red) determined using Cell Counting Kit-8. Cells were incubated in EMEM containing CLNCGTP/GTP*⊃DOX ([CLNCGTP/GTP*] = 1.6 μg ml–1, [DOX] = 1.2 μM) for 2.5 h, rinsed with D- PBS, and further incubated in EMEM (10% FBS) for 21.5 h. Bars represent mean values ± SD from three different samples.

Effects of encapsulation of DOX in $^{CL}NC_{GTP/GTP*}\supset DOX$ for cytotoxicity test

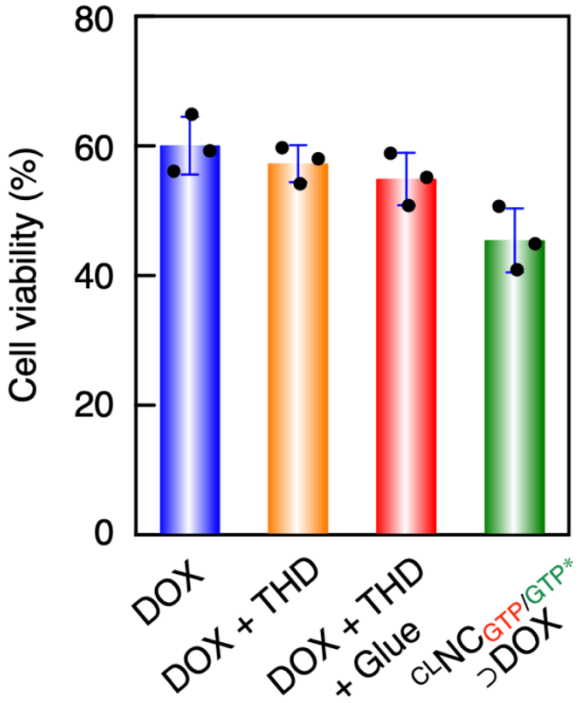

Supplementary Figure S4.90. Normalized viabilities of Hep3B cells determined using Cell Counting Kit-8. Hep3B cells were incubated in EMEM for 2.5 h containing DOX (1.2 μM; blue), a mixture of DOX and THDGDP ([DOX] = 1.2 μM, [THDGDP] = 1.6 μg; orange), a mixture of DOX, THDGDP, and GlueCO2– ([DOX] = 1.2 μM, [THDGDP] = 1.6 μg, [GlueCO2–] = 12.3 μM; red), and CLNCGTP/GTP* ⊃DOX ([CLNCGTP/GTP*] = 1.6 μg ml–1, [DOX] = 1.2 μM; green), rinsed with D-PBS, and further incubated in EMEM (10% FBS) for 21.5 h. Bars represent mean values ± SD from three different samples.

Appendix References

1. Zhang, Y., Forli, S., Omelchenko, A. & Sanner, M. F. AutoGridFR: Improvements on AutoDock Affinity Maps and Associated Software Tools. *Journal of Computational Chemistry* **40**, 2882–2886 (2019).

2. Santoshi, S. & Naik, P. K. Molecular insight of isotypes specific β-tubulin interaction of tubulin heterodimer with noscapinoids. *Journal of Computer-Aided Molecular Design* **28**, 751–763 (2014).

3. Messaoudi, A., Belguith, H. & Ben Hamida, J. Homology modeling and virtual screening approaches to identify potent inhibitors of VEB-1 β-lactamase. *Theoretical Biology and Medical Modelling* **10**, 1–10 (2013).

4. Tomalia, D. A. & Rookmaker, M. The Polymer Data Handbook. Poly(1,3-trimethyleneimine) dendrimers. in *Polymer Data Handbook, 2nd ed.* (ed. Mark, J.) 979–982 (Oxford University Press, 2009).

5. Maingi, V., Jain, V., Bharatam, P. V. & Maiti, P. K. Dendrimer building toolkit: Model building and characterization of various dendrimer architectures. *Journal of Computational Chemistry* **33**, 1997–2011 (2012).

6. Opitz, A. W. & Wagner, N. J. Structural investigations of poly(amido amine) dendrimers in methanol using molecular dynamics. *Journal of Polymer Science, Part B: Polymer Physics* **44**, 3062–3077 (2006).

7. Barraza, L. F., Zuñiga, M., Alderete, J. B., Arbeloa, E. M. & Jiménez, V. A. Effect of pH on Eosin Y/PAMAM interactions studied from absorption spectroscopy and molecular dynamics simulations. *Journal of Luminescence* **199**, 258–265 (2018).

8. Caballero, J., Poblete, H., Navarro, C. & Alzate-Morales, J. H. Association of nicotinic acid with a poly(amidoamine) dendrimer studied by molecular dynamics simulations. *Journal of Molecular Graphics and Modelling* **39**, 71–78 (2013).

9. Kanchi, S., Gosika, M., Ayappa, K. G. & Maiti, P. K. Dendrimer Interactions with Lipid Bilayer: Comparison of Force Field and Effect of Implicit vs Explicit Solvation. *Journal of Chemical Theory and Computation* **14**, 3825–3839

(2018).

10.Kavyani, S., Amjad-Iranagh, S., Dadvar, M. & Modarress, H. Hybrid Dendrimers of PPI(core)-PAMAM(shell): A Molecular Dynamics Simulation Study. *Journal of Physical Chemistry B* **120**, 9564–9575 (2016).

11.Ramos, M. C., Horta, V. A. C. & Horta, B. A. C. Molecular Dynamics Simulations of PAMAM and PPI Dendrimers Using the GROMOS-Compatible 2016H66 Force Field. *Journal of Chemical Information and Modeling* **59**, 1444–1457 (2019).

12.Lee, I., Athey, B. D., Wetzel, A. W., Meixner, W. & Baker, J. R. Structural molecular dynamics studies on polyamidoamine dendrimers for a therapeutic application: Effects of pH and generation. *Macromolecules* **35**, 4510–4520 (2002).

13.Porcar, L. *et al.* Structural investigation of PAMAM dendrimers in aqueous solutions using small-angle neutron scattering: Effect of generation. *Journal of Physical Chemistry B* **112**, 14772–14778 (2008).

14.Rathgeber, S., Monkenbusch, M., Kreitschmann, M., Urban, V. & Brulet, A. Dynamics of star-burst dendrimers in solution in relation to their structural properties. *Journal of Chemical Physics* **117**, 4047–4062 (2002).

15.Liu, Y., Bryantsev, V. S., Diallo, M. S. & Goddard, W. A. PAMAM dendrimers undergo pH responsive conformational changes withoutswelling. *Journal of the American Chemical Society* **131**, 2798–2799 (2009).

16.Maiti, P. K., Çağin, T., Lin, S. T. & Goddard, W. A. Effect of solvent and pH on the structure of PAMAM dendrimers. *Macromolecules* **38**, 979–991 (2005).

17.Topp, A., Bauer, B. J., Tomalia, D. A. & Amis, E. J. Effect of solvent quality on the molecular dimensions of PAMAM dendrimers. *Macromolecules* **32**, 7232–7237 (1999).

18.Scherrenber, R. *et al.* The molecular characteristics of poly(propyleneimine) dendrimers as studied with small-angle neutron scattering, viscosimetry, and molecular dynamics. *Macromolecules* **31**, 456–461 (1998).

19.Prosa, T. J., Bauer, B. J., Amis, E. J., Tomalia, D. A. & Scherrenberg, R. A SAXS study of the internal structure of dendritic polymer systems. *Journal of Polymer Science, Part B: Polymer Physics* **35**, 2913–2924 (1997).

20.Jain, V., Maingi, V., Maiti, P. K. & Bharatam, P. V. Molecular dynamics simulations of PPI dendrimer-drug complexes. *Soft Matter* **9**, 6482–6496 (2013).

21.Wu, C. PH response of conformation of poly(propylene imine) dendrimer in water: A molecular simulation study. *Molecular Simulation* **36**, 1164–1172 (2010).

Proudly written by a human being without the use of AI.